

DEVELOPMENT, CHARACTERIZATION AND APPLICATIONS OF
MAGNETORHEOLOGICAL FLUID BASED 'SMART' MATERIALS ON THE
MACRO-TO-MICRO SCALE

by

SURAJ SHARADCHANDRA DESHMUKH

B.Tech., Chemical Engineering (2001)
Indian Institute of Technology, Bombay

M.S., Mechanical Engineering (2003)
Massachusetts Institute of Technology

Submitted to the Department of Mechanical Engineering
in Partial Fulfillment of the Requirements for the Degree of

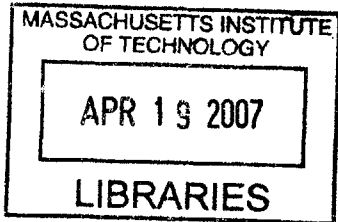
Doctor of Philosophy in Mechanical Engineering

at the

MASSACHUSETTS INSTITUTE OF TECHNOLOGY

February 2007

© 2006 Massachusetts Institute of Technology
All rights reserved




BARKER

Signature of Author.....

Department of Mechanical Engineering
September 29, 2006

Certified by.....


Gareth H. McKinley
Professor of Mechanical Engineering
Thesis Supervisor

Accepted by.....

Lallit Anand
Professor and Chairman, Department Committee on Graduate Students

Development, Characterization and Applications of Magnetorheological Fluid based
'Smart' Materials on the Macro-to-Micro scale

by

Suraj Sharadchandra Deshmukh

Submitted to the Department of Mechanical Engineering
on September 29, 2006 in partial fulfillment of the
requirements for the Degree of Doctor of Philosophy in
Mechanical Engineering

ABSTRACT

Magnetorheological fluids belong to the class of field-responsive fluids that undergo large, reversible and fast changes in their rheological properties when acted upon by an external magnetic field. 'Smart' or controllable composite materials have been obtained by doping polymers, foams, fabrics etc. with these field-responsive fluids. The resulting composite materials have potential applications in numerous fields ranging from adaptive energy absorption, automotive crash protection to microfluidic valves, mixers and separation devices.

A series of stable magnetorheological (MR) fluids have been systematically characterized under steady shearing, creep and large amplitude oscillatory shear (LAOS) flow conditions. A rheometer fixture for applying nearly uniform magnetic fields up to 0.4 T has been fabricated to measure both steady-state and transient changes in the fluid properties under applied fields. Stable MR fluids with a markedly improved dynamic response (yield stress as a function of magnetic field) compared to commercial fluids have been formulated by increasing the constituent particle size and by stabilizing the system against sedimentation. A new "soft-glassy rheology" model has been used to model the fluid response time and visco-elasto-plastic response under creep conditions and oscillatory loadings. The experiments and model show that the evolution of chain

structure and plastic collapse in these suspensions exhibits a universal scaling with the dimensionless stress $s = \sigma/\sigma_y$.

Structure evolution, pattern formation and dynamics of MR fluid flow in microchannel geometries has been analyzed using high-speed digital video microscopy. In order to elucidate the mechanisms that control MR structure formation, experiments have been performed while varying the magnetic field, particle size, channel geometry, concentration and fluid composition. Excellent qualitative agreement has been obtained with Brownian Dynamics simulations and useful scalings based on interplay of magnetostatic & viscous forces have been extracted to understand the field-dependent fluid response on the macro & micro scale.

Novel MR elastomeric materials and microparticles have been synthesized by doping photo-curable or thermo-curable polymers with field-responsive fluids. A high-throughput micromolding technique for synthesis of controllable particles of anisotropic shapes and sizes has been developed. Flexible and permanent chain-like structures have also been synthesized using amidation chemistry. Potential microfluidic applications such as field-responsive valves, mixers and separation devices using these ‘smart’ materials have also been investigated.

Thesis Supervisor & Committee Chair:

Gareth H. McKinley (Professor of Mechanical Engineering)

Thesis Committee Members:

Patrick Doyle (Professor of Chemical Engineering)

Alice Gast (Professor of Chemical Engineering)

T. Alan Hatton (Professor of Chemical Engineering)

Anette Hosoi (Associate Professor of Mechanical Engineering)

ACKNOWLEDGEMENTS

I would like to express my deepest gratitude to my advisor, Prof. Gareth H. McKinley, for his expert guidance and constant encouragement. I have loved bouncing ideas off him and he has always patiently listened and encouraged me to work on them. I have learned a lot from his vast knowledge and will always admire his friendly nature and witty humor.

This thesis would not have been possible without the support of my family throughout these years. I am also indebted to my friends who have made every moment of my life here exciting and precious.

I would like to thank the Non-Newtonian Fluids group for their invaluable suggestions and all the people at Hatsopoulos Microfluids Laboratory for making this lab such a fun place to be in. Finally, I would like to acknowledge the financial support received from the Institute of Soldier Nanotechnology (ISN).

Table of Contents

Abstract	3
Acknowledgements	5
Chapter 1 Introduction	11
1.1 FIELD-RESPONSIVE FLUIDS	11
1.1.1 <i>Background</i>	11
1.1.2 <i>Magnetorheological (MR) vs Electrorheological (ER) Fluids</i>	13
1.1.3 <i>Challenges for MR/ ER Fluids</i>	14
1.2 MOTIVATION	15
Chapter 2 Magnetorheological Fluids: Bulk Characterization	19
2.1 COMPOSITION	19
2.1.1 <i>Laboratory Formulation of MR fluids</i>	23
2.2 APPARATUS FOR CHARACTERIZATION OF MR FLUIDS	28
2.2.1 <i>Rheometer: Previous fixture designs</i>	28
2.2.2 <i>Custom Rheometer Fixture Design</i>	30
2.3 STEADY STATE FLOW BEHAVIOR	39
2.3.1 <i>Background</i>	39
2.3.2 <i>Steady State flow behavior of commercial fluids</i>	42
2.3.3 <i>Steady State flow behavior of laboratory formulated MR fluids</i>	44
2.3.4 <i>Yield stress comparison of different MR fluids</i>	46
2.3.5 <i>Wall slip and migration of sample</i>	48
2.4 TIME-DEPENDENT RHEOLOGY: CREEP	50
2.5 VISCO-ELASTO-PLASTIC MODEL	55
2.5.1 <i>Previous models for yield stress fluids</i>	55
2.5.2 <i>Models for “soft-glassy materials”</i>	56
2.5.3 <i>Comparison of model predictions with experimental creep data</i>	62
2.6 OSCILLATORY FLOW	66

2.7	LISSAJOUS CURVES (LAOS SHAPES)	73
2.8	CONCLUSIONS	78
Chapter 3	Adaptive Energy Absorbing Materials	79
3.1	CONCEPT AND DEVELOPMENT OF THE ADAPTIVE MATERIAL	80
3.2	APPLICATION POTENTIAL FOR THE ADAPTIVE MATERIAL	83
3.2.1	<i>Automotive energy management</i>	83
3.2.2	<i>Protective armor</i>	85
3.2.3	<i>Challenges</i>	88
3.3	CONCLUSIONS	88
Chapter 4	Structure Formation and Dynamics of MR Fluid Flow in Microchannels	89
4.1	MODELING: PARTICLE INTERACTIONS	90
4.1.1	<i>Magnetic Interactions</i>	90
4.1.2	<i>Hydrodynamic Interactions</i>	92
4.1.3	<i>Brownian Motion</i>	93
4.1.4	<i>Dimensionless groups</i>	93
4.2	EXPERIMENTAL MATERIALS AND METHODS	95
4.2.1	<i>Background</i>	95
4.2.2	<i>Materials</i>	95
4.2.3	<i>Experimental setup: High-Speed Video Microscopy</i>	96
4.2.4	<i>Image Analysis Technique</i>	100
4.3	AGGREGATION PHENOMENA: QUIESCENT CASE	103
4.4	AGGREGATION PHENOMENA: PRESSURE-DRIVEN FLOW	110
4.4.1	<i>Background</i>	110
4.4.2	<i>Effect of Magnetic field strength on Structures</i>	113
4.4.3	<i>Effect of Flow rate on Structures</i>	116
4.4.4	<i>Effect of volume fraction on Aggregation phenomena</i>	119
4.4.5	<i>Effect of geometrical ratios on structures</i>	123
4.5	MECHANISMS OF AGGREGATION: SCALINGS	124

4.6	CLUSTER ANALYSIS: OTHER TECHNIQUES	135
4.7	COMPARISON OF EXPERIMENTAL RESULTS WITH BROWNIAN DYNAMICS SIMULATIONS	140
4.8	CONCLUSIONS	149
Chapter 5	Microscale Applications of ‘Smart’ Fluids & Materials	151
5.1	SYNTHESIS OF MAGNETIC MICROSTRUCTURES	152
5.1.1	<i>Magnetic Chains</i>	152
5.1.2	<i>Anisotropic Monodisperse Magnetic Microparticles</i>	160
5.2	MAGNETIC MICROSCALE APPLICATIONS	168
5.2.1	<i>Magnetic microfluidic separation chips</i>	168
5.2.2	<i>Magnetic microrheology probes</i>	170
5.2.3	<i>Magnetic microfluidic actuators and valves</i>	170
5.2.4	<i>Magnetic microfluidic mixers</i>	180
5.3	CONCLUSIONS	184
Chapter 6	Conclusions and Future Work	185
6.1	CONCLUSIONS	185
6.2	FUTURE WORK	188
	Bibliography	193

Chapter 1

Introduction

Adaptive materials or ‘smart’ fluids that can be user-controlled in response to external conditions have potential applications in a wide variety of fields ranging from energy management in automobiles, protective armor, sporting equipment and ‘artificial muscles’ to microfluidic actuation, biomaterial separations, micromechanical sensors and microrheology probes.

‘Smart’ materials with their adaptive capabilities and integrated designs can be actively controlled in response to the external environment. The field of ‘smart’ materials is interdisciplinary and comprises of a wide range of technologies such as piezoelectric materials, electrostrictive and magnetostrictive materials, shape memory alloys (SMA), conducting polymers, biometric gels and field-responsive fluids (Schwartz, 2002).

1.1 *Field-Responsive Fluids*

1.1.1 Background

Field-responsive fluids (FRFs) may be characterized as materials that undergo large changes in their rheological (i.e. flow) properties such as viscosity, elasticity or plasticity in response to changes in magnetic, electric or stress fields. Magnetorheological fluids (‘MR’ fluids), electrorheological (ER) fluids, shear-thickening fluids, liquid crystals and ferrofluids belong to the class of ‘field-responsive’ fluids (figure 1.1).

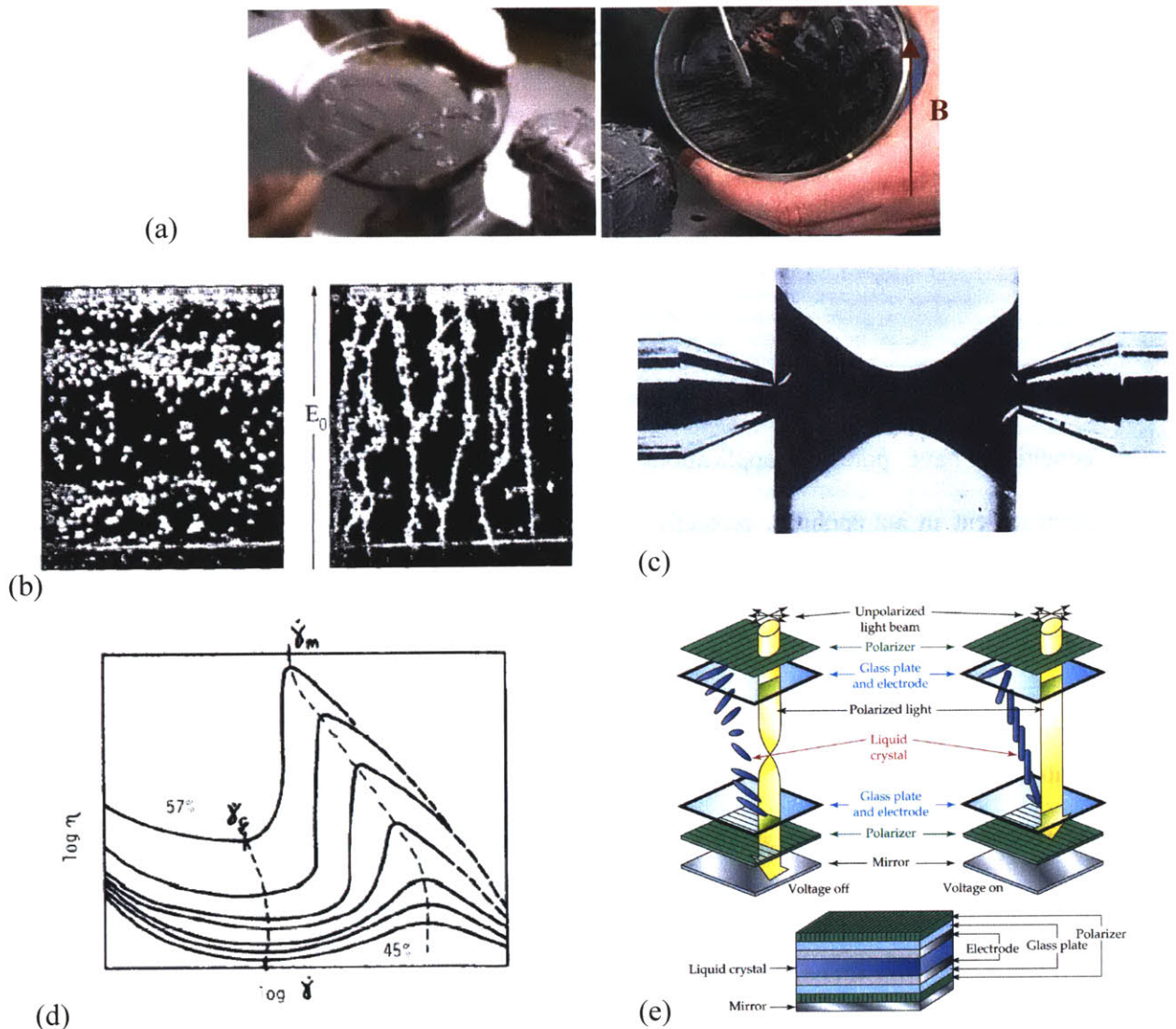


Figure 1.1 Field responsive fluids (a) Magnetorheological fluids (b) Electrorheological fluids (Parthasarthy and Klingenberg, 1996) (c) Ferrofluids (Rosensweig, 1985) (d) Shear-thickening fluids (Barnes, 1989) (e) Liquid crystals (McMurry and Fay, 2004).

MR fluids and ferrofluids both show dramatic & reversible changes in response to external magnetic fields. MR fluids are typically composed of micron-sized particles while the particles constituting ferrofluids are typically tens of nanometers in size. Ferrofluids which are typically composed of single domain magnetite particles show an increase in their viscosity with

increasing magnetic field though they maintain a fluid-like state (figure 1.1(c)). MR fluids, on the other hand, can reversibly change between a free-flowing liquid and a semi-solid state within few tens of milliseconds in the presence of a magnetic field (figure 1.1(a)). Electrorheological (ER) fluids are electric field analogs of MR fluids and show rapid and large changes in their rheological behavior in response to an applied electric field (figure 1.1(b)). Shear-thickening fluids respond to increasing deformation fields with large and reversible increase in their viscosity (figure 1.1(d)). Liquid crystals align in the presence of electric fields and hence show changes in their optical properties (figure 1.1(e)).

1.1.2 Magnetorheological (MR) vs Electrorheological (ER) Fluids

Magnetorheological fluids have been the focus of many studies since they can provide a simple, rapid-response interface between electronic controls and mechanical systems. They were first discovered and developed by Jacob Rabinow (1948) at the US National Bureau of Standards. W. M. Winslow (1947) is credited with the initial development of ER fluids.

The ultimate strength of MR fluids depends on the saturation magnetization of the dispersed particles and hence pure iron (saturation magnetization 2.15 T), or iron/cobalt alloy (saturation magnetization 2.4 T) particles are chosen. The maximum energy density in ER fluids, on the other hand, is determined by the dielectric breakdown (i.e. critical electric field when conduction paths within the fluid lead to destructive breakdown) for the particles and is about 2 orders of magnitude less than the MR fluids. The maximum yield strength of ER fluids is hence around 2–5 kPa as compared to nearly 150 kPa obtained for MR fluids¹. The active fluid needed for MR devices is thus much less as compared to ER devices resulting in much smaller devices. However, giant electrorheological (GER) suspensions comprising of nanoparticles coated with a low conducting material were recently reported of breaking this theoretical upper bound for ER yield stress and reached a maximum yield strength of 130 kPa (Wen *et al.*, 2003).

¹ <http://www.rheonetic.com>

ER fluids are hampered by a number of issues such as surface charge, electrode polarization, adsorbed water and field inhomogeneities (Promislow and Gast, 1995). The constituent particles are stabilized in the medium by the use of surfactants and other additives. ER fluids are sensitive to these additives and other impurities, while these do not affect the polarization mechanism in MR fluids leading to enhanced stability, lubricity etc. Further, temperature variations do not have a strong effect on magnetic polarization so that MR fluids can operate over a much larger temperature range (-40 °C to 150 °C) as compared to ER fluids. Hence, though MR fluids have appeared in number of commercial applications, ER fluid based applications have remained elusive.

However, since iron particles comprise most of the MR fluids, the fluids tend to be much heavier as compared to ER fluids and particle settling becomes an important concern.

1.1.3 Challenges for MR/ ER Fluids

ER fluids have been plagued by a number of problems and their inferior rheological properties and poor long-time stability as compared to MR fluids have prevented their use in commercial products. MR fluids on the other hand have a huge cost limitation and many more applications would quickly become commercial if the material cost could be reduced (Klingenberg 2001).

The saturation magnetization of MR particles, which is a material property attained when all the magnetic moments in the sample are aligned, is the limiting factor for determining the strength of MR fluids and a higher strength would clearly make many new applications viable. Since iron particles usually comprise an MR fluid, particle settling is an important concern though a viscoplastic medium or an absorbent matrix has been used to overcome these problems to a certain extent. In-use-thickening (IUT) or increase in the off-state force with time, as particles undergo wear and tear, is a significant challenge for the use of these fluids (Carlson 2001). Some recent patents (U.S. Patent No. 0045540) have claimed the development of durable

MR fluids, which reduce the agglomeration of particles with time, by use of mechanically hard magnetic particles and some anti-wear additives. However, much research effort is needed in understanding field-responsive fluid rheology before these limitations and challenges can be overcome and commercialization of new applications can be facilitated.

1.2 Motivation

The primary focus of this thesis work is to develop controllable materials by using field-responsive fluids by themselves or in adaptive ‘smart’ composites for doping and modifying existing material properties. These materials can then conform to the demands of the user and satisfy different requirements under a variety of external conditions.

A wide range of materials such as polymers, cellular solids, fabrics, plastics etc. can be ‘doped’ with MR/ ER fluids to obtain field-controllable materials that show dramatic & reversible changes in their mechanical properties in response to magnetic or electric fields. As an example, a ‘smart’ material consisting of a cellular solid impregnated with a field-responsive fluid such as a magnetorheological fluid can prove beneficial as an adaptive energy-absorbing material (Deshmukh and McKinley, 2007). Energy absorption, dissipation or shunting is an extremely important issue in automobiles, armor, protective gear and sporting equipment and controllable materials can provide an elegant energy management solution.

As an example, consider the car headrest, which is required to be soft and compliant so it is comfortable to the passengers but at the same time, during a rear-end crash, it is required to be rigid enough to absorb passenger head-impact energy and prevent whiplash. This is further complicated by the fact that different passengers, such as an adult or child, require different amounts of impact energy to be absorbed. A material that is rigid enough to satisfy adult impact energy requirements usually is too stiff to cushion a child’s head impact without harming it. New incoming Federal and European community legislations (FMVSS 201/202, EURO NCAP, EEVC

WG 17) introduce stringent impact protection requirements for car headrests, knee-bolsters, A, B, C pillars to be implemented in the next few years and this is a major concern in the automotive industry. A tunable headrest such as a magnetorheological fluid impregnated cellular solid can potentially resolve this ‘conflict of stiffness’ problem.

Another potential area of application of such tunable materials is as an ‘artificial muscle’ in robotic motion or as a microfluidic actuator. It may be possible to ‘dope’ PDMS, which is widely used in manufacturing of microfluidic devices, using magnetorheological fluids so that it can be controlled and actuated using external magnetic fields.

In microfluidic devices and applications, field-responsive fluids can be used as ‘smart’ fluids in bio-fluid analysis and DNA separation chips. The structure and patterns formed by MR fluids in microchannel geometries can be controlled by controlling the magnetic field which can then be used to separate or analyze DNA of different sizes (Doyle *et al.*, 2002).

However, in order for these applications to satisfy the functional requirements of various applications, it is equally important to understand the properties of field-responsive fluids and their property changes with variation in magnetic field, particle concentration and other parameters. Hence, a large part of this work is focused on characterizing and modeling the behavior of these field-responsive fluids, in particular magnetorheological fluids, on the micro and macro scale under different conditions.

A flowchart detailing the organization of this thesis work is shown in figure 1.2. The dissertation can be broadly divided into three parts – namely, synthesis or formulation of magnetorheological fluids, characterization and modeling of fluid behavior and application development. Since a fundamental understanding of the microstructural properties is vital to further our understanding of the bulk behavior, the characterization and application development of magnetorheological fluids and MR fluid based ‘smart’ composite materials is further organized into two separate but interconnected parts - macroscale and microscale.

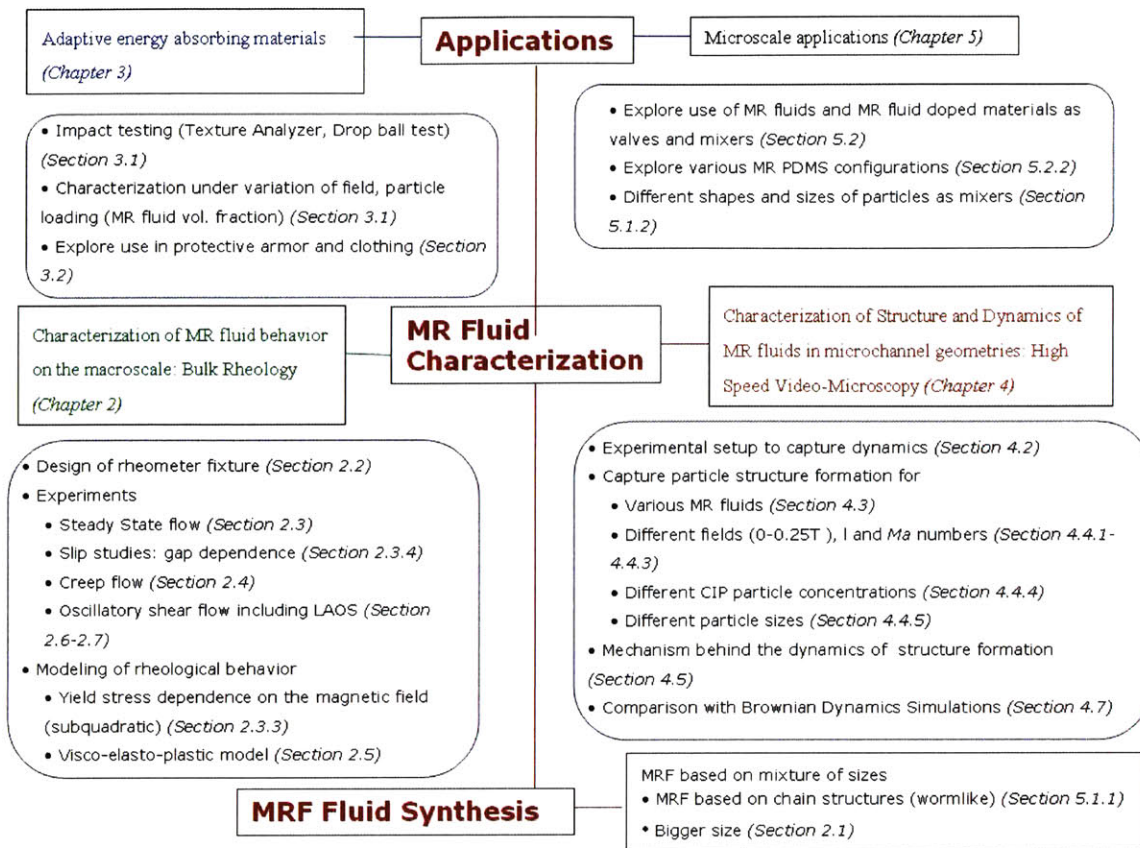


Figure 1.2 Thesis organization flowchart. The thesis work is divided into 3 main sections – synthesis or formulation of MRF’s, characterization and application of MR fluid and fluid-doped composite materials.

The detailed sectional organization of this thesis work is described in figure 1.2. The bulk rheological characterization of magnetorheological fluids in a range of flow conditions that are encountered in applications is described in chapter 2. Chapter 3 describes the application potential of magnetorheological fluids and MR fluid doped materials as an adaptive energy management solution in automotive applications, protective armor and sporting equipment. Chapter 4 discusses the structure and dynamics of magnetorheological fluids on the microscale and the use of high-speed video microscopy to elucidate the mechanisms of aggregation phenomena that ultimately govern the bulk behavior. Applications of controllable materials in micro-devices such

as microfluidic chips, 'artificial muscle' actuators and micro sensors are explored in detail in chapter 5. Conclusions and future work are outlined in chapter 6.

Chapter 2

Magnetorheological Fluids: Bulk Characterization

Magnetorheological fluids ('MR fluids') belong to the class of so-called "smart" or controllable materials (Ginder, 1996). A number of commercially-available and research-stage applications utilize the controllable nature along with the large, reversible changes in the rheological properties of magnetorheological fluids (Carlson, 1999; Klingenberg, 2001). Understanding the bulk rheological behavior and properties of these fluids is vital to these applications and also necessary for optimizing and designing composite "smart" materials doped with MR fluids (Deshmukh and McKinley, 2007).

2.1 Composition

Magnetorheological fluids are typically 20–50 % (by volume) suspensions of colloidal particles, usually 1-10 microns in size, in a carrier fluid such as a mineral oil, silicone oil, water or glycerol etc (Genc and Phule, 2002; Carlson, 2001). The magnetizable particles are soft magnetic solids (Ginder *et al.*, 1996) with a high saturation magnetization in the case of MR fluids while in the case of ER fluids they have a high dielectric constant and a suitable conductivity (e.g. alumina) (Klingenberg *et al.*, 1989; Klingenberg and Zukoski, 1990; Larson, 1999).

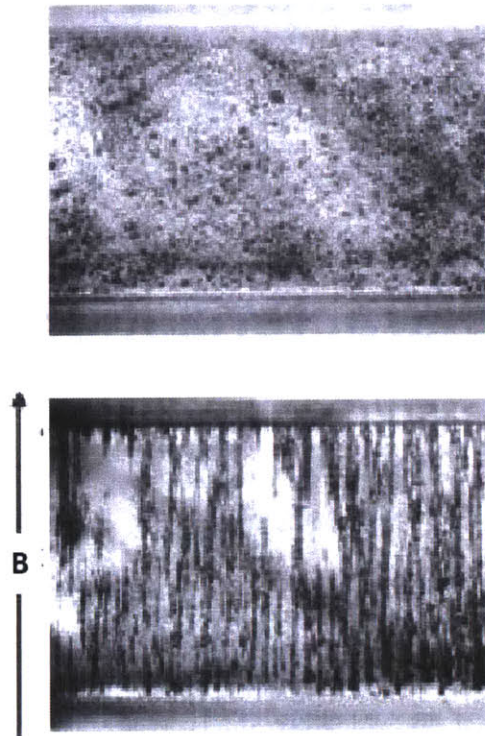


Figure 2.1 MR suspensions (2 vol%, 50 μm dia. iron particles in silicone oil) before and after application of a magnetic field (Klingenberg 2001).

The saturation magnetization is the maximum induced magnetic moment that can be obtained in a magnetic field (Ginder, 1996). The magnetic properties of any material are represented by B-H curves and are described by the equation

$$B = \mu_0 \mu_r H \quad (2.1)$$

where B is the magnetic induction, H is the magnetic field, μ_0 is the permeability of free space and μ_r is the relative permeability of the material. MR fluid particles in contrast to ferrofluids (as described in section 1.1.1) are micron-sized and hence consist of multiple magnetic domains. In the absence of an applied magnetic field, the particles possess very small net dipole moments (hence they are called soft magnetic solids), which permits reversible particle

aggregation in an applied field (Ginder, 1996). The application of a field causes domain-wall motion and alignment of magnetic domains along the field direction and thus interparticle magnetic attraction (please refer to section 4.1 for particle interaction models). Hence, a high saturation magnetization allows us to obtain the largest magnetic moments and hence the strongest interparticle attractions, which in turn defines the magnetorheological effect (Larson, 1999; Ginder, 1996; Carlson, 2001).

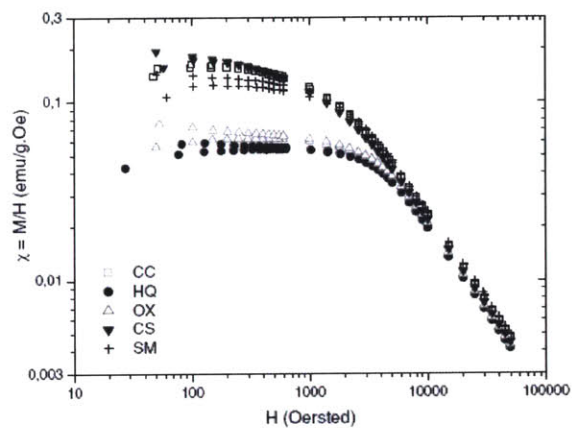
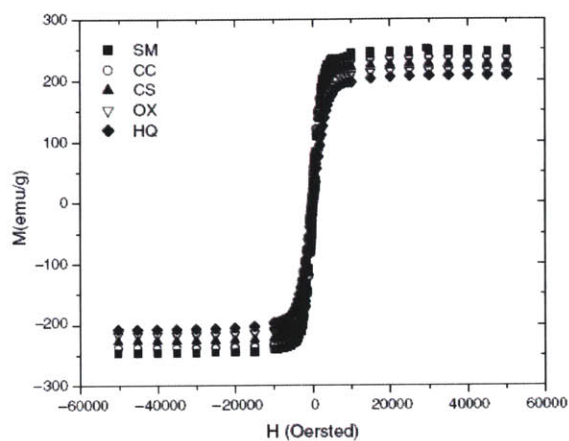
Mostly, carbonyl iron particles have been used in preparation of MR suspensions though other formulations using ferromagnetic or ferrimagnetic particles, like magnetite (Fe_3O_4), $Fe-Co$ alloy and $Ni-Zn$ ferrites have also been described (Carlson, 2001; Chin *et al.*, 2001; Genc and Phule, 2002). Ferromagnetic materials exhibit a long-range ordering phenomenon at the atomic level, which causes the unpaired electron spins to line up parallel with each other in a region called a domain. Ferrimagnetic particles, like ferromagnetic materials, hold a spontaneous magnetization below the Curie temperature. However, this is due to opposing but unequal magnetic moments of the atoms on different sublattices. Kormann *et al.* (1996) have studied magnetorheological fluids made of nanosized ferrite particles, which are typically used to formulate a ferrofluid. MR fluids have also been made from superparamagnetic particles (e.g. polystyrene particles studded with nanometer size iron oxide inclusions) dispersed in a solvent (Fermigier and Gast, 1992). Superparamagnetic particles are soft ferromagnetic or antiferromagnetic particles that do not possess any residual magnetization.

However, the MR fluids based on particles with smaller size have a weaker magnetorheological effect. This is because, for an equivalent volume of magnetizable powder, the surface area is inversely proportional to the particle size.

$$\frac{S_A}{V} \propto \frac{1}{d} \quad (2.2)$$

The iron oxide layer that forms on the surface of those particles has a much lower magnetic susceptibility thus decreasing the overall magnetization of the particles.

CIP Grade	10% ≤	50% ≤	90% ≤	Span
CC	1.17	2.11	4.27	1.467
CS	2.33	3.70	6.68	1.177
HQ	0.44	0.72	1.52	1.516
OX	1.48	2.38	4.29	1.178
SM	0.56	1.00	2.78	2.226



CIP	CC	CS	HQ	OX	SM
Fe %	99.6	99.7	97.5	96.4	99.3
C %	0.016	< 0.05	0.79	0.74	0.1
N %	< 0.01	< 0.01	0.99	1.12	< 0.01
O %	0.24	0.2	0.47	N.A.	0.6
Coating	0.1% SiO ₂	N.A.	N.A.	5% Fe ₂ O ₃	N.A.
M _s (emu/g)	238	227	208	217	245

N.A.: not applicable.

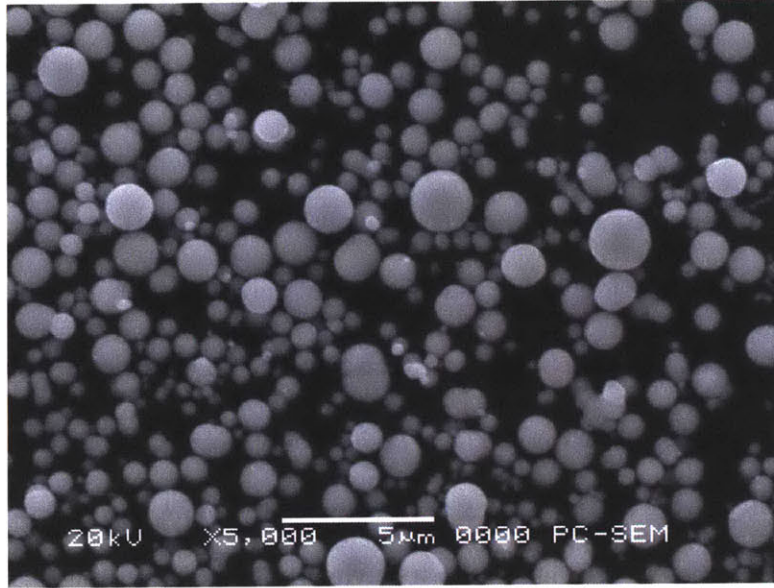
Figure 2.3 Magnetization curves and composition for carbonyl iron particles of different sizes obtained from BASF AG (Bombard *et al.*, 2003).

Thus, even though a larger size of particles leads to particle settling and destabilization issues, micron sized carbonyl iron particles (saturation magnetization ~ 2.03 Tesla) are typically used for MR fluid formulations. A number of proprietary additives such as surfactants and thixotropic agents are added to promote stabilization of particles. Chin *et al.* (2001) have used nanosized ferromagnetic particles ($Co-\gamma-Fe_2O_3$) and CrO_2 particles to enhance dispersion stability. Nanostructured silica and surfactants such as oleates and stearates have been added in earlier works for improving redispersibility (Phule and Ginder 1999, U.S. Patent No. 5,985,168). For improved stabilization of MR fluids against gravity, a viscoelastic medium having a low yield stress like grease has also been used as the continuous phase (Rankin *et al.* 1999). LORD Corp commercially produces numerous formulations of MR fluids using different types of carrier fluids¹.

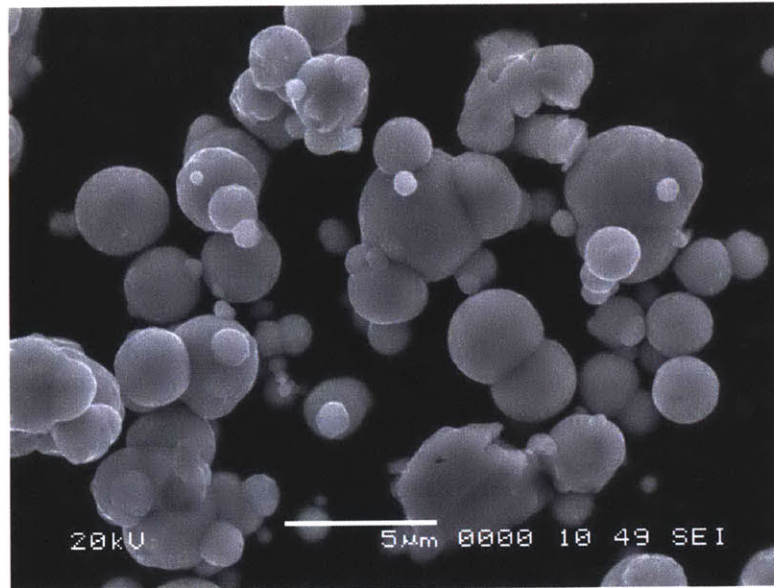
2.1.1 Laboratory Formulation of MR fluids

A severe limitation of commercially available MR fluids for industrial applications is their high cost (\$600/ litre). Also, these fluids are found to be plagued by stability issues as the particles settle over a period of time leaving a clear supernatant liquid. Hence, in this thesis work stable magnetorheological fluids have been formulated using in-house technology at a fraction of this cost and the rheological properties of the fluid are compared with the commercial MR fluids.

¹ <http://www.rheonetic.com>



(a)



(b)

Figure 2.3 SEM images of Carbonyl Iron particles from BASF used in formulation of Magnetorheological fluids (a) 1 μm (HQ grade) (b) 7 μm (CR grade)

Carbonyl iron particles (saturation magnetization $\sim 2.03\text{T}$), 1.1 μm in size (BASF Corp. HQ grade) or 7 μm in size (BASF Corp. CR grade) at a volume fraction of 36% comprise the

magnetizable matter in the laboratory formulated MR fluids. SEM images of these Carbonyl Iron powders are shown in figure 2.2. As can be seen from the figure, the powders are fairly polydisperse e.g. CR grade of carbonyl iron particles has a particle size distribution of 3-17 microns with a mean diameter of 6.72 microns. Carbonyl iron powder (CIP) is obtained by the thermal decomposition of iron pentacarbonyl ($\text{Fe}(\text{CO})_5$). In the course of the decomposition process, spherical particles form on a nucleus thereby forming a shell structure². The decomposition conditions decide the properties of the particles including the particle size distribution.

The magnetization curve of these carbonyl iron powders was shown earlier in figure 2.2 (Bombard *et al.*, 2003) and it can be observed that the magnetization of the powder with larger particle size is much higher (1.5-3 times) than the smaller size carbonyl iron powder.

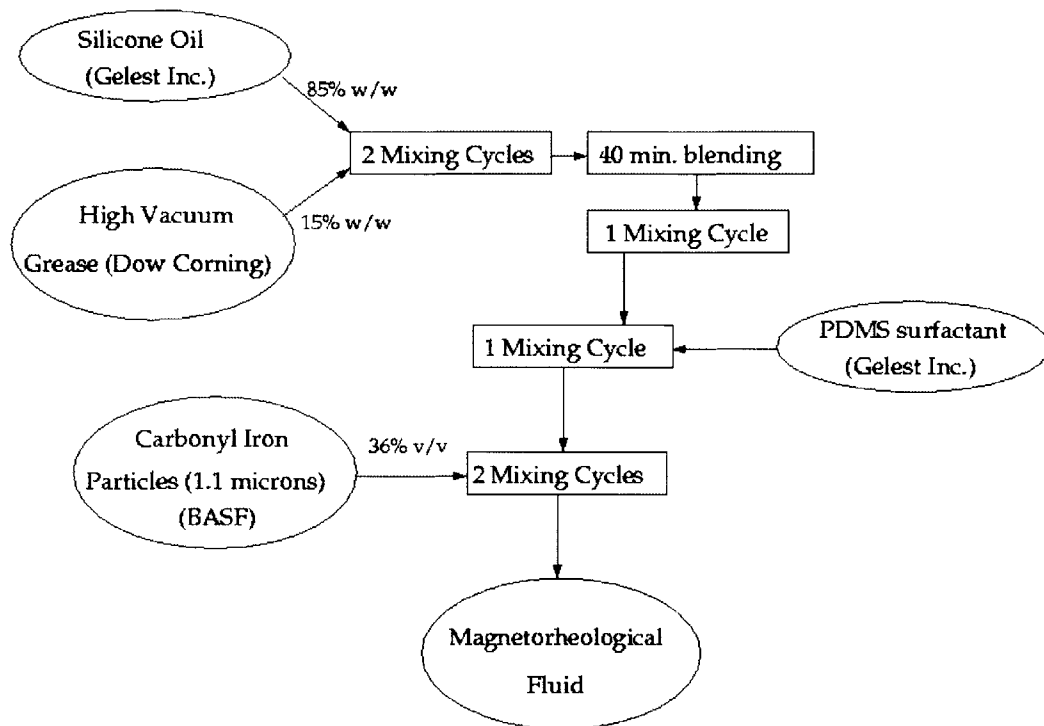
Polydimethyl siloxane, trimethylsiloxy terminated (PDMS) with a viscosity of 0.1 Pa.s (Gelest Inc., DMS-T21) formed the carrier base of the MR fluid. Silicone oil is used because of its low volatility, low dependence of viscosity on temperature and inert nature towards other solid and liquid constituents. A surfactant, silanol terminated polydimethylsiloxane (Gelest Inc., DMS-S21), stabilizes the particles against agglomeration. This surfactant has a $-\text{OH}$ terminal group which provides an affinity towards the carbonyl iron particles, while the PDMS part has an affinity towards the carrier fluid. A PDMS surfactant with an amine terminal group (Gelest Inc., AMS-132) is also found to stabilize the particles in the fluid.

A viscoplastic base, Dow Corning high vacuum grease, which blends well with the carrier fluid is utilized to provide a low off-state yield stress to the MR fluid and prevent the particles from settling under gravitational forces. A simple force balance gives the yield stress required in order to prevent the particles from settling

$$\sigma_y^{crit} (\pi r^2) \approx (\rho_p - \rho) \left(\frac{4}{3} \pi r^3 \right) g \quad (2.3)$$

² <http://www.basf.com>

where σ_y^{crit} is the critical yield stress to prevent settling, r is the radius of particle and ρ_p is the density of the particles. The critical yield stress works out to be nearly 0.05Pa for carbonyl iron particles with diameter 1.1 μm and is around 0.16Pa for particles with diameter 7 μm (ρ_p of 7800 kg/m^3 for carbonyl iron powder).



1 Mixing Cycle is 3 min. Mixing + Degassing in Conditioning mixer

Figure 2.3 Formulation of a Magnetorheological fluid. A flowchart showing all the components and mixing steps for formulation of a 36% v/v 1 μm particle-based MR fluid.

A step-by-step flowchart of the formulation process is shown in figure 2.4. A conditioning mixer (Thinky Corp., AR-100) has been used for both mixing and degassing purposes. The mixing cycle of three minutes includes a one-minute combined rotation (160 rpm) and revolution (400 rpm) followed by a two-minute defoaming phase at a revolution speed of

2200 rpm. Rheological measurements (figure 2.4) show that the blend of 15wt% grease in silicone oil has a low yield stress of approximately 0.7Pa in the field-off state, which is sufficient to prevent the 1.1 μm carbonyl iron particles from settling.

Using a carrier fluid with higher off-state yield stress, (for example 25wt% blended grease in silicone oil that has a yield stress of $\sigma_y \sim 4 \text{ Pa}$, instead of the 15wt% blended grease) as shown in figure 2.4, is found to be sufficient enough to prevent 7 μm carbonyl iron particles from settling under gravity. The MR fluid thus formulated is observed to have a gel-like consistency and excellent long-term stability. The yield stress of the MR fluid at a particular magnetic field strength is expected to increase as the particle size increases because of increased magnetization. Stability becomes a bigger concern for larger particle sizes, which has been successfully countered by using the appropriate viscoplastic base.

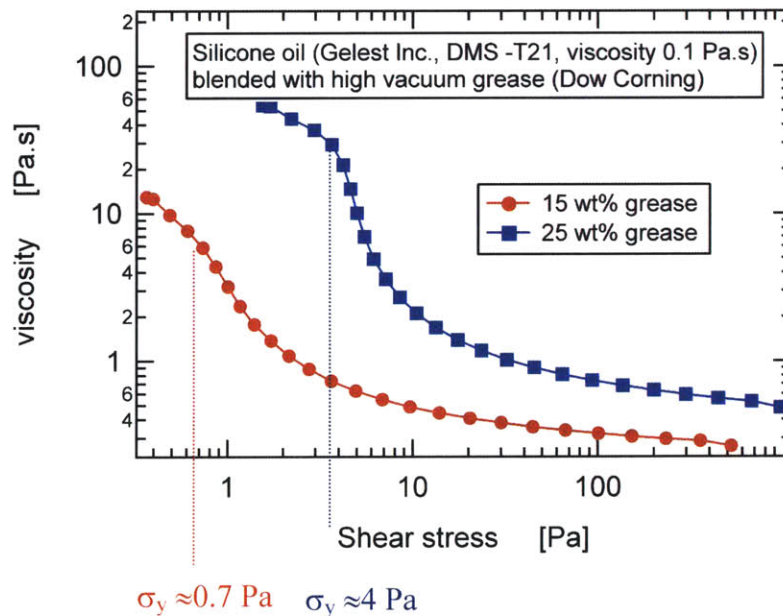


Figure 2.4 Steady shear data for silicone oil blended with grease at different weight fractions illustrating the low but finite yield stress in the field-off state.

2.2 Apparatus for Characterization of MR Fluids

2.2.1 Rheometer: Previous fixture designs

Field-responsive fluids are characterized by their steady-shear and linear viscoelastic properties, which can be determined using rheological and optical techniques. A number of rheological instruments such as capillary viscometer, slit rheometer, stress or strain controlled rheometer or a light scattering setup with either a parallel-plate arrangement, Couette cell arrangement or a cone and plate arrangement are used to measure these desired material functions (Macosko, 1994).

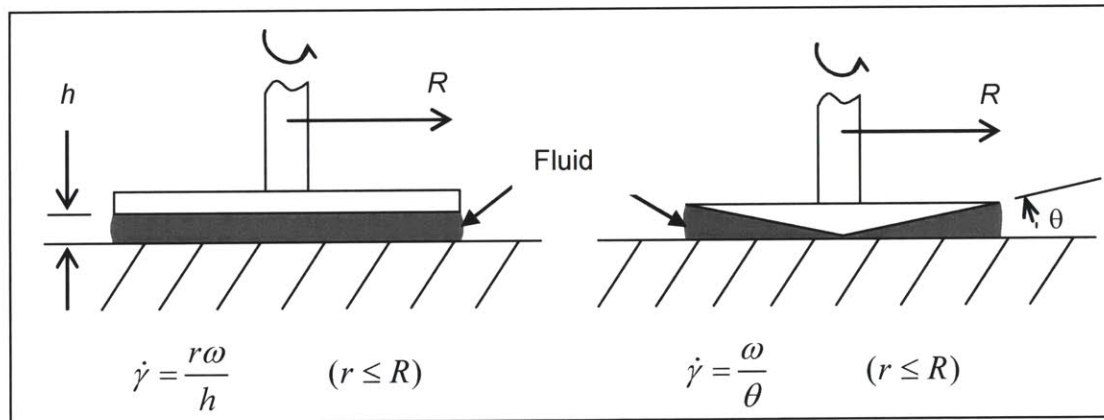


Figure 2.6 ‘Parallel-disk’ and a ‘cone and plate’ type arrangements for a rheometer used to determine material properties of complex fluids.

The two most widely used configurations are shown in figure 2.6, in which small volumes of fluid sample are tested between two coaxial circular parallel plates or between a small angle cone and plate, under shear, oscillatory or creep flows. A more detailed discussion relating

the mechanically measured quantities with the desired material functions can be found in the treatise by Bird *et al.* (1987).

Rheological properties of MR fluids are also dependent on the magnetic field and custom-made or commercial attachments to standard rheometers have been used for this purpose. Li *et al.* (1999, 2002) and Wollny *et al.* (2002) have used a commercially available MR cell for the UDS 200 rheometer with parallel-plate geometry, which generates a magnetic field perpendicular to the shear direction. Rankin *et al.* (1999) used a Bohlin VOR rheometer modified by inserting the rheometer plate shafts through holes drilled into an electromagnetic iron yoke (figure 2.6). A big disadvantage of these designs is that the magnetic field is a function of the gap between the top and bottom plates and hence it is not possible to perform gap-dependent studies.

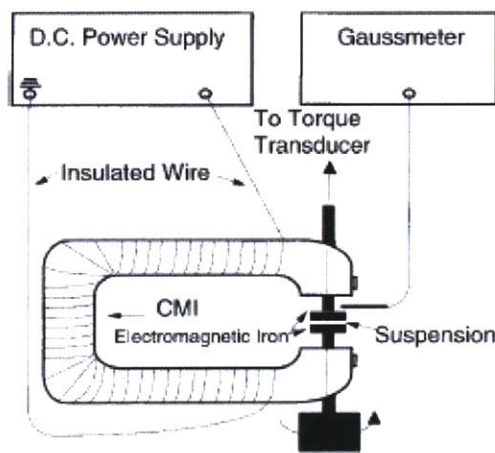


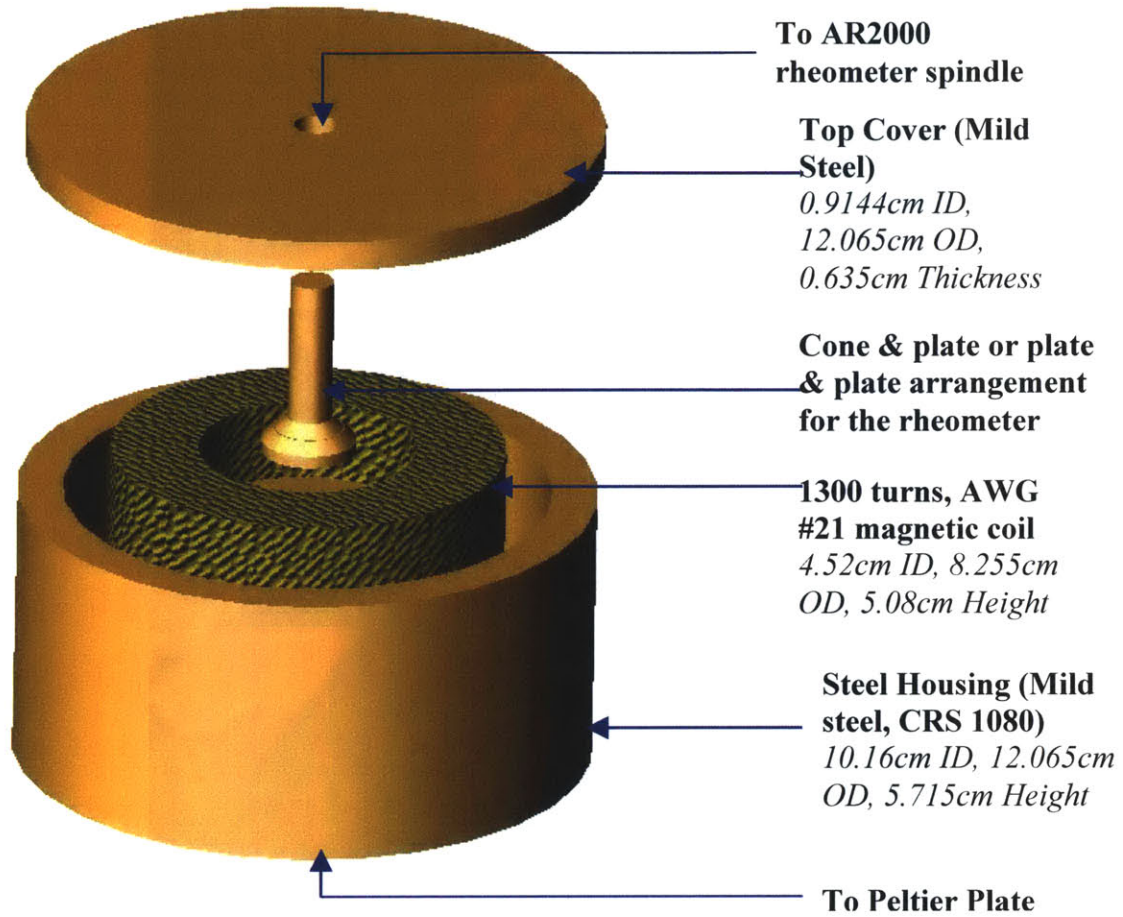
Figure 2.7 Schematic diagram of a Bohlin VOR rheometer modified using a iron yoke electromagnet (Rankin *et al.* 1999).

Helmholtz coils have been used by Cutillas *et al.* (1998) to generate a uniform but low strength magnetic field in the fluid sample space. Chin *et al.* (2001) have designed a solenoidal coil for creating a homogenous but weak magnetic field between the two plates of the rheometer.

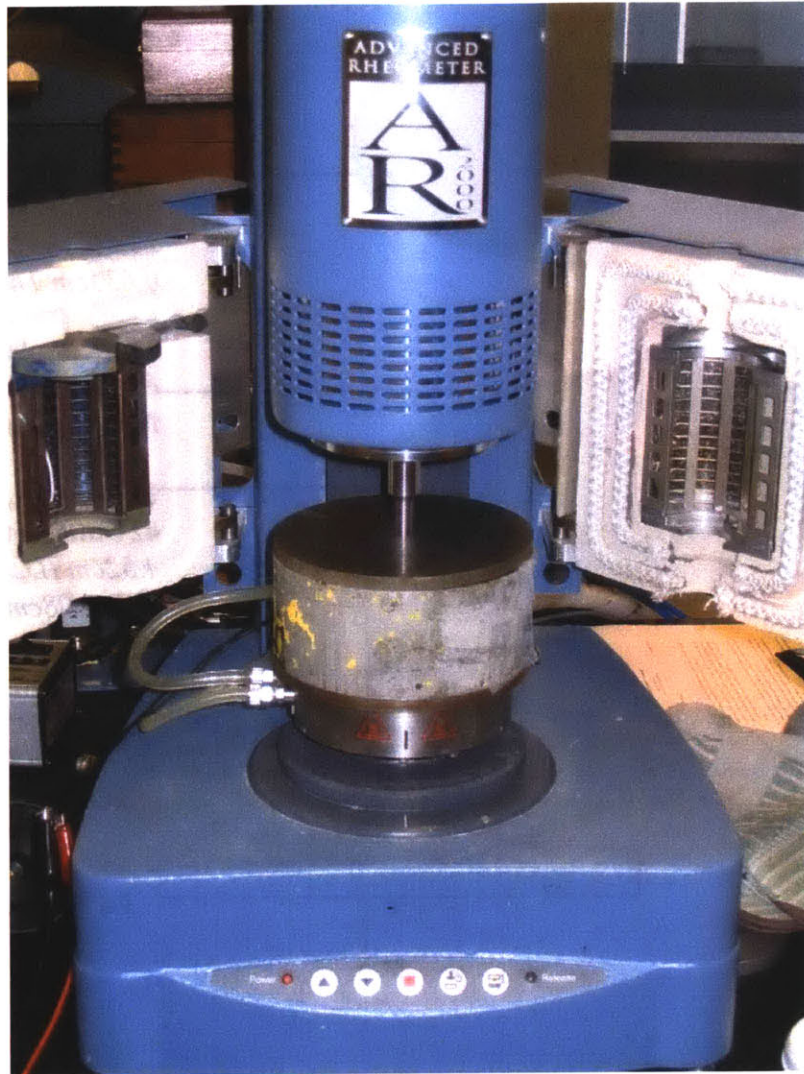
2.2.2 Custom Rheometer Fixture Design

Two stress-controlled shear rheometers (TA instruments' AR 1000N and AR 2000) are used to determine the steady-state rheological and linear viscoelastic properties of MR fluids. In general, a parallel plate (2cm diameter stainless steel plate with a gap height of 0.5 mm) arrangement and occasionally a cone-and-plate (2cm diameter 4° stainless steel cone) arrangement is used for the experiments. Since the fluid properties are a strong function of the magnetic field, a custom-made fixture is designed and built as a removable attachment to the rheometers for control and generation of a uniform magnetic field in the fluid sample space. The magnetic field generated is orthogonal to the direction in which the sample is sheared so that the MR fluid particle chains need to collapse before the sample starts flowing, thus allowing the measurement of magnetic field-dependent yield stress.

An exploded view of the custom-built MR fluid rheometer fixture is shown in figure 2.8. The fixture is designed to allow a maximum gap of 1500 microns for the fluid sample between the top and the bottom plate. The bottom plate (4.52cm diameter) is formed from CRS (Cold Roll Steel)-1080 (McMaster Carr), which is a soft-magnetic (does not retain residual magnetism when the applied magnetic field is removed) but mechanically hard material. The outer and inner housing of the magnetic coil have been machined out of mild steel to concentrate the magnetic field lines through the sample. The fixture can also be made to snugly fit onto the Peltier plate of the rheometer, which allows for external temperature control.



(a)



(b)

Figure 2.8 (a) SOLIDWORKS model of the custom-built MR fluid fixture for the TA instruments' AR series rheometers. (b) Fixture setup on the AR2000 rheometer (TA Instruments).

1300 turns of wound AWG #21 (0.7329mm diameter) copper wire (RODON Products Inc.) form the base field-generating coil. FEMM3.2 software has been used to determine the coil parameters such that a high magnetic field of up to 0.4 Tesla can be obtained in the fluid sample

space³. Depending on the area of cross-section (A_{cs}) available, the current density (J) is determined as follows

$$I_{total} = JA_{cs} \quad (2.4)$$

where I_{total} is the total current that is required for the high magnetic field. The copper wire diameter and the number of turns (N) is then chosen such that the current per turn (I_{turn}) doesn't exceed its current carrying capacity as follows

$$\begin{aligned} I_{turn} &= \frac{I_{total}}{N} \\ d_{wire} &\approx \sqrt{\frac{1.15A_{cs}}{N}} \end{aligned} \quad (2.5)$$

where d_{wire} is the copper wire diameter.

The resulting coil without the use of a cooling water system can then support a maximum current of 3.0A. A DC power supply (BK Precision Model 1670) provides a variable current from 0-2.5A and figure 2.9 shows the corresponding magnetic field obtained in the sample space.

³ <http://femm.foster-miller.net/>

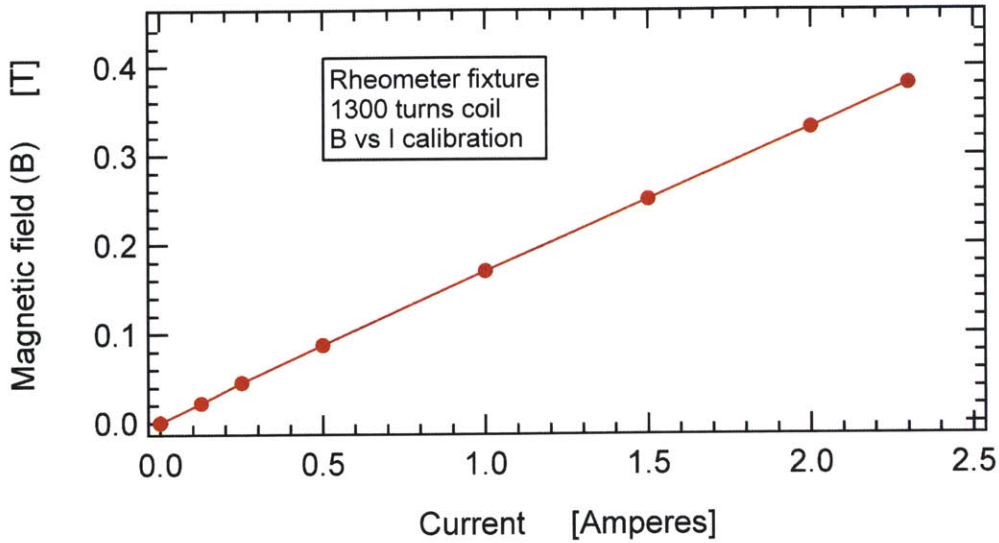


Figure 2.9 Magnetic field strength (B) in Tesla, obtained in the fluid sample space using the custom-built MR fluid rheometer fixture, as a function of the DC current flowing through it.

A gaussmeter (F.W. Bell Model 5060) with a transverse probe is used to calibrate the magnetic field versus the input current. FEM analysis is used to validate gaussmeter based experimental measurements and also to test the uniformity of the magnetic field. The magnetic field strength computed from FEM analysis shows a maximum variation of 8% over the fluid sample space. Helmholtz coils could have been used to get a more uniform magnetic field but the field strengths obtained are typically very small (0 - 0.025 Tesla) and not suitable for complete characterization of fluid properties (Cutlass *et al.*, 1998). Figure 2.10 depicts the magnetic field lines and flux gradient for the rheometer fixture generated using FEMM 3.2 software. The axisymmetric longitudinal sectional view is color-coded, for example, the shades of green in the fluid sample space observed in the figure depict the magnetic field variation around 0.4 Tesla. A comparison of our in-house built MR fluid fixture for determining rheological properties with other commercial or custom-built fixtures from literature is presented in Table 4.1.

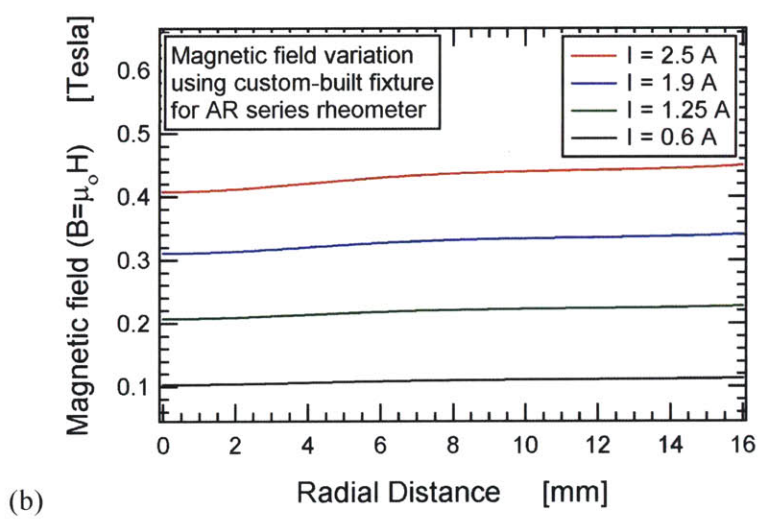
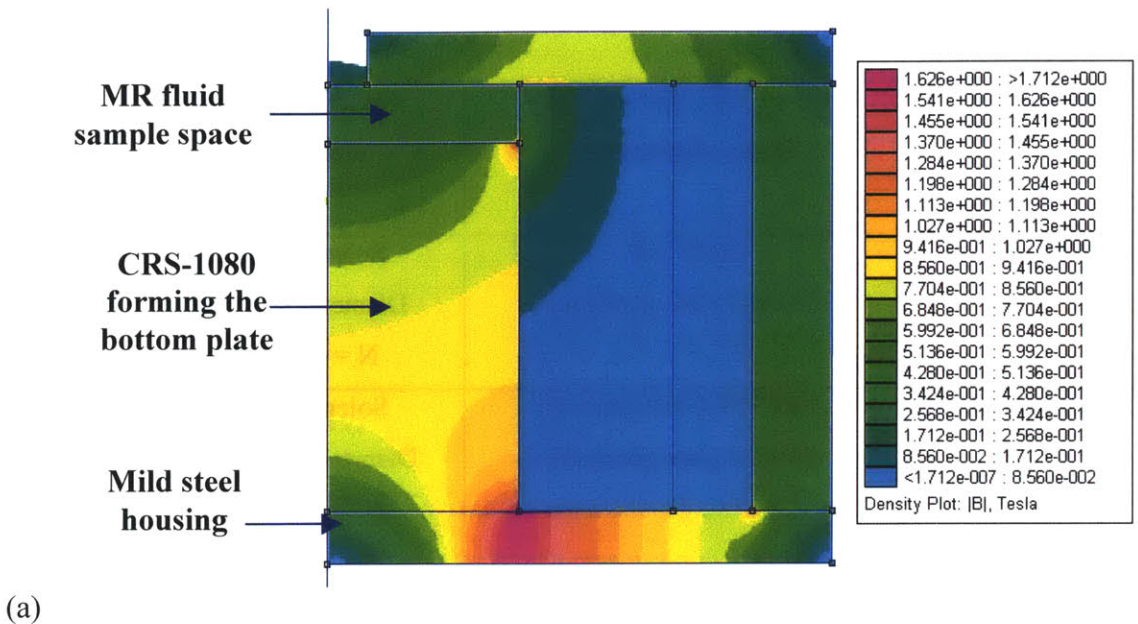


Figure 2.10 (a) Magnetic field lines and gradients illustrated using a longitudinal section color-coded for different magnetic fields for the MIT rheometer fixture designed for MR fluids ($I=2.5$ Amperes). (b) Variation of magnetic field strength in the fluid sample space as a function of the current in the coil. A maximum variation of 8% in the magnetic field strength is computed in a 2cm fluid sample space.

Reference:	Rheometer Type of geometry	Fixture type and dimensions	Maximum magnetic field (B)
Paar Physica Co.	UDS 200 Parallel plate geometry	Solenoidal coil Diameter = 20 mm N = 495 turns	0.34 T
Chin <i>et al.</i> (2001)	ARES (TA Instruments) Parallel plate geometry	Solenoidal Coil Diameter = 0.75 mm N = 2500 turns	~0.33 T
Cutillas <i>et al.</i> (1998)	Shear rheometer Parallel plate geometry	Helmholtz coil	0.025 T
Rankin <i>et al.</i> (1999)	Bohlin VOR rheometer Parallel plate geometry	Electromagnet wound with a coil N = 1000 turns	0.355 T
Claracq <i>et al.</i> (2004)	ARES (TA Instruments) Cone and plate geometry	Inductive coil N = 735 turns	0.04 T
Deshmukh and McKinley (2006)	AR 2000/ 1000N rheometer (TA Instruments) Parallel plate and cone and plate arrangement	Solenoidal Coil Diameter = 8-40 mm N = 1300 turns	0.635 T

Table 4.1 Comparison of fixtures, commercially available or custom-built, for determining the rheological properties of MR fluids.

An improved version of this custom built fixture has also been designed for future use as a magnetic field attachment for the AR series of rheometers (TA instruments). It uses a tighter gap in the magnetic field housing and a smaller air gap of 5080 microns (as compared to 7620

microns earlier), which allows the field lines to be concentrated in the fluid sample space. This further reduces the weight of the fixture and is easier to manage on a peltier plate with a maximum normal force rating of 50N.

However, it requires modifications of the rheometer top plate so that the chamfer where the plate connects to the shaft is removed. These modifications increase the allowance for different gap sizes in the fluid sample space to 2500 μm (as compared to 1500 μm in the original design) while also increasing the maximum attainable magnetic field (without water cooling) in the fluid sample space to 0.635 Tesla. The magnetic field variation in the fluid sample space is increased at these higher magnetic fields and the maximum variation is 10% as compared to 8% in the earlier version (figure 2.11).

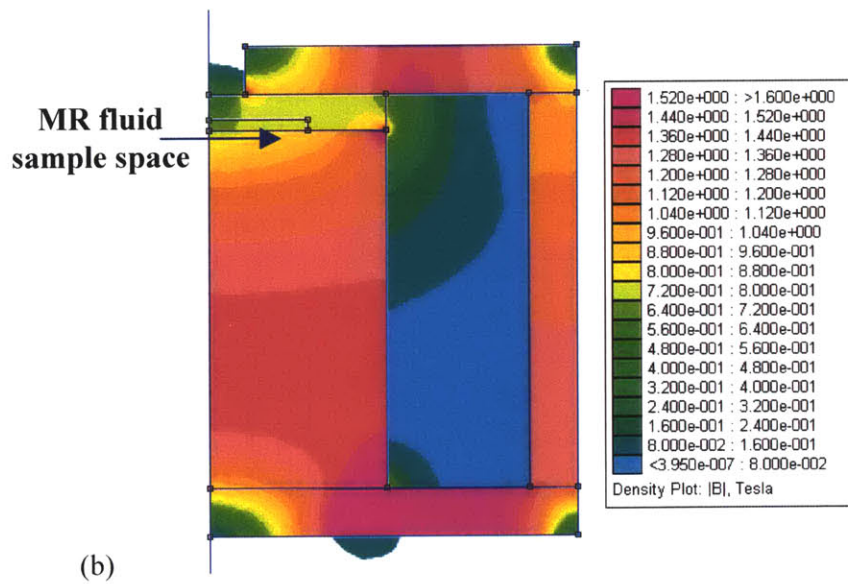
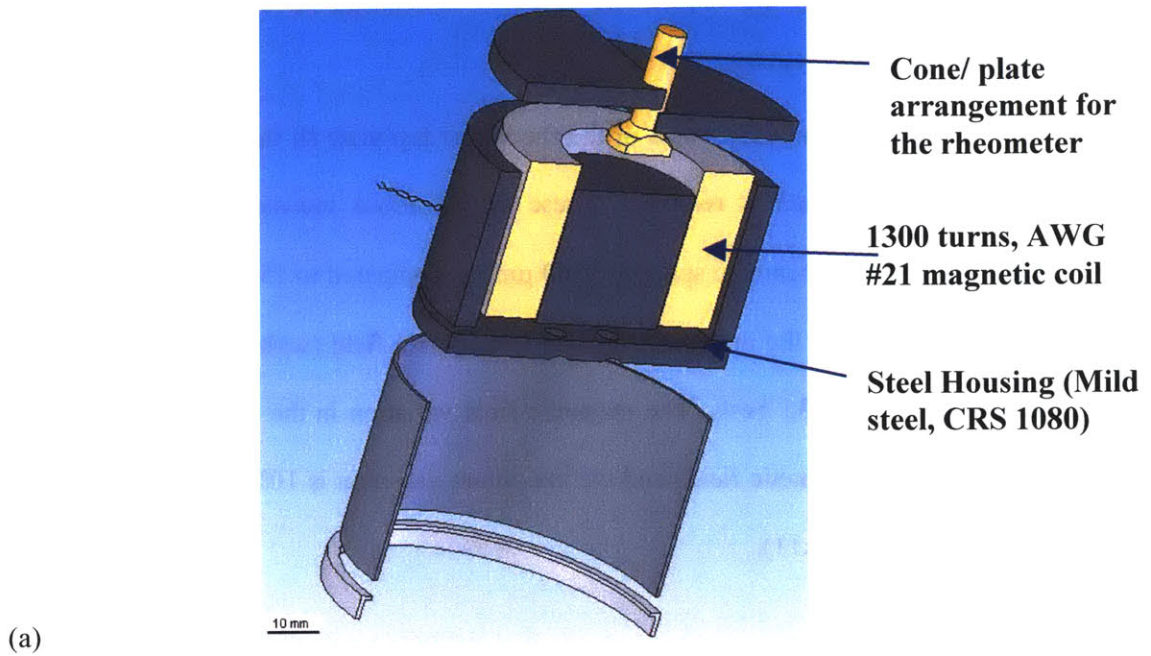


Figure 2.11 (a) Exploded section view of MIT Rheo-Magnetic fixture for the AR series of rheometers. (b) Magnetic field lines and gradients illustrated using a longitudinal section color-coded for different fields at a current of 2.5 Amperes.

2.3 Steady State Flow Behavior

2.3.1 Background

MR fluids are typically in the liquid-like state with the consistency of motor oil (viscosity $\sim 0.1-1$ Pa.s) until a magnetic field is applied. The constituent soft magnetic particles then acquire a dipole moment. The induced dipolar particles then align with the external field relative to the non-magnetized dispersed phase to form fibrous columns or aggregates as shown in figure 2.1. The columns need to be broken for the suspension to flow again which gives rise to a yield stress (i.e. the magnitude of stress at which appreciable deformation takes place without any appreciable change in the stress (Barnes, 1999)) as a function of the magnetic flux density.

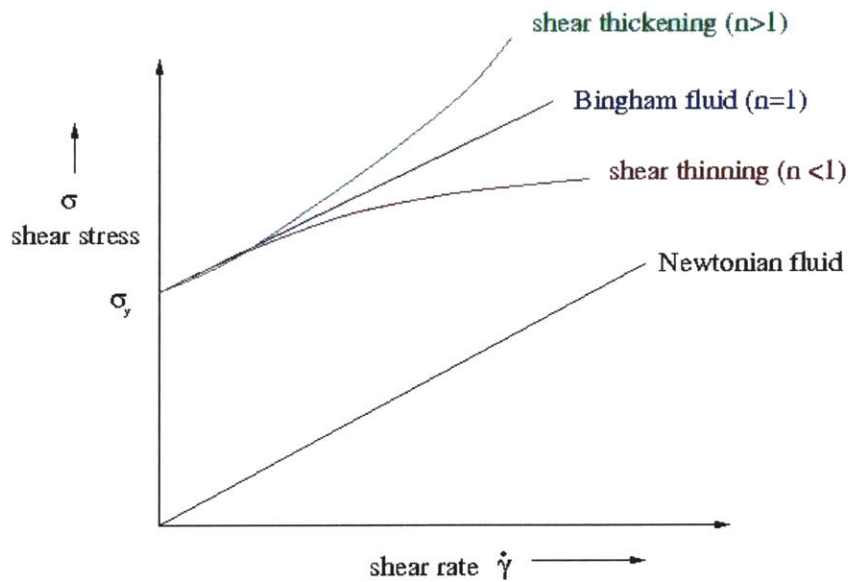


Figure 2.12 Herschel Bulkley viscoplastic model for Field-Responsive fluids where σ_y is the yield stress at which the fluid starts flowing and the exponent n describes the non-Newtonian behavior observed after yield.

The Herschel -Bulkley viscoplastic model is often used to describe this yield stress and the non-Newtonian behavior observed in FRFs after yield

$$\begin{aligned}\sigma &= \sigma_y(B) + \eta \dot{\gamma} \quad \sigma > \sigma_y \\ \eta &= k |\dot{\gamma}|^{n-1}\end{aligned}\tag{2.6}$$

where σ_y is the yield stress of the material, η is the viscosity, $\dot{\gamma}$ is the shear rate, B is the magnetic field strength, k is the ‘consistency index’ and n is the power-law exponent (figure 2.12).

The yield stress is a function of the applied magnetic field and has been observed up to ~120 kPa for micron size particles at magnetic fields higher than 1 Tesla (Genc and Phule, 2002). Tang *et al.* (2000) have observed a yield stress of 800 kPa for enhanced structures obtained by compressing the MR fluid along the field direction. MR fluids have been studied extensively under steady shear flow and representative data is shown in figure 2.13. The dynamic yield stresses can be determined from such measurements by extrapolating to zero shear-rate (Genc and Phule 2002).

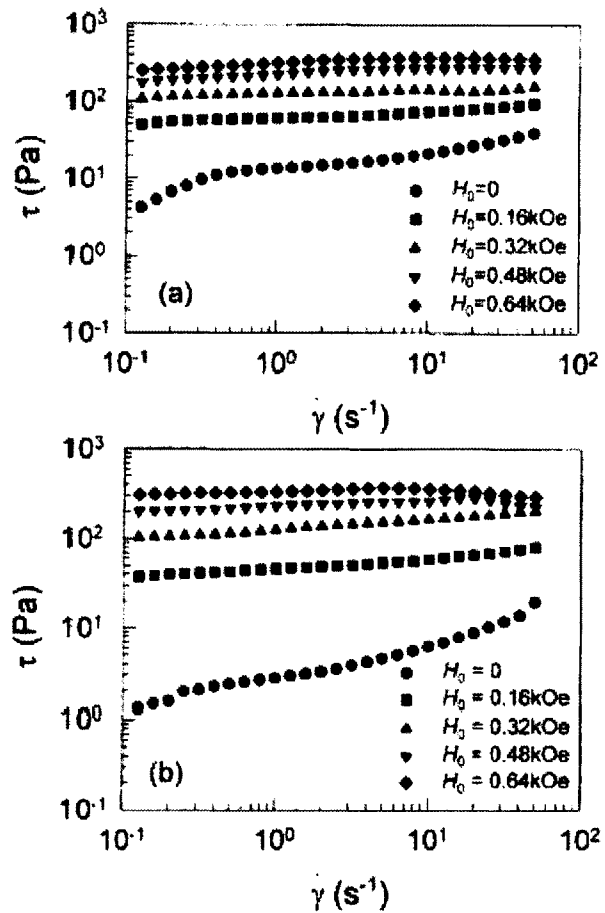


Figure 2.13 Steady shear flow data for a Fe_3O_4 in silicone oil MR fluid showing dependence of yield stress on the magnetic field strength a) $\phi = 20\%$ b) $\phi = 40\%$ (Chin *et al.* 2001).

The effect of particle volume fraction on the dynamic yield stress is also evident from figure 2.13 and $\sigma_y(B)$ is observed to increase almost linearly with volume fraction at a constant magnetic field (Chin *et al.* 2001). Experiments have also been carried out for various dispersing mediums, notably the use of a viscoplastic medium, like grease, to prevent sedimentation of the constituent particles (Rankin *et al.* 1999).

At small field strengths the field-induced yield stress is proportional to the square of magnetic flux density but becomes sub-quadratic with increasing field strength. This occurs because the particles tend to reach their saturation magnetization first locally at the surface near

the contact points between the particles (Ginder, 1996). This in turn limits increase of the field strength in the gaps between the particles and the magnetic field dependence becomes subquadratic as shown in figure 2.14.

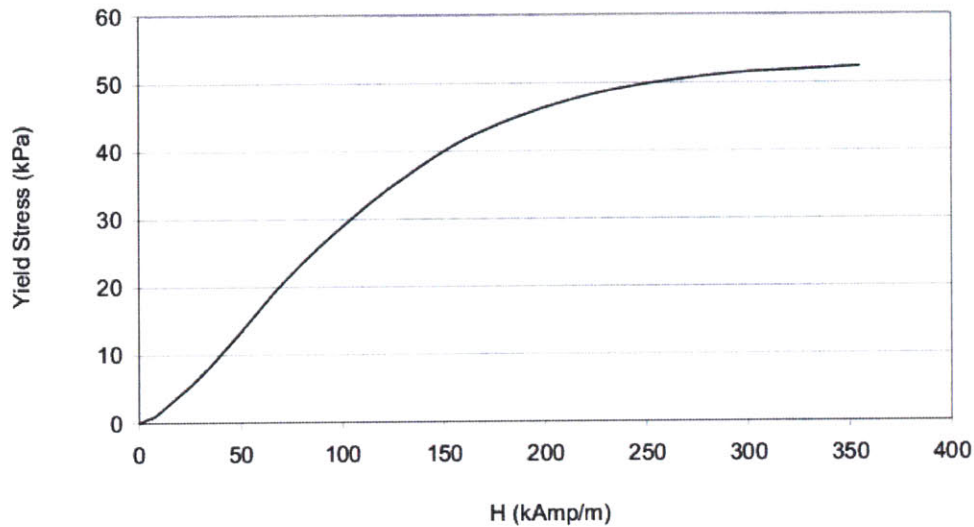


Figure 2.14 Graph showing the sub-quadratic dependence of yield stress on the magnetic field strength for the commercially available MR fluid, MRF – 336AG formulated by LORD Corp⁴.

2.3.2 Steady State flow behavior of commercial fluids

MRF-336AG, a silicone oil based magnetorheological fluid supplied by LORD Corp. and commonly used in automotive suspensions and dampers has been characterized under steady shear. The silicone oil based MR fluid has been used for characterization as it is inert to temperature variation and also provides a direct comparison to the in-house formulated MR fluid. MRF-336AG is composed of 36% v/v carbonyl iron particles or iron-cobalt alloy particles (~1 μm) in a silicone oil carrier fluid along with a number of proprietary additives. The rheological properties of the fluid under steady shear flow for different magnetic field strengths are shown in figure 2.15. The fluid has a weak yield stress (~ 150 Pa) even in the absence of a magnetic field

⁴ <http://www.rheonetic.com>

indicating the presence of a thixotropic additive. As the magnetic field is increased, the shear stress at which the fluid starts flowing also increases as can be observed from figure 2.15. The yield stress results are reproducible to within $\pm 5\%$ if a standard test protocol is followed as outlined below.

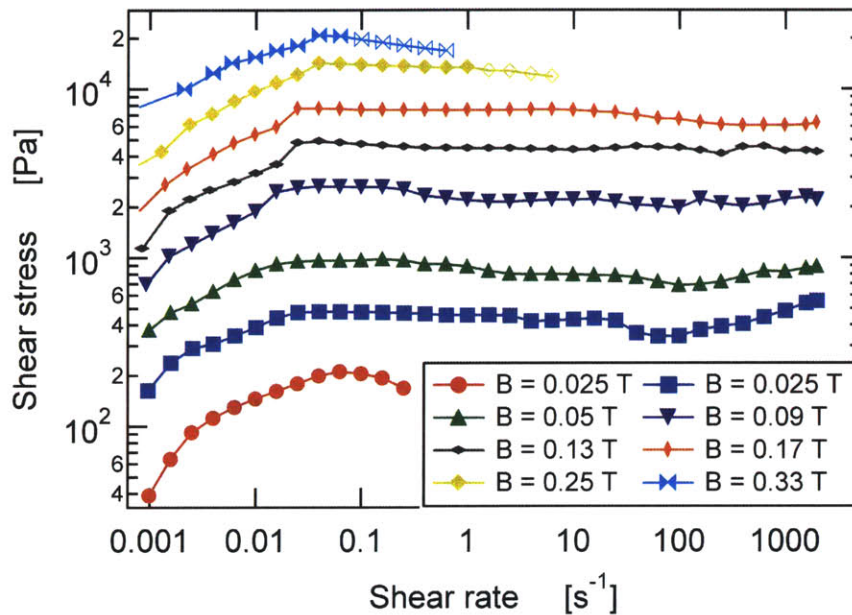


Figure 2.15 Rheological behavior of MRF-336AG fluid in steady state flow using a 2cm roughened plate at a gap height of 0.5 mm for different magnetic field strengths.

The rheological behavior of magnetorheological fluids was found to be dependent on the rest time and the loading conditions like other “soft-glassy” materials and gels. Hence, a standard pre-test protocol has been developed and used for all the experiments to ensure reproducibility and eliminate any effects due to thixotropy and rheological aging. The experiments were performed using a 2 cm diameter roughened plate arrangement. The protocol consisted of loading the sample onto the rheometer fluid sample space, slowly bringing the top plate to the required gap while maintaining the normal stress value below 1 Pa, applying a magnetic field for 30s to allow reformation of structure, pre-shearing after switching-off of the magnetic field for 60s at a

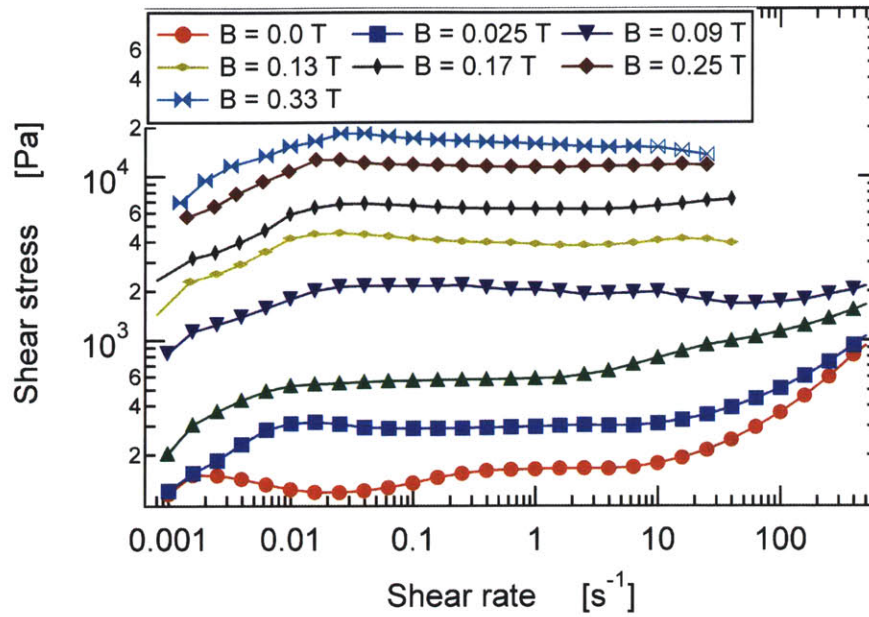
shear rate nominally higher than the zero-field yield stress value. The fluid sample is then assumed to be free of any dependence on loading history and rest time. This was indeed confirmed in the test runs.

The experiments have been carried out using 2cm diameter roughened plates and the magnetic field is varied from 0 to 0.4 Tesla. The test protocol used on the AR2000 rheometer is a steady state flow step with the shear rate being controlled and varied from 0.001 to 2000 s⁻¹. Five points are measured per decade of shear rate with the sample being sheared for 60 seconds before an average value of the torque is recorded.

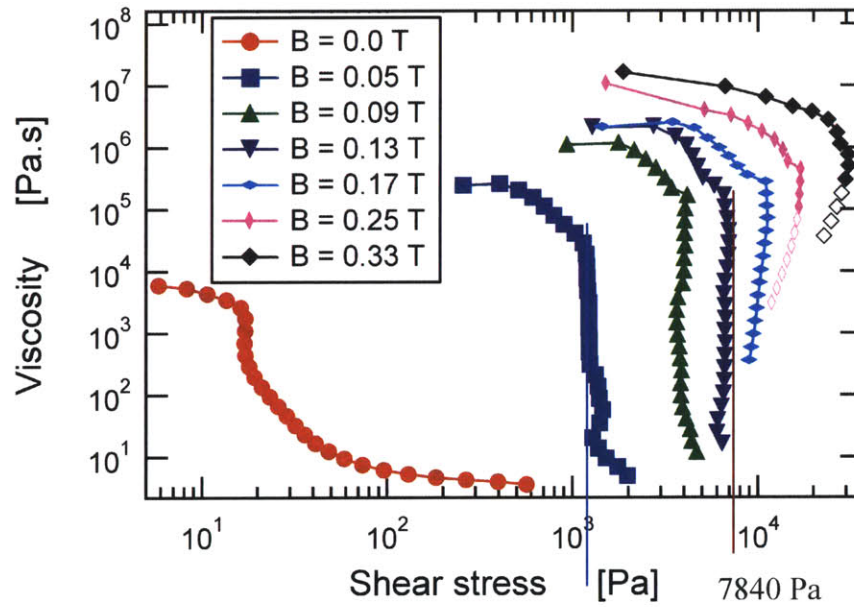
In order to minimize wall slip, the top and bottom plates of the rheometer are roughened by coating them with a very thin layer of carbonyl iron particles using a low viscosity glue (Permabond 910 cyanoacrylate) such that the roughness is of the order of the particle size. However, at higher shear rates there is still migration of the sample out of the plates, similar to that observed in other yield-stress fluids such as peanut butter, cream cheese etc. (Citerne *et al.* 2001; Erni P. through private communication). A steady state viscosity plateau after the yield point is thus not always observed in the samples and the data points where migration of sample is observed are shown with hollow symbols.

2.3.3 Steady state flow behavior of laboratory formulated MR fluids

The steady state flow behavior of MR fluids based on 1 μm carbonyl iron particles (BASF AG, HQ grade) at 36% v/v is shown in figure 2.16(a). The yield stress or the stress threshold at which the MR fluid starts flowing again is observed to increase with the magnetic field. Once the stress threshold is overcome the fluid is found to be highly shear thinning with a drop of 4 to 7 orders of magnitude of viscosity, as shown in figure 2.16(b) for the 7 μm carbonyl iron particle (BASF CR grade) based MR fluid.



(a)



(b)

Figure 2.16 MR fluid (36% v/v, 1.1 μm CIP) rheological properties under steady shear flow for different magnetic field strengths.

The creep viscosity at stresses below the yield stress is of the order of $10^4 - 10^7$ Pa.s indicating a solid-like behavior (for reference, the creep viscosity of peanut butter $\sim 10^3$ Pa.s at

room temperature (Barnes, 1999)). On a microstructure level when the chain and column structures that form in the presence of magnetic field collapse plastically, the stress threshold is said to have been overcome and the material starts flowing again displaying a liquid-like behavior and viscosity of the order of the carrier fluid viscosity (the steady shear viscosity of silicone oil used for laboratory formulated MR fluids ~ 0.1 Pa.s).

2.3.4 Yield stress comparison of different MR fluids

The magnitude of the yield stress of the MR fluid ($\tau_y(B)$) is its defining characteristic for most applications and it can be extracted from the steady shear data as illustrated in figure 2.16(b).

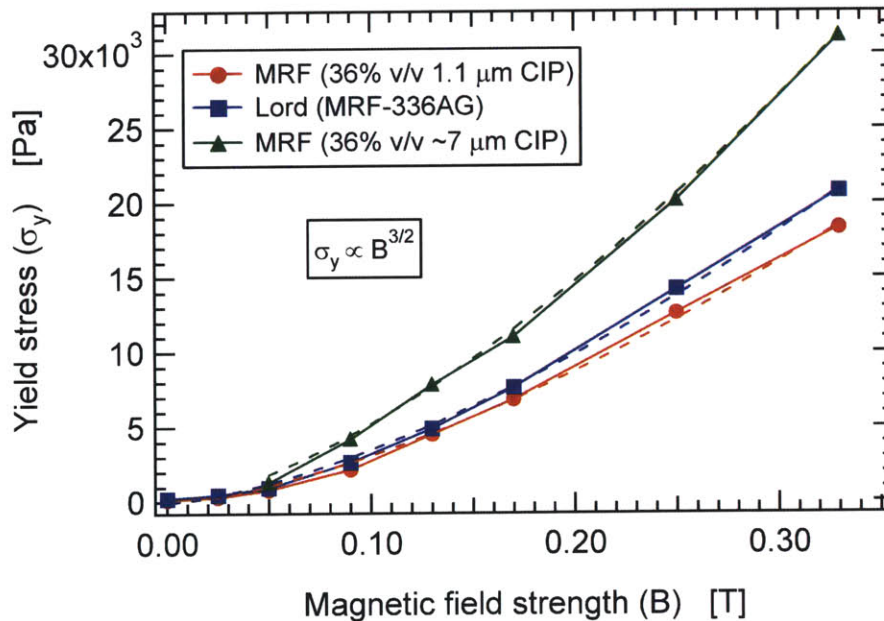


Figure 2.17 Yield stress comparison for three MR fluids – commercial fluid from LORD Corp. (MRF -336AG) with laboratory formulated MR fluids (1 mm and 7 μm CIP at 36% v/v).

At the yield point there is a sharp drop in the viscosity due to the collapse of particle chains in MR fluids and this threshold stress can be read off from the viscosity versus shear stress plots. As an example, dotted lines in figure 2.16(b) mark the yield stress values for magnetic fields of 0.09 and 0.17 Tesla.

The variation in the yield stress with the magnetic field calculated for the three fluids thus calculated is shown in figure 2.17. The yield stress data for the 1 micron carbonyl iron particle based MR fluid is found to be comparable to the commercial fluid which is not surprising given the similar sizes of particles. A marginally higher yield stress for the commercial MRF-336AG fluid is due to the use of iron-cobalt alloy particles that have a higher saturation magnetization than carbonyl iron particles (2.4T saturation magnetization of iron-cobalt alloy particles as compared to 2.1T for carbonyl iron particles (Ginder, 1996)).

The yield stress for 7 micron carbonyl iron particle based MR fluid is found to be higher than commercial or 1 micron CIP based MR fluids by nearly 50% as measured up to magnetic fields of 0.4 T. This is due to the higher magnetization of larger particle sizes due to a lower surface area to volume ratio and hence a smaller amount of low magnetic susceptibility iron oxide layer on the surface of these particles. Also, a subquadratic dependence of the yield stress with the magnetic field is observed, as shown in figure 2.17, which is in accordance with the scalings proposed by Ginder (1996) for the yield stress

$$\sigma_y = \sqrt{6\phi\mu_0} M_s^{1/2} H^{3/2} \quad (2.7)$$

where σ_y is the yield stress, M_s is the saturation magnetization and H is the magnetic field strength. Since the magnetic susceptibility and hence the magnetization of the 7 micron size carbonyl iron particles is nearly twice the magnetic susceptibility of 1 micron size particles (figure 2.2), the 50% ($\sqrt{2} = 1.414$) increase in the yield stress is in good agreement with Ginder's scaling for the yield stress.

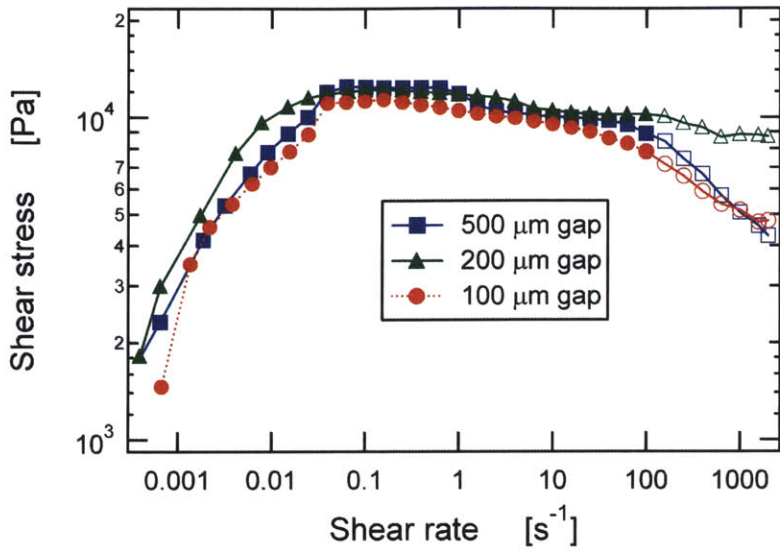
Plotting the yield stress against the magnetic field strength provides valuable information about forces, energy absorption capacity and flow properties of MR fluids and its composites (Klingenberg, 2001; Carlson, 2000; Jolly *et al.*, 1999). Hence, this increase in the yield stress and potential further improvements are highly advantageous in damping and energy management applications, which are discussed in further detail in chapter 3.

2.3.5 Wall slip and migration of sample

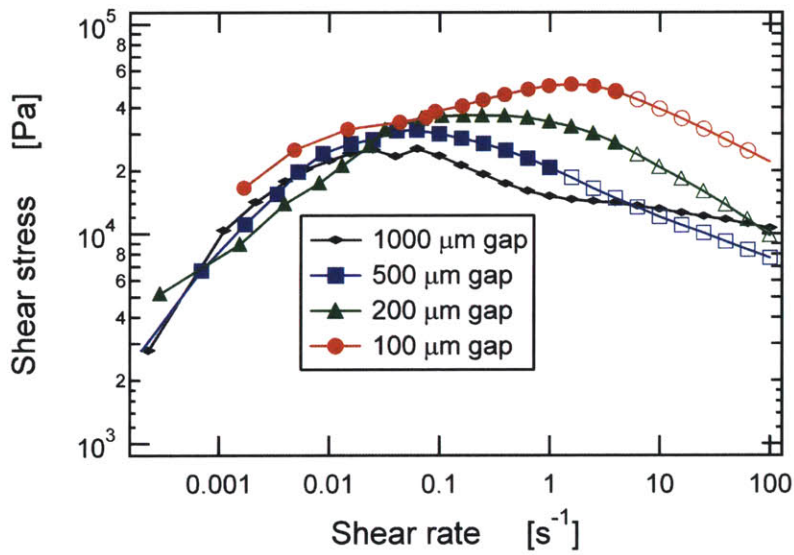
Wall slip is always a big concern in dense suspensions and elimination of wall slip is of primary importance in obtaining good and reliable data (Barnes, 1999). The experiments are performed using roughened cone and plates to minimize wall slip. Roughening of plates is carried out by glueing a layer of carbonyl iron particles onto the surface (so that the roughness is of the order of particle size). In the case of a cone-plate arrangement, an adhesive based grit paper with the roughness of the order of microns is used in order to maintain the cone angle.

Also, gap dependent studies can be performed by varying the gap in steady state flow tests while maintaining the rest of the parameters such as magnetic field, fluid composition etc. constant. Yield stress obtained from these steady state flow tests can then be used to obtain the corrected yield stress value and shear flow curves (Yoshimura and Prudhomme, 1987).

Gap dependent studies for 7 micron CIP based MR fluid (36% v/v) at two different magnetic fields are shown in figure 2.18. As can be seen from the figure, there is negligible dependence of the gap until the yield stress is reached so that the yield stress values shown in previous section remain unaffected due to wall slip.



(a)



(b)

Figure 2.18 Steady flow curves for MR fluid based on 7 micron particle size carbonyl iron powder at 36% v/v. (a) $B = 0.17\text{T}$ (b) 0.33 T .

However, after the stress threshold, at higher shear rates and especially at higher magnetic fields wall slip coupled with radial migration of sample out of the two plates is observed which leads to systematic errors in the results as shown by hollow symbols. The migration of sample is confirmed by performing single point shear rate tests and observing the secondary flow

of the fluid out of the gap between the two plates. We suspect that the migration of the sample is due to a high second normal stress difference, possibly coupled with slip, after the material is yielded.

$$N_2 = \Pi_{22} - \Pi_{33} \quad (2.8)$$

where N_2 is the second normal stress difference, Π_{22} is the total stress along the direction of the velocity gradient and Π_{33} is the total stress along the radial direction.

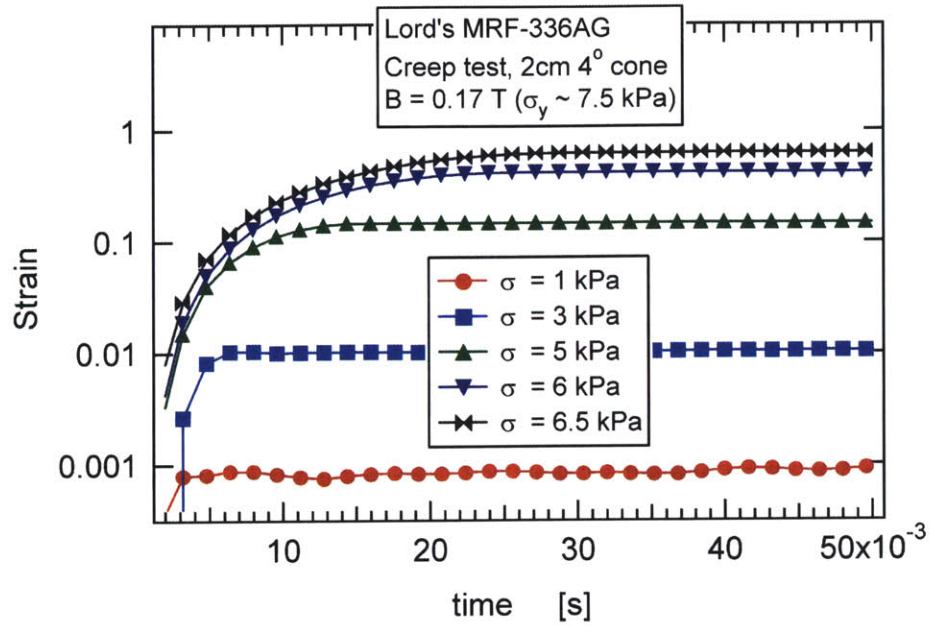
Inertial effects are ruled out since migration of sample is not observed in other fluids of comparable viscosity (viscosity after the yield point in the liquid like state). A magnetic field gradient being the cause behind this secondary flow is also ruled out as a similar phenomenon has been observed in non-magnetic yield stress fluids such as peanut butter and cream cheese (Citerne *et al.*, 2001; Erni and McKinley, through private communication). Thus, a high negative second normal stress difference is strongly suspected to be reason behind this migration of sample.

2.4 Time-dependent rheology: Creep

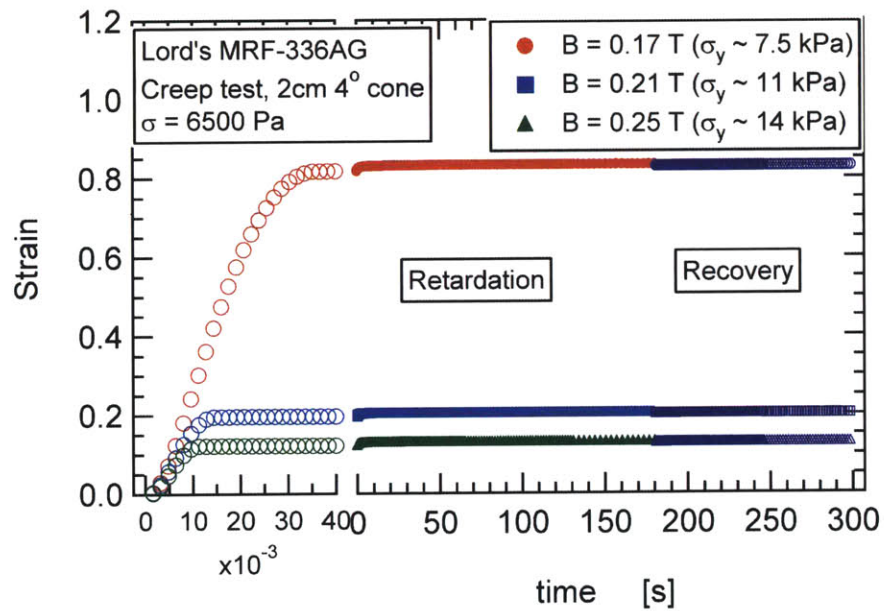
The viscoelastic properties of a MR fluid are dependent on the structure formation (and collapse) of chains of induced dipoles dependent. The creep test is a very useful method of studying these properties especially the time response of the material. In a creep experiment, the accumulated strain is recorded with time at a constant applied shear stress. A MR fluid like other yield stress materials will creep below the yield point implying that even though for all practical purposes the material does not flow, the sample shows irreversible plastic deformation in response to the applied stress and the accumulated strain increases with time (see Barnes 1999 for further discussion on material flow at the yield stress). A part of this time-dependent deformation is recovered when the applied stress is removed which provides a measure of the elastic properties of the material (Li *et al.*, 2002). The most vital information derived from a creep test however is the transient temporal response of the material or the time required for structure

formation and deformation in the material. Applications involving impact require a very-fast (millisecond) time response (Deshmukh and McKinley, 2007), and hence MR fluids with their millisecond response time (Klingenberg, 2001) are ideal candidates for use in impact applications.

The creep behavior of an MR fluid at an applied shear stress (σ) below the yield stress (σ_y) is shown in figure 2.19. The pre-test protocol is similar to that described in section 2.3 for steady state flow behavior. The fluid is then subjected to the desired magnetic field and a step increase in the loading stress applied at time $t=0$. The accumulated strain, and hence the compliance, is observed to attain a steady state value when the applied stress is below the yield stress and this steady state value increases as the applied stress approaches the yield stress. The yield stress is held constant by maintaining a constant field strength e.g. $B_{avg} = \mu_0 H = 0.17$ Tesla for figure 2.19(a). The response time of the material can then be obtained from the time required for the total accumulated strain to reach a steady value. The response time varies from 3-15 milliseconds as the loading stress progressively approaches the yield stress as shown in figure 2.19.



(a)



(b)

Figure 2.19 (a) Creep behavior of MRF-336AG sample at different applied stresses below the yield stress. (b) Creep experiment for different magnetic field strengths at an applied shear stress showing both the creep and recovery phase. The applied shear stress is removed at 180 seconds.

Because MR fluids have a magnetic field dependent yield stress, a creep experiment wherein the applied stress is held constant but the magnetic field strength is varied such that $\sigma < \sigma_y$ can also be carried out as shown in figure 2.19(b). For stresses below the yield stress, the total strain decreases as the magnetic field strength is increased or effectively the yield stress is increased. The fast time response of the material when the strain climbs to its steady value is shown in the initial logarithmic section of the figure. The recovery phase of the fluid after unloading of the applied stress is also shown and is found to be minimal suggesting that the elastic component of the creep strain is small and the finite viscoplastic deformation of fluid is the dominant response in creep flow. The creep behavior observed in figures 2.19(a) & (b) suggests a collapse of data with a model considering the total strain as a function of a scaled stress, $s = (\sigma/\sigma_y)$ which is indeed the case as will be shown later.

Above the yield stress, plastic collapse of the chains and structure formed on application of magnetic field leading to steady shearing deformation is observed as seen in figure 2.20 for the laboratory synthesized MR fluid based on 7 μm (BASF HQ grade) carbonyl iron particles. Figure 2.20 also shows the behavior below the yield stress where the accumulated strain reaches a steady state value. The strain scale is divided into two parts, a log scale initially in order to compare the creep behavior in the regime $\sigma < \sigma_y$ with the steady flow when the loading stress is above the yield stress $\sigma > \sigma_y$ on a linear scale for the strain afterwards.

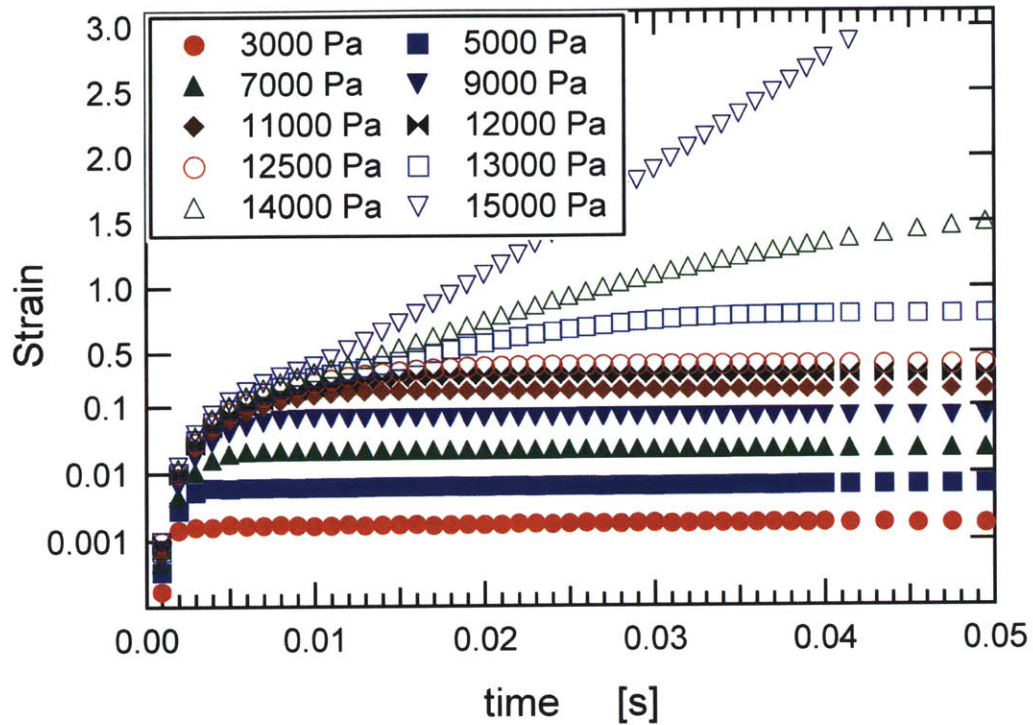


Fig 2.20 Creep flow behavior of (a) Lord's MRF-336AG at $B=\mu_0H=0.17$ T (b) 7micron CIP MR fluid at $B=\mu_0H=0.17$ T

The yield stress for MR fluids can also be obtained by analyzing these differences in the two regimes in creep flow above and below the yield stress. However, the yield stress value thus obtained is the “static” yield stress value (stress threshold above which the fluid initially at rest starts flowing) as compared to the “dynamic” yield stress values obtained earlier in section 2.3 and is usually higher by about 5%.

As was noted earlier, creep behavior for different MR fluids at different magnetic fields and applied stresses is observed to be self-similar which can be qualitatively explained since even under different experimental conditions evolution of similar field-aligned chain structures is followed. The measured accumulated strain value is observed to be a function of the scaled stress and figure 2.21 shows this scaling for different values of the dimensionless stress ($s = \sigma/\sigma_y$) for creep behavior under a wide variety of experimental conditions.

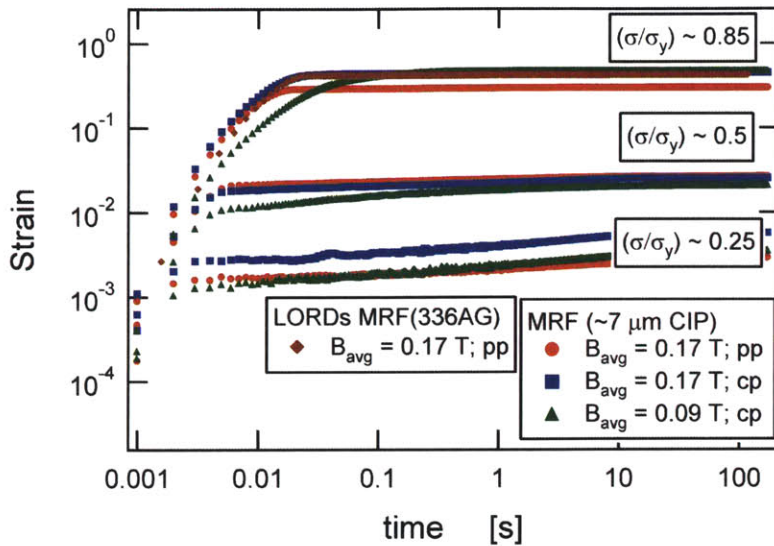


Fig 2.21 Rheological behavior of MR fluids under creep flow scaled for different fluid compositions, magnetic fields, loading stresses and measurement techniques using a dimensionless stress $s = \sigma/\sigma_y$.

Since the chain structures are self-similar under variations of applied stress, magnetic field, particle size and fluid composition, dedimensionalizing the loading stress with a characteristic fluid parameter that takes into account the behavioral dependence on experimental test conditions and the fluid composition such as the yield stress results in excellent scaling of the creep function.

2.5 Visco-Elasto-Plastic Model

2.5.1 Previous models for yield stress fluids

Previous modeling efforts for yield-stress fluids have typically been based on the Generalized Newtonian Fluid (GNF) model in which the viscosity is described as a function of the shear rate and the yield stress. These models such as the Bingham model or its modification, the Herschel-Bulkley model (figure 2.12 and equation 2.5) describe the steady state flow behavior

of yield-stress fluids and hence MR fluids very well. However, they fail to predict the yield-stress fluid response below the yield stress when only finite and time dependent visco-elasto-plastic deformation occurs as shown in figure 2.22.

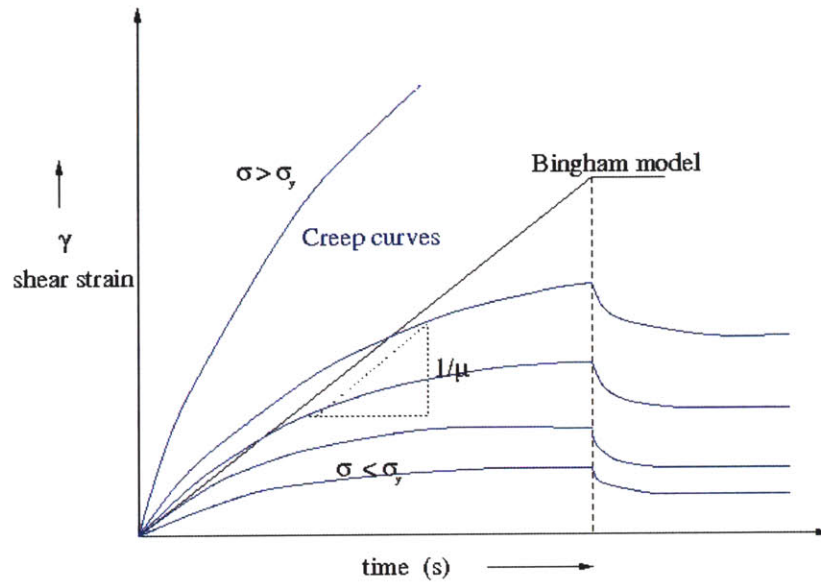


Figure 2.22 Bingham model prediction of yield-stress fluid behavior below the yield stress.

Hence, a microscopic visco-elasto-plastic model that probes the origin of plastic deformation in addition to the viscoelastic response below the yield stress and plastic collapse above the yield stress would describe the MR fluid behavior and yield-stress fluids better.

2.5.2 Models for “soft-glassy materials”

Magnetorheological fluids show quite a few striking similarities with other soft-glassy materials. Soft-glassy materials, such as foams, emulsions, gels are characterized by the properties of “structural disorder” and “metastability” (Sollich, 1998). Even though their thermodynamic least free energy state is an ordered state, the energy barriers in reaching this

ordered state are high and thermal motion is not enough for the system to cross these barriers. As a result the system settles into a “metastable” disordered state and deformations (in the form of applied shear), thermal motion or other interactions can lead to molecular rearrangement.

A number of efforts have been made in disparate fields to model these materials while drawing inspiration from the current “trap models” (Bouchaud, 1992) for glassy materials or mode-coupling class of models for granular solids (Hebraud and Lequeux, 1998). The mode-coupling theories follow directly the interactions between the particle trajectories. The “trap models”, on the other hand, consider individual elements “hopping” from one trap to another in an energy landscape. The hopping process was considered to be thermally initiated by Bouchaud (1992) for “glassy” materials and was extended to include deformations and interactions in the case of “soft-glassy” materials by Sollich (1998). Another common feature of these trap models, besides “metastability” and “structural disorder” is the conceptual use of mesoscopic regions, also called “shear-transformation zones” by Falk and Langer (1998). Deformations or interactions with other zones leads to molecular rearrangements within a particular shear transformation zone until the elements in a mesoscopic region cannot transform in the same direction and the region is said to be in a jammed state. The elements then “hop” out of a trap and this hopping event can also be considered a yield event and yield energy is related to the trap depth. Further, these rearrangements of the individual elements can propagate through the zones in the material and lead to further rearrangements elsewhere due to these interactions.

Thus, at small applied stresses, much below this yield stress, reversible elastic deformation occurs. As this applied stress is increased and approaches the yield stress, deformation is mostly plastic in nature and irreversible and at the yield stress unbounded plastic flow occurs.

The SGR model (soft-glassy rheology model) for “soft-glassy” materials proposed by Sollich *et al.* (1997;1998) models the effects of this structural disorder by assuming a distribution

of yield energies corresponding to different trap depths and characterizes the material by a time evolution of the probability distribution of these trap depths

$$\frac{\partial}{\partial t} P = -\dot{\gamma} \frac{\partial}{\partial l} P - \Gamma_0 \exp\left(-\left(E - \frac{1}{2}kl^2\right)/x\right) P + \Gamma(t)\rho(E)\delta(l) \quad (2.9)$$

where $P(l, E; t)$ is the probability distribution, l is the mesoscopic region strain, E is the yield energy corresponding to trap depths, Γ_0 is the attempt frequency of yielding occurring in these zones, $\rho(E)$ is the prior distribution of the trap depths which is time independent and x is the “effective noise temperature” which incorporates all interactions including the thermal motion.

This model is an extension of Bouchaud’s (1992) “glassy dynamics” model for glassy materials where hopping events occur due to thermal motion described by the temperature variable x . Figure 2.23 shows an illustrative potential well picture with different trap depths with solid lines corresponding to the energy dissipated in the “hops”. (Sollich, 1998).

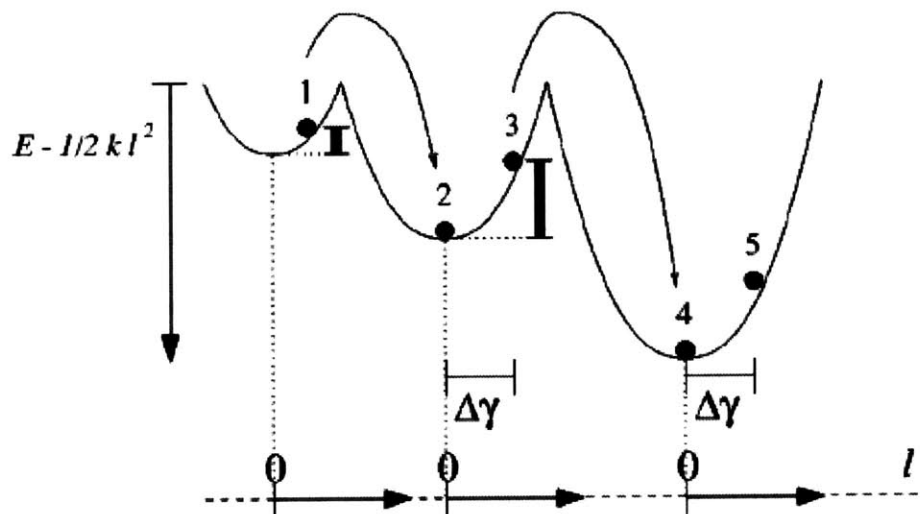


Figure 2.23 Illustrative picture of a distribution of “trap” depths with hopping due to deformation and other interactions leading to energy dissipation as shown by solid vertical lines (Sollich, 1998).

Falk and Langer (1998) explore a similar trap model drawing inspiration from Bouchaud’s glassy model for describing the viscoplastic deformation in amorphous solids. They assume these mesoscopic regions or “shear transformation zones” to be bistable that can transform back and forth between these two energy wells. Further, they assume that the probability of these transformations is dependent on the excess free volume available for the elements in a zone in which to rearrange themselves as shown in figure 2.24.

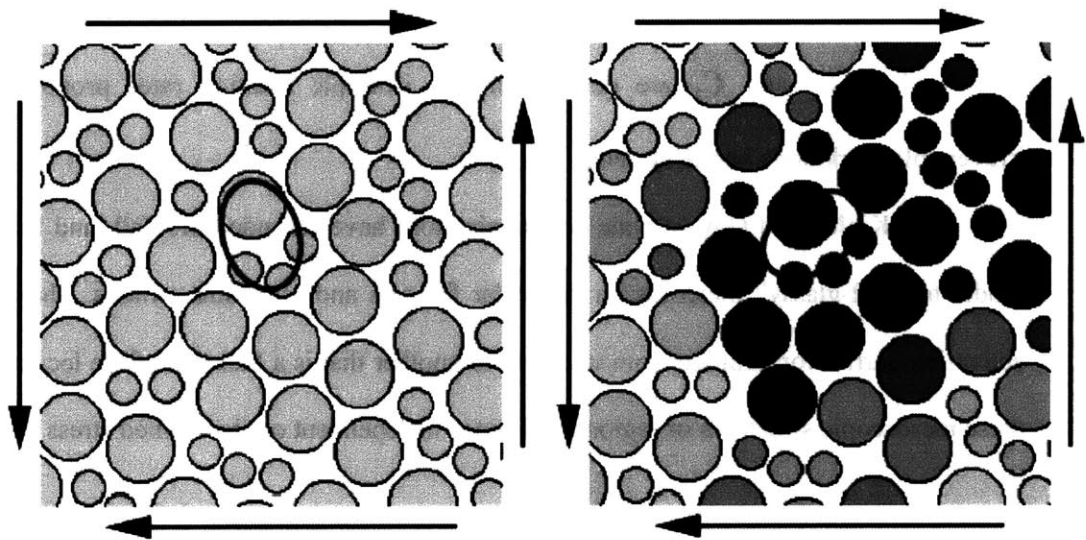


Figure 2.24 Schematic of molecular rearrangement in a “shear transformation zone” and its interactions with other zones propagating the effect through the material (Falk and Langer, 1998).

Hence, they propose a transition rate for the transformation between the two states to be of the following form

$$R_{\pm} = R_0 \exp\left[-\frac{\Delta V^*(\pm\sigma_s)}{v_f}\right] \quad (2.10)$$

$$R_0 \cong v^{1/2} \left[(\dot{\epsilon}_s^{el})^2 + (\dot{\epsilon}_s^{in})^2 \right]^{1/4}$$

where R_0 is the attempt frequency which depends on the inelastic and elastic shear rate, $\dot{\epsilon}_s^{el}$ is the elastic shear rate, $\dot{\epsilon}_s^{in}$ is the inelastic shear rate, v_f is the average free volume per particle and is same as “effective temperature” and ΔV^* is the excess free volume. Further, the number densities of zones in the two states is described by

$$\dot{n}_{\pm} = R_{\mp} n_{\mp} - R_{\pm} n_{\pm} - C_1 (\sigma_s \dot{\epsilon}_s^{in}) n_{\pm} + C_2 (\sigma_s \dot{\epsilon}_s^{in}) \quad (2.11)$$

where C_1 and C_2 are destruction and isotropic creation rates proportional to the irreversible work done on the system.

McKinley and Gay (private communication) have extended the Falk and Langer (1998) model to “soft-glassy” materials, in particular for gels and yield-stress fluids. They propose an activation barrier for hopping from one state to another that is a function of the localized strain in these mesoscopic structures or regions and hence is dependent on the applied stress as follows

$$R^{\pm} = R_0 \exp(\pm\sigma/G) \quad (2.12)$$

where σ is the loading stress and G is the shear modulus of the fluid. Further, they eliminate these microscopic variables to obtain evolution equations for deformation rate of the fluid in terms of three macroscopically observable and measurable parameters: relaxation time τ , shear modulus G and stress threshold or the yield stress σ_y as follows

$$\begin{aligned}
\dot{\gamma} &= \frac{1}{\tau G} [N(t)\sigma - G\Delta(t)] \\
\dot{\Delta} &= \dot{\gamma} \left[1 - \frac{G\sigma}{\sigma_y^2} \Delta(t) \right] \\
\dot{N} &= \frac{G(\sigma\dot{\gamma})}{\sigma_y^2} [1 - N(t)]
\end{aligned} \tag{2.13}$$

where $\Delta \sim (C_1/C_2)(n^+ - n^-)$ is the population imbalance between the two states + and - and $N \sim (n^+ + n^-)$ is the total site density of these binary interaction sites.

The model, also assumes, that work done on the system is dissipated towards creation of more defects and a higher population imbalance. Rheological aging is also captured in the model as the total number of defects N depends on the initial state of the sample and hence the rest time and loading conditions.

Dedimensionalizing the model equations provides us information on scalings for the macroscopic strain and the loading stress as follows

$$s = \frac{\sigma}{\sigma_y}; \quad \gamma^* = \frac{\gamma G}{\sigma_y}; \quad t^* = \frac{t}{\tau} \tag{2.14}$$

The scaling transformation for the loading stress is very typical of the scalings observed in experimental creep behavior of magnetorheological fluids in section 2.4. Hence, this yield stress model is expected to capture the behavior of magnetorheological fluids below and above the yield stress better than previous models such as the Bingham model.

2.5.3 Comparison of model predictions with experimental creep data

The visco-elasto-plastic model has an exact solution for creep flow if the fluid initial state is maintained constant by pre-shearing (such that $N = 1$), i.e. when a constant increase in stress is applied ($\sigma = \sigma_0 H(t)$) and the accumulated strain is measured as follows

$$\dot{\gamma}^* = \frac{(1-s^2)\exp(-(1-s^2)t^*)}{1-s^2\exp(-(1-s^2)t^*)} \quad (2.15)$$

Thus at loading stresses below the yield stress, the accumulated strain reaches a steady state value depending on the dimensionless stress $s = \sigma/\sigma_y$ while above the yield stress, unbounded plastic flow occurs and strain increases linearly with time. Model predictions for a MR fluid in the two regimes above and below the yield stress are shown in figure 2.25. The model does an excellent job of capturing the finite plastic deformation below the yield stress and the plastic collapse above the yield stress of the chain and column structures that are formed on application of the magnetic field.

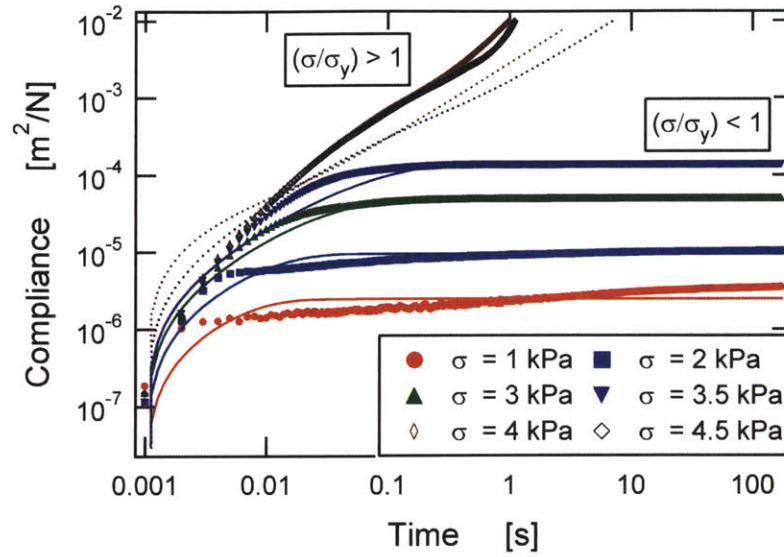


Figure 2.25 Creep flow behavior of MR fluid (7 micron CIP) at $B=\mu_0H=0.09$ T ($\sigma_y=3.8$ Pa) modeled using the visco-elasto-plastic model.

The model captures the compliance of MR fluids over a large range (5 orders of magnitude of compliance and time) to an excellent degree. There are, however, discrepancies in the experimental and model predicted shear-modulus values as shown in figure 2.26. Falk and Langer (1998) report a similar order of magnitude difference in the model predicted values in their simulations of amorphous solid behavior which they further propose is due to the presence of soft internal elastic nodes within the mesoscopic zones.

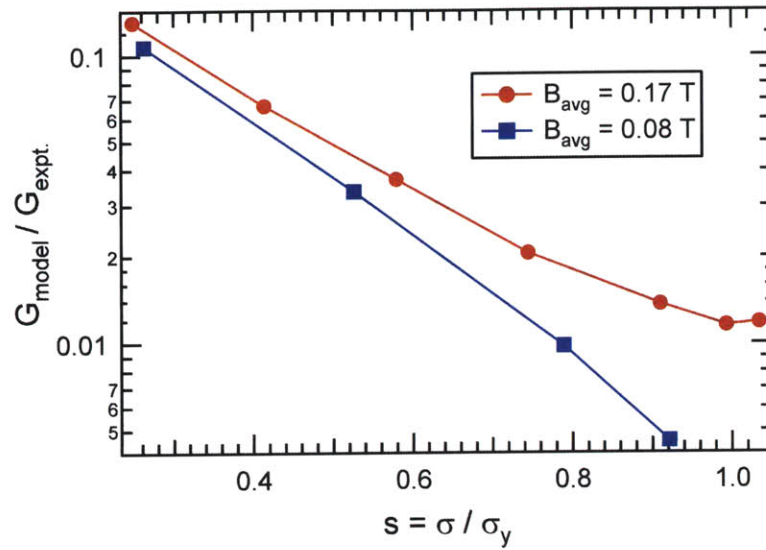


Figure 2.26 Discrepancy in model shear modulus values as compared to experimentally measured shear modulus values.

A possible explanation for this discrepancy is the use of a single constant retardation time for describing this complex gel-like behavior. Also, creep behavior at small times, especially at low dimensionless stress ($s \ll 1$) values is not captured well with a single retardation time model as seen in figure 2.27(a) & 2.27(b). A retardation spectrum based model fit captures the experimental creep behavior to a better degree while also maintaining good agreement with the experimental shear modulus values, as shown in figure 2.27(c) using two retardation times. Another possibility is the use of a more complex dependence of the retardation time on the applied stress, such as the White-Metzner modification of the Maxwell model, instead of a full retardation spectrum to capture the creep behavior.

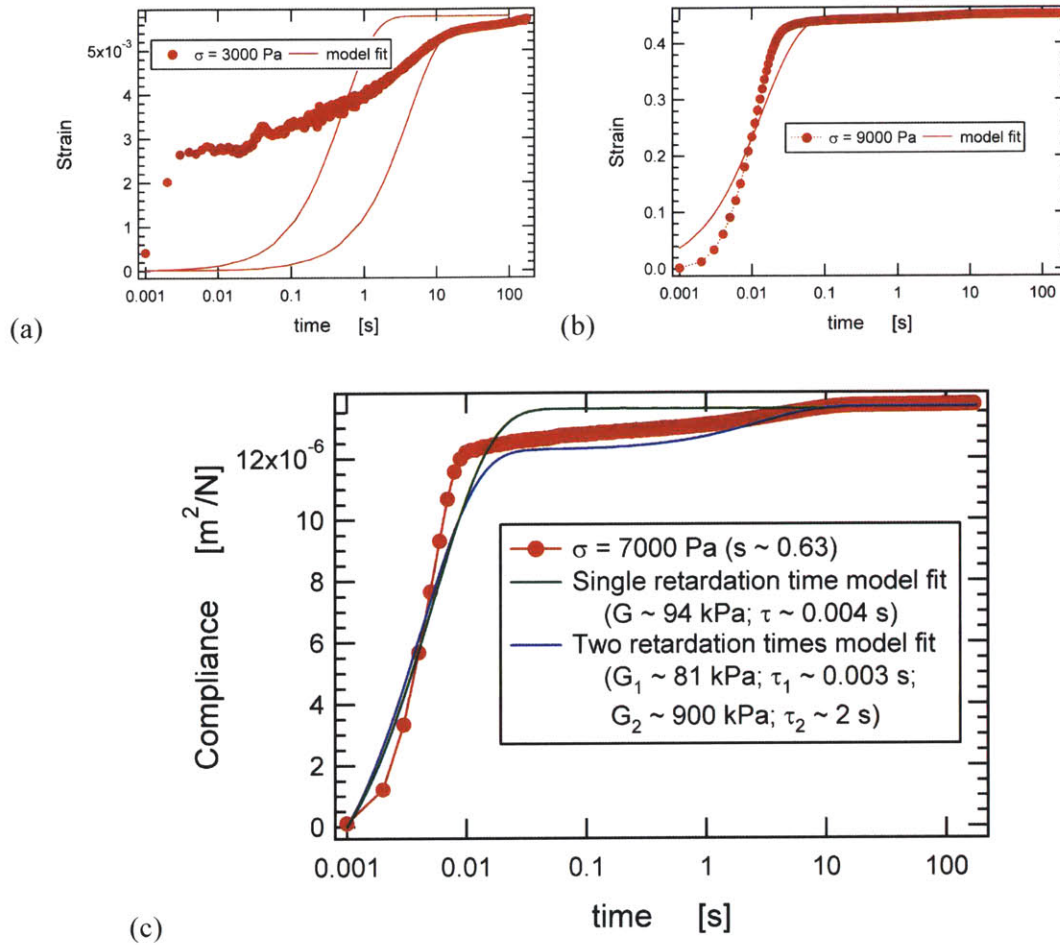
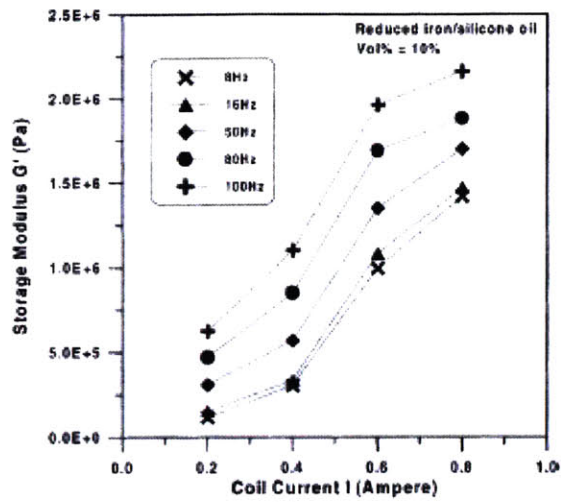


Figure 14 (a) Model prediction using a single retardation time compared with experimental creep curves for $\sigma = 3000$ Pa, $\sigma_y = 12800$ Pa, $B_{avg} = \mu_0 H = 0.17$ Tesla (b) $\sigma = 9000$ Pa, $\sigma_y = 12800$ Pa, $B_{avg} = \mu_0 H = 0.17$ Tesla. (c) Comparison of a single and double retardation time model fit with experimental creep curve at $\sigma = 9000$ Pa, $\sigma_y = 12800$ Pa, $B_{avg} = \mu_0 H = 0.17$ Tesla.

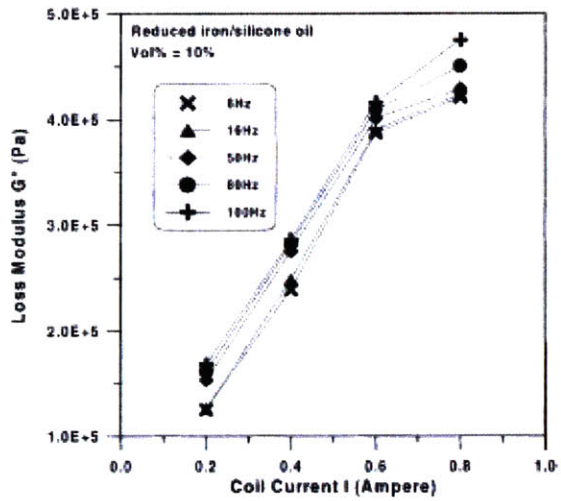
2.6 Oscillatory flow

Magnetorheological fluids are widely used in dampers, shock absorbers and automotive suspensions which operate under oscillatory loading conditions. However only a few recent studies have looked at their properties and behavior under such loading conditions (Li *et al.*, 2003; Claracq *et al.*, 2004). Small-amplitude oscillatory shear experiments in which the upper plate or cone undergoes small-amplitude sinusoidal oscillations in its own plane with a frequency (ω) and displacement ($\gamma \ll 1$) so that the instantaneous velocity is almost linear, is typically used to obtain characteristic material functions. Representative measurements of linear viscoelastic properties, G' (storage modulus) and G'' (loss modulus) obtained for MR fluids from such experiments are shown in figure 2.28. In the linear viscoelastic region, both G' and G'' increase with magnetic field and volume fraction of particles (Li *et al.* 1999).

Claracq *et al.* (2004) observed the frequency dependence of storage and loss modulus in the linear and quasilinear viscoelastic region to be a constant ratio of 0.1 not unlike many other soft-glassy materials. Further, they found the critical strain γ_c when the fluid shows a transition from gel-like to liquid-like behavior to be proportional to the square root of Mason number.



(a)



(b)

Figure 2.28 Dependence of the linear viscoelastic moduli (G' , G'') on the magnetic field strength (represented by current flowing through the electromagnet in amperes) and the frequency of the oscillatory flow for 10% suspensions of iron powders (Li *et al.* 1999).

However, large amplitude oscillatory flow is typically encountered in the applications based on MR fluids wherein the behavior is highly nonlinear. These nonlinearities because of presence of plastic deformation and collapse along with the viscoelastic response have not been studied previously. Hence, in this thesis work, we looked at the rheological behavior of MR fluids

in oscillatory shear flow conditions with particular focus towards nonlinearities encountered in large amplitude oscillatory loading.

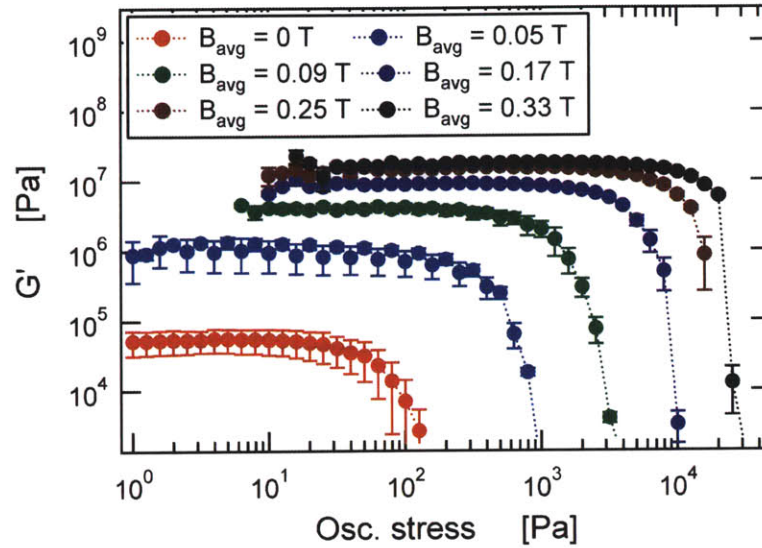
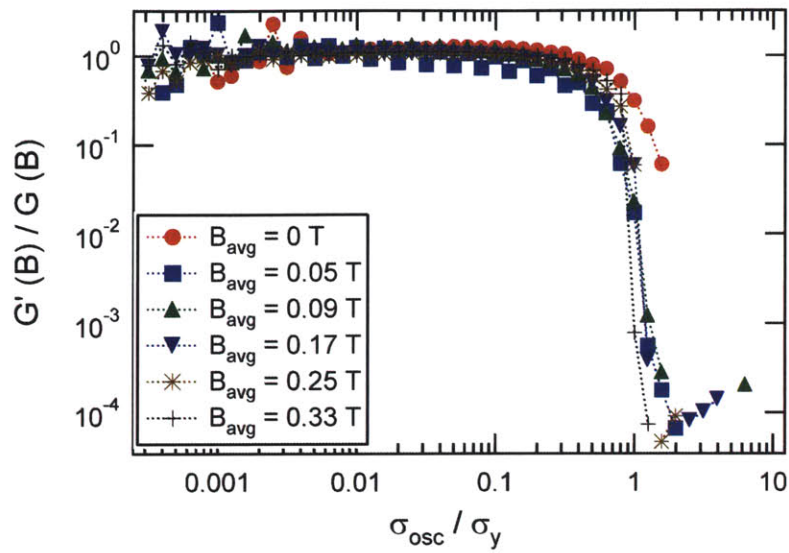
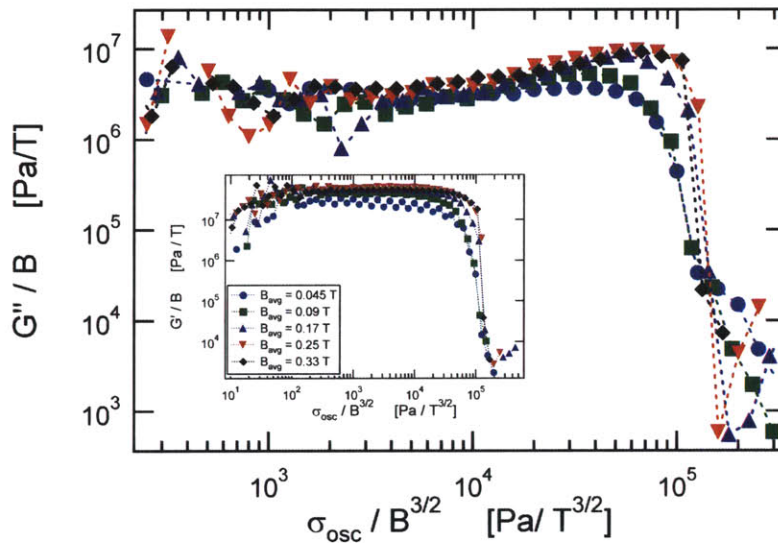


Fig 2.29 1st harmonic of the storage modulus Modulus for oscillatory shear flow experiments at different magnetic fields for 7 micron (BASF CR grade) based MR fluid at 36% v/v illustrating the visco-elasto-plastic response of MR fluid.

Figure 2.29(a) shows the first harmonic of the storage modulus as a function of the oscillation stress amplitude. The loss modulus is found to be an order of magnitude lower than the storage modulus and both the moduli show a plateau region for $\sigma \ll \sigma_y$. As the stress approaches the yield stress, i.e. the oscillation stress amplitude becomes large, the chain structure evolves until it collapses leading to a sharp decrease in the storage and loss modulus.



(a)



(b)

Figure 4.30 Modulus for oscillatory shear flow experiments at different magnetic fields for 7 micron (BASF CR grade) based MR fluid at 36% v/v. (a) Scaling of the storage moduli at different magnetic fields using the fluid parameters: shear modulus and yield stress. (b) Scaling of the loss moduli at different magnetic fields using the magnetic field dependence proposed by Ginder (1996) for the shear modulus and the yield stress. Inset shows the scaling for the storage moduli.

The magnetic field dependence of the moduli can be captured by using the shear modulus and the yield stress to scale the storage or loss modulus and the oscillatory loading stress respectively as shown in figure 2.30(a). Ginder (1996) proposed the following scalings for the shear modulus and yield stress of an MR fluid using FEA calculations of magnetizable particles in a chain

$$\begin{aligned}\sigma_y &\approx \sqrt{6}\phi\mu_0 M_s^{1/2} H^{3/2} \\ G &\approx 3\phi\mu_0 M_s H\end{aligned}\tag{2.16}$$

where ϕ is the particle concentration, M_s is the saturation magnetization of the particles and H is the magnetic field strength. The sub-quadratic dependence of the yield stress and the linear dependence of the shear modulus on the magnetic field can be further used to obtain a stronger scaling for the oscillatory shear flow data as shown in figure 2.30 (b).

The scaled loss modulus shows an overshoot when the oscillatory stress has a large amplitude and is close to the yield stress as shown in figure 2.31. This weak strain overshoot is typical of a Class III complex fluid (Sim *et al.*, 2003) and is also observed in fumed silica suspensions, electrorheological fluids, dough etc. This is a hallmark of competing processes leading to creation and destruction of structures in the complex fluid with the destruction rate slightly higher than the creation rate leading to strain hardening at higher strain amplitudes.

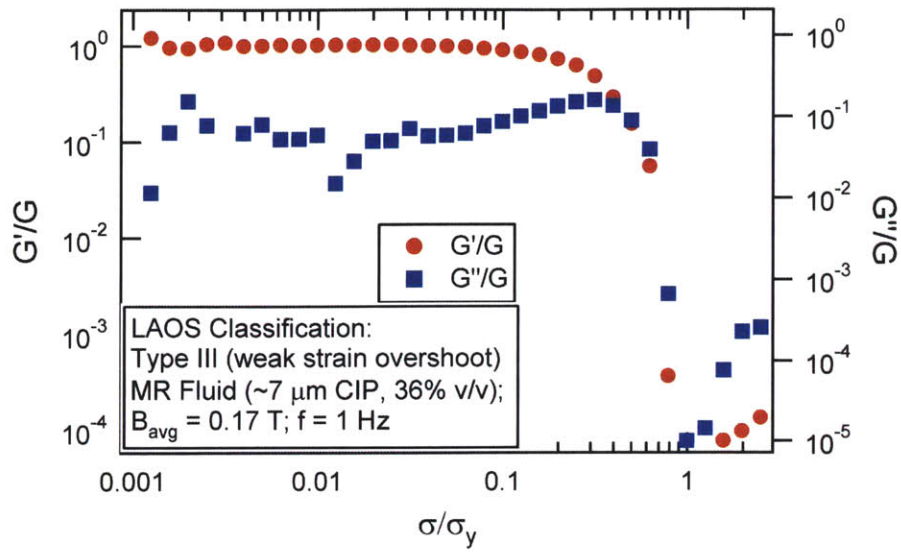


Fig 2.31 MR fluids can be typically described as type III complex fluids because of the overshoot in the normalized loss modulus as compared to the storage modulus.

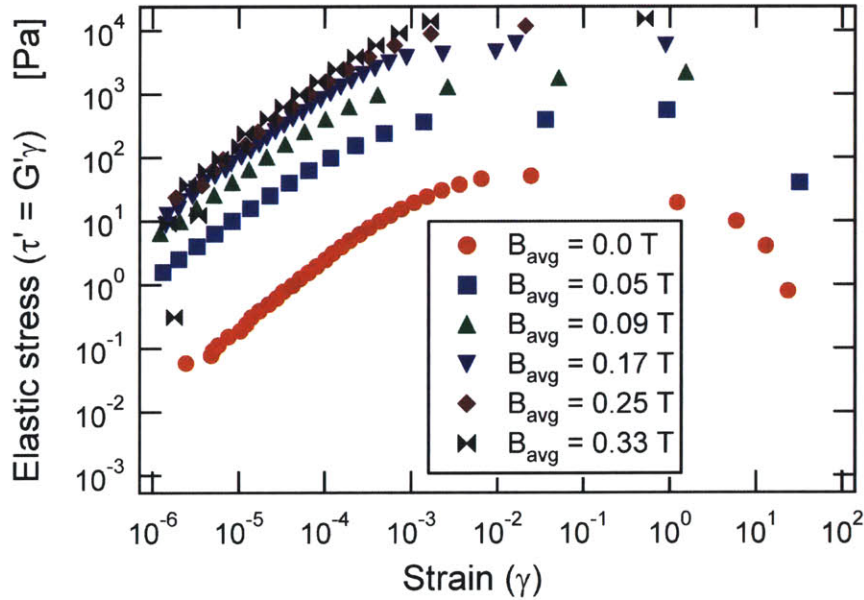


Fig 2.32 Elastic stress for 36% v/v 7 micron CIP based MR fluid at 36% v/v. A critical strain of about 10^{-2} which is only weakly dependent on the magnetic field leads to plastic chain collapse and change from gel-like to liquid-like behavior.

Elastic stress ($\tau' = G' \gamma$) is a measure of energy that can be stored elastically in these chain structures with increasing deformations and is shown in figure 2.32. It can be observed that with increasing magnetic field a higher elastic stress is possible though the chains collapse at a critical strain γ_c which is only a weak function of the magnetic field. This critical strain is a very small value $\gamma_c \sim 10^{-2}$ as has also been reported in simulations of MR fluid behavior using polarization models. This critical strain marks the point where the MR fluid behavior changes from a solid-like response to more fluid-like response. A possible method of improving on the yield stress of MR fluids would be increasing this critical strain by use of flexible chain like structures or anisotropic shapes and sizes that are stable until higher value of strains.

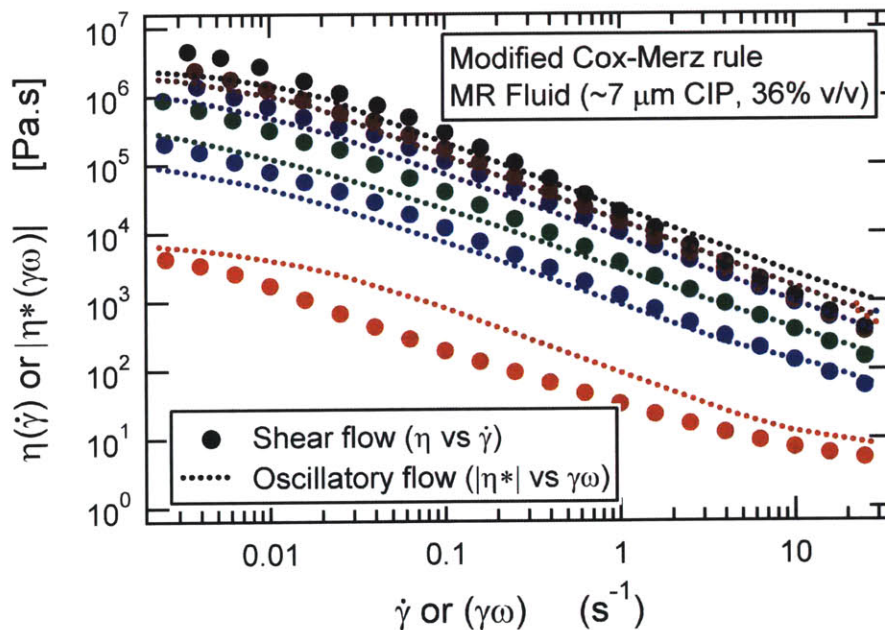


Fig 2.33 Modified Cox Merz rule can be used to relate the oscillatory shear flow and steady state flow behavior for MR fluids to a fair degree.

Also, the oscillatory shear data can be related to the steady shear data using the Modified Cox-Merz rule (Doraiswamy *et al.*, 1991) to a fair degree as shown in figure 2.33. This rule

relates the fluid behavior in oscillatory and simple shear flow such that the complex viscosity of the fluid (η^*) observed in a small amplitude oscillatory shear test is equivalent to the steady state flow viscosity (η) when the shear rate ($\dot{\gamma}$) in the sample is same as the equivalent shear rate ($\gamma\omega$) in oscillatory shear flow. The modified Cox-Merz rule is a modification to the original Cox-Merz rule wherein the equivalent shear rate is considered the same as the frequency. This empirical modification has been previously found to hold true for a number of other concentrated suspensions.

2.7 Lissajous Curves (LAOS Shapes)

The non-linearities observed in the oscillatory shear flow tests imply that the first harmonic of the storage and loss modulus are frequently not enough to capture and understand completely the rheological behavior of the fluid (Citerne *et al.*, 2001). In order to further characterize the nonlinearities, techniques such as Fourier-transform rheology (Wilhelm, 2002) or analysis of Lissajous curves are used. We analyze the Lissajous curves obtained from large amplitude oscillatory shear data by comparing their shapes and area enclosed by these curves for different magnetic fields and fluid compositions. Lissajous curves are hysteresis loops obtained by plotting the input stress signal against the output strain signal from a oscillatory stress amplitude sweep test. They can also be obtained by performing an oscillatory strain amplitude sweep test for strain controlled rheometers. A Hookean elastic solid will show only elastic deformation and hence its Lissajous curve is a straight line while a Newtonian fluid will have a circle as its Lissajous curve due to a 90 degree phase lag between the stress and strain signal as shown in figure 2.34. Visco-elastic fluids have a phase lag less than 90 degrees and hence an elliptical shape is obtained. The area enclosed by this hysteresis loop is an indication of the energy dissipated per unit volume.

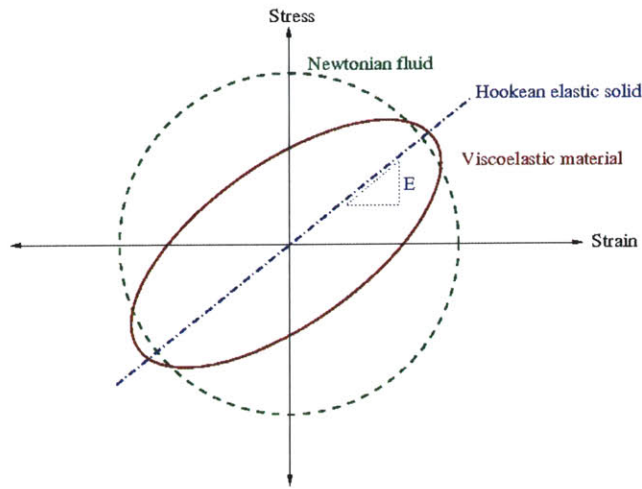


Fig 2.34 Schematic of Lissajous curves for a Hookean solid, Newtonian fluid and a viscoelastic material.

MR fluids are visco-elasto-plastic materials and their viscoelastic response coupled with plastic deformation can indeed be observed very clearly from the Lissajous curves. At low loading stresses, elliptical lissajous curves are obtained as can be seen from figures 2.35(a)-(b) which indicates a visco-elastic fluid response. However, at large amplitude of oscillatory stresses, nonlinear behavior leads to deviation from this elliptical shape into a more rhombohedral shape with a substantial increase in the amount of energy dissipated. At the yield stress, as the loading stress crosses the stress threshold the material strains dramatically leading to a nearly square Lissajous curve with a huge associated increase in the energy dissipation as can be seen in figure 2.35(c). Figure 2.35 also shows the visco-elasto-plastic model predictions for the LAOS shapes at different values of dimensionless stress and an excellent agreement between the experimental data and model predictions is observed.

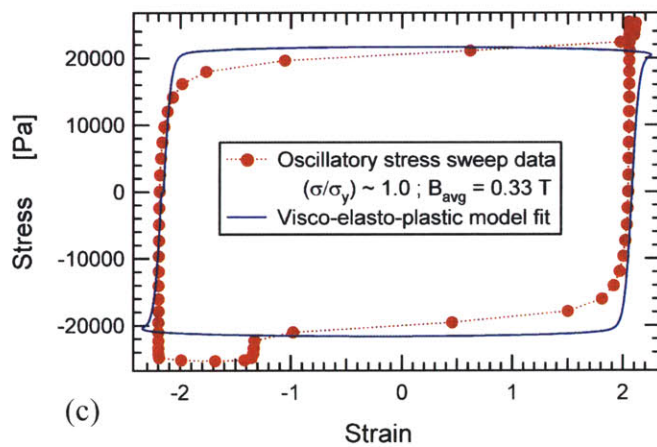
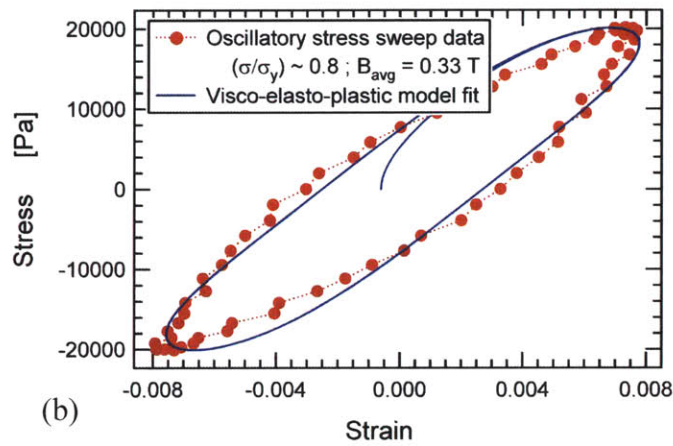
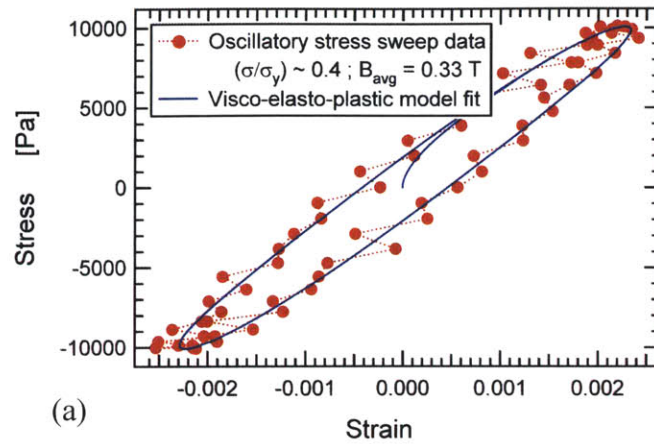


Fig 2.35 Lissajous curves as the dimensionless stress ($s = \sigma/\sigma_y$) is steadily increased in an oscillatory stress sweep test for 7micron CIP based MR fluid at 36% v/v along with visco-elasto-plastic model predictions. As the dimensionless stress approaches 1, which is the yield

point, Lissajous curves deviate from the elliptical shape with an associated increase in the energy dissipation. (a) $s = \sigma/\sigma_y = 0.4$ (b) $s = \sigma/\sigma_y = 0.8$ (c) $s = \sigma/\sigma_y = 1.0$.

The progressive change in the large amplitude oscillatory shear flow shapes from elliptical to a rhombohedral or a squarish shape is found to be identical at different magnetic fields. Figure 2.36 shows the Lissajous curves obtained at two different magnetic fields at the same dimensionless stress ($s = \sigma/\sigma_y$).

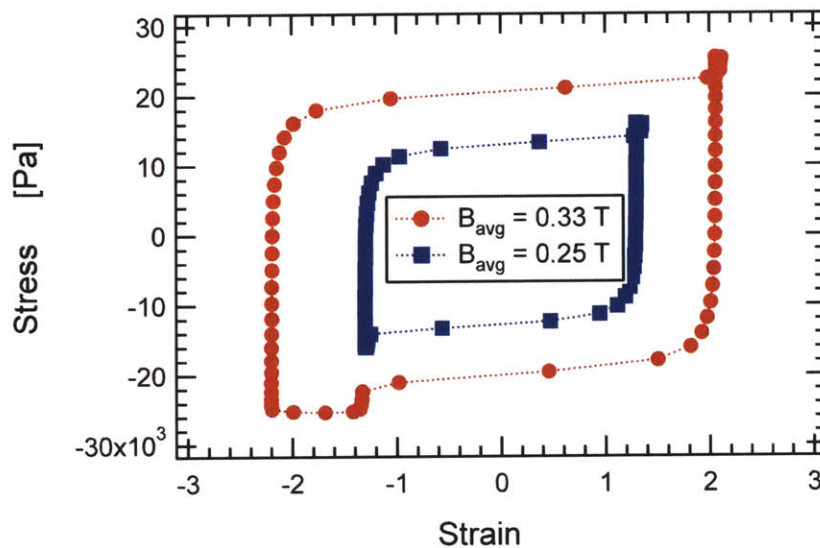


Figure 2.36 Lissajous curves shape profile is independent of the magnetic field for MR fluids (in this case 36% v/v 7 micron CIP based MR fluid) at the same dimensionless stress ($s = \sigma/\sigma_y$). Lissajous curves at $s \sim 1.0$ (yield point) at two different magnetic fields, $B_{avg} = 0.25$ T & $B_{avg} = 0.33$ T are shown in the figure.

The applied stress when these identical shapes are observed is dependent on the magnetic field but this magnetic field dependence is captured well by the yield stress. Further, the area enclosed by the LAOS shapes also increases with an increase in the magnetic field as shown in

figure 2.36 which is also captured well by the scalings of strain ($\gamma^* = \gamma G / \sigma_y$) and stress ($s = \sigma / \sigma_y$) as predicted by the visco-elasto-plastic model.

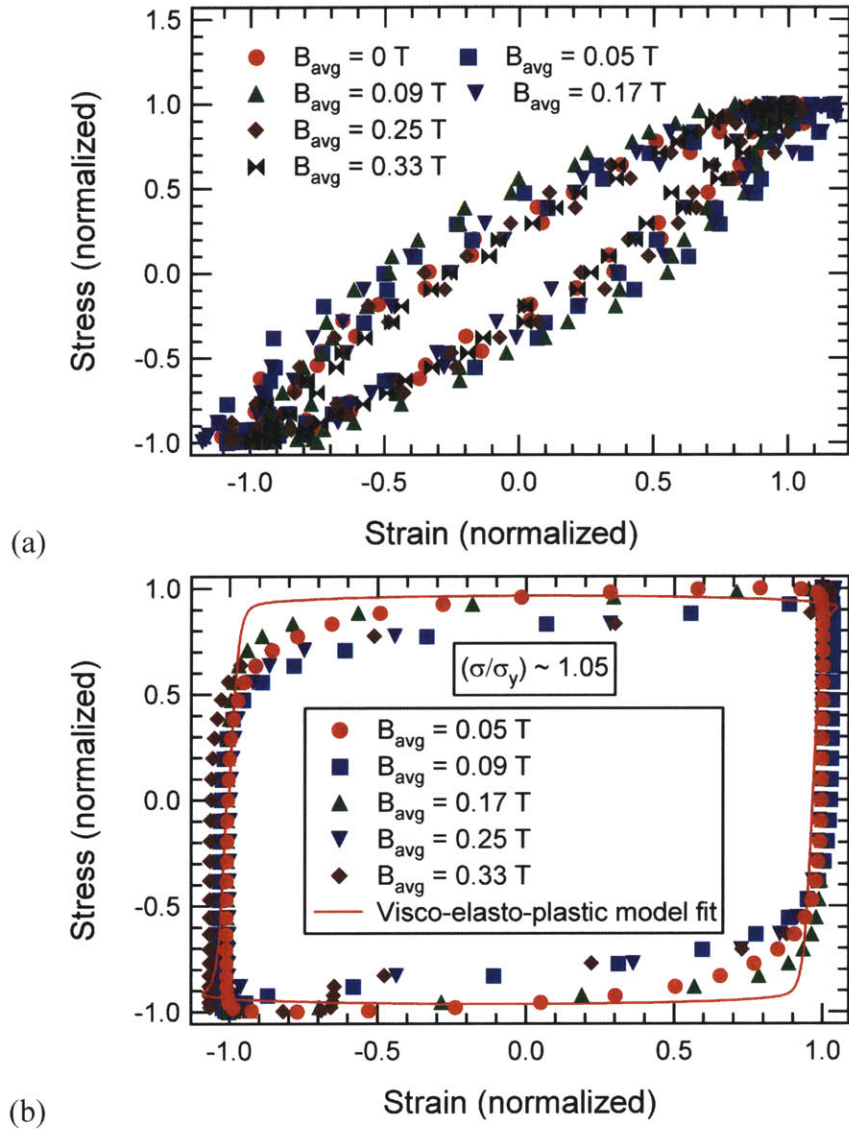


Fig 2.37 (a) Scaled LAOS curves for $s = \sigma / \sigma_y = 0.4$ (b) Scaling of Lissajous curves near the yield point ($s = \sigma / \sigma_y \sim 1.0$), for different magnetic fields in excellent agreement with the visco-elastic-plastic model prediction.

We can use the scalings predicted by the visco-elasto-plastic model to dedimensionize the stress and strain signals for different magnetic fields to obtain universal LAOS shapes for the MR fluid as shown in figure 2.37(a) & (b). Figure 2.37 shows the scaled Lissajous curves at two different values of dimensionless stress ($s = 0.4$ & $s = 0.1$) in agreement with the “soft-glassy” rheology model prediction for the curve. The scalings for the stress and strain in the experimental system provide strong corroboration for the validity of the visco-elasto-plastic model assumptions and predictions.

2.8 Conclusions

Rheological behavior of MR fluids, commercial and laboratory synthesized, has been studied in detail under steady state flow, oscillatory shear and creep flow. MR fluid behavior shows striking similarities with the response of other “soft-glassy” materials and the behavior is captured well by a “soft-glassy” rheology model. The scalings and nonlinearities observed in creep and large amplitude oscillatory shear flow are also well described by the visco-elasto-plastic model that is based on microscopic mechanisms of plastic deformation in yield stress fluids. We expect these scalings observed for MR fluids to be more general in nature and applicable to generalized yield stress fluids.

Chapter 3

Adaptive Energy Absorbing Materials

Energy absorbing materials and structures are used in a number of applications ranging from vehicles, ballistic armor, blast protection to helmets, sporting equipment and clothing (Gibson and Ashby, 1997; Cheeseman and Bogetti, 2003). Such materials will shunt (divert and distribute energy to sturdier areas), convert or dissipate energy via viscosity, friction, visco-elasticity or plasticity. However, typically passive systems like cellular solids, foams, fabrics, sandwich structures etc. are utilized, which, although effective under certain pre-defined scenarios, provide little to no utility under a different set of conditions. Many of these applications, on the other hand, require an adaptive structure that can be controlled to absorb varying amounts of energy depending on the external conditions (Courtney and Oyadiji, 2001; Holnicki-Szulc *et. al.*, 2003).

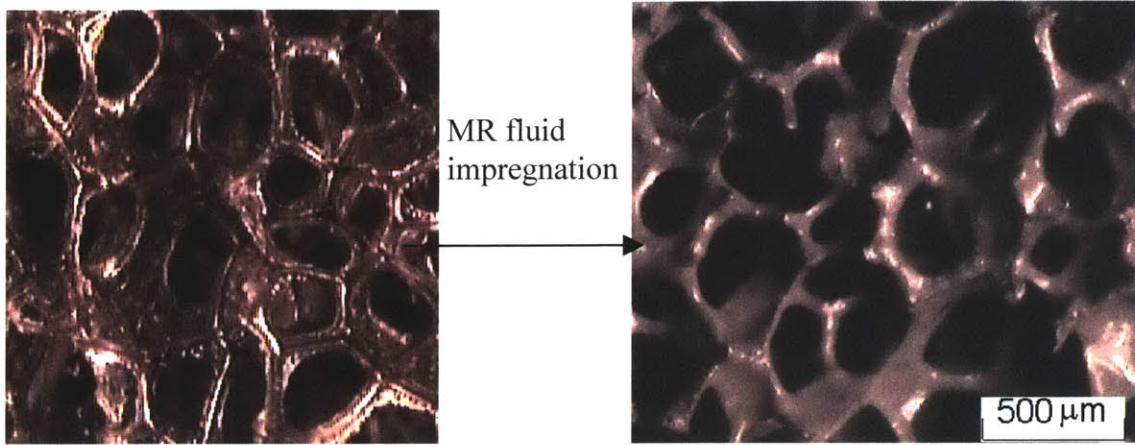
A representative application area is the automotive industry where it could prove beneficial in overcoming the energy management concerns in occupant protection components for passenger and vehicle safety. A compliant material forming these parts generates low forces and is comfortable but absorbs very little energy, while thicker, stiffer materials will absorb more energy but conflict with design and passenger demands for slim, narrow structures. Hence, there is a trade-off in the optimal stiffness property of the selected materials and an adaptive material is necessary to resolve this conflict. This is commonly referred to as the *conflict of stiffness* problem (Courtney and Oyadiji, 2001; Ullrich, 2003).

3.1 Concept and development of the adaptive material

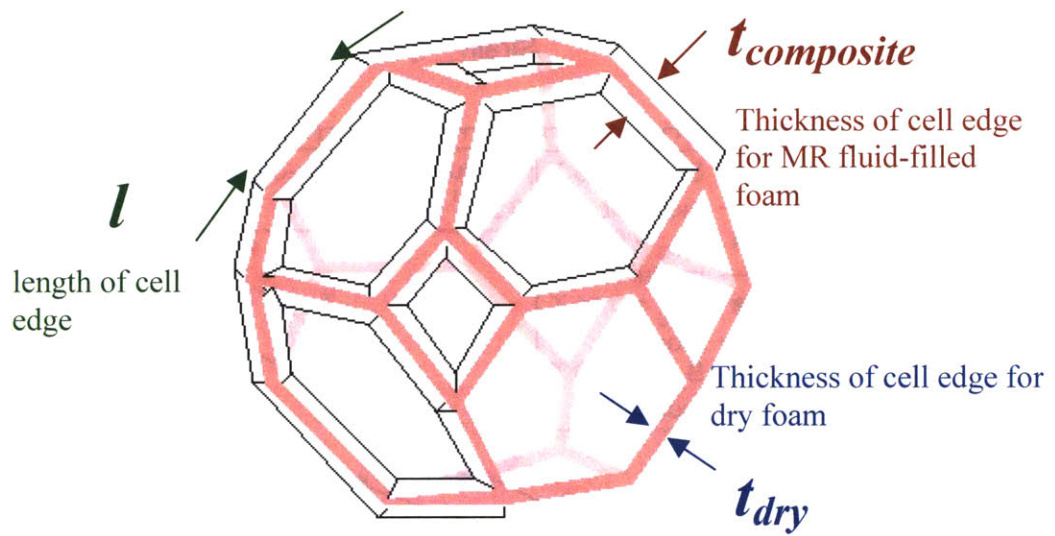
A 'smart' (responsive to external conditions or user-controllable) energy-absorbing fluid-solid composite can be obtained by impregnating an elastomeric-foam or a fabric with a field-responsive fluid (FRF) such as a magnetorheological fluid (MRF) or a shear-thickening fluid (STF) (Deshmukh and McKinley, 2003).

The stiffness and the energy absorbing properties of this composite can be varied by controlling and adjusting the field strength in the vicinity of the material. The field-responsive fluid when used for impregnation of a fabric or foam forms a secondary layer of MR fluid on the fibers or the cell struts (figure 2.1) and hence magnetic field strength becomes the important user-controllable parameter. The magnetic field strength determines the yield stress of the MRF (see chapter 2), which in turn controls the solid elastic modulus of the composite material and also its ultimate energy absorption capacity. Hence, as the magnetic field is increased to moderate levels of $B_{avg} \sim 0.2$ Tesla, while keeping other parameters constant, the yield stress of the MR fluid increases and correspondingly an upward shift in the stress-strain curve can be obtained. The energy absorbed per unit volume or the *energy absorption capacity* that is given by the area enclosed by the stress-strain curve for the material also increases dramatically with increasing magnetic field.

The jump in the stress-strain curve is quite dramatic for magnetorheological fluid impregnated cellular-solids (Deshmukh and McKinley, 2007). The energy absorbed for MR fluid-impregnated foams increases significantly even at moderate magnetic fields and low volume fractions of the fluid. It is observed to increase by a factor of 30-50 times the energy absorbed at zero-field as shown in figure 2.2(a). The figure is shown partially in a logarithmic scale and partially in a linear scale in order to illustrate the low amounts of energy absorbed in the absence of magnetic fields. A 'two-layer' model can be effectively used to model the stress-strain behavior variation as a function of magnetic field and volume fraction as shown in figure 2.2(b).

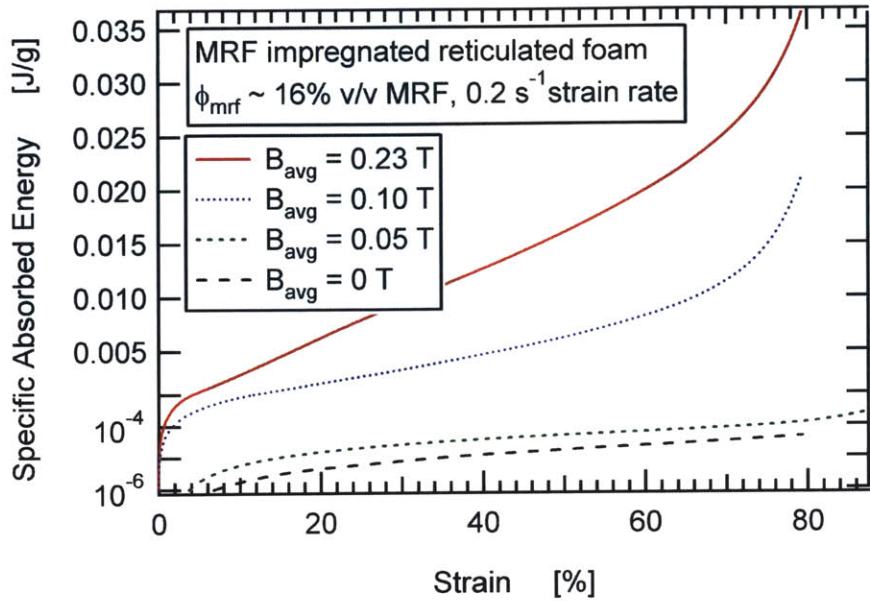


(a)

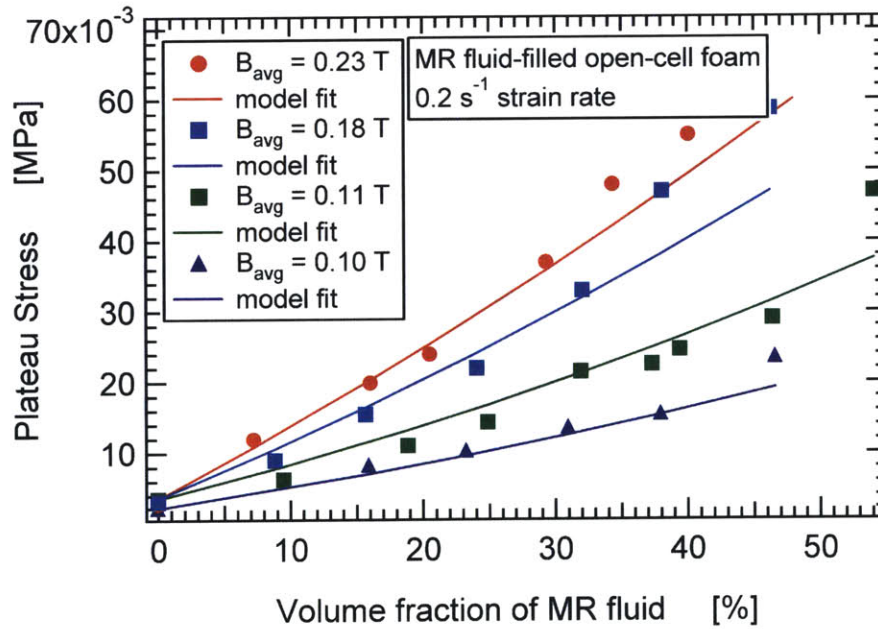


(b)

Figure 2.1 (a) Optical micrograph (*Olympus SZX9 microscope*) of a dry low-density reticulated foam after impregnation with a commercially available MR fluid (*LORD's MRF-336AG*). (b) Schematic of a single tetrakaidecahedron cell of the MR fluid-foam composite showing a secondary layer of MRF on the solid foam cell edges (Deshmukh and McKinley, 2003).



(a)



(b)

Figure 2.2 (a) Variation of energy absorption capacity by modulating the magnetic field strength for 16% v/v MR fluid-filled open cell foam. (b) ‘Two-layer’ model fit to observed values of the plateau stress for MR fluid-filled open-cell foam samples (Deshmukh and McKinley, 2007).

Varying the volume fraction of the MR fluid that is impregnated into the fabric or the foam increases the thickness of the secondary layer of MR fluid that forms on the fibers or the struts of the foam and hence the composite material stress. Also, more fluid needs to be squeezed out as the sample undergoes compression and hence the stress increases at lower densification strains. The energy absorbed by the MR fluid-impregnated foam can thus be modulated to satisfy specific requirements by controlling external parameters such as the applied magnetic field (B_{avg}) and the volume fraction (ϕ_{mrf}) of MR fluid. Also, due to the fast response time of the FRFs, the energy absorption capacity can be rapidly switched to different levels in order to satisfy the application demands.

3.2 Application potential for the adaptive material

3.2.1 Automotive energy management

A number of application areas from ballistic armor to automotive components can be envisaged for this *smart material*. In the automotive industry, energy management is a big concern as new incoming Federal and European community legislations (FMVSS 201/202, EURO NCAP, EEVC WG 17) (Ullrich, 2003) introduce stringent impact protection requirements. Automobile parts would need to provide protection for two distinctly different sizes (adult and child) of pedestrian and passenger, which present many 'conflict areas' with different stiffness requirements under various conditions. A possible solution to this *conflict of stiffness* problem involves constructing interior components of the vehicle such as the headrest, A/B/C pillar trims, head-liners, knee and side impact foam parts with an adaptive material so that the different energy absorption criteria under varying impact conditions and constraints of interior/exterior space and design can be satisfied (Deshmukh and McKinley, 2003).

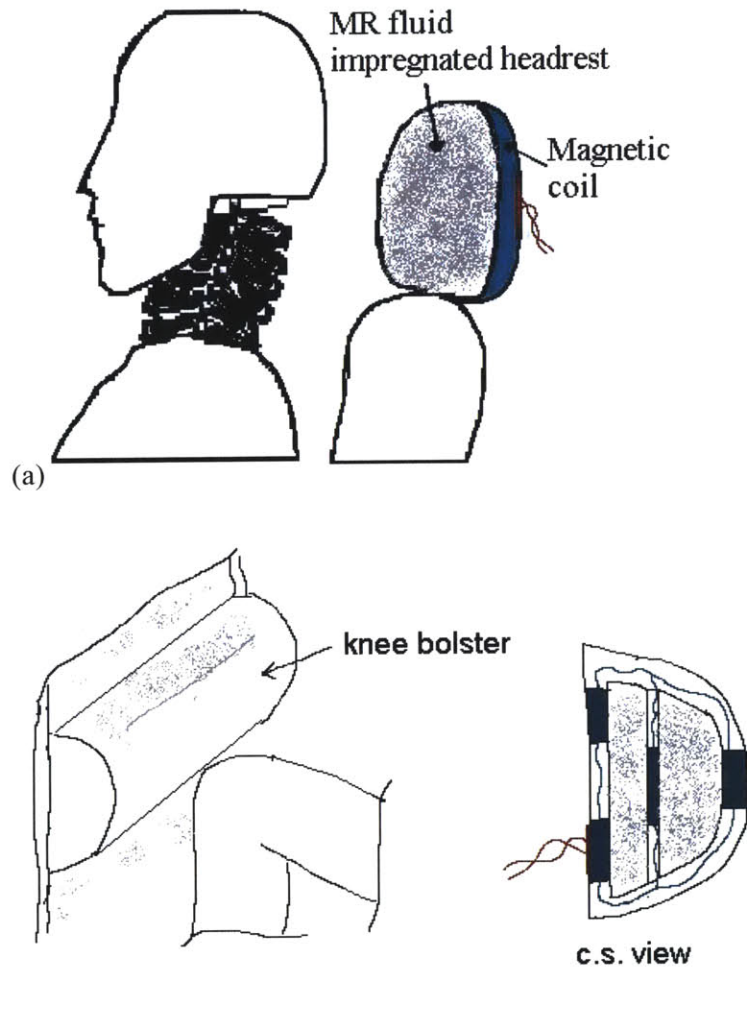


Figure 2.3 (a) Illustration of a MR fluid impregnated headrest in an automobile to satisfy the neck injury criterion and prevent whiplash-associated disorders in a rear-end crash. (b) A field-responsive fluid impregnated knee bolster with coils or circuitry to control its energy absorption depending on the passenger (child or adult) during a frontal crash.

This *adaptive composite* could also be extremely beneficial in automotive injury prevention (figure 2.3). NHTSA estimated that there were 805,851 occupants with whiplash injuries alone, annually between 1988 and 1996 in the United States resulting in a total annual

cost of \$5.2 billion. Whiplash associated disorders are influenced mainly by seat and head-restraint properties and their positions with respect to the head and torso. The number and extent of injuries can be reduced by maximizing the amount of energy absorption, by minimizing the occupant acceleration or by reducing the relative movement between the head and the torso (Svensson *et al.*, 1996). A soft compliant headrest though comfortable, would imply a high risk for whiplash injury because of large head-neck relative movement. A field-responsive fluid-impregnated headrest would allow the same headrest to be soft and compliant under normal driving conditions but then can be switched into a high impact energy absorbing stiff material during a crash.

3.2.2 Protective armor

Impact protection and ballistic protection is the primary function of soldier body armor and user-controllable energy dissipation through field-responsive fluid impregnated clothing serves the dual purpose of providing comfort under normal use and protection from impact and blunt trauma in threat-posing conditions. The ballistic impact on a fabric is associated with a sharp rise in stress and a longitudinal strain wave is generated that propagates along the axis of the yarns (Cheeseman and Bogetti, 2003). The field-responsive fluid can lead to enhanced energy absorption by forming a connecting structure between the yarns (in presence of field) and increasing the friction between the yarns, thus, transmitting the impact to a broader number of strands besides the principal yarns (figure 2.4). The yarn-yarn and interfilament friction is expected to be a function of the field dependent yield stress (see chapter 2) and hence, using external fields the subsequent breaking of yarns can be controlled.

Adaptive energy absorbing materials can also prove useful for controllable blast protection, vibration dissipation and recoil reduction in military equipment and weaponry systems.

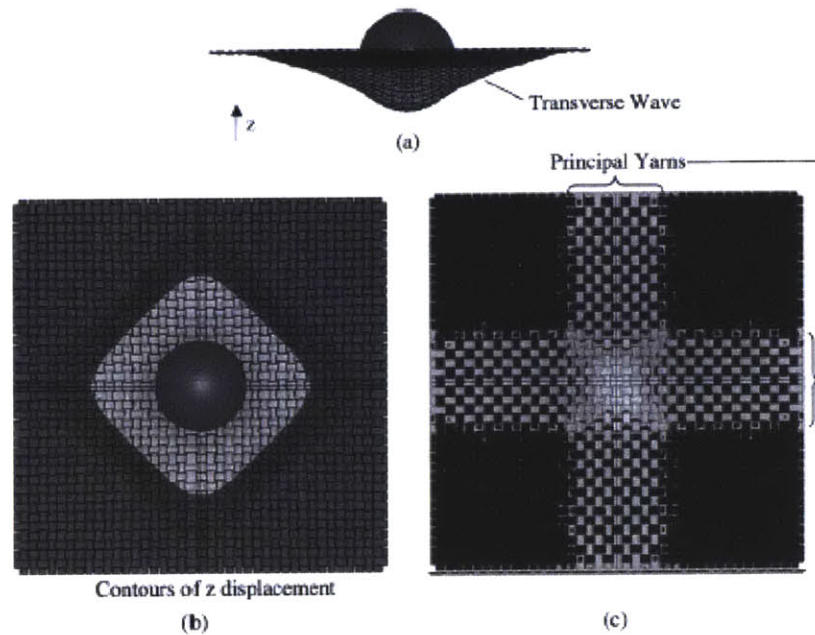


Figure 2.4 Projectile impact on a single ply of a fabric illustrating the propagation of a transverse wave primarily through the principal yarns. A field-responsive fluid would form a connecting matrix around these yarns and the increased friction would ensure a broader number of yarns are engaged and enhance the amount of energy absorbed.

The human body is susceptible to damage due to external stress, impact and shocks. Protective clothing and garments such as orthopedic supports, braces, splints, slings and wraps are commonly used for injury, fracture prevention and protection. These garments or devices usually use fabric or foam based padding materials together with a rigid load-bearing frame that surrounds the susceptible body tissues and bones for energy dissipation and load shunting. Tunable materials will prove useful in these and numerous other protective devices for a large range of conditions that are experienced in everyday use such as normal use to simple bruises, cuts to high-impact physical activity and accidents (figure 2.5(a)).

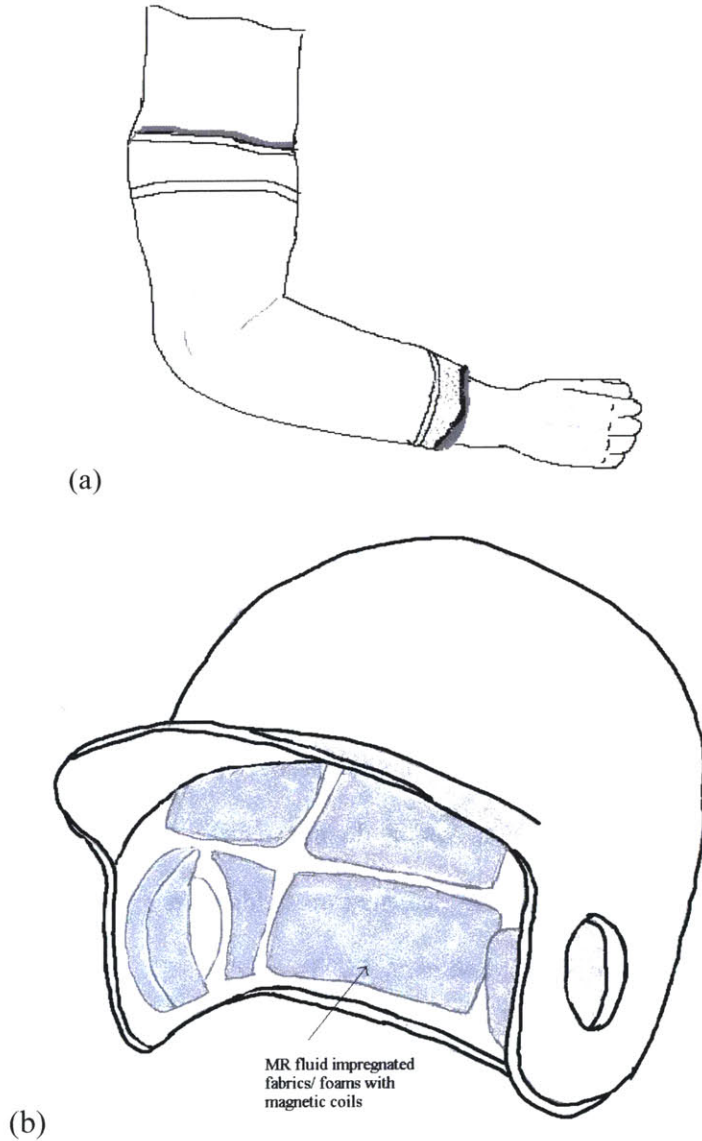


Figure 2.5 (a) Conformable and tunable splint or brace made of field-responsive fluid doped materials (b) Protective gear and sporting equipment for impact and injury protection while maintaining compliance under normal conditions as desired by the user.

Sporting gear like shoes, helmets, gloves, supports and braces is commonly used for both comfort and injury prevention. A fluid-based device is especially useful since it is conformable to the body part in contact and, in the case of field-responsive fluids, the energy absorption capacity of the device can adjust to the applied loads, stresses. Hence, comfort, compliance and protection

characteristics of the device can be actively controlled using an external field as shown in figure 2.5.

3.2.3 Challenges

A number of challenges lie before achieving the goal of putting adaptive energy absorbing materials practical use.

In case of MR/ ER fluids, generation of magnetic and electric fields is a big concern. The generation of fields is associated with extra cost, circuitry and in the case of body armor and clothing, maximum strength of the current and field.

Further, impregnation of clothing and armor with fluids add to the weight of the protective clothing which is especially significant for MR fluids comprising of iron particles (density of 7.81 g/cc). In order to provide ballistic protection a sophisticated array of sensors is required as the total time for ballistic impact is of the order of microseconds.

Hence, shear-thickening fluids which do not require external fields but can respond passively (or actively with actuators) to deformation fields hold a lot of promise for protective gear and clothing (Bettin *et al.*, 2006; Lee *et al.*, 2003).

3.3 Conclusions

Field-responsive fluids can be used to modulate the stiffness and energy absorption capacity of cellular solids, fabrics, polymers etc. Shear-thickening fluids, which belong to the class of field-responsive fluids and respond when acted upon by a stress field, can also be impregnated into reticulated foams to provide a passive or even an active mechanism for adaptive energy absorption. Thus, a 'novel' class of conformable field-responsive fluid based composites has been developed so that they can be used for wide-ranging rapidly switching energy absorbing applications.

Chapter 4

Structure Formation and Dynamics of MR Fluid Flow in Microchannels

The structure evolution, pattern formation and dynamics of MR fluids on the microscale are important from both a scientific and application development viewpoint. Also, understanding the structures formed from a microscopic perspective along with the study of dynamics of the structure evolution provides useful insights into bulk rheological properties that were described in chapter 2.

A few recent studies (Fermigier and Gast, 1992; Promislow *et al.*, 1995; Furst and Gast, 2000; Climent *et al.*, 2004) have focused on looking into the aggregation dynamics in the absence of bulk fluid flow which provides an excellent background for taking it one step further with the aim of understanding how flow affects the interplay of various forces and mechanisms responsible for the structure formation. This study is also novel in the respect of studying the aggregation dynamics & structure evolution of carbonyl iron particle based MR fluids in the presence of bulk fluid flow. The characterization of aggregation phenomena of these fluids on the microscale is vital to development and optimization of micro and macroscale applications as a majority of commercial applications based on MR fluids use carbonyl iron particles as their constituent particles in conditions of flow.

Further, microfluidic applications, typically, use pressure driven flow and understanding the effect of flow is vital to the use of field-responsive fluids in microfluidic devices such as

DNA separation chips (Doyle *et al.*, 2002), dynamic supraparticle patterning masks for fabrication of micro-optical filters and gratings (Hayes *et al.*, 2001), continuous flow lithographic chip for magnetic microparticle synthesis, magnetic fluid switches, valves and mixers (see chapter 5 for further details on applications).

4.1 Modeling: Particle Interactions

The chaining of particles, brought about by their polarization in the presence of a field, is responsible for the field-controllable aggregation and yield behavior of MR fluids. This chaining occurs if there is a magnetization or a dielectric (in the case of ER fluids) mismatch between the particles and the carrier liquid. The polarization model can, in principle, predict the aggregation dynamics and the associated yield stress. Electrostatic/ magneto static, hydrodynamics, steric and Brownian forces are together used to compute the aggregation dynamics of these particles, which are themselves typically modeled as hard spheres (Larson, 1999).

4.1.1 Magnetic Interactions

The aggregation dynamics depends strongly on the magnetic interactions between the particles. Furst and Gast (2000) have demonstrated that the mutual induction between particles and multipole effects leading to localized variations in magnetic field also need to be considered in order to capture the structure evolution especially the rupture of chains. The magnetic moment acquired by a magnetizable particle of radius a in the presence of a magnetic field \bar{H} is then given by

$$\bar{m}_i = \frac{4}{3} \pi a^3 \chi \left[\bar{H} + \sum_{j \neq i} \frac{3 \hat{r}_{ij} (\hat{r}_{ij} \cdot \bar{m}_j) - \bar{m}_j}{4 \pi \mu_0 r_{ij}^3} \right] \quad (4.1)$$

$$\bar{r}_j - \bar{r}_i = r_{ij} \hat{r}_{ij}$$

where \bar{m}_i is the magnetic dipole moment of particle i , χ is the magnetic susceptibility of the particles, a is the particle radius and μ_0 is the permeability of free space.

The dipolar interaction potential (W_{ij}^m) between pair wise particles can then be used to calculate the net magnetic force (\bar{F}_i^m) on the i^{th} particle as follows

$$W_{ij}^m = \left(\frac{1}{4\pi\mu_0} \right) \frac{\bar{m}_i \cdot \bar{m}_j - 3(\hat{r}_{ij} \cdot \bar{m}_i)(\hat{r}_{ij} \cdot \bar{m}_j)}{r_{ij}^3} \quad (4.2)$$

$$\bar{F}_{ij}^m = - \left(\frac{\partial W_{ij}^m}{\partial \bar{r}_{ij}} \right) \quad \bar{F}_i^m = \sum_{i \neq j} \bar{F}_{ij}^m$$

where \bar{F}_{ij}^m is the force on particle i produced by particle j

Neglecting the multipole effects in the case of widely separated particles leads to considerable simplifications (Climent *et al.*, 2004). The magnetostatic force acting on a particle i is then obtained from the interaction potential between two particles i and j assuming a point-dipole approximation as follows (Ginder, 1996)

$$\bar{m} = \frac{4}{3} \pi a^3 \chi \bar{H}$$

$$W_{ij}^m = - \left(\frac{m^2}{4\pi\mu_0 r_{ij}^3} \right) (3 \cos^2 \theta_{ij} - 1) \quad (4.3)$$

where θ_{ij} is the angle between the field and the line joining the centers of mass of particles i and j .

Similarly for ER fluids, electrostatic forces can be determined and are given by (Larson, 1999)

$$W_{ij}^e = - \left(\frac{4\pi\epsilon_0\epsilon_s u^2}{r_{ij}^3} \right) (3 \cos^2 \theta_{ij} - 1) \quad (4.4)$$

where u is the dipole moment of an isolated particle, ε_0 is the permittivity of the space and ε_s is the permittivity of the suspending medium.

The dipole moment \bar{u} of an isolated particle is given by the Clausius-Mossotti relationship as

$$\bar{u} = \beta a^3 \bar{E} \quad \beta = \frac{(\varepsilon_r - 1)}{(\varepsilon_r + 2)} \quad (4.5)$$

where β is the effective polarizability of the particle and ε_r is the relative permittivity of the particle.

4.1.2 Hydrodynamic Interactions

The Stokesian approximation is generally used to capture the hydrodynamic interactions as the Reynolds number $Re = \rho Va/\eta \ll 1$ is very small for micron sized particles in microchannel geometries. Hence, inertia forces are neglected compared to viscous forces and the Stokes drag equation is used to capture the hydrodynamic effects

$$\bar{F}_i^H = 6\pi\eta a \frac{d\bar{r}_i}{dt} \quad (4.6)$$

where a is the radius of the spherical particle, η is the viscosity of the carrier fluid and \bar{F}_i^H is the hydrodynamic drag force on i^{th} particle

However, single sphere stokesian approximation which is valid only for widely separated particles is reported to be a poor representation so that multibody hydrodynamic interactions have also been employed in a few studies to capture the aggregation dynamics (Bonnecaze and Brady, 1992; Climent *et al.*, 2004).

4.1.3 Brownian Motion

Thermal fluctuations become important, typically, for sub-micron size particles and random white noise forcing based on the Langevin model for Brownian motion is generally used to describe these fluctuations. Climent *et al.* (2004) use a fluctuating force with zero mean and without correlation in time or other particles as follows

$$\bar{F}_i^B = \xi \sqrt{\frac{12\pi\eta a k_B T}{dt}} \quad (4.7)$$

where ξ is a random vector with Gaussian distribution and dt is the time step for numerical integration.

4.1.4 Dimensionless groups

The magnetic interactions along with hydrodynamic forces and thermal fluctuations can be cast into a particle evolution equation so that aggregation phenomena of the particles can be studied using Lagrangian tracking of the particles. The particle evolution equation also considers short-range repulsive forces (\bar{F}_i^R) arising from phenomena such as Born repulsion, solvation forces or steric interactions. (Parthasarthy and Klingenberg, 1996) as follows

$$m \frac{d\bar{V}_i}{dt} + \bar{F}_i^H = \bar{F}_i^m + \bar{F}_i^B + \bar{F}_i^R \quad (4.8)$$

where m is the mass of the particle and \bar{V}_i is the velocity of the i^{th} particle.

The inertial term of left hand side of the equation is neglected because Reynolds number is small $\text{Re} = \rho Va/\eta \ll 1$.

The parameter λ is independent of the shear rate ($\dot{\gamma}$) and takes into account the change in the yield stress coming from magnetostatic forces and due to Brownian motion. Brownian motion will not only prevent the particles from settling but also from forming aggregates and chains, hence reducing the yield stress.

$$\lambda = \frac{\text{magnetostatic forces}}{\text{brownian forces}} = \frac{\pi\mu_0\chi^2 d^3 H^2}{72k_B T} \quad (4.9)$$

In the case of MR fluids, which are composed of micron sized carbonyl iron particles, the Brownian motion is negligible as compared to magnetostatic forces and thermal fluctuations play little role in breaking the chains as happens to be the case for nanometer sized particles in a ferrofluid. The dimensionless group (λ) is typically of the order of 10^6 for the carbonyl Iron particles based MR fluids.

Hence, the structure evolution and aggregation dynamics of MR fluids in the presence of bulk fluid flow, particularly carbonyl iron particle based fluids, is decided mainly by the coupling of the hydrodynamic and magnetostatic forces. Mason number (Mn) which is the ratio of these two forces is thus used to characterize the aggregation phenomena observed during experiments or simulations performed while varying different parameters.

$$Mn = \frac{\text{hydrodynamic forces}}{\text{magnetostatic forces}} = \frac{144\eta_s \dot{\gamma}}{\mu_0 \chi^2 H^2} \quad (4.10)$$

where η_s is the carrier fluid viscosity and $\dot{\gamma} = V_{avg}/C_L$ is the shear rate based on a characteristic dimension. The characteristic dimension used to define the Mason number could be either d diameter of the particle, $h/2$ height of the channel or $W/2$ width of the channel.

The Péclet number (Pe) describes the relative importance of advection to diffusion and determines how fast the structure or the field induced chains form and if thermal motion causes them to deform or collapse. In the present study involving MR fluid flow in microchannels, $Pe \ll 1$, so that the thermal fluctuations can be neglected.

$$Pe = \lambda Mn = \frac{\text{hydrodynamic forces}}{\text{brownian forces}} = \frac{2\pi d^3 \eta_s \dot{\gamma}}{k_B T} \quad (4.11)$$

4.2 Experimental Materials and Methods

4.2.1 Background

The study of aggregation phenomena of superparamagnetic particles (typically polystyrene beads with ferromagnetic inclusions) in the quiescent case has been the focus of a number of experimental and simulation studies (Fermigier and Gast, 1992; Promislow *et al.*, 1995; Climent *et al.*, 2004). A typical experimental setup consists of a micro cell or chamber to hold the suspension in a magnetic field environment on a microscope stage. A CCD camera is generally used to capture the cluster size evolution with time at 1-30 frames per second. Volume fraction of the particles is usually limited to 0.1%-5% as visualization of particles & calculation of reliable cluster size data becomes difficult at higher volume fractions.

Other experimental methods that have been used earlier to investigate the interaction forces and structure evolution include measurement of mechanical properties of individual dipolar chains using optical tweezers (Furst and Gast, 2000) and 2-D light scattering technique to study the aggregation kinetics of ER fluids (Martin *et al.*, 1998).

4.2.2 Materials

MR fluids that are used in the current study are composed of carbonyl iron particles obtained from BASF AG (CS, CR, HQ CIP grades) varying from 1 to 10 microns in diameter. Formulation of these MR fluids is described in detail in chapter 2. Particles are fairly polydisperse (e.g. CR CIP grade had a d50 value of 6.72 microns, d10 value of 3.25 microns and d90 value of 16.57 microns) and are used as received in the formulation of the fluids. Superparamagnetic polystyrene beads (with 62% w/w magnetite inclusions) and a mean diameter of 1.5 microns are also used as a constituent of a few test fluids. Low volume concentration of particles in MR fluids is used (0.5%-3%) in order to facilitate cluster size variation analysis. Imaging of higher concentration MR fluids becomes difficult as ferromagnetic particles are opaque to transmitted

light and appear as dark spots on a light background in the image. Hence, at a volume fraction of 1.5%, the 2D projected image of approximately 10 planes of particles (for 1 micron size particles flowing in a 10 micron height channel) has a filled surface fraction of 90%.

$$\begin{aligned}\phi_v &= N \frac{\pi d^3}{6V}; \quad \phi_{sf} = N \frac{\pi d^2}{V/h} \\ \phi_{sf} &= 6\phi_v \left(\frac{h}{d} \right)\end{aligned}\tag{4.12}$$

where ϕ_v is the volume fraction, ϕ_{sf} is the surface fraction, h is the height of the channel, V is the volume of the viewing window of the experimental cell and N is the number of particles in the viewing window.

4.2.3 Experimental setup: High-Speed Video Microscopy

Carbonyl iron particle based MR fluids have a fast response time, typically, of the order of a few milliseconds. Hence conventional image capture techniques such as with a CCD camera cannot be effectively used to capture the aggregation dynamics. Hence, we use a Phantom 5.1 (Vision Research Inc.) high speed camera that can take images at a speed of 30-10000 frames per second. Images were typically captured at 1000 fps (total capture time 4-8s) in order to capture the initial unsteady dynamics of chain and cluster formation and evolution. The camera is connected to a Nikon TE-2000 inverted microscope and traditional transmitted brightfield illumination technique (Nikon 100W halogen lamp) is used to obtain images wherein particles appear as dark objects on a light background.

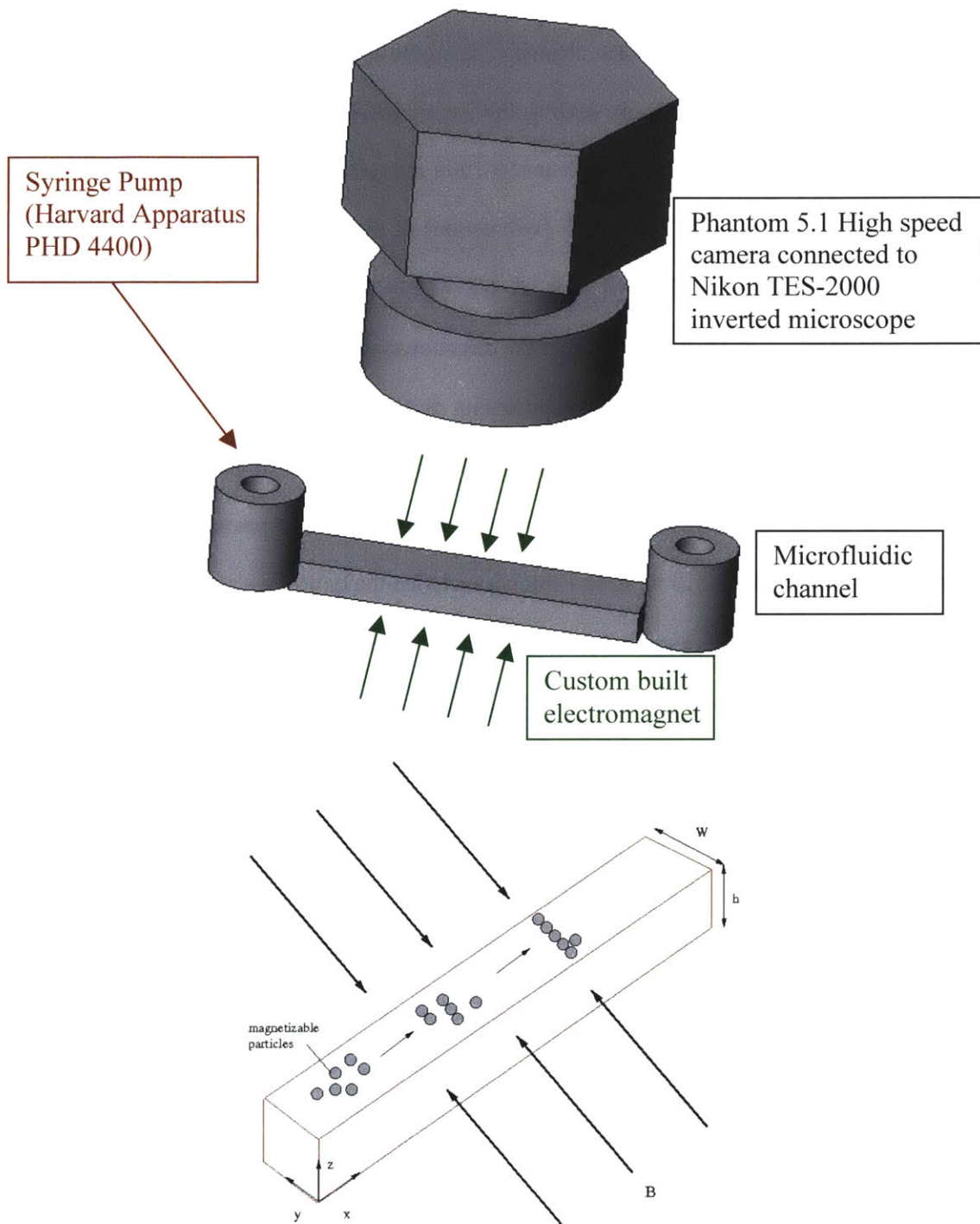
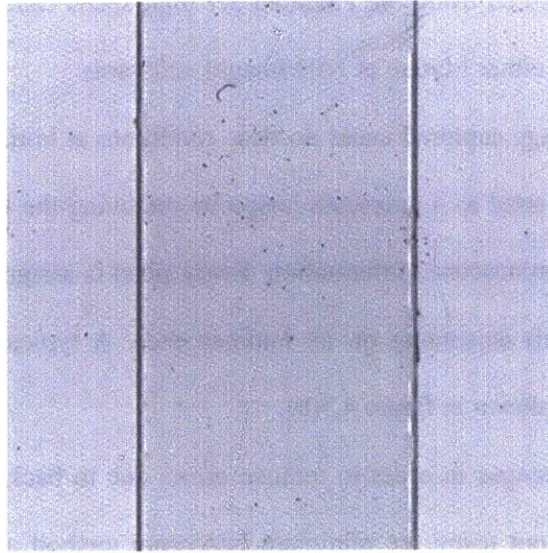
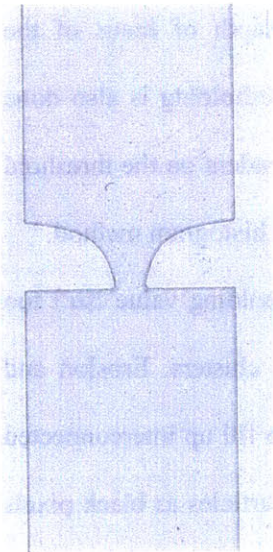


Figure 4.1 Schematic of the experimental setup showing typical microchannel geometry on an inverted microscope with a high-speed camera mounted on it. The figure also illustrates the flow (x), field (y) & height (z) directions.

Glass capillaries and PDMS channels microfabricated using the soft lithography technique (McDonald *et al.*, 2000) are used as the experimental flow cell. Channels of different dimensions – width (y-direction) varying from 50-1000 microns and height (z-direction) varying from 50-100 microns are used. The length (x-direction) of the microchannel is typically 25mm with inlet and outlet ports at the two ends. A custom-built electromagnet is used to apply a magnetic field of ($B_{avg} = \mu_0 H$) 0 - 0.2 Tesla in the direction (y-direction) perpendicular to the flow direction (x-direction). A syringe pump (for constant displacement flow) or a nitrogen pressure tank (for constant pressure flow) is used to obtain pressure driven flow of the magnetorheological fluids in these microchannel geometries. The syringe pump (Harvard Apparatus, PHD 4400) can provide a range of flow rates (10 nl/ hr to 1 ml/ hr) such that the typical average particle velocities obtained in the microchannels vary from 0.01 $\mu\text{m}/\text{ms}$ to 5 $\mu\text{m}/\text{ms}$.



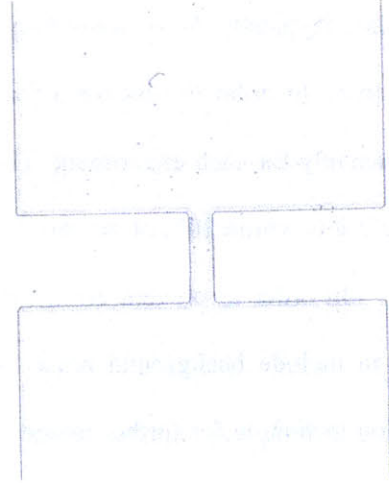
(a)



(b)



(c)



(d)

Figure 4.2 PDMS channels microfabricated using the soft-lithography technique (a) Straight channel geometries were typically used for studying the effects of flow on the structure evolution and aggregation dynamics. (b) hyperbolic channel geometry (c) obstacle channel geometry (d) contraction (4:1) channel geometry.

4.2.4 Image Analysis Technique

Image frames captured using the Phantom 5.1 high speed camera at 1000 frames every second are analyzed using either Matlab or NIH ImageJ softwares.

An illustrative image captured under no-flow conditions at initial time is shown in figure 4.3(a). The image is converted to a grayscale image by removing the hue and saturation values while keeping only the luminescence information. Every pixel is assigned a value from 0 (black pixel) to 256 (white pixel) depending on its luminescence. A typical histogram showing the distribution of intensity is shown in figure 4.3(b).

Thresholding of images in order to remove errors due to background noise and out-of-focus particles is carried out using the minimum histogram method as shown in figure 4.3(b) (Russ, 1999). Thresholding allows us to visualize and analyze only the in-focus planes of particles (typically 5-10 depending on the particle diameter and the depth of focus of the objective). In order to observe a fixed number of planes of particles, thresholding is also done interactively for each experiment. The results are found to be weakly dependent on the threshold value if it is within 20% of the threshold value obtained from the minimum histogram method.

In order to prevent erroneous results, it is ensured that the thresholding value isn't too high to include background noise or too low to create false pockets in clusters. Erosion and dilation technique for further image processing is not used as it is found to fill up interconnected clusters and lead to erroneous results. The resulting binary image shows particles as black pixels on a white background as shown in figure 4.3(c).

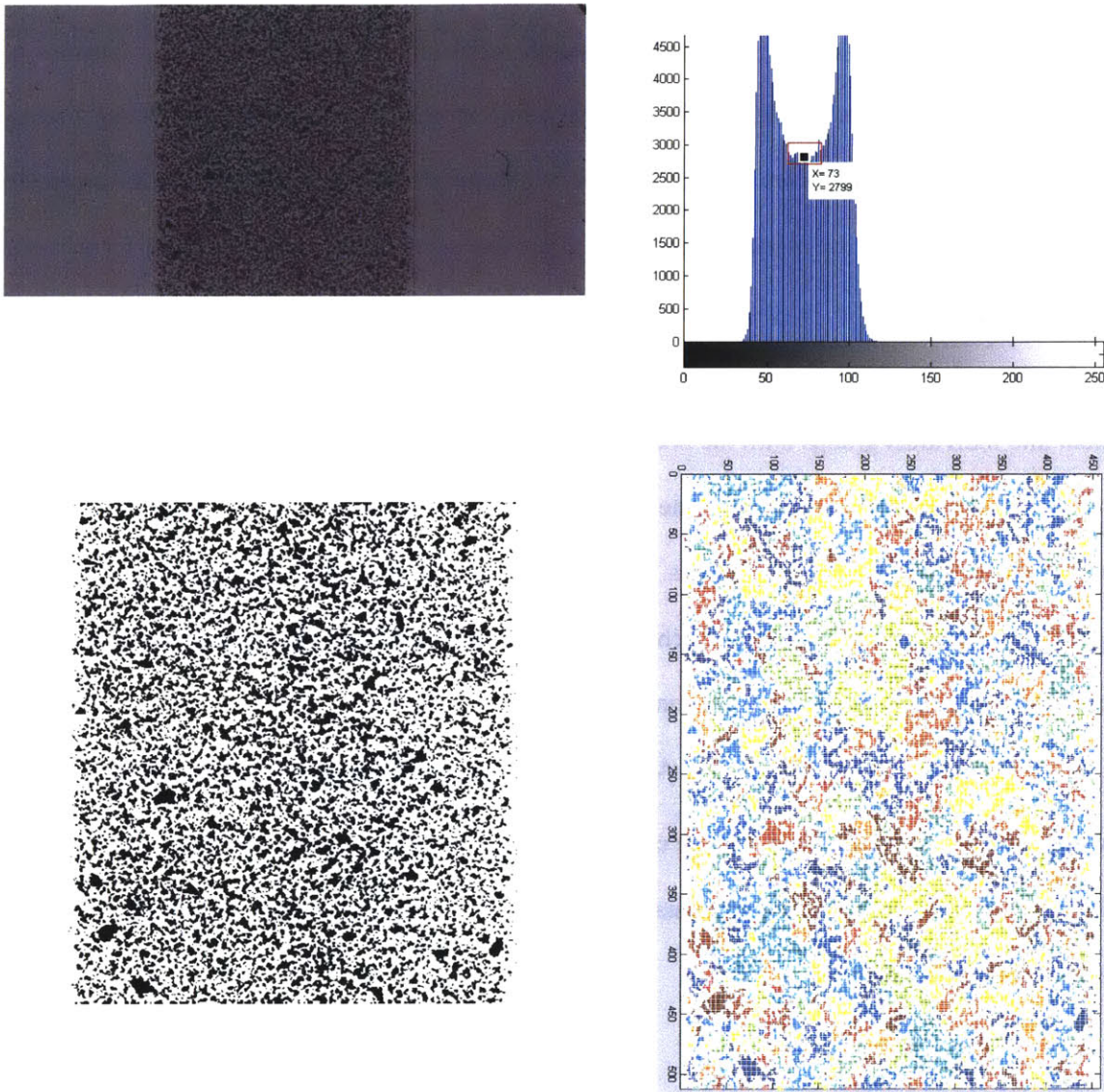


Figure 4.3 Illustration of the image analysis technique. Image shown here is captured at 0 ms (initial configuration), $B_{\text{avg}} = \mu_0 H = 0.08$ Tesla, 2.5% v/v 7 micron CIP based MR fluid under no flow conditions. (a) Image captures at 1000 frames per second using a 10x objective lens (700 X 775 μm) (b) Histogram of grayscale intensity showing the minimum in histogram (c) Binary image (after thresholding) (d) Clusters detected using a cluster detection algorithm are shown with different colors.

A pixel based cluster detection algorithm (appendix A) is used to detect clusters of particles. The algorithm locates particles in neighboring positions of every particle by finding dark pixels around every pixel (maximum of 8 neighboring pixels can be dark in a 2D projected image). Depending on the objective lens and the particle size (1pixel is equivalent to 1.1 microns for 10x lens) a cluster of 1-5 pixels may appear dark (luminescence value of 0) for every particle in the channel. Clusters are then detected by tracing out neighbors of each pixel and organizing them into individual groups until the boundary, with no dark pixels surrounding it, is demarcated.

Cluster size variation with time is used mainly for characterizing the structure evolution of MR fluids flowing in microchannels. A number of secondary analysis techniques are also used to refine our understanding of the mechanisms and processes behind the aggregation phenomena and these have been described in section 4.6.

The total number of clusters (N), the cluster size distribution ($n(s)$) for clusters of size s and the mean cluster size $\langle s \rangle$ are calculated for every image capture (or 10 images for every decade of time in order to save computational time) using programs written in Matlab. The mean cluster size is defined as

$$\langle s \rangle = \frac{\sum_s s^2 n(s)}{\sum_s s n(s)} \quad (4.13)$$

The analyzed video then allows us to look at the evolution of clusters, mean cluster size etc. with time which can then be further analyzed to compare aggregation rates and to understand the mechanisms behind this aggregation process.

4.3 Aggregation Phenomena: Quiescent case

Understanding the aggregation phenomena in the absence of flow is a rich field of literature and has been the focus of numerous studies. In the absence of bulk fluid flow, aggregation kinetics and structure formation is governed by the coupling of three forces, namely, thermal fluctuations, hydrodynamic drag forces and magnetic interactions. Hence, the dimensionless group λ is typically used to characterize the observed aggregation phenomena.

The structure evolution with time for an MR fluid composed of 1.5 micron superparamagnetic particles is shown in figure 4.4. Initially, due to Brownian forces the monodisperse particles resist formation of any clusters and show random fluctuations around their mean positions in the channel. As soon as the magnetic field is applied the single domain magnetic inclusions in the polystyrene beads orient themselves along the direction of the magnetic field (y-direction). This results in the particles acquiring a net magnetization along the field direction and they act as induced dipoles interacting with other particles through the dipolar interaction potential. The random motion of the particles due to thermal energy then changes into ballistic motion provided the particles are close enough (capture volumes overlap) leading to head to tail aggregation. The capture volume depends on the dipolar interaction strength (λ) and is defined by the $U = k_B T$ surface (Promislow *et al.*, 1995)

$$r_c = \left[4(3 \cos^2 \theta - 1) \right]^{1/3} a \lambda^{1/3} \quad (4.14)$$

where r_c is the threshold interparticle separation for spherical particles and is a function of θ .

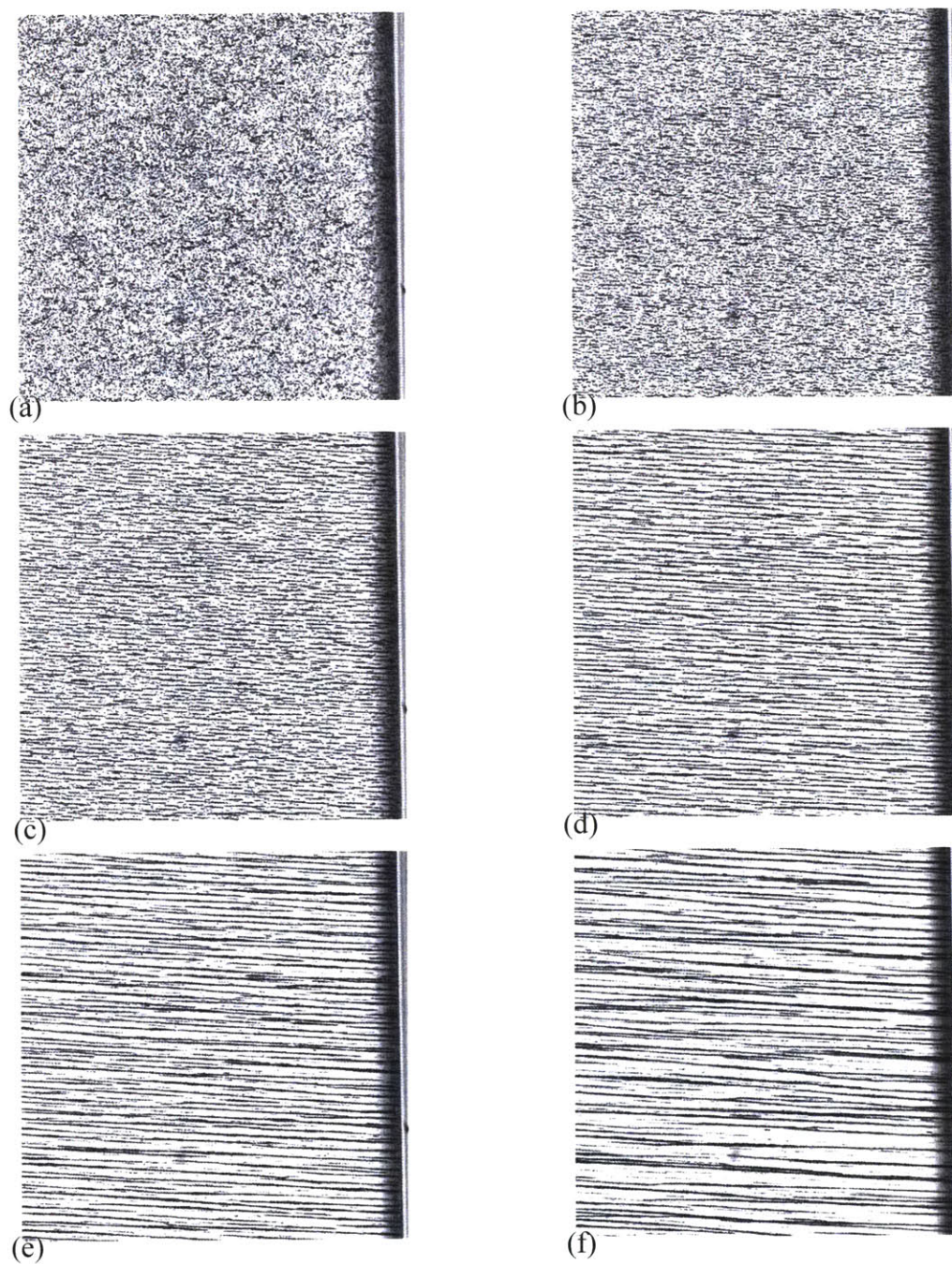


Figure 4.4 Snapshots showing aggregation dynamics of MR fluid comprising of superparamagnetic particles (latex beads with ferromagnetic inclusions) at 0.6%, $B_{avg} = \mu_0 H = 0.1$ T in the absence of flow. (Image size 250 X 250 μm) (a) initial configuration $t=0\text{ms}$ (b) $t = 20\text{ms}$ (c) $t = 100\text{ms}$ (d) $t = 500\text{ms}$ (e) $t = 2000$ ms (f) $t = 5000$ ms

The tip-to-tip aggregation leads to the formation of doublets, triplets and so on until long chains spanning the width of the channel are formed as shown in figure 4.4(a)-(d). This tip-to-tip aggregation occurs on a very short time scale and during the formation of these chains, on an average, horizontal connections for particles are increasing. However, at the same time lateral interactions lead to formation of interconnects and vertical connections between chains as shown in figure 4.4(e)-(f). These interconnects lead to lateral coalescence of chains to form thicker columns or stripes though this coarsening occurs over a much longer time scale as compared to the head to tail aggregation process.

The lateral interactions occur due to thermal fluctuations of particles that lead to local variations in the magnetic field near a dipolar chain. Even though the magnetic field of perfectly ordered chains decays exponentially, the Landau-Peierls fluctuations in the transverse direction lead to a much longer range coupling between the dipolar chains. The dominant force for lateral interactions comes from fluctuations of wave vector k along the chain that are of the order of ρ^{-1} where ρ is the distance separating two dipolar chains (Martin *et al.*, 1998). Halsey and Toor (1992) used the equipartition theorem to determine the free energy of the chains and the mean-squared field around a fluctuating chain as follows

$$\langle H^2 \rangle \sim \frac{k_B T a}{\mu_0 \rho^4} \quad (4.15)$$

where the field decays as a power law independent of the magnetic field strength. Martin *et al.* (1998) modified the Halsey-Toor theory to include the power law dependence of the coarsening on the magnetic field strength by considering the dipole moment per unit length of the dipolar chain. Furst and Gast (2000) measured the lateral interactions between dipolar chains directly using an optical tweezer technique and outlined the dominant mechanisms of interactions in different regimes depending on the dipolar interaction strength and the volume fraction (figure 4.5).

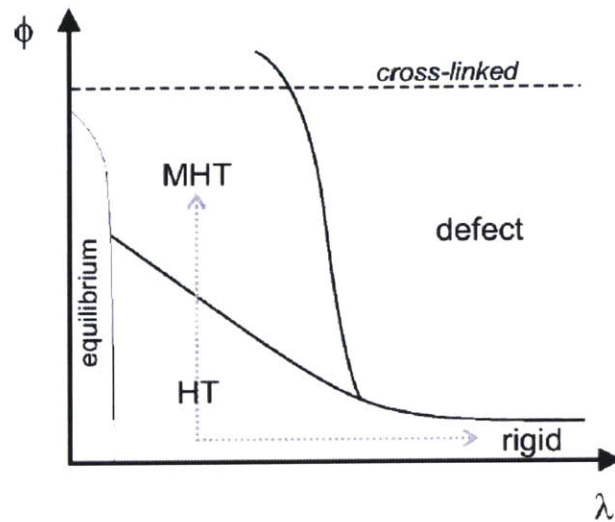


Figure 4.5 Mechanisms of lateral interactions in different regimes depending on the dipolar interaction strength and volume fraction of the magnetorheological suspension (Furst and Gast, 2000).

Thermal fluctuations play little role in the case of MR fluids based on carbonyl iron particles ($\lambda \sim 10^6$) and the aggregation process is a result of interplay between magnetic and hydrodynamic interactions. Figure 4.6 shows the aggregation kinetics as function of magnetic field for a carbonyl iron particle based MR fluid. As the magnetic field is increased, the dipolar interaction strength increases leading to a faster tip to tip aggregation process (figure 4.6(a)-(c)). Chains spanning the width of the channel are formed similar to those observed for MR fluids based on superparamagnetic particles as shown in figure 4.6(c)(ii). However, Landau-Peierls thermal fluctuation driven lateral interactions are absent in the CIP based MR fluids. Lateral coalescence, on the other hand, occurs due to the presence of defects in dipolar chains in these fluids. These topological defects are introduced during the tip to tip aggregation process and remain stable in the absence of Brownian motion to re-disperse them (figure 4.6(c)(ii)). The presence of topological defects in the chains leads to a local variation in the dipole moment

density which drives lateral interactions and eventually coalescence of chains into thicker stripes or columns.

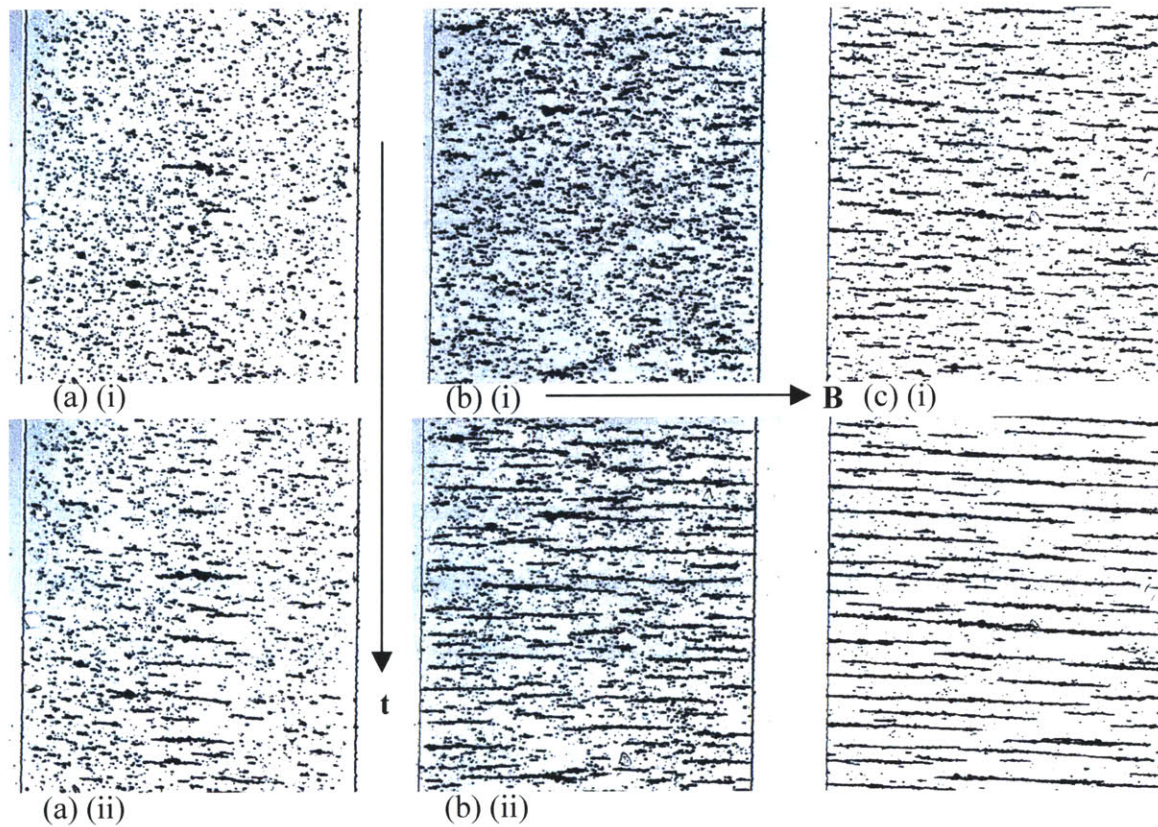


Figure 4.6 Effect of increasing magnetic field on the structure evolution in the absence of flow for a MR fluid (7 micron CIP, 0.5%/v) in a microchannel geometry (Image size 700 X 775 μm)
 (a) $B_{\text{avg}} = \mu_0 H = 0.036 \text{ T}$ (b) $B_{\text{avg}} = \mu_0 H = 0.08 \text{ T}$ (c) $B_{\text{avg}} = \mu_0 H = 0.17 \text{ T}$ (i) $t = 150\text{ms}$ (ii) $t = 7000 \text{ ms}$

At lower concentrations, due to a larger interparticle distance, the chains or columns formed are not able to interact via defect driven magnetic field variations or Landau-Peierle's fluctuations and effectively partition the space into strips as shown in figure 4.6. At higher volume fractions, lateral interactions become more important as the interparticle distance is reduced and an interconnected network structure or a 'fibrous' structure can also be formed. Fermigier and Gast

(1992) observed this fibrous structure for superparamagnetic particles at high volume fractions of $\phi_v > 1\%$ and is shown in figure 4.7.

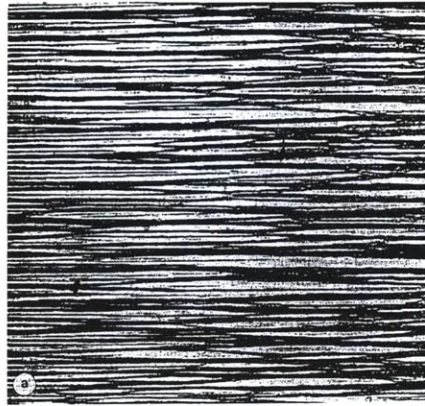


Figure 4.7 Lateral Interactions leading to a fibrous or connected structure at higher volume concentrations of MR fluids (Dynabeads (magnetite inclusions in latex beads), $\lambda=285$) forming a fibrous structure due to Landau-Pierle's fluctuations (Fermigier and Gast, 1992).

We observe a fibrous interconnected structure for carbonyl iron particles based MR fluids for volume fractions $\phi_v > 2\%$. The critical volume fraction required for formation of a fibrous structure is higher in the case of these MR fluids as thermal fluctuation driven lateral interactions are absent. On the other hand, the coarsening is driven by topological defects and at volume fractions above 2% the interparticle distance is small enough for defects introduced during the initial head to tail aggregation process to form a 'percolated' network structure spanning the entire sample.

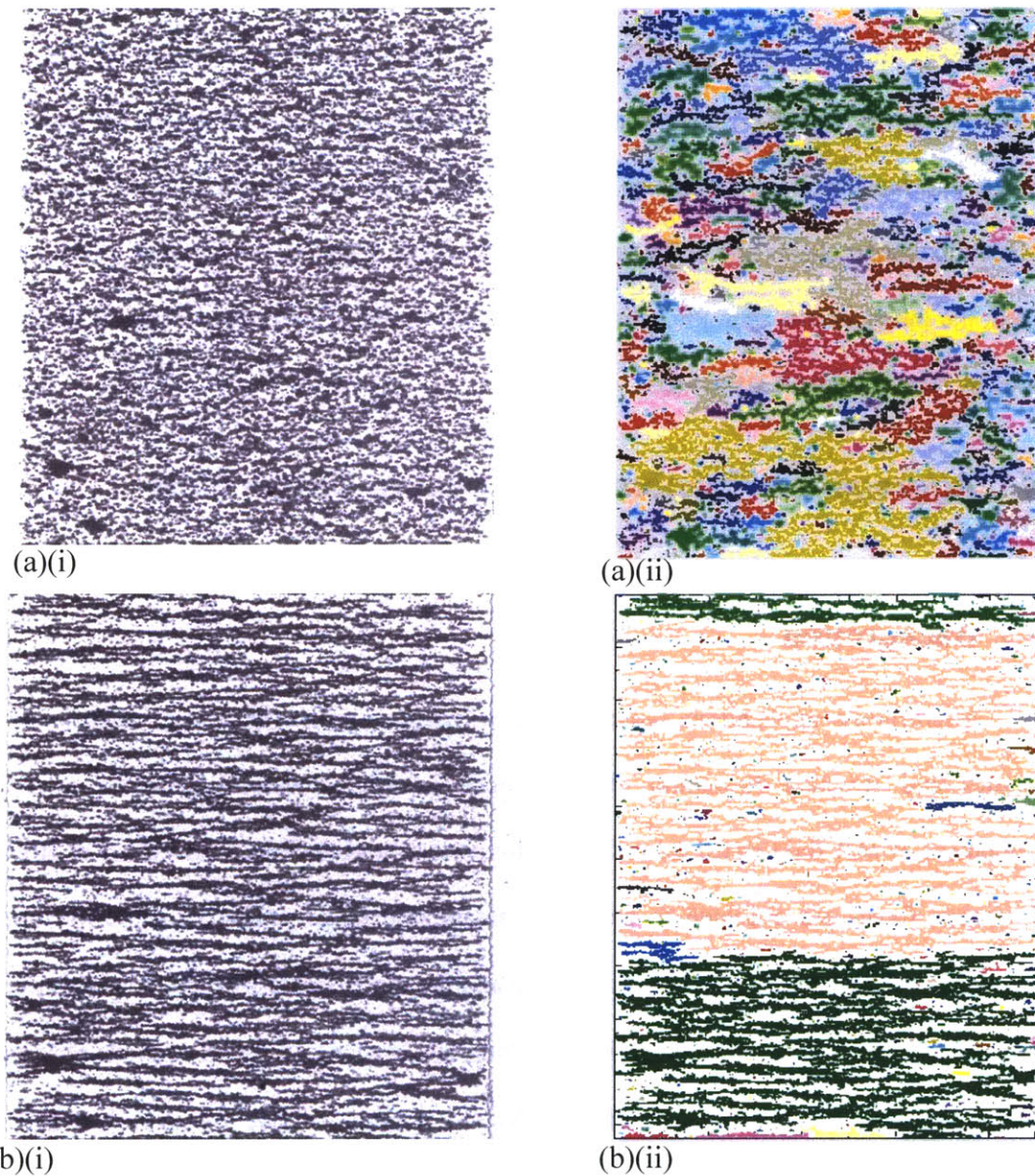


Figure 4.8 Lateral Interactions and defect-driven coarsening leading to a fibrous or connected structure at higher volume concentrations. of MR fluids (7 micron CIP, 2.5% v/v, $B_{avg} = \mu_0 H = 0.08$ T) (Image frame size is 700 X 775 μm) (a) $t = 20$ ms (b) $t = 2000$ ms (i) snapshot (ii) cluster-detection algorithm results – an interconnected structure formed due to defect driven coarsening.

Figure 4.8 shows this aggregation process in further detail. At short times (tens of milliseconds), as seen from figure 4.8(a)(i)-(ii), a large number of topological defects are introduced into the dipolar chains that are being formed as a result of tip to tip aggregation process. The local interactions due to these defects lead to formation of lateral interconnects between the dipolar chains and in the time scale that chains spanning the width of the channel are formed, the interconnects span the entire sample space so that a ‘percolated’ network structure is formed as seen in figure 4.8(b)(i)-(ii).

4.4 Aggregation Phenomena: Pressure-Driven Flow

4.4.1 Background

Microfluidic applications typically utilize pressure driven flow and understanding of dynamics and structure formation of MR fluids in microchannel geometries is vital to development of MR fluid based microfluidic components and devices. Convection of structures and viscous forces are expected to play a dominant role in governing structure evolution as compared to thermal forces. The Péclet number and the dimensionless group λ give an idea of the relative importance of hydrodynamic forces and the dipolar interaction strength as compared to thermal fluctuations. MR fluids based on carbonyl iron particles have λ and $Pè \gg 1$ and hence the structure formation and the aggregation dynamics is primarily governed by the coupling of magnetic and hydrodynamic interactions.

Other important dimensionless groups include volume fraction & geometrical ratios such as the ratio of the particle diameter to the width of channel and the ratio of particle diameter to the height of channel.

Brunet *et al.* (2005) looked at mean chain lengths when the flow direction is along the direction of the magnetic field. In this thesis work, we will mainly be concerned with the study of

aggregation phenomena when flow is perpendicular to magnetic field (see figure 4.1) as it can be directly related to microfluidic devices and is also a natural step forward to build on the rich literature on the aggregation dynamics in the quiescent case.

The aggregation dynamics of superparamagnetic particle based MR fluid in the presence of bulk fluid flow is shown in figure 4.9. The effect of flow can be observed by comparing the snapshots with figure 4.4 wherein experimental conditions (magnetic field, particle size, geometrical parameters) are equivalent but without any bulk fluid flow. The initial tip-to-tip aggregation process due to dipolar interactions between the particles is similar to the quiescent case and the time scale of this process is also comparable in both the quiescent and bulk fluid flow case (refer to section 4.5 for a detailed discussion on time scales). Figure 4.9(a)-(d) illustrates this head to tail aggregation process leading to the formation of chains spanning the width of the channel. However, convection of the chains close to other chains radically alters the structures formed after the initial horizontal connections are formed. Lateral interactions in the presence of bulk fluid flow are dominated by the advection of chains within the capture volume of another chain flowing either above or below the chain. This leads to a ‘zippering’ action and the chains coalesce laterally to form a thicker column or stripe as shown in figure 4.9(d)-(f). This can be compared to the quiescent case shown in figure 4.4(d)-(f) wherein lateral interactions are only governed by the thermal fluctuations of the dipolar chains.

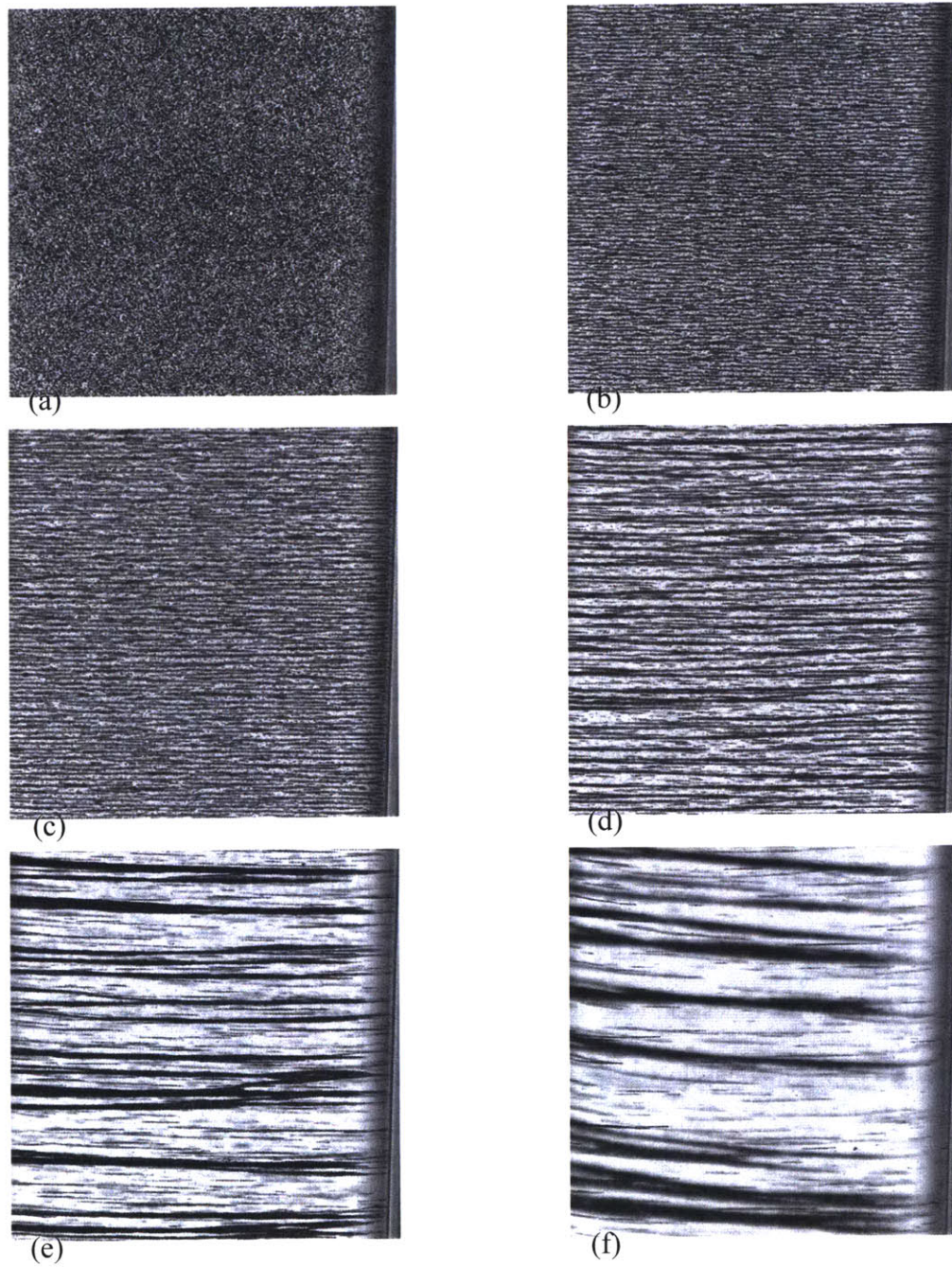


Figure 4.9 Snapshots showing aggregation dynamics of MR fluid comprising of superparamagnetic particles (latex beads with ferromagnetic inclusions) at 0.6%, $B_{avg} = \mu_0 H = 0.1$ T in the presence of flow. (Image size 250 X 250 μm) (a) initial configuration $t=0\text{ms}$ (b) $t = 35\text{ms}$ (c) $t = 100\text{ms}$ (d) $t = 500$ ms (e) $t = 2000$ ms (f) $t = 5000$ ms

4.4.2 Effect of Magnetic field strength on Structures

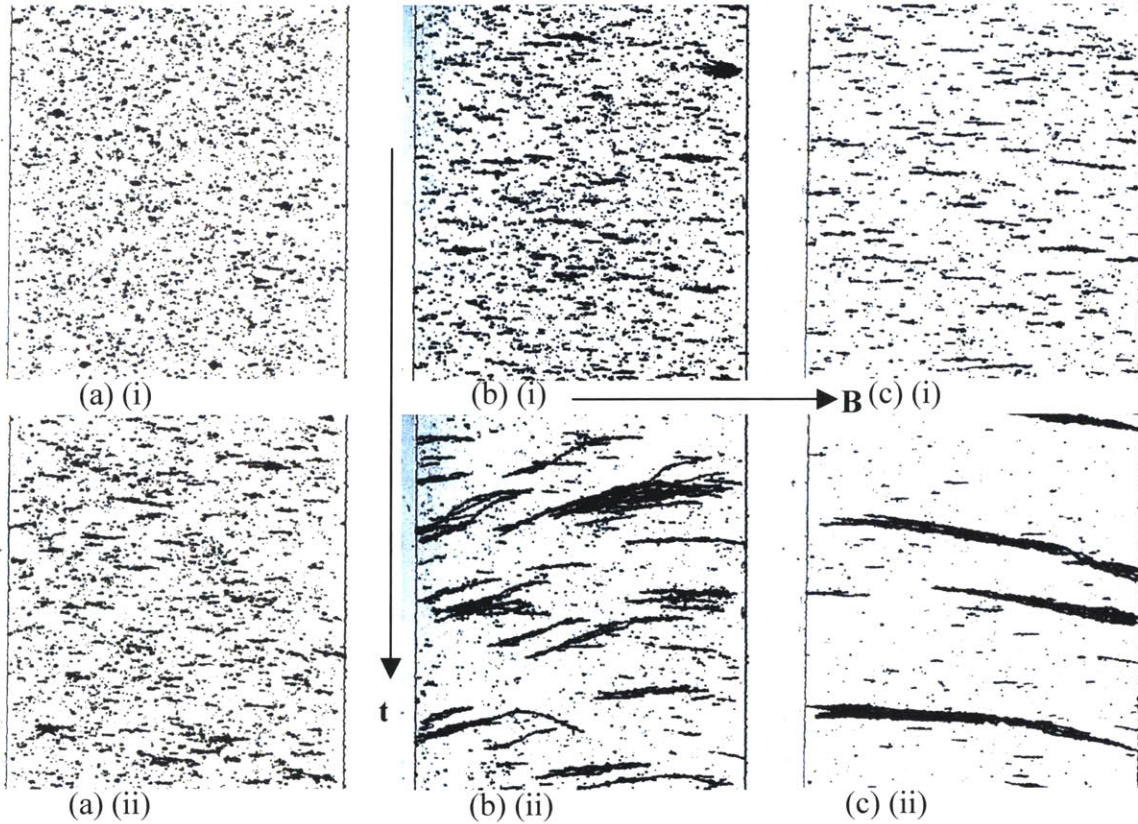
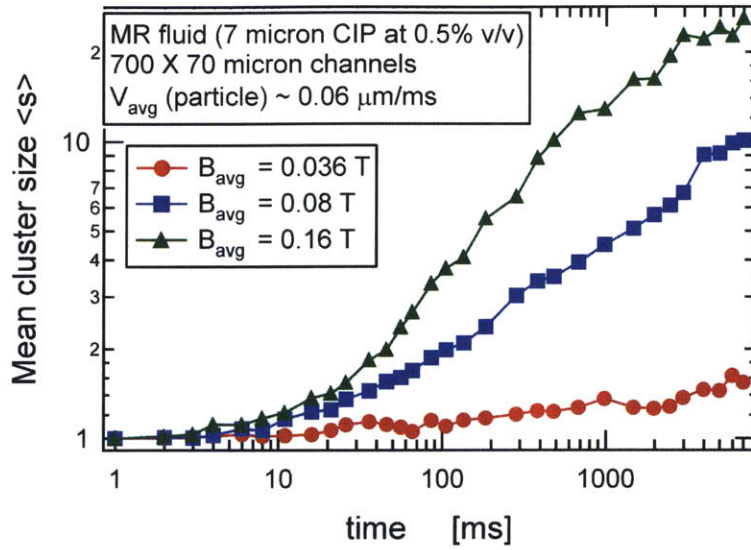


Figure 4.10 Effect of increasing magnetic field on the structure evolution in the presence of flow for a MR fluid (7 micron CIP, 0.5%v/v) in a microchannel geometry (700 X 70 μm), $V_{\text{avg}} \sim 2 \mu\text{m/ms}$ (a) $B_{\text{avg}} = \mu_0 H = 0.1 \text{ T}$ (b) $B_{\text{avg}} = \mu_0 H = 0.08 \text{ T}$ (c) $B_{\text{avg}} = \mu_0 H = 0.16 \text{ T}$ (i) $t = 150\text{ms}$ (ii) $t = 5000 \text{ ms}$

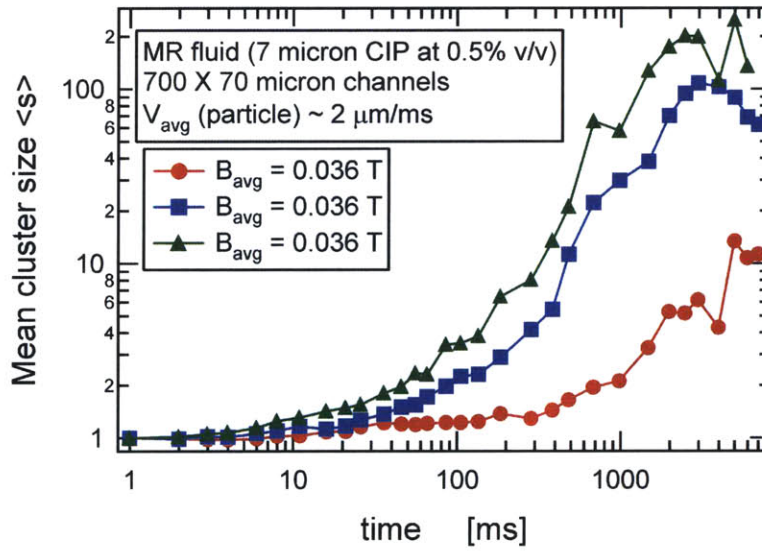
Magnetic field affects the dipolar interaction strength which in turn affects the tip to tip aggregation rate of induced dipoles. Hence, as the magnetic field is increased (horizontal arrow direction in figure 4.10), the rate at which doublets, triplets and finally chains are formed is also increased (figure 4.10(a)-(c)). Further, for these carbonyl iron particle based MR fluids, lateral coalescence occurs through defect driven coarsening and magnetic field affects the local variations in dipole moment density and hence the number of defects formed. Figure 4.10(b)

shows a higher number of lateral interactions (even at later times) than figure 4.10(a) due to a higher magnetic field. In figure 4.10(b)-(c), these higher numbers of defects along with the convection of chains into one another leads to the formation of thicker stripes through the ‘zippering’ process.

The increased aggregation rate at higher magnetic fields can also be observed by analyzing the mean cluster size ($\langle s \rangle$) (equation 4.13) from the image captures. Figure 4.11 shows this increase in the mean cluster size with time due to increased rate of addition of horizontal and vertical connections for different magnetic fields. The difference in the aggregation rate is less pronounced, although not negligible, at short times (50-100ms) when primarily horizontal connections are being added through the tip to tip aggregation process. At longer times, the difference in lateral connections due to a higher number of defects at higher magnetic fields amplified by the convection ‘zippering’ process lead to a more pronounced effect of the magnetic field on the cluster size distribution as can be observed from figure 4.11.



(a)



(b)

Figure 4.11 Mean cluster size variation on increasing the magnetic field in the presence of flow for a MR fluid (7 micron CIP, 0.5%v/v) in a microchannel geometry (700 X 70 μm) (a) Average Velocity of chain $\sim 0.06 \mu\text{m/ms}$ (b) Average Velocity of chain $\sim 2 \mu\text{m/ms}$.

4.4.3 Effect of Flow rate on Structures

The effect of the magnetic interactions is thus coupled with the effect of varying the shear rate as can be seen from figures 4.11(a) & (b).

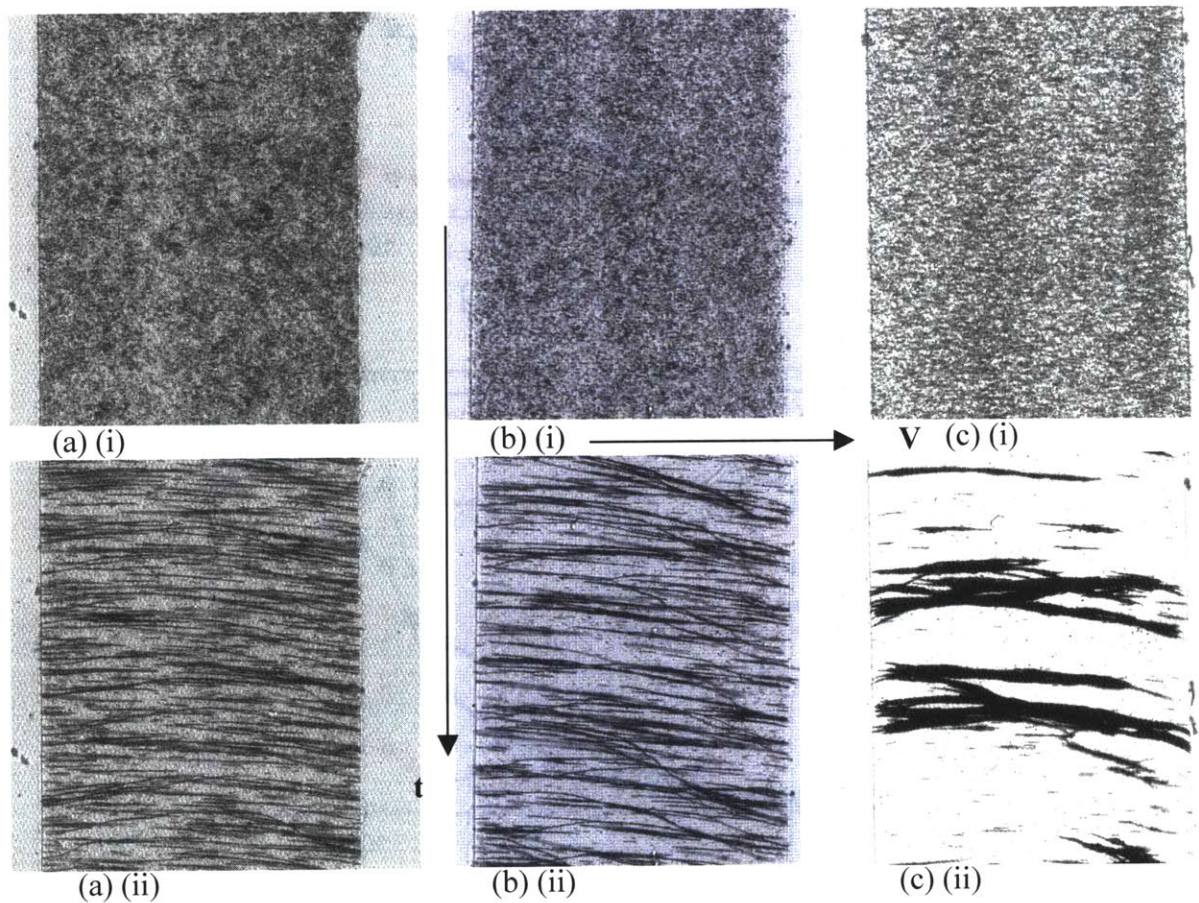


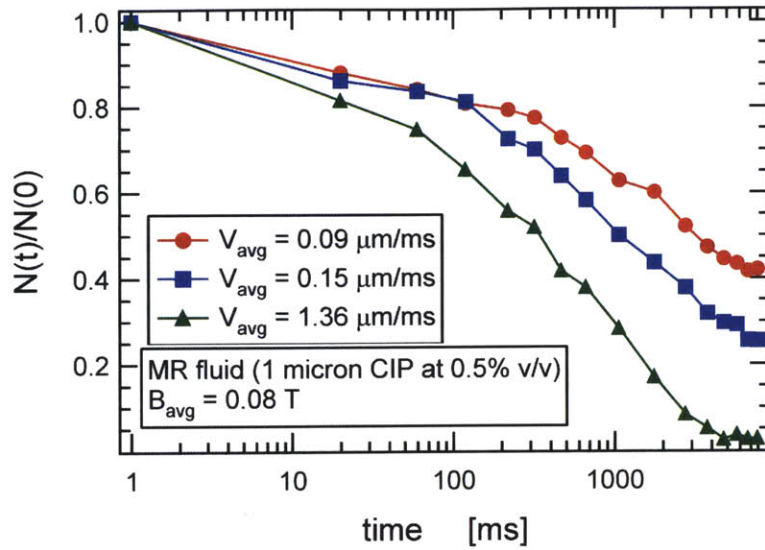
Figure 4.12 Effect of increasing flow rate on the aggregation dynamics for a MR fluid (1 micron CIP, 0.5%v/v) in a microchannel geometry (400 X 40 μm) $B_{\text{avg}} = \mu_0 H = 0.08 \text{ T}$ (a) $V_{\text{avg}} = 0.09 \mu\text{m/ms}$ (b) $V_{\text{avg}} = 0.15 \mu\text{m/ms}$ (c) $V_{\text{avg}} = 1.36 \mu\text{m/ms}$ (i) $t = 20\text{ms}$ (ii) $t = 7000 \text{ ms}$

Figure 4.12 illustrates the effect of increasing the flow rate of the MR fluid flowing in a microchannel through image captures. Figure 4.13 illustrates the effect of varying the flow rate on the evolution of the total number of clusters with time.

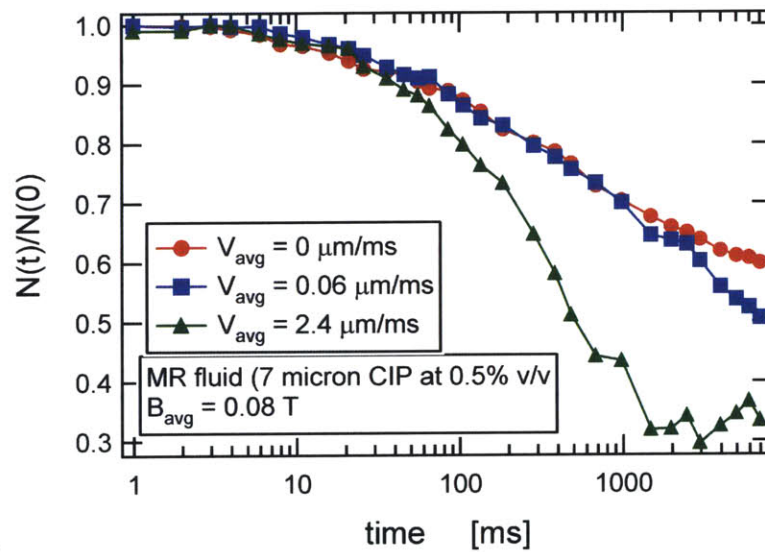
The initial aggregation rate due to dipolar interactions is not affected to large degree due to a change in flow rate. Single particles or smaller chains are convected into the capture volume of other doublets, triplets and chains, which increases the aggregation rate by a small amount as can be seen in figure 4.13 (initial 50-100ms).

Further, at very low flow rates, the mean cluster size variation is not unlike that observed in the quiescent case as shown in figure 4.13(b). This indicates that besides the tip to tip aggregation process during which chains spanning the width of the channel are formed, lateral interactions due to defects in the dipolar chains also occur at a rate comparable to the quiescent case. However, at longer times, convection does play a role in lateral coalescence of chains as can be seen from figure 4.13(b). The relative importance, in lateral interactions, of ‘zippering’ due to advection of chains as compared to defect-driven coarsening is governed by the flow rate of the fluid in the microchannel. A convection based ‘zippering’ becomes the dominant process of structure evolution and cluster formation at higher flow rates as can be seen from figures 4.11(b), 4.12 & 4.13.

This ‘zippering’ process due to advections of chains can be further classified into two distinct but simultaneously occurring processes. In-plane zippering occurs if 2 chains are of different sizes and at different positions so that they experience different drag forces and convection can bring them close enough for the magnetic interactions to play a role. Depending on whether the chains are in-phase or out-of-phase, these magnetic interactions can be attractive or repulsive. The out of plane zippering occurs due to parabolic nature of velocity profile along the z direction. The chains in the center of the channel ($z = h/2$ where h is the height of the channel) move faster than chains closer to the surface of the channel and can ‘zipper up’ with other chains while passing over them. These two ‘zippering’ processes along with the lateral interactions due to topological defects occur simultaneously and lead to the formation of thicker columns or stripes.



(a)



(b)

Figure 4.13 Cluster size evolution with time depicting effects of variation in flow rate on the aggregation dynamics of MR fluids in a microchannel geometry ($400 \times 40 \mu\text{m}$), $B_{avg} = \mu_0 H = 0.08 \text{ T}$ (a) 1 micron CIP, 0.5%v/v (b) 7 micron CIP, 0.5%v/v

Further, from figures 4.12 to 4.15 it can be observed that structure evolution occurring at lower flow rates or magnetic fields also occurs at higher flow rates or magnetic fields albeit at a

slower rate. This indicates a possible scaling of the time scale using a coupling of the magnetic field and flow rate, which will be explored in further detail in a latter section.

4.4.4 Effect of volume fraction on Aggregation phenomena

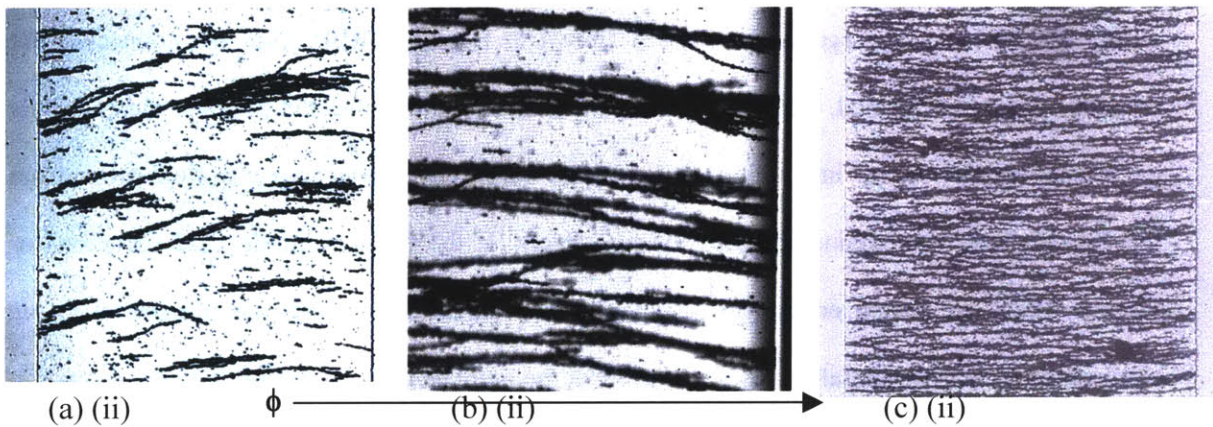


Figure 4.14 Snapshots illustrating differences in aggregation dynamics as the concentration of carbonyl iron particles is increased. Images are for 7 micron CIP based MR fluid flowing in a microchannel geometry (700 X 70 μm), $B_{\text{avg}} = \mu_0 H = 0.08 \text{ T}$, $t = 1500 \text{ ms}$ (i) 0.5% v/v (ii) 1.91% v/v (iii) 2.5% v/v

The study of effect of increasing the volume fraction of the MR fluids flowing in the microchannels is important because it provides us useful insights into bulk rheological behavior and also because commercial macroscale applications are based on MR fluids at a much higher volume fraction of 36% v/v CIP.

Figure 4.14 shows the structural differences as the concentration is increased. At high enough volume fractions of CIP ($\phi_v > 2\%$) a fibrous or an interconnected structure is formed quite similar to the quiescent case as shown in figure 4.14(c). We suspect these fibrous and interconnected chains and columns to be the reason behind the gel-like structure and large yield

stress observed in MR fluids at 36% v/v. As the particle concentration is increased, the average interparticle distance decreases, which results in higher lateral interactions. Lateral interactions in the carbonyl iron particles based MR fluids is primarily due to the formation of defects in the dipolar chains and additionally in the presence of flow, due to convection. The defect-driven coarsening process occurs on a faster time scale than the convective time scale and hence, the defect-driven lateral interactions are primarily responsible for the crosslinked chains formed during the tip-to-tip aggregation process as shown in figure 4.14(b). After the connected but defective chains are formed, the further formation of a fully interconnected structure then depends on the strength of lateral interactions due to local variations in the magnetic field around the topological defects in chains and also viscous forces. If the local magnetic field variations or viscous forces are strong enough to disrupt the topological defects that are introduced in the chains then the chains laterally coalesce starting at the point of the defect leading to the formation of thick columns or stripes as can be seen in figure 4.14(a). At high enough particle concentrations, however, the defect driven coarsening that occurs on a faster time scale quickly leads to a interconnected or 'percolated' network structure. Viscous forces or magnetic forces due to local field variations are then not strong enough to disrupt this fully interconnected network structure as can be seen in figure 4.14(c).

However, it should be noted that, in the presence of flow, especially at higher flow rates, viscous forces slowly but steadily break these interconnected structures so that they evolve into thicker column structures. At very long times (outside the scope of this measurement technique), hence, we expect the percolated network structure to indeed evolve into thicker columns.

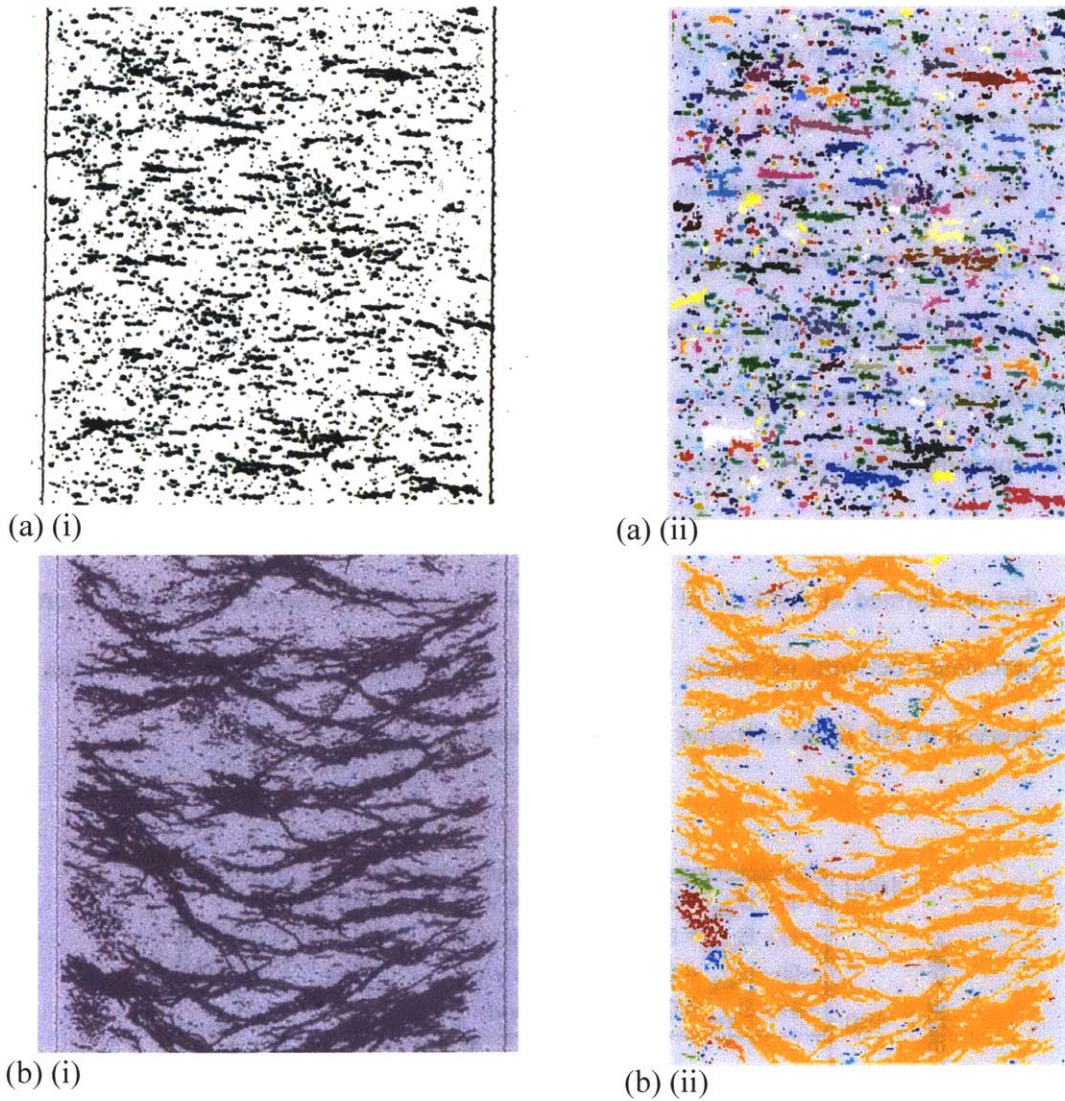


Figure 4.15 Structure evolution when the viscous forces are high as compared to magnetic forces ($Mn \sim 0.01$) as the particle concentration is varied. Images are for 7 micron CIP based MR fluid flowing in a microchannel geometry ($700 \times 70 \mu\text{m}$), $B_{\text{avg}} = \mu_0 H = 0.036 \text{ T}$, $t = 1500 \text{ ms}$ (a) 0.5% v/v (b) 2.5% v/v (i) Snapshot (ii) Clusters detected using cluster detection algorithm.

The strength of this percolated network can be related to the yield stress in bulk rheological measurements using a constant pressure flow instead of a constant displacement flow

that is obtained using a syringe pump in the present experiments. The magnitude of the yield stress that needs to be overcome by the viscous forces can be gauged from the aggregation behavior of MR fluid at 2.5% v/v when the Peclet and Mason number are very high. Figure 4.15(b) shows snapshots of such an experiment wherein MR fluid (2.5% v/v) flowing in a microchannel (average particle velocity $\sim 2.5 \mu\text{m}/\text{ms}$) is subjected to a magnetic field strength of $B_{\text{avg}} = 0.036 \text{ T}$. The interconnected fibrous structure bends to the point of rupture due to interplay of viscous forces and magnetic forces but doesn't zipper up to form thicker columns. This single sample spanning network structure that is formed at higher concentrations (2.5% v/v) is illustrated in figure 4.15(b)(ii) which can be compared to the defective but unconnected dipolar chains that are formed at 0.5%v/v of CIP (figure 4.15(a)(ii)). We expect this lateral interaction driven percolated network of chains & columns to be primarily responsible for the high yield stress observed in MR fluids at higher volume fractions.

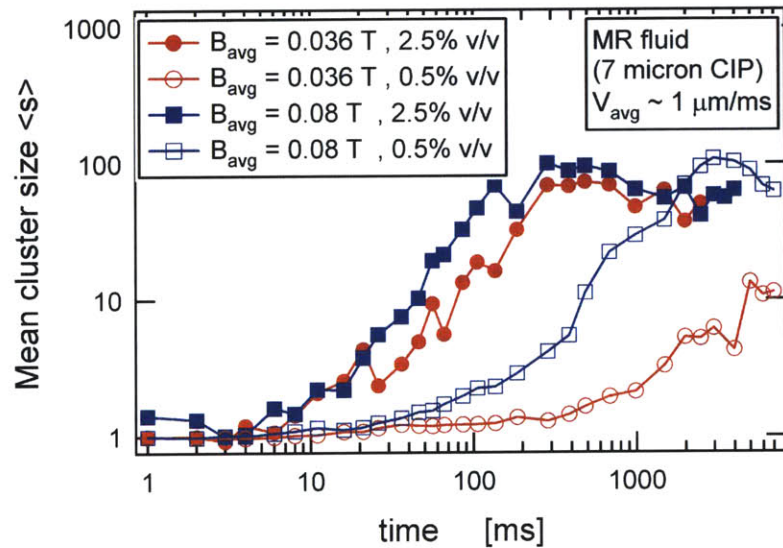


Figure 4.16 Mean cluster size variation with increasing particle concentration. Images are for 7 micron CIP based MR fluid flowing in a microchannel geometry ($700 \times 70 \mu\text{m}$), $V_{\text{avg}} \sim 1 \mu\text{m}/\text{ms}$.

The mean cluster size variation can also be used to shed more light on the effect of increasing particle concentration as shown in figure 4.16. The formation of a percolated network at higher concentration (2.5% v/v) quickly leads to a few large clusters which then evolve very slowly as can be observed from the plateau in the curves with filled symbols. On the other hand, at lower concentrations (0.5% v/v), the larger clusters are formed over a much longer period of time due to convection leading to zippering of chains to form thicker columns or stripes. The cluster size further strongly depends on the magnetic field strength and the flow rate (curves with open symbols) at lower particle concentrations.

4.4.5 Effect of geometrical ratios on structures

The structure evolution is a function of geometrical ratios such as the particle diameter to the width of the channel ratio and the ratio of the width to height of the microchannel. The time required for the tip to tip aggregation process to lead to formation of chains spanning the width of the channel is a function of the ratio of the particle diameter to width of the channel. Topological defects are introduced during this process and hence, lateral interactions and defect driven coarsening is observed to be higher in channels with larger particle diameter to width of the channel ratio.

Further, the velocity profile and hence the shear rate, in particular, is determined by the geometry of the channel which in turn affects the structures and patterns formed as shown in figure 4.17. The shear rate in turn determines the maximum flow rate when the chains break and hence the shape and cluster size of the dipolar chains.

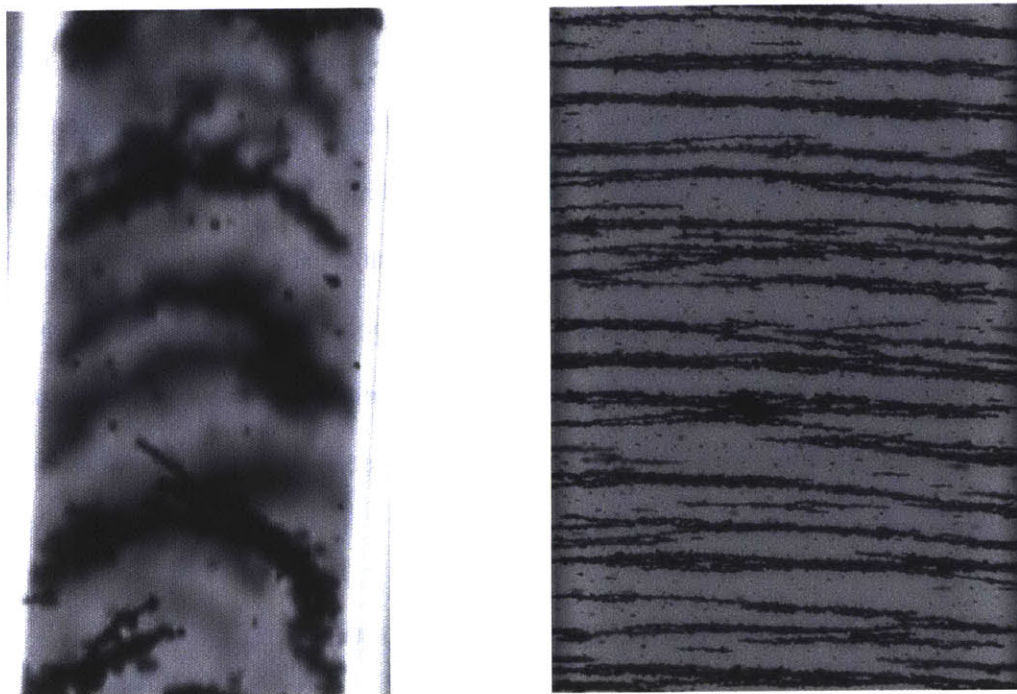


Figure 4.17 Snapshots illustrating the effect of the geometrical ratio on the shape of the dipolar chain that spans the width of the channel (7 micron CIP based MR fluid) (a) Square channel (100 X 100 microns) viewed using a 40x objective lens (b) Large ratio rectangular channel (1000 X 100 microns) observed using a 10x objective lens.

4.5 Mechanisms of Aggregation: Scalings

In the previous section, effect of individually varying parameters such as magnetic field, flow-rate etc. was described. We now utilize these results from parametric studies to derive useful scalings which will help us understand the mechanism behind the formation of various patterns and the structure evolution with time.

The aggregation dynamics is essentially decided by the interplay of two forces – namely, magnetic forces and viscous forces. In the case of carbonyl iron based MR fluid, thermal

fluctuations can be neglected. It can be observed from snapshots that as the dipolar strength or the viscous forces are varied very similar structures are formed albeit at different real times.

At short times, as soon as the magnetic field is applied, the particles form induced dipoles and align with the direction of the magnetic field. These dipolar particles then attract each other and aggregate tip-to-tip to form doublets, triplets and so on as shown in figure 4.18. The dipolar interaction potential described in section 4.1.1 can be used to explain this tip to tip aggregation that occurs at short times.

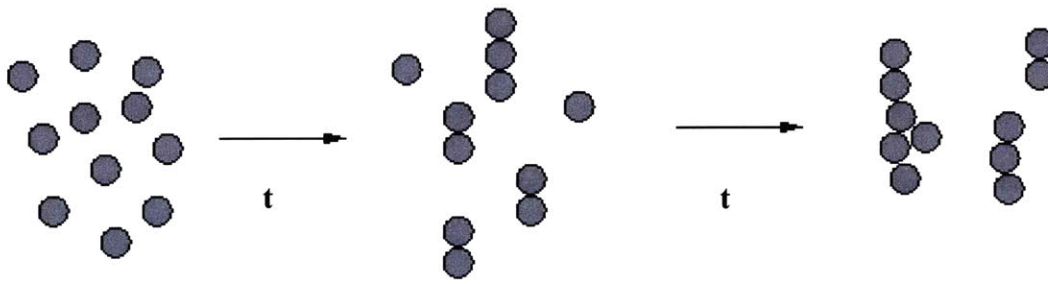


Figure 4.18 Schematic of the tip-to-tip aggregation process that occurs at short times i.e. as soon as the magnetic field is applied. The induced dipolar particles interact with each other as described by the dipolar interaction potential leading to formation of chains along the direction of magnetic field.

As this head-to-tail aggregation occurs even in the quiescent case, a number of dimensionless time scales have been proposed in earlier literature as a means to capture the dipolar interactions. Fermigier and Gast (1992) propose a modification to a purely Brownian characteristic time by using a stability factor W as follows

$$\begin{aligned}
W &= \int_{2a}^{\infty} \frac{\exp(U(r)/k_B T)}{r^2} dr = 9.16 \lambda^{-4/3} \\
\lambda &= \frac{\pi \mu_0 \chi^2 d^3 H^2}{72 k_B T} \\
t_{BW} = t_B W &= \frac{1}{6} \frac{a^2}{D \phi} \frac{9.16}{\lambda^{-4/3}}
\end{aligned} \tag{4.16}$$

where $U(r)$ is the interaction potential and is assumed spherically symmetric, t_B is a purely Brownian time scale and $D = k_B T / 6 \pi \eta_s a$ is the particle diffusion coefficient.

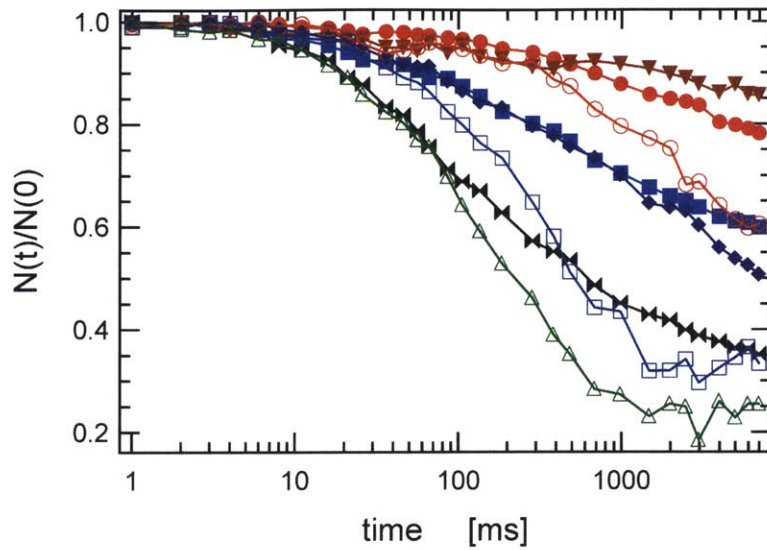
Promislow *et al.* (1995) later suggested a further modification to this time scale based on the capture volume of an induced dipolar particle. Their hypothesis was that as soon as a particle enters the capture volume of another particle as defined by the $U = k_B T$ surface they would undergo ballistic aggregation. The time scale proposed by them hence was much more sensitive to changes in the magnetic field strength as follows

$$t_B^* = \frac{1}{24 \left[(1/3)^{1/2} - (1/3)^{3/2} \right]} \frac{a^2}{D \phi \lambda} \tag{4.17}$$

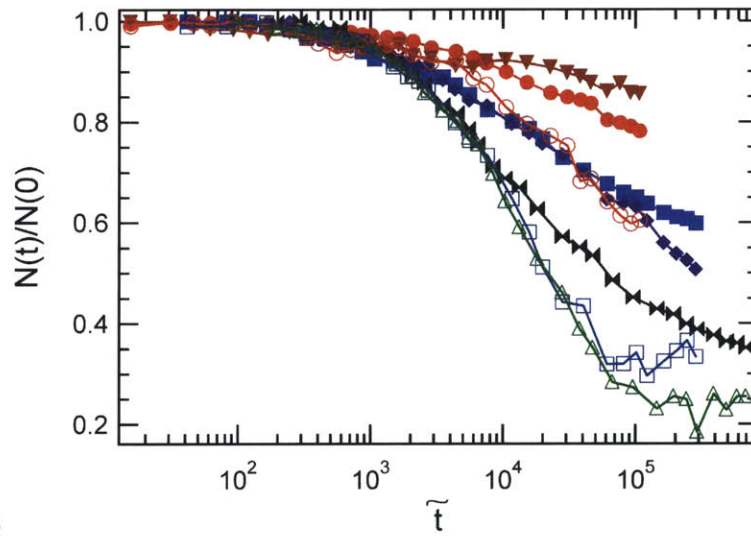
We use the time scale proposed by Promislow *et al.* (1995) with minor modifications to the prefactor as follows

$$\tilde{t} = \frac{3}{2} \frac{t}{d^2 / D \lambda} \tag{4.18}$$

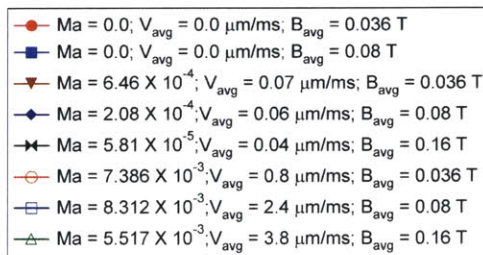
where \tilde{t} is the time required by a particle to move a distance equal to its diameter due to dipolar interaction with another particle. The particle concentration is assumed constant $\phi = 0.005$ for all cases. This characteristic time has been used to collapse cluster variation for different experiments at short times as shown in figure 4.19.



(a)



(b)



(c)

Figure 4.19 Scaling at short time scales for 7 micron CIP based MR fluid flowing in microchannel geometry ($700 \times 70 \mu\text{m}$). (a) Variation of the number of clusters for different experimental conditions (b) Scaling using the characteristic time scale based on the dipolar

interaction indicating that tip to tip aggregation governs the aggregation dynamics at short time scales. (c) Experimental conditions.

After the initial head-to-tail interactions, lateral interactions firstly due to defects formed during the tip-to-tip aggregation process and secondly due to convection of particles, doublets, triplets etc. also starts playing a role in structure evolution. The structures then formed are due to interplay of a number of processes occurring simultaneously. Defects in chains lead to local variations in magnetic field and further coarsening along directions lateral to the magnetic field. Two chains either repel or attract each other depending on the number of particles in each chain N and whether they are in phase (aligned ends) or out of phase (chain ends are offset by $N/2$). If these magnetic or viscous forces are strong enough they can lead to a “zippering” action as depicted in figure 4.20(a) which results in a thicker column or stripe. Further, depending on the Péclet number, convection leads to an in-plane or out-of-plane zippering as shown in figure 4.20(b).

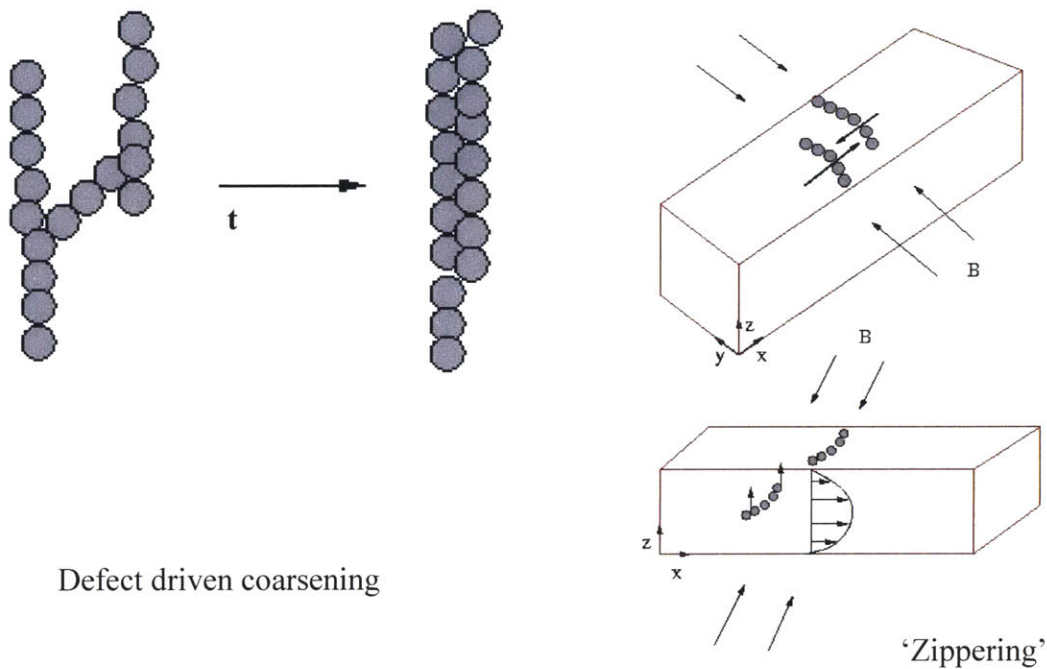


Figure 4.20 Schematic of the aggregation phenomena due to the ‘zippering’ process. (a) Defect driven lateral interactions lead to defective chain structures which then zipper up to form thicker columns. (b) Convection leading to in-plane or out-of-plane zippering depending on the size, velocity of the chain and distance between the two chains.

At longer times, this convective ‘zippering’ is in fact the dominant process responsible for structure evolution as tip-to-tip aggregation process saturates when chains spans the width of the channel are formed. This is illustrated in figure 4.21 wherein a convective time scale is used to scale the aggregation dynamics of experiments performed for 1 micron carbonyl iron particle based MR fluid

$$t^* = \dot{\gamma}t \tag{4.19}$$

where $\dot{\gamma} = V_{avg}/H$ is the shear rate along the z direction, H is the height of the channel and V_{avg} is the average particle velocity.

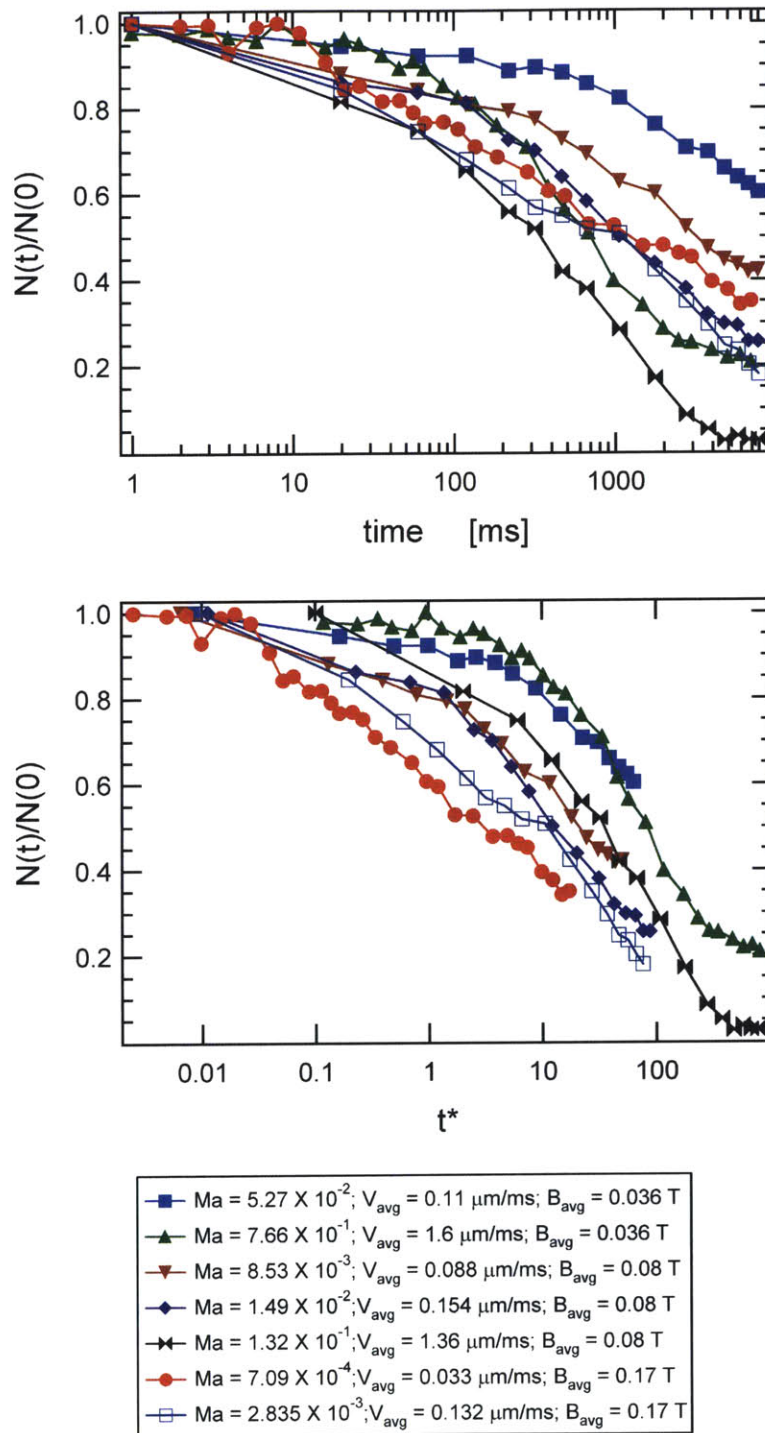


Figure 4.22 Scaling at long times for 1 micron CIP based MR fluid flowing in microchannel geometry (400 X 40 μm). (a) Variation of the number of clusters for different experimental

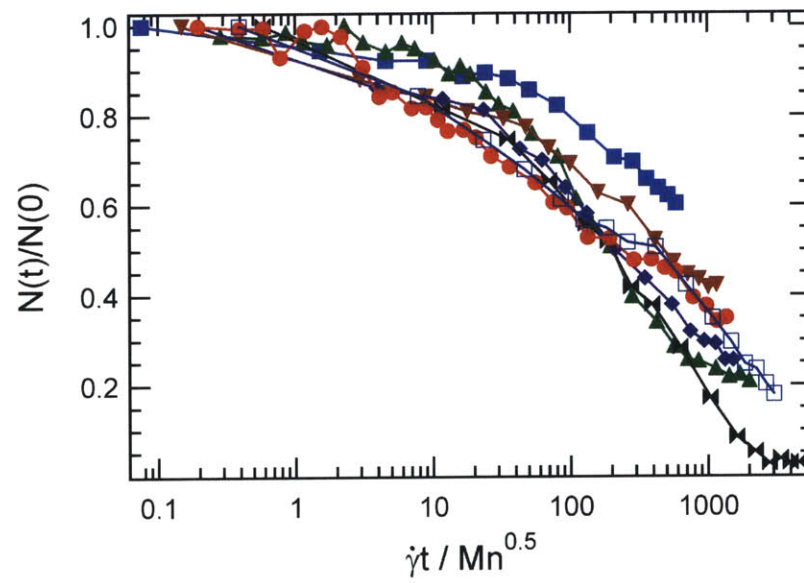
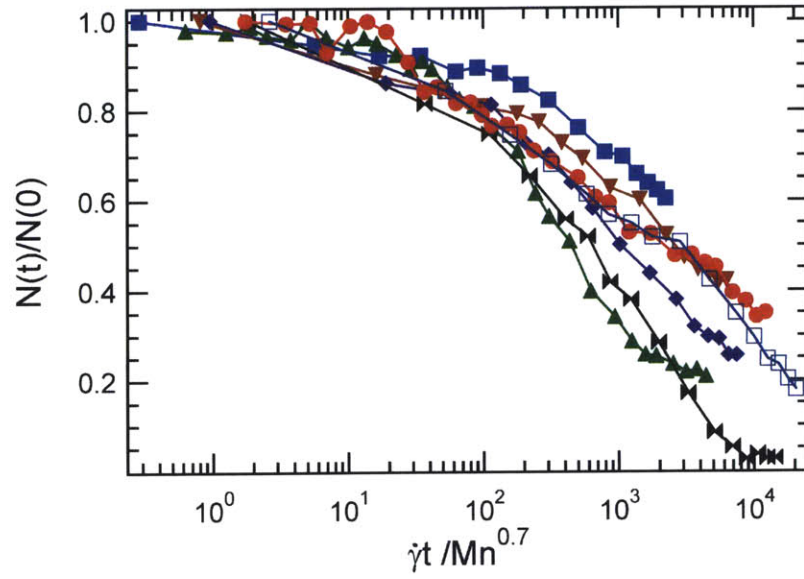
conditions (b) Scaling using the convective time scale that primarily governs the aggregation dynamics at long times. (c) Experimental conditions. Mason number is based on particle diameter as the characteristic dimension $Ma = \frac{144\eta_s}{\mu_0\chi^2 H^2} \frac{V_{avg}}{d}$ for future comparison with Brownian dynamics simulation results.

Mason number is the ratio of the viscous and magnetic forces and as the structure evolution is primarily dependent on the interplay of these two forces, we use this number to characterize the aggregation dynamics. Mason number, in figures 4.19 and 4.21 is based on the particle diameter as the characteristic dimension ($Ma = \frac{144\eta_s}{\mu_0\chi^2 H^2} \frac{V_{avg}}{d}$) for future comparison with Brownian dynamics simulation results. The characteristic time based on the dipolar interaction strength and the convective time scale which govern the structure evolution at short and long times respectively can in fact be represented as functions of the Mason number as follows

$$\begin{aligned}
 Mn &= \frac{\text{hydrodynamic forces}}{\text{magnetostatic forces}} = \frac{144\eta_s \dot{\gamma}}{\mu_0\chi^2 H^2} \\
 \tilde{t} &= \frac{3}{2} \frac{D\lambda}{d^2} t = \frac{\pi\mu_0\chi^2 H^2}{144\eta_s} t = \frac{\dot{\gamma} t}{Mn^{1.0}} \\
 t^* &= \dot{\gamma} t = \frac{\dot{\gamma} t}{Mn^{0.0}}
 \end{aligned} \tag{4.20}$$

where $\dot{\gamma}$ is the shear rate based on the height of the channel. As time progresses, the time scale governing the aggregation kinetics changes smoothly from the characteristic time based on the dipolar interaction strength to a convective time scale. This can be interpreted as a smooth transition of the power of Mason number governing the structure evolution from 1 to 0. Figure 4.22 shows the scaling of these results using a time scale based on different powers of Mason

number and the transition from a dipolar strength based time scale to a convective time scale can be seen from figures 4.22(a) to (c).



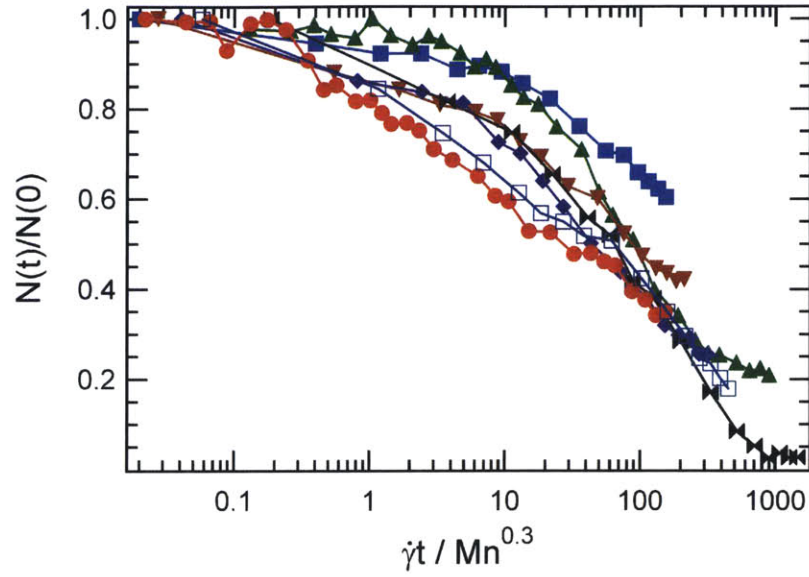


Figure 4.22 Scaling at different times for 1 micron CIP based MR fluid flowing in microchannel geometry (700 X 70 μm) using characteristic times based on different powers of Mason number (a) characteristic time scale = $\dot{\gamma}t/Mn^{0.7}$ (b) characteristic time scale = $\dot{\gamma}t/Mn^{0.5}$ (c) characteristic time scale = $\dot{\gamma}t/Mn^{0.3}$

Hence, the structure evolution can be regarded as a competition between two processes – the tip-to-tip aggregation process and the ‘zippering’ process due to lateral interactions and advection. The head-to-tail aggregation process takes precedence at short time scales but lateral interactions govern the aggregation kinetics at longer times. Hence, a characteristic time scale can be obtained by assuming that these two uncorrelated aggregation rates act in parallel as follows

$$\begin{aligned}
 t_{Mn}^* &\rightarrow \frac{\dot{\gamma}t}{Mn}; t \rightarrow 0 \\
 t_{Mn}^* &\rightarrow \frac{\dot{\gamma}t}{Mn^0}; t \rightarrow t_\infty \\
 \ln t_{Mn}^* &= a \ln\left(\frac{\dot{\gamma}t}{Mn}\right) + (1-a) \ln(\dot{\gamma}t)
 \end{aligned} \tag{4.21}$$

where t_∞ is the time when the clustering process has reached a steady state and there is no net change in the number of clusters with time. Here, a is a function of time and varies from 1 to 0 such that, as time progresses, the system time scale moves from a tip-to-tip aggregation characteristic time to a convective time scale. Moreover, at intermediate times when a lies between 0 and 1, scaling with fractional powers of Mason number is observed as shown in figure 4.22.

$$\begin{aligned}
 t_{Mn}^* &= \left(\frac{\dot{\gamma}l}{Mn} \right)^a (\dot{\gamma}t)^{1-a} \\
 t_{Mn}^* &= \dot{\gamma}t \left(\frac{1}{Mn} \right)^a \\
 t &\rightarrow 0; a \rightarrow 1 \\
 t &\rightarrow t_\infty; a \rightarrow 0
 \end{aligned} \tag{4.22}$$

The lateral interactions and the defect driven coarsening can also be captured using this simple scaling model by using the time scale for lateral interactions t_{HT} suggested by Halsey and Toor (1990).

$$t_{HT} = \frac{k_B T \phi^{3/2}}{\eta l^3} t \tag{4.23}$$

where l is the distance separating two columns. Hence, a parameter b can be used to capture the relative importance of the defect driven coarsening in comparison with the lateral interactions due to pure convection at longer time scales as follows

$$\begin{aligned}
 \ln t_{Mn}^* &= a \ln \left(\frac{\dot{\gamma}l}{Mn} \right) + (1-a-b) \ln(\dot{\gamma}t) + b \ln \left(\frac{k_B T \phi^{3/2}}{\eta l^3} t \right) \\
 Pe &\rightarrow \infty; b \rightarrow 0
 \end{aligned} \tag{4.24}$$

where b is a number which is much smaller than a and is also a function of the Péclet number. Thus, when the Péclet number is high only the convective time scale becomes important at longer times while as the fluid flow rate slows down, defect-driven coarsening becomes more and more important especially at longer times.

4.6 Cluster Analysis: Other Techniques

Mean cluster size variation or the variation of total number of clusters with time has been used mainly to analyze the experimental results and aggregation phenomena. As the mean cluster size is only an average number it is an excellent tool to capture the gist of the aggregation dynamics but it also masks many details of the structure evolution process.

An example where the mean cluster size fails to capture the complete picture of structures formed is shown in figure 4.23. A thicker column wherein two or more chains are zippered together has the same mean cluster size as a laterally connected cluster. We have used a connectivity analysis technique in order to distinguish between these differently connected clusters. Connectivity can be defined as the statistical average of the number of contact points per particle (Mohebi *et al.*, 1996). Horizontal and vertical connectivity is calculated by analyzing neighbors of each particle along the horizontal or vertical direction and taking their average. Hence, particles in a laterally connected cluster will have a much lower vertical connectivity than those forming a thicker column like structure.

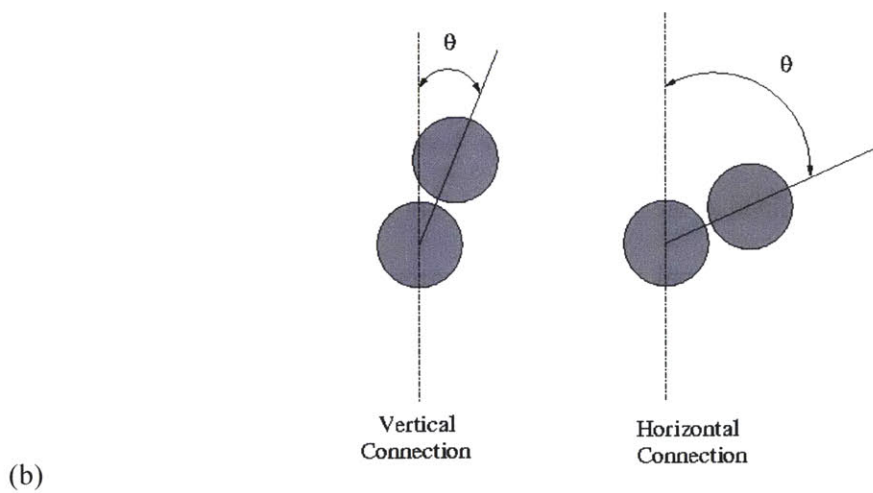
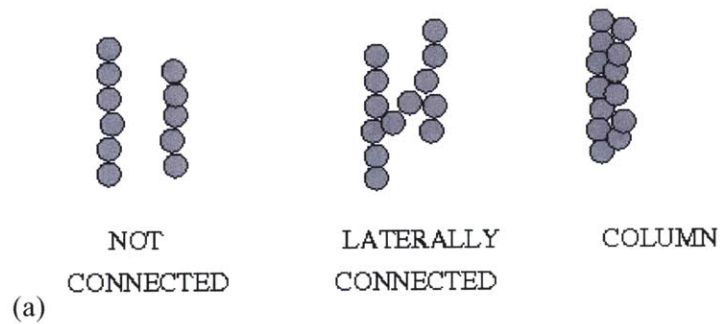


Figure 4.23 (a) Connectivity values help to distinguish between interconnected, laterally connected or column structures various (b) Horizontal ($30^\circ < \theta < 90^\circ$) and vertical connectivity ($0^\circ < \theta < 30^\circ$) of a particle depending on the positions of any neighboring particles.

Figure 4.24 shows the horizontal & vertical connectivity variation as the flow rate is increased while keeping the other parameters such as the particle size, magnetic field etc. constant. It can be seen from the figure that as the flow rate increases, horizontal and vertical connections increase at a faster rate, due to convection driven zipping of chains, resulting in formation of thick stripes and columns.

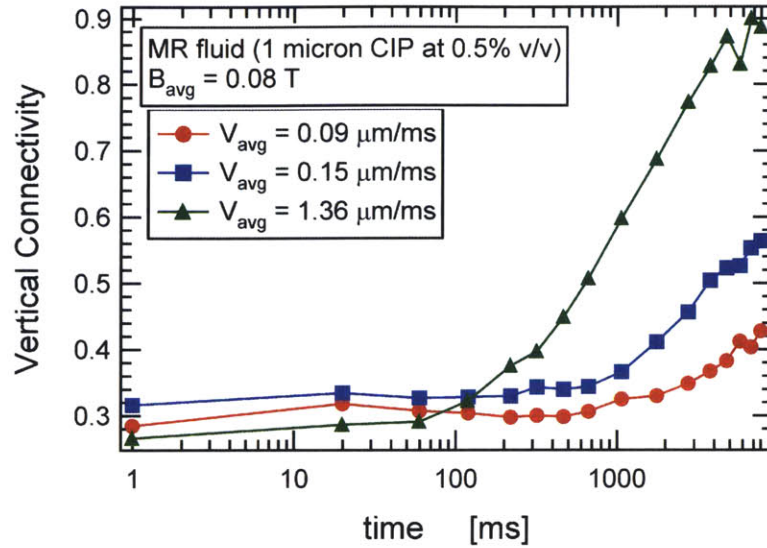


Figure 4.24 Effect of increasing the flow rate on the vertical connectivity of MR fluid particles (1 micron CIP, 0.5%v/v) in a microchannel geometry (400 X 40 μm) $B_{\text{avg}} = \mu_0 H = 0.08 \text{ T}$.

However the connectivity analysis technique is applicable only when the particle is the same size as a single pixel. If the size of a single particle corresponds to more than one dark pixel in the image then particles need to be identified in the image before doing connectivity analysis which is a computationally intensive task besides being error-prone for 2D projected images.

A more refined measure of connectivity that is especially useful in distinguishing between ‘percolated’ network structures observed at higher particle concentrations from thick stripes or columns is ‘conductivity’. Conductivity of the structures can be measured by replacing particles by resistor nodes and defining a contact resistance between two connected nodes (or neighboring particles). As a first approximation, the contact resistance can be assumed to be a constant independent of the orientation of the line joining two particles (or nodes) with the magnetic field direction. This has been used by Martin *et al.* (1998) to analyze simulation results in the quiescent case. The resistance of percolated networks will be much higher than the

resistance for thick stripe structures and hence can be very effectively used to distinguish between a wide variety of connected structures. However, this method is computationally very intensive and hence remains a candidate for future investigation.

More information can be gleaned by analyzing the variation of the cluster size distribution with time, in combination with the mean cluster size value. As time progresses, the number of single particles or smaller chains continuously decreases while the size of the larger clusters increases as shown by dotted lines in figure 4.25.

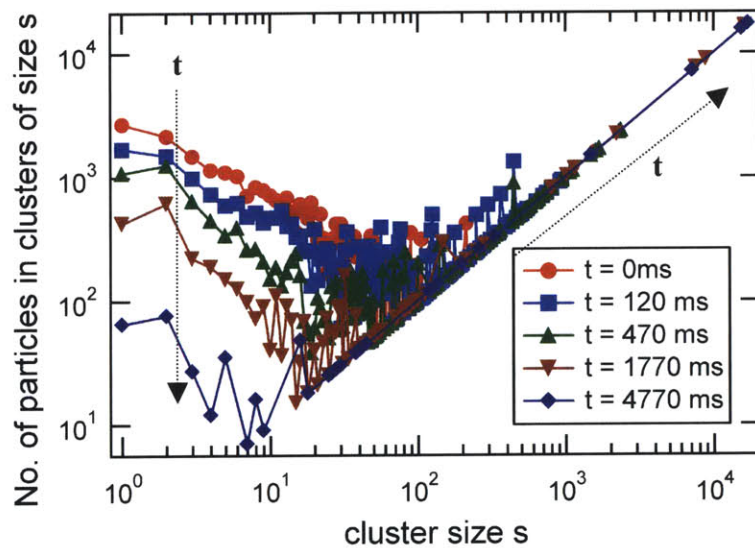


Figure 4.25 Cluster size distribution variation with time in the presence of flow for a MR fluid (1 micron CIP, 0.5%v/v, $B_{avg} = \mu_0 H = 0.08$ T) in a microchannel geometry.

Aggregates can also be analyzed in the frequency space using a 2D fast fourier transform (2D FFT). FFT allows us to look closely at any periodicity that might be present in the original spatial-domain image. Frequencies that are frequently encountered in the image appear as a peak in the power spectrum (represented by darker colors in the 2D power spectrum shown in figure 4.26(ii)). The low frequency terms are indicative of sample spanning structures while the higher

frequencies provide the finer details. Furthermore, removing a single frequency from the spectrum is equivalent to subtracting the corresponding information from every part of image while preserving the rest of the structural details.

Also, 2D power spectrum images bear close resemblance to light scattering data that has been observed for MR fluids in microchannel geometries. Hence, 2D FFT provides an excellent tool for comparison of data obtained from two different experimental setups.

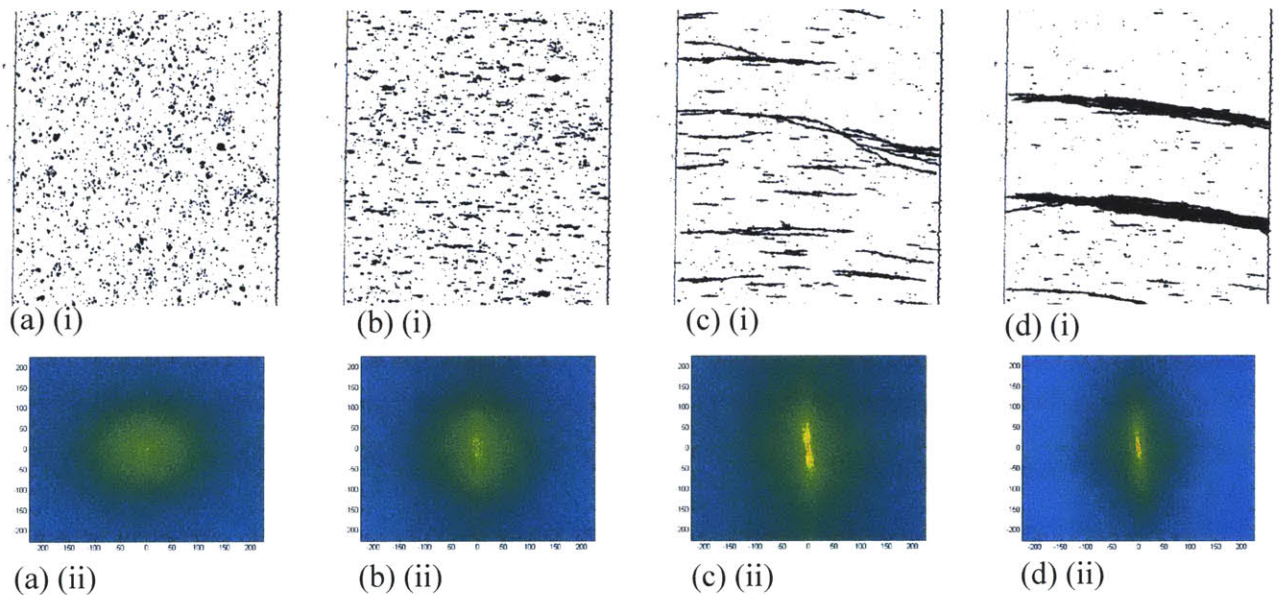


Figure 4.26 Fast fourier transform (FFT) analysis of structure evolution of MR fluid (7 micron CIP 0.5% v/v) flowing in a microchannel geometry ($B_{avg} = \mu_0 H = 0.16$ T) (a) initial configuration $t=0$ ms (b) $t = 56$ ms (c) $t = 686$ ms (d) $t = 4986$ ms (i) spatial-domain image (ii) 2D power spectrum

An illustrative series of FFT images is shown in figure 4.26 along with their corresponding spatial-domain image captures. Initially the particles are well dispersed in the system and hence the FFT shows a diffuse power spectrum very similar to light scattering data. As time progresses and particles chain up along the horizontal direction, the power spectrum

becomes more concentrated around the smaller frequencies indicating the presence of larger structures in the horizontal direction i.e. columns spanning the width of the channel.

Thus, a number of techniques are available for in-depth analysis of the structures & patterns formed and have been used to demystify the aggregation phenomena.

4.7 Comparison of Experimental Results with Brownian Dynamics Simulations

The experimental results have been compared to Brownian dynamics simulation results that are obtained by using a particle evolution equation which takes into account Stokesian hydrodynamic interactions, magnetic interactions and Brownian diffusion for MR fluids flowing in microchannel geometries (Haghoosie and Doyle through private communication). Secondary effects in the aggregation process due to multibody interactions were assumed to be negligible in these simulation studies.

The simulation and experimental results show excellent qualitative agreement as can be seen from snapshots of the structure evolution with time in figure 4.27. The simulations based on mainly the dipolar polarization model along with the Stokesian drag approximation are able to capture the tip-to-tip aggregation process and the lateral interactions leading to the formation of thick columns or stripes.

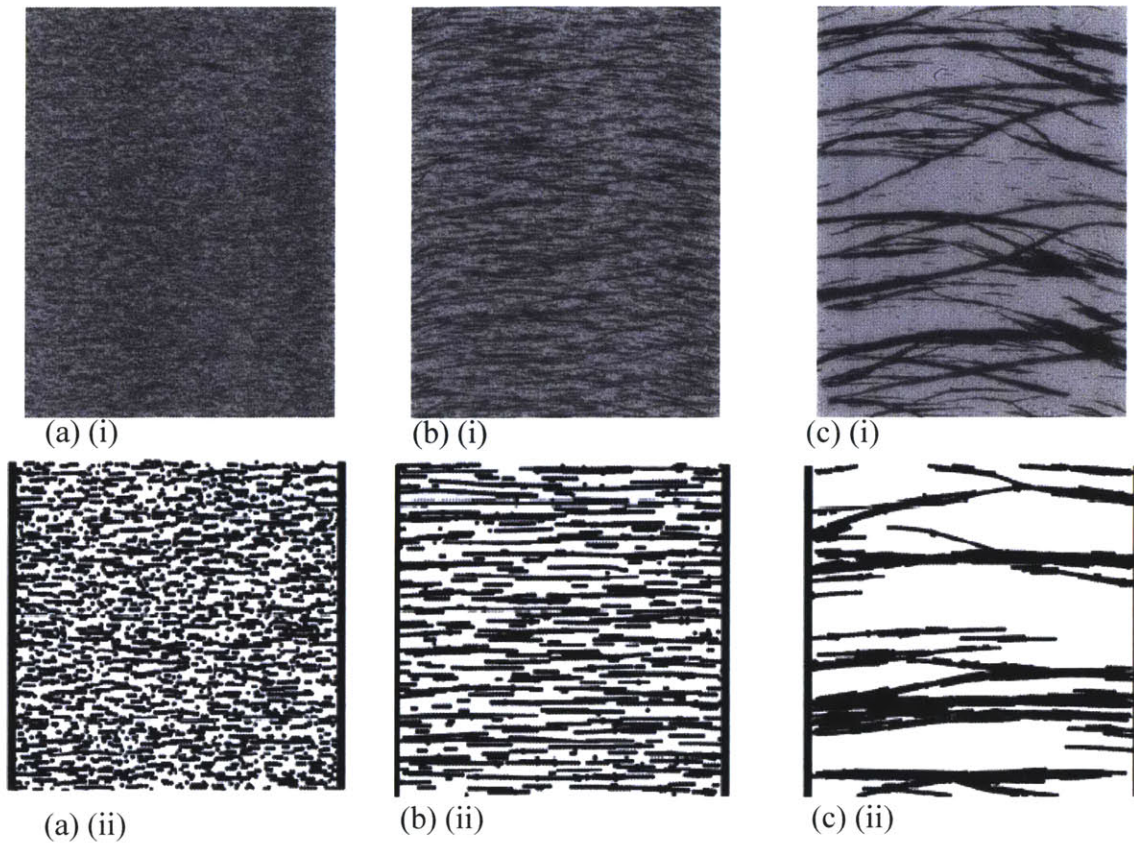


Figure 4.27 Qualitative comparison of experimental and BD simulation results (0.5% v/v, $Ma = 0.1$) for a MR fluid flowing in a microchannel geometry (40 X 400 microns). Experimental results are for a 1 micron CIP based MR fluid at 0.5% v/v, $B_{avg} = \mu_0 H = 0.08$ T (a) $t = 60$ ms (b) $t = 320$ ms (c) $t = 2770$ ms (i) Snapshots (ii) BD simulation results

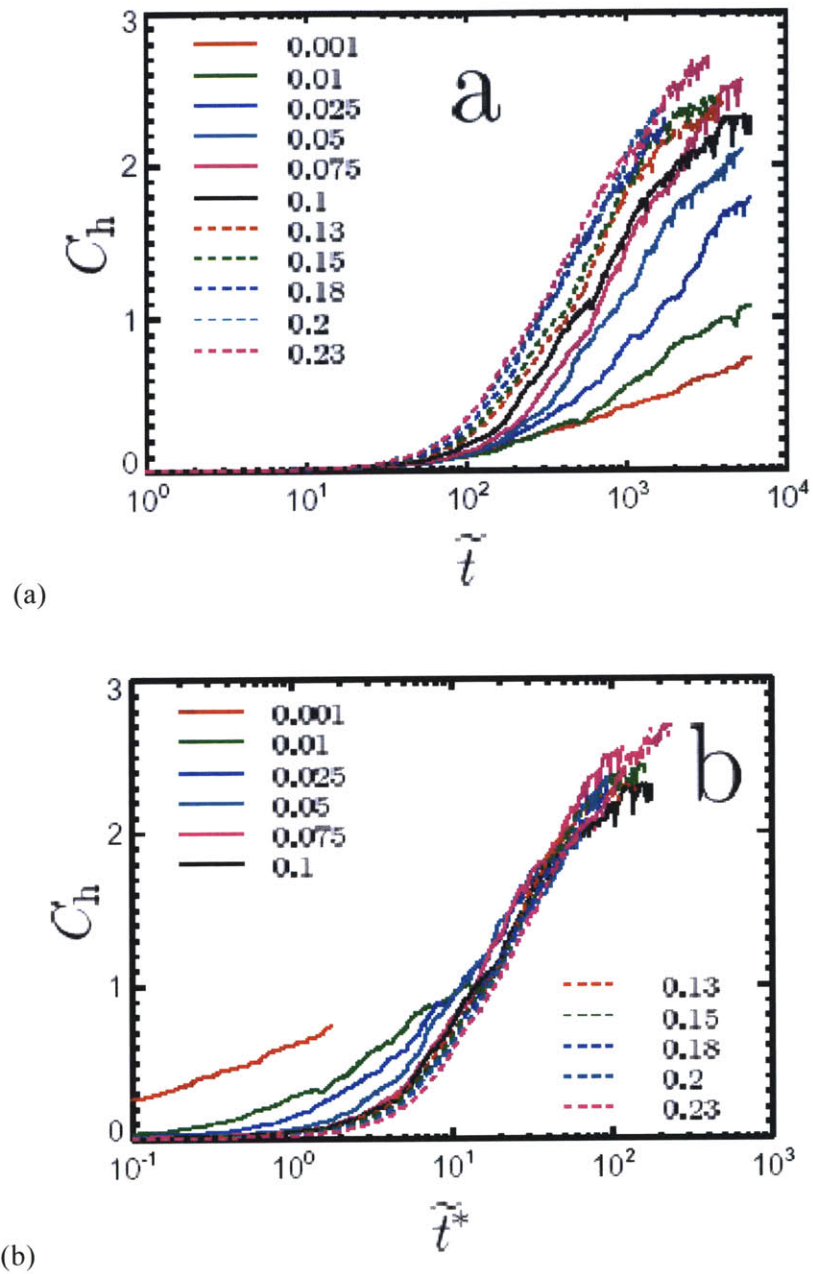
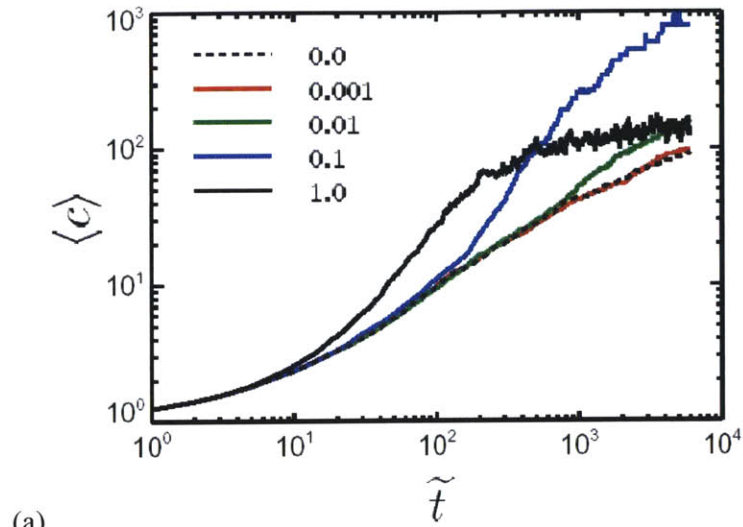


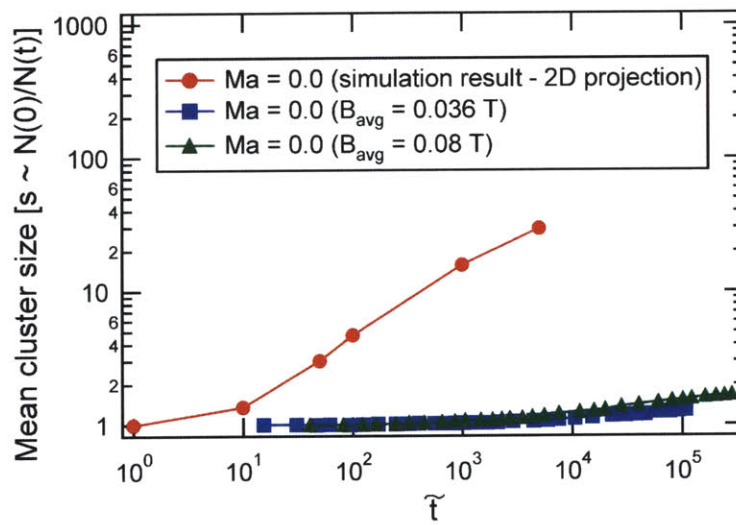
Figure 4.28 Scalings predicted by Brownian Dynamics simulations for different Mason numbers. (a) Dipolar interaction strength time scale governing the head to tail aggregation at short times (b) Vertical or lateral connectivity scaled using the convective time scale showing collapse of curves at long times (Haghoosie and Doyle through private communication).

Simulation results are also able to predict the scalings that are observed in the experiments (figure 4.19 & figure 4.21). At short times, the simulations capture the scaling based on the dipolar interaction characteristic time thus predicting to an excellent degree the head to tail aggregation process leading to an increase in horizontal connections as shown in figure 4.28(a). In experiments, lateral interactions due to convection were observed to govern the structure evolution at long times (figure 4.19). Simulation results validate this observation and the variations in the increase of lateral connections are found to collapse at long times using the convective time scale as shown in figure 4.28(b).

Thus, the primary physical mechanisms and dynamics are captured using a single body representation of the hydrodynamic and magnetic forces acting on the particles. However, discrepancies in the mean cluster size variation results obtained from simulation and experiments are observed as shown in figure 4.29.



(a)



(b)

Figure 4.29 Discrepancies in the mean cluster size variation between experimental and simulation results due to multibody effects and 2D projection cluster analysis technique. (a) Mean cluster size variation for 3D simulations at different Mason number values (Haghgoie and Doyle through private communication) (b) Comparison of simulation results analyzed using the 2D cluster analysis technique with experimental results.

A possible cause for the mismatch between the experimental and simulation results is that a multipole representation of the hydrodynamic interactions is required to capture the finer details of the aggregation dynamics of clusters, chains and column structures. As the mean cluster size is only an average number of the cluster size distribution it is found to be extremely sensitive to smaller ‘rogue’ clusters. These small ‘rogue’ clusters persist in experiments without getting assimilated by larger clusters but are not observed in simulations possibly due to multibody hydrodynamic interactions that are not accounted for in the BD simulations. Figure 4.30(a) shows the clusters at time $t \sim 5s$ when the dominant structures are thick stripes that flow along the channel. However, besides the 5-10 stripes/ columns or larger clusters, a number of smaller ‘rogue’ clusters persist (shown by different colors in figure 4.30(a)(ii) and enclosed by the dark red elliptical shape in the cluster size distribution in figure 4.30(b)). These smaller clusters that are flowing in different planes than the larger clusters are unaffected by the magnetic interactions with the larger clusters. This is possibly due to the difference in drag forces that is experienced by the clusters which resists the aggregation that might be initiated by the magnetic interactions.

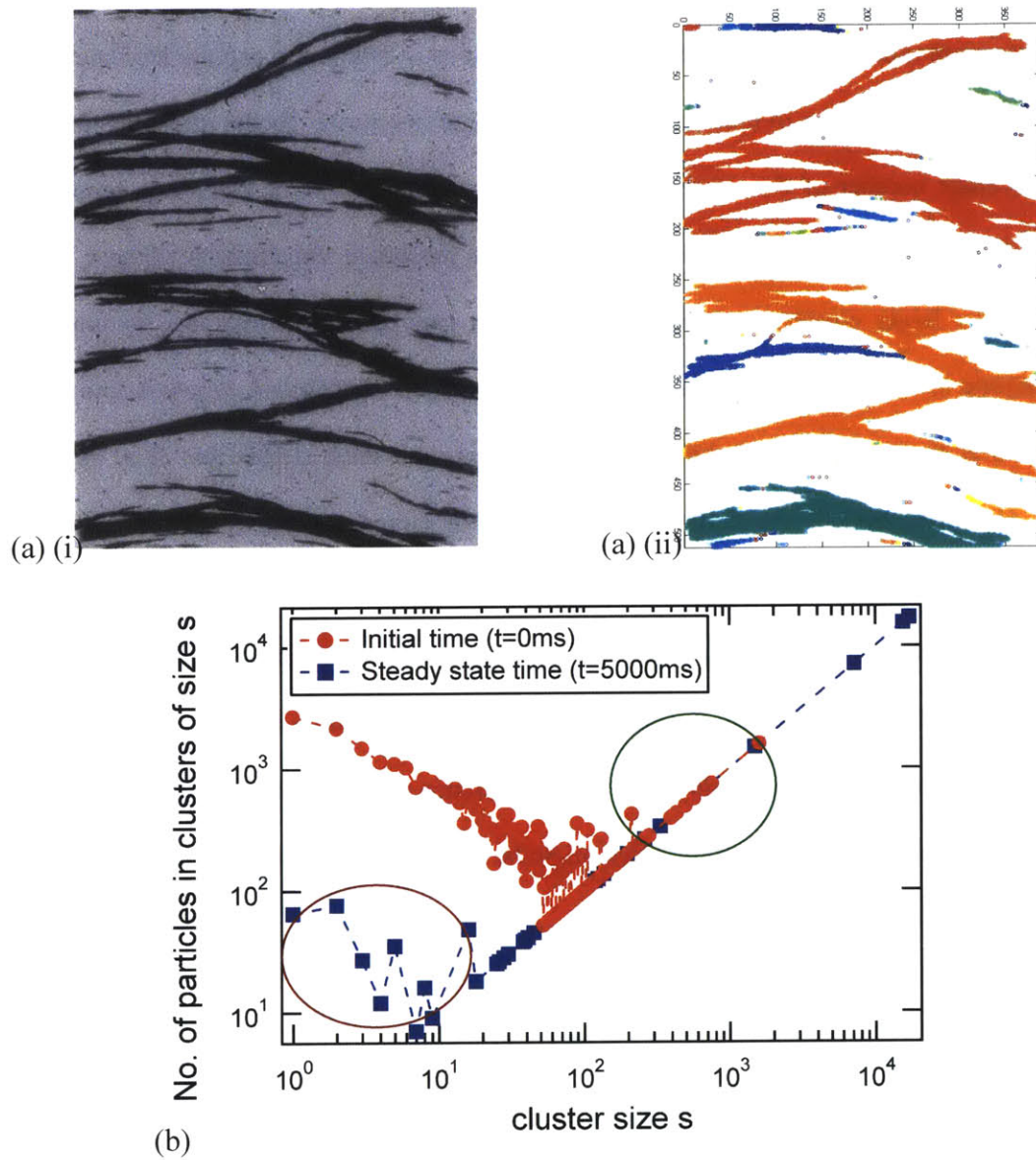
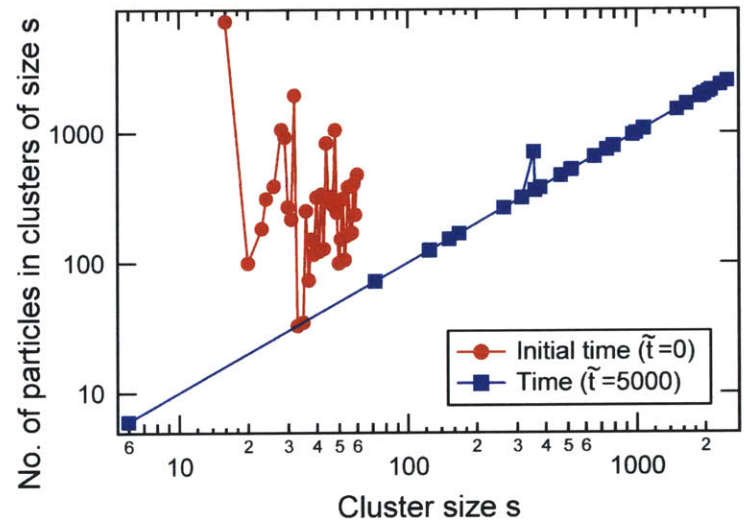
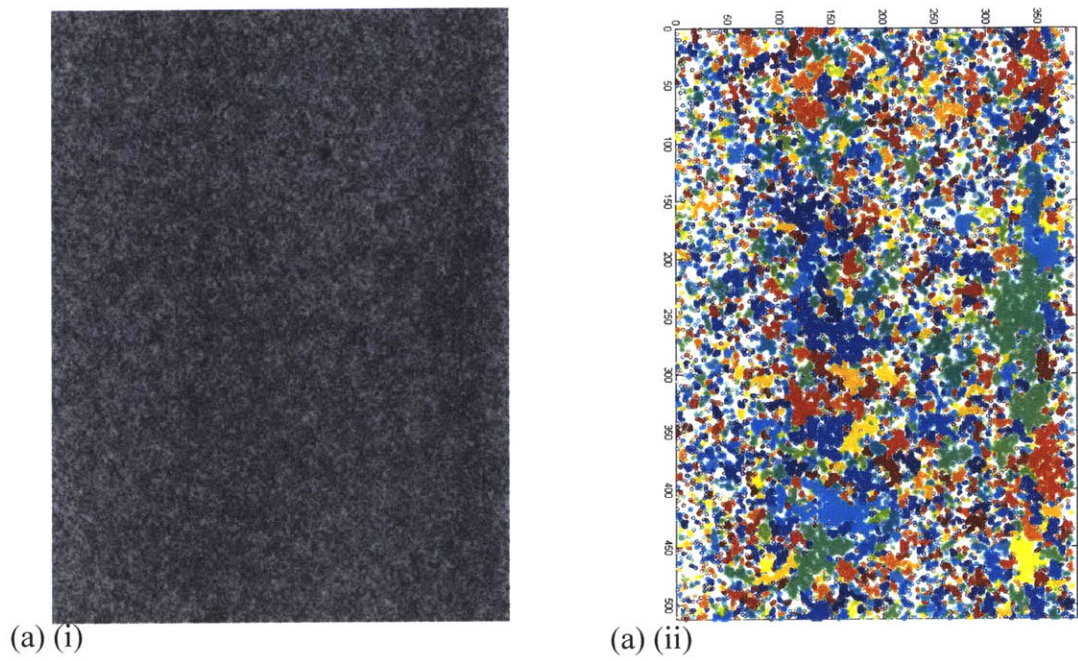


Figure 4.30 Discrepancies in the mean cluster size variation between experimental and simulation results due to presence of ‘rogue’ clusters (small clusters that persist and are not assimilated by the larger clusters possibly due to multibody hydrodynamic interactions) (a) Image capture for MR fluid (1 micron CIP 0.5% v/v, $B_{avg} = \mu_0 H = 0.08$ T) $t = 4770$ ms (i) Snapshot (ii) Clusters detected. (b) Cluster size distribution at initial time and $t = 4770$ ms. (Dark brown ellipse indicates the ‘rogue’ clusters)

The quantitative comparison of the mean cluster size is further complicated due to the comparison of cluster analysis of 2D projected images of 3D experiments or simulations. 2D projection results in two or more particles in different planes, which are otherwise not in a cluster, to appear connected together as shown in figure 4.31(a). These clusters are illustrated in figure 4.31(b) with a green elliptical shape and can be seen in the cluster size distribution at initial times.

2D projection image analysis of monodisperse particles randomly distributed in a 3D simulation box also show this diffuse cluster size distribution, as shown in figure 4.31(b), instead of the theoretical cluster size distribution that would show a single sharp peak.



(b)

Figure 4.31 Discrepancies in the mean cluster size variation between experimental and simulation results due to 2D projected image analysis (a) Image capture for MR fluid (1 micron CIP 0.5% v/v, $B_{avg} = \mu_0 H = 0.08$ T) $t = 0$ ms (i) Snapshot (ii) Clusters detected. (b) Cluster size distribution for 2D projected images of 3D simulation results.

Polydispersity also plays a role in leading to a diffused cluster size distribution. However, it is found to be only a secondary issue in resolving these discrepancies as the initially diffuse cluster size distribution and smaller ‘rogue’ clusters at long times are observed even in experiments performed with MR fluids based on monodisperse superparamagnetic particle. Figure 4.32 shows the cluster size distribution at initial ($t=0s$) and later times ($t=5s$) for a MR fluid based on monodisperse magnetizable particles (0.6% v/v 1 micron Dynabeads).

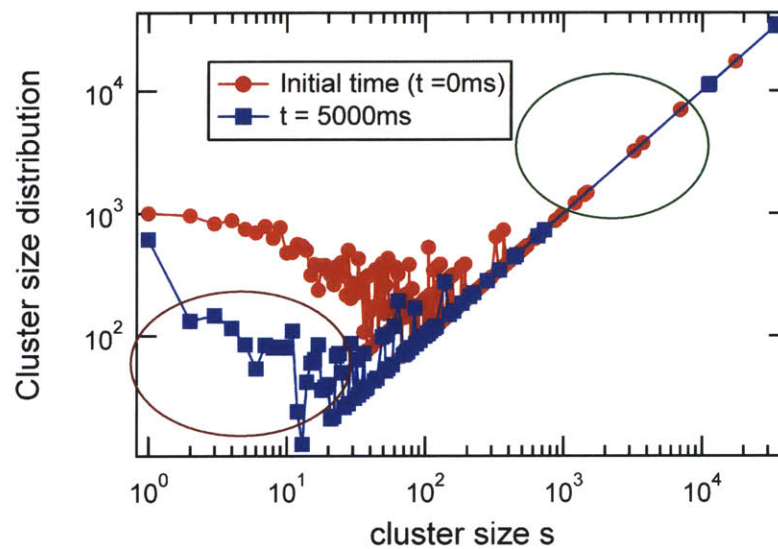


Figure 4.32 Cluster size distribution at initial ($t = 0ms$) and long ($t = 5000 ms$) times for a MR fluid (1 micron monodisperse Dynabeads at 0.6% v/v) flowing in a microchannel geometry (100 X 1000 microns) ($B_{avg} = \mu_0 H = 0.1 T$).

4.8 Conclusions

The study of aggregation dynamics and structure formation of MR fluids in microchannel geometries in the presence of bulk fluid flow has provided us with useful insights into development and further improvement of applications both on the microscale and macroscale.

High speed video microscopy technique allowed us to capture the fast dynamics and aggregation rates of carbonyl iron particles based MR fluids which has hitherto not been done. Further, it shed more light on the longstanding question of the mechanism behind the formation of fibrous, interconnected network structures in MR fluids at higher volume fractions. The presence of flow leads to the formation of a wide variety of structures depending on the interplay of magnetic and hydrodynamic interactions and this study has endeavored to capture the important scalings and mechanisms behind these structure formations. Even though good qualitative agreement is obtained between the experimental and simulation results for flow of MR fluids in microchannels, quantitative comparison after refinements in both the experimental setup and the modeling of particle interactions used in the simulation study needs to be investigated in future.

Chapter 5

Microscale Applications of ‘Smart’ Fluids & Materials

Microfluidics is the science of manipulation of small amounts of fluid (10^{-9} to 10^{-18} litres) in spaces as small as 10-1000 microns (Whitesides, 2006). Microfluidics offers the advantage of providing a tool to test and analyze small quantities of fluid with a high resolution and sensitivity. However, microfluidics is in its early development stage and a number of challenges lie in the path of commercialization of this technology as a lab-on-a-chip platform or as a drug analytical & delivery tool. Some of the major challenges lie in the technology of building blocks of these systems which includes switches, valves, mixers & pumps. These basic components require a technology so that they can be easily fabricated, packaged & manipulated during actual use. Developing a simple technology for the fabrication of these elements has been the focus of many studies. However, the only commercially viable method for fabrication and usage of these components is based on pneumatic actuation which has the advantages of low cost & high effectiveness (high on/ off flow ratio $\sim 10^4$) (Thorsen *et al.*, 2002). It however suffers from the drawback of requiring a continuous pressure supply and an array of pressure regulators which make it difficult if not impossible to incorporate into portable devices.

In this thesis work, the use of magnetic actuation is explored in developing these basic components in an effort to make microfluidic devices into truly portable analytical systems and tools. Magnetic actuation offers the unique advantage of providing an external (to the channel)

means (such as a miniature permanent magnet or a coil) of controlling these basic elements. Further, with a fast response time (order of milliseconds) & portability they hold great potential in developing into an exciting and feasible technology. The challenge in making the magnetic actuation technology commercially viable lies in attaining a high effectiveness (such as the on/off flow ratio for valves) at practically achievable magnetic fields of 0-0.4 Tesla.

Magnetic fields have been used previously in the area of microfluidics for a number of different applications (Pamme, 2006) but primarily as a technique to manipulate magnetic fluids in the microchannels (Hatch *et al.*, 2001) or for separation of magnetic particles or magnetically labeled biomaterials (Deng *et al.*, 2002). We explore the use of magnetic materials, ‘MR’ fluids and MR fluid-doped ‘smart’ materials for use as basic elements in microfluidic devices such as valves, mixers, pumps etc.

5.1 Synthesis of Magnetic Microstructures

Synthesis and formulation of ‘MR’ fluids based on superparamagnetic particles, carbonyl iron particles of different sizes and development of ‘smart’ materials based on MR fluids such as fabrics and foams doped with MR fluids was discussed in earlier chapters. In this section, a few other synthesis techniques that are used to develop microstructures are described in detail for use in microscale applications.

5.1.1 Magnetic Chains

5.1.1.1 Depletion flocculated magnetic chains

Flexible magnetic chains have a wide variety of applications such as micromechanical sensors (Goubault *et al.*, 2003), microvalves and micromixers (Terray *et al.*, 2002; Biswal and Gast, 2003) and in DNA separation chips (Doyle *et al.*, 2002). These wormlike magnetic chains can also, in principle, be used to improve the rheological response of magnetorheological fluids.

As described in detail in chapter 2, the yield stress of magnetorheological fluids is limited by the critical plastic strain when the chains collapse. This critical strain is very small ($\gamma_c \sim 10^{-2}$) and wormlike chains of the right size, would in principle form the backbone of the column-like structures, which are formed in the presence of a magnetic field (refer to chapter 4 for details), leading to an increase in the strain when the column structure collapses. Further, in the absence of magnetic field, the flexibility of the chains would ensure that they do not add significantly to the zero-field viscosity and yield stress thus maintaining the high gain (on-off ratio).

Goubault *et al.* (2003) have recently synthesized flexible magnetic filaments from superparamagnetic colloids using a depletion flocculation technique. We use this depletion flocculation technique to make flexible carbonyl iron particle based wormlike chains for the first time.

Carbonyl iron particles have a much higher magnetic susceptibility ($\chi = 14.72$ for 7 micron BASF CR grade particles and $\chi = 5.4$ for 1 micron BASF HQ grade particles below saturation magnetization) as compared to superparamagnetic particles such as magnetite or polystyrene beads with magnetite inclusions ($\chi = 1$ below saturation magnetization) and also a higher saturation magnetization. The linear magnetic field response is directly proportional to the magnetic susceptibility while the rotational dynamics is a function of the square of the magnetic susceptibility. A high response or effectiveness (on/ off gain ratio) is vital to the use of these magneto-responsive chains in microfluidic devices and hence, carbonyl iron particle based chains have great potential in these devices. Further, higher magnetic fields can be exploited for carbonyl iron particles due to a higher saturation magnetization (2.1T for carbonyl iron particles).

Depletion flocculation occurs if the adsorption of an added polymer is unfavourable so that the center of mass of polymer coils is displaced from the interface of the particles leading to a ‘polymer depleted zone’ (Jenkins and Snowden, 1996). This absence of polymer creates an osmotic pressure leading to weak reversible particle aggregation. Poly(acrylic acid) (PAA) is

used in a number of systems as a depletion flocculant. Figure 5.1(a) shows the phase diagram of a PEO grafted polystyrene latex bead system where adding PAA (170000 MW) causes reversible aggregation (Liang *et al.*, 2003). We use PAA (MW 250000) at 0.05-0.1% v/v to aggregate MR fluid (1 micron carbonyl iron particles at 0.05-0.1% v/v in water with carboxymethylcellulose added as a dispersant and thickener) in microchannel geometries and microcells in the presence of 0.1-0.4 T magnetic field obtained using a Neodymium-boron-iron permanent magnet. Figure 5.1(b)-(c) show these flexible depletion flocculated magnetoresponse chains of different sizes. The length of the chains can be easily controlled by using different geometries and they show a strong response to magnetic fields. However, the aggregation is found to be very sensitive to the concentration of PAA and can be easily reversed by varying the pH (figure 5.1(a)).

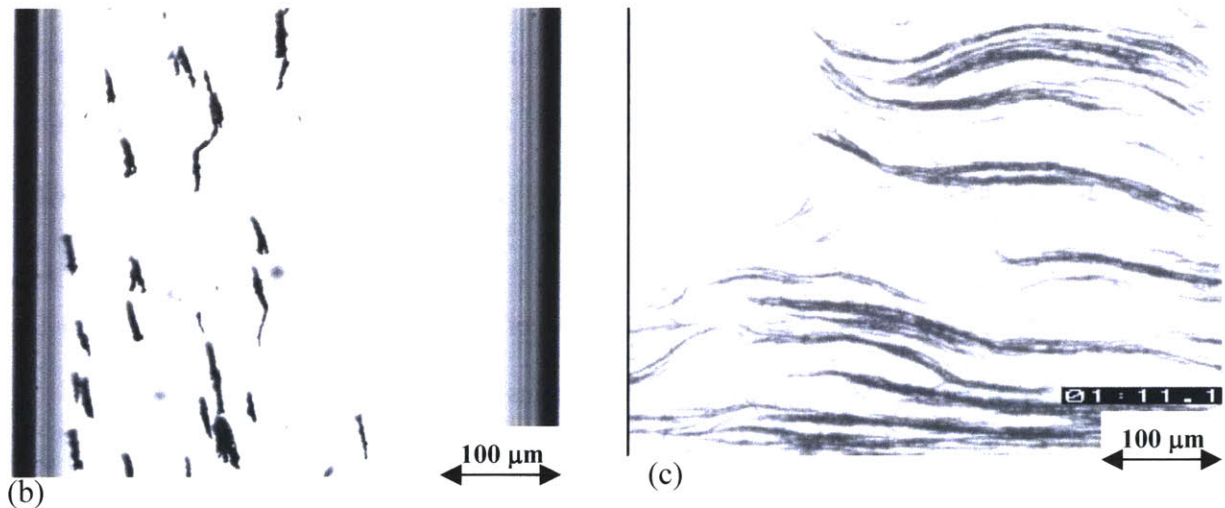
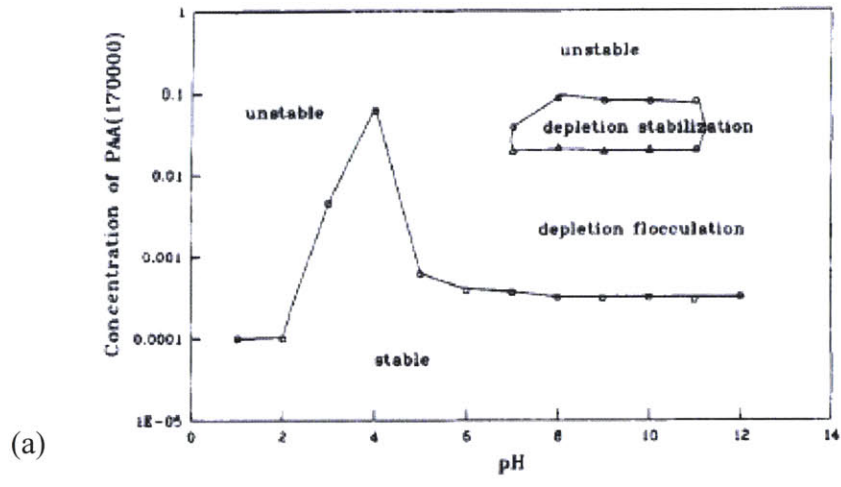


Figure 5.1(a) Phase diagram of PEO-grafted polystyrene latex beads system with concentration of poly(acrylic acid) (PAA) added and pH of the system. (b) Flexible magnetic chains formed by depletion flocculation of carbonyl iron particle based MR fluid (0.1% v/v) using PAA at 0.1% v/v. (c) Flexible chains with length controlled by the width of the microchannel geometry.

5.1.1.2 Permanent linked chains using amidation chemistry

Chains aggregated by using depletion flocculation suffer from the drawback of not being very stable in presence of shear forces once the magnetic field is removed. Further, they are very sensitive to different medium conditions (concentration of bridging polymer) and chains can get disrupted or phase separate depending on the fluid environment. Since, in microfluidic applications, the chains will frequently experience different flow and fluid environment, we explore a technique based on amidation chemistry to permanently link carbonyl iron particles and form flexible or rigid chains. Singh *et al.* (2005) have exploited this technique to form permanently linked chains of core-shell magnetic beads with rigidity that is dependent on the size of the amine linker molecule. Other types of linker molecules have also been used previously, for example, Gast group (Furst *et al.*, 1998; Biswal and Gast, 2003) used a streptavidin-biotin binding chemistry to synthesize semiflexible chains using polystyrene beads with ferromagnetic inclusions (62% iron oxide w/w).

In this subsection, we demonstrate the use of amine linking chemistry described by Singh *et al.* (2005) to make rigid magnetoresponseive chains from carbonyl iron particles.

Carbonyl iron particles of different sizes (BASF AG) at 0.05-0.2% v/v are first coated with negatively charged poly(acrylic acid) (PAA, MW 250,000, Sigma Aldrich) at 0.05-0.2% v/v in deionised water (Ricca chemical company). 1-[3-(dimethylamino)propyl]-3-ethylcarbodiimide hydrochloride (EDC, Sigma Aldrich) at 0.005 M is then added which coats the negatively charged PAA. PAA-EDC coated carbonyl iron particles are then linked using Poly(ethylene glycol) (PEG) diamine (XTJ 502, MW 2000, Huntsman) linker at 0.005 M in the presence of a magnetic field as shown in figure 5.2. A magnetic field of 0.1-0.4 T generated using rare earth (neodymium-boron-iron) magnets is used for the chaining purpose. The reaction is carried out for 1-24 hours depending on the desired thickness of the chain. The length of the chains is

determined by the cell/ chamber used during the linking experiment and can vary from 50 – 5000 microns.

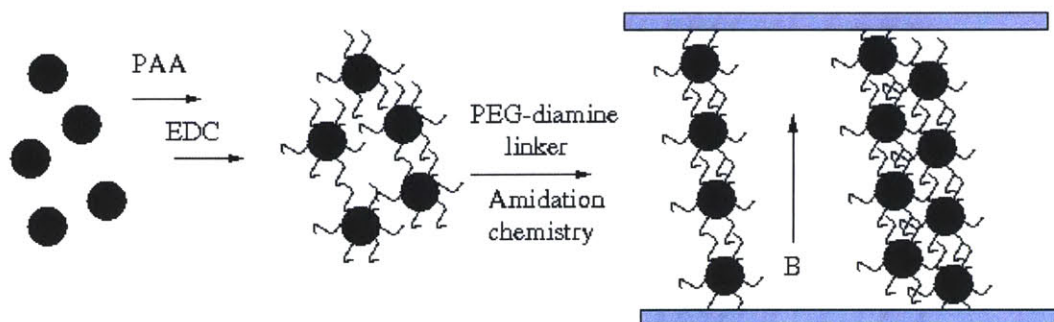


Figure 5.2 Amidation chemistry used for permanently linking carbonyl iron particles of different sizes to synthesize permanently linked magnetoresponsive chains.

Figure 5.3 shows carbonyl iron particle based magnetoresponsive chains of different sizes. The thickness and length of the chains depends on the experimental cell and the magnetic field setup used during the linking process. Fairly monodisperse chains are formed in microchannel geometries with fixed channel width or in a glass microcell (two glass microscope slides separated by Teflon spacers of known thickness) as shown in figure 5.3(a). The reaction time for forming chains of a single particle thickness is about 2 hours.

At higher concentrations of carbonyl iron particles (0.2% w/w), permanent rigid chains with thickness of the order 10-50 microns (10-50 particle diameters) are obtained. Linking along two directions (length i.e. the direction of the magnetic field and lateral linkages along the thickness direction) leads to chains or needle shapes with high mechanical rigidity, which are stable even under high shear forces obtained in conventional mixers. However, they are fairly polydisperse as shown in figure 5.3(b).

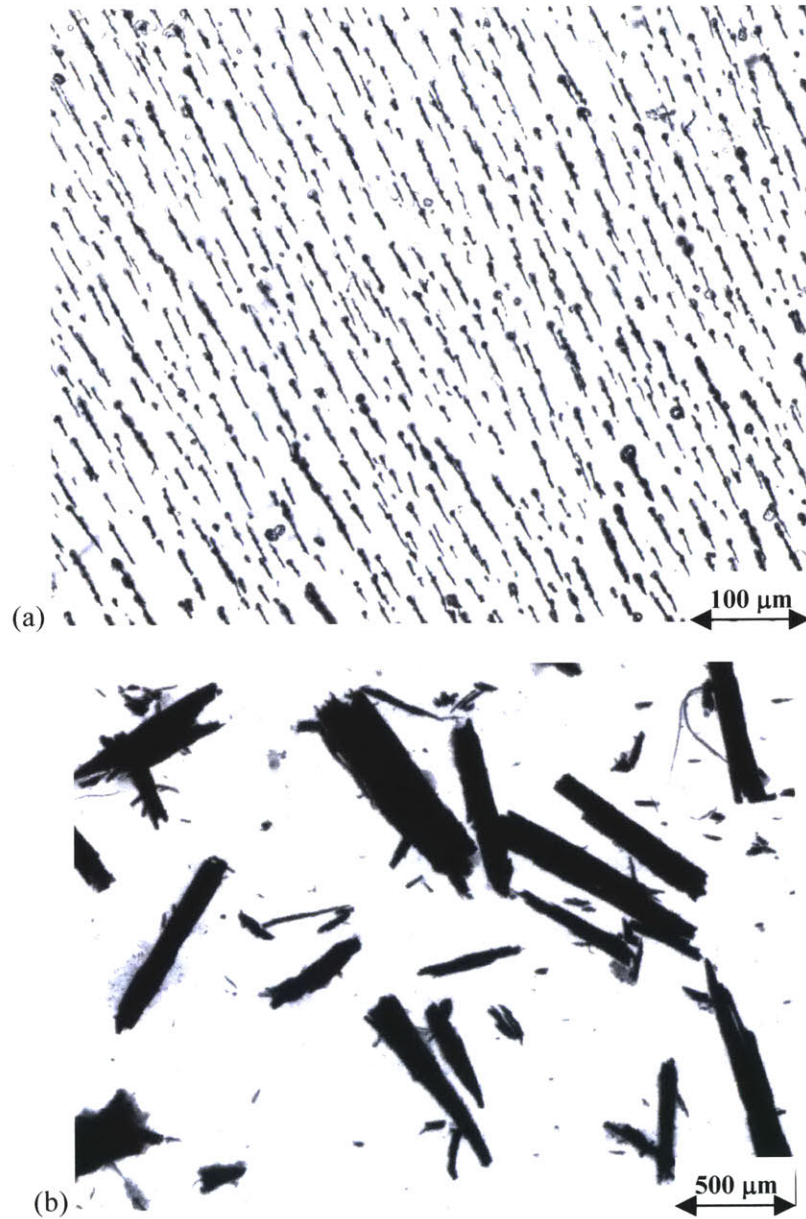


Figure 5.3 Permanently linked magnetoresponsive chains of carbonyl iron particles (1 μm CIP) (a) Monodisperse magnetic wires formed in glass microcells (0.05% v/v CIP), $B_{\text{avg}} = 0.2$ T (b) Magnetic needle shapes formed from 0.2% v/v carbonyl iron particles in the solution. $B_{\text{avg}} = 0.2$ T

The permanently linked chains are not sensitive to fluid environments commonly encountered in microfluidic devices. However, during the linking process, the amidation

chemistry is very sensitive to concentrations of various constituents such as the PAA concentration. A higher concentration of PAA (>0.2% v/v) leads to depletion flocculation of carbonyl iron particles and eventually phase separation. The linker molecules (EDC & PEG diamine), when present in excess, lead to gel like structures with encapsulated oriented magnetic chains of carbonyl iron particles as shown in figure 5.4.

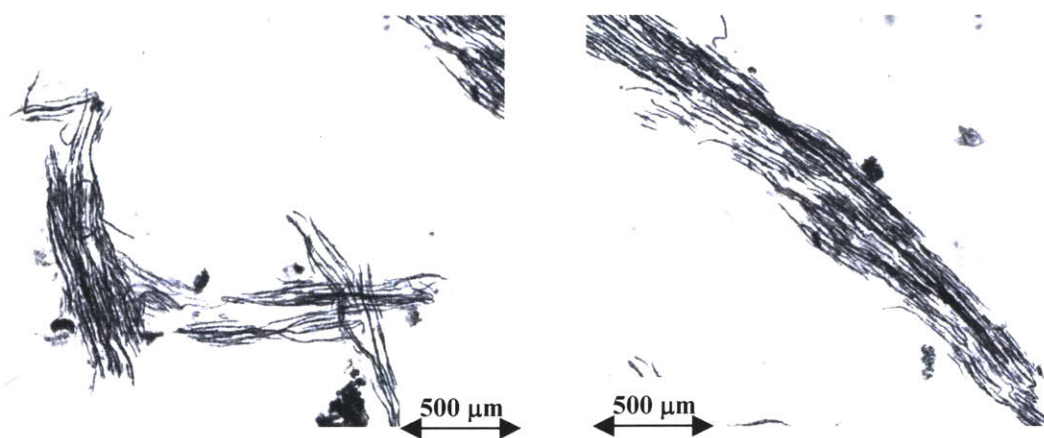


Figure 5.4 Magnetoresponsive gel with oriented carbonyl iron particle based chains formed at 0.02 M concentrations of EDC & PEG diamine during the linking process.

The structures formed during this linking process are also sensitive to magnetic field gradients and the microcell geometry. Magnetoresponsive chains, needle shapes or gels are formed in a closed microcell (top and bottom surface decide the length of the chain) in the presence of a uniform magnetic field. On the other hand, an open microcell that is exposed to the atmosphere in presence of high magnetic field gradients leads to the formation of fractal magnetic structures as shown in figure 5.5. These fractal structures are also sensitive to the relative concentrations of PAA and carbonyl iron particles in the reaction mixture. Fractal structures have been observed previously during evaporation of particulate suspensions (Niklasson *et al.*, 1988) and the physical mechanism and fractal dimensions remain to be investigated in the future.

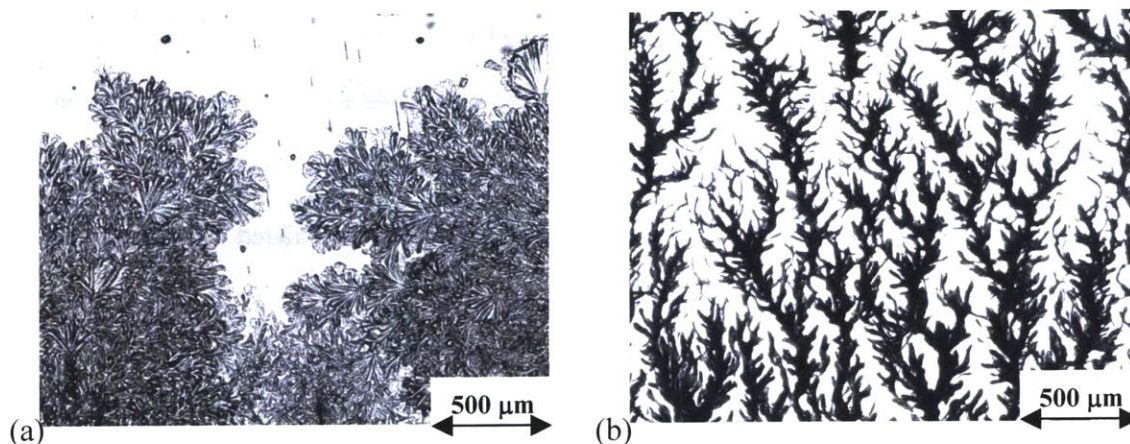


Figure 5.5 Fractal aggregates obtained in microcells in the presence of a magnetic field gradient (microscope slide exposed to the atmosphere with a rare earth magnet (0.4 T) below it) due to evaporation of carrier liquid during the reaction process. (a) 0.1% v/v CIP + 0.2% v/v PAA solution with 0.005M EDC & PEG diamine linker. (b) 0.1% v/v CIP + 0.1% v/v PAA solution with 0.005M EDC & PEG diamine linker.

5.1.2 Anisotropic Monodisperse Magnetic Microparticles

Microparticle synthesis has developed into a rich field of literature over the past few years as microfluidic devices with their low Reynold's number flow provide a highly controlled route for synthesis of monodisperse spherical and anisotropic shape particles (Thorsen *et al.*, 2001; Dendukuri *et al.*, 2005). Different techniques for microparticle synthesis include continuous flow lithography (CFL) (Dendukuri *et al.*, 2006), co-flow (Nisisako *et al.*, 2006) or crossflow microfluidic systems (Thorsen *et al.*, 2001) and batch approaches (Rolland *et al.*, 2005; Jiang *et al.*, 2001).

Continuous flow lithography (CFL) can be used to synthesize complex particles of different shapes, sizes and multiple chemistries in a continuous manner (Dendukuri *et al.*, 2006). Magnetic particles synthesis has been limited to spherical shapes using conventional techniques (reduction of iron pentacarbonyl, co-precipitation etc.) or chains, needle structures assembled

from spherical particles as described in previous subsection. Anisotropic monodisperse magnetic shapes have tremendous application potential because of their novel responses to magnetic fields as single particle probes and elements or as constituents in magnetorheological fluids.

We used the continuous flow lithography technique to synthesize anisotropic magnetic particles based on carbonyl iron particles and explored their use in microfluidic devices. The continuous flow lithography technique consists of a PDMS microchannel, micro-fabricated using the soft-lithography technique, mounted on an inverted microscope (Axiovert 200, Zeiss) stage with an attached CCD camera (KPM1A, Hitachi) as shown in figure 5.6. A 100 W HBO mercury lamp with a UV filter set (11000v2, UV, Chroma) with a VS25 shutter system (Uniblitz) is used to expose the fluid to UV light pulse for a specified time. A photomask with the desired shape and size (feature size reduced by a factor of 7.8 for 20x objective lens) is inserted in the field-stop of the microscope (Dendukuri *et al.*, 2006).

MR fluid used for the synthesis of microparticles consists of 0.1% v/v of carbonyl iron particles dispersed in poly(ethylene glycol) diacrylate (PEG-DA 400, Polysciences) with 5% photoinitiator (Darocur 1173, Ciba Speciality Chemicals). PEG-DA forms crosslinked networks on exposure to UV light due to radical induced polymerization. Thinky (Thinky Corporation, Japan) mixer and an ultrasonic mixer is used to ensure particles are well dispersed in the diacrylate solution. Figure 5.7 shows magnetic particles of triangular shape synthesized using the CFL technique. Other anisotropic shapes of magnetic particles can also be stamped out using photomasks of different shapes and sizes. These particles show a weak response to magnetic field and can be manipulated with fields of 0.2-0.4 T.

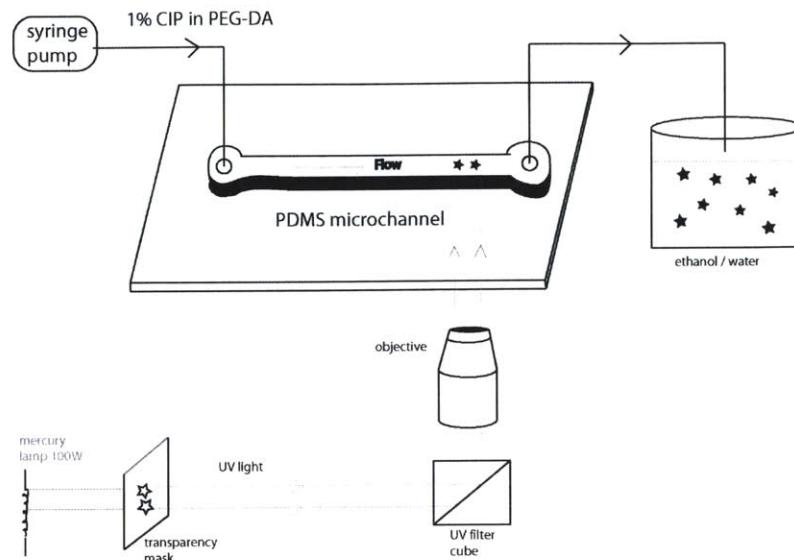


Figure 5.6 Continuous flow lithography (CFL) setup for controlled microparticle synthesis of complex shapes, sizes & chemistries in a continuous manner (Adapted from Dendukuri *et al.*, 2006).

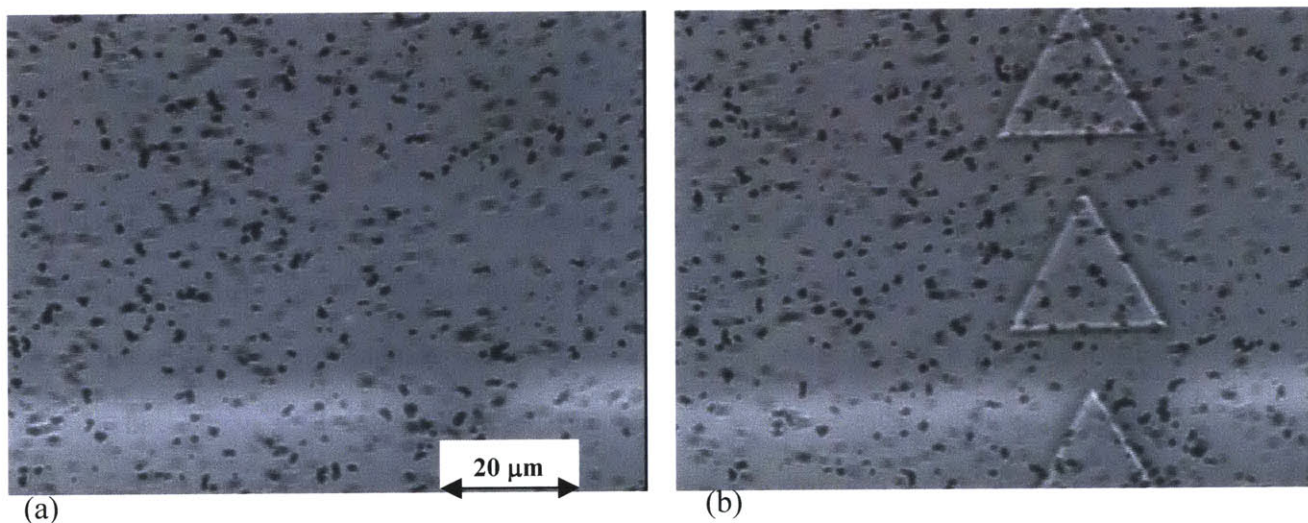


Figure 5.7 Continuous flow lithography (CFL) used for synthesis of anisotropic magnetic microparticles (a) MR fluid (0.1% 1 μm CIP in PEG-DA with 5% photoinitiator) flowing in a microchannel (500 X 70 microns) (b) Triangular shaped magnetic particles (20 micron edge length and 50 micron thickness) stamped out on exposure to UV light in the specified area for 1/3s.

CFL is an excellent tool to continuously synthesize magnetic microparticles for low volume fractions of magnetic fields (0.1% - 1%). However, a higher concentration of particles is

desired for large response to magnetic fields as the magnetic susceptibility decreases in proportion to the volume of the non-magnetic material present in the microparticle ($\chi = 0.005$ for MR fluid with 0.1% of 1 μm CIP in PEG-DA).

At higher particle concentrations, as described in detail in chapter 4, surface fractions of particles becomes high and since, the carbonyl iron particles are opaque to the UV light source it results in a higher curing time and diffuse light at the boundaries. Further, at higher volume fractions, there is agglomeration of carbonyl iron particles in a diacrylate based carrier fluid and clogging of microfluidic channels becomes a serious concern.

The longer curing time required at higher particle concentrations can be countered by using a UV lamp source with a higher luminous flux and using quiescent fluid in the microchannel. However, this no-flow approach towards synthesis of microparticles, wherein the desired shape and size is projected onto a diacrylate based MR fluid in a microcell resulted in particles with diffuse boundaries as shown in figure 5.8. Further, the shape and size is found to be a strong function of the time of exposure which is itself a function of the particle concentration.

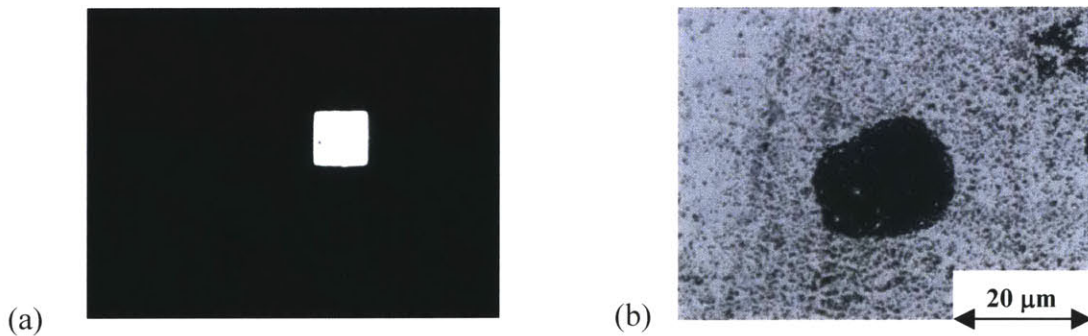


Figure 5.8 UV light projection lithography used for synthesis of magnetic microparticles from MR fluid in a microcell in the absence of bulk fluid flow (a) Photomask (Adobe Illustrator 10) printed using high resolution printer (Mika color) with a 100 X 100 micron square shape (b) Magnetic microparticle UV cured (5% v/v CIP) with diffuse boundaries.

In order to allow for higher curing times and sharp boundaries (defined by the microcell itself), we employ a batch approach for the synthesis of magnetic microparticles with higher magnetic content. Batch processes towards synthesis of monodisperse microparticles have previously utilized macroporous polymer templates (Jiang *et al.*, 2001) or photocurable perfluoropolyether (PFPE) embossing molds (Rolland *et al.*, 2005).

We utilize a PDMS mold microfabricated using standard soft lithography techniques (McDonald *et al.*, 2000) as outlined below. A photolithography mask is designed using Adobe illustrator (as shown in figure 5.9(a)) and printed using a high resolution printer (Mika Color, CA) on a transparency. These transparency features are then transferred using a KS aligner onto a silicon wafer coated with high contrast, epoxy based negative photoresist (SU-8-50, Microchem). The silicon wafer with these features forms the master which can be used repeatedly to obtain PDMS molds with microparticle shape boundaries defined in the mold itself. Poly(dimethyl siloxane) (PDMS) (Dow Corning, Sylgard 184) at 1:10 ratio of the curing agent to prepolymer is used to cast molds for these particles using the standard soft lithography technique.

This batch mold technique is fairly straightforward to implement and scale up for commercial use which makes it appealing for industrial particle foundries. These molds also have the advantage of permitting generation of particles with high magnetic volume. Further, these molds allow high throughput generation of microparticles as compared to continuous or co-flow systems. Figure 5.9(a)-(b) shows nearly 1000 particles on a 3" mold as compared to 20 parallel microchannels in a continuous flow system. The batch mold approach however suffers from the drawback of permitting only homogenous or immiscible fluid based particle synthesis while CFL allows for synthesis of particles with two or more functionalities (magnetic, chemical or optical) using co-flowing streams that exploit the diffusion-limited mixing in microchannels (Dendukuri *et al.*, 2006).

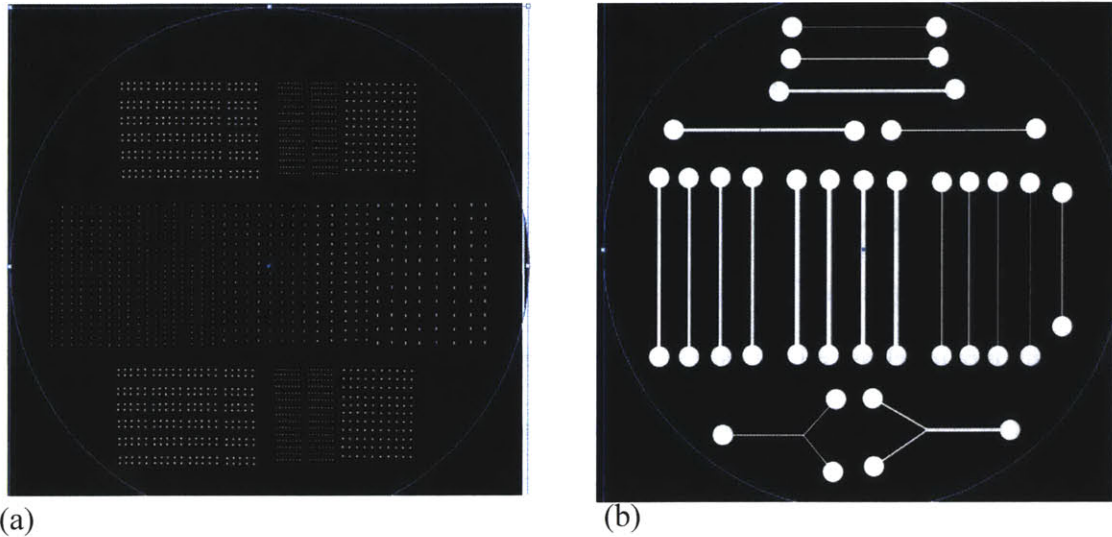


Figure 5.9 Photolithography masks designed for 3" wafer using Adobe Illustrator 10 for high resolution printing on transparency. Minimum feature size is defined by the printing resolution (typically 10-25 microns) (a) Photolithography mask for batch PDMS mold technique with approximately 1000 particles of different shapes and sizes. (b) Photolithography mask for CFL technique illustrating co-flow system that permits generation of Janus (two faced) particles.

Figure 5.10 shows the assembly line for synthesis of monodisperse anisotropic magnetic particles using the batch PDMS mold technique. MR fluid (1-50% of 1-10 micron CIP in PEG-DA with either a thermal or photoinitiator) is injected on the mold so that all the features are filled with the fluid. The excess layer of liquid on the mold is then scraped off using a flat non-wetting surface such as a glass cover-slip or a silicon wafer. The excess layer of MR fluid can also be squeezed out by carefully covering it with a non-wetting PDMS coated cover slip. The mold with MR fluid in the molded features (particle of different shapes & sizes) is then exposed to either a UV light source or baked in an oven depending on whether a photo or thermal initiator is used. The time of exposure to UV light (or baking time in oven) depends on the carbonyl iron particle concentration and the luminous flux of the UV lamp source (temperature of the oven). Two UV light sources (15W UV lamp, McMaster Carr and 100W HBO mercury lamp (2200

Lumens luminous flux with 1700 cd/mm^2 mean luminous density), Nikon) are used in the current study. A UV filter set is chosen for the mercury lamp UV source so that only the band of wavelengths around the UV emission peak at 365nm is allowed by the excitation filter ('band-pass' filter) while the barrier or emission filter blocks any background light going to the eye or camera observation systems. The mold is cleaned using an ethanol-water mixture and then dipped into the mixture to release all the particles in the solution. Ethanol dissolves unpolymerized PEG-DA (extent of polymerization depends on the exposure time) so that the microparticles come free from the mold and can now be used in microfluidic devices either dispersed in the ethanol-water mixture or other solvents.

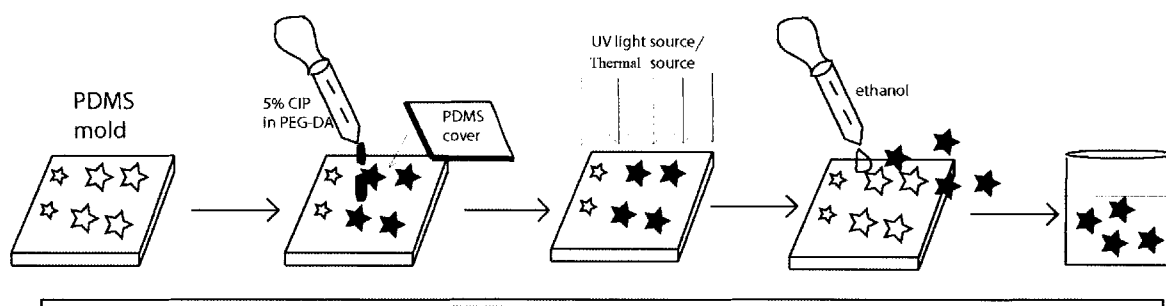


Figure 5.10 Assembly line for the batch PDMS mold technique for synthesis of magnetoresponsive microparticles.

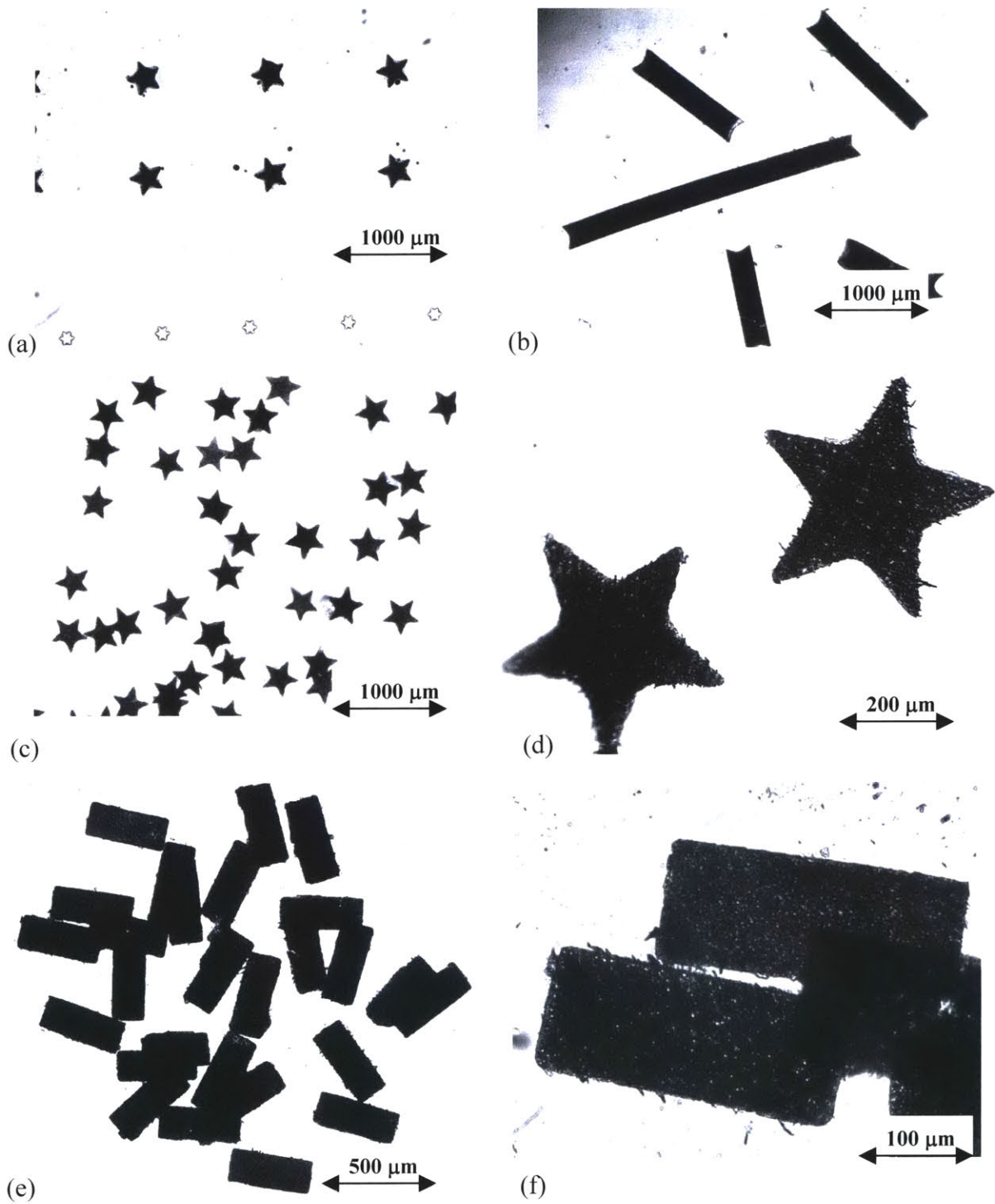


Figure 5.11 Anisotropic magnetic microparticles synthesized by curing of MR fluid (5% v/v 1 micron CIP in PEG-DA with 5% photoinitiator) using the batch mold technique (a) PDMS mold partially filled with MR fluid (b) Rectangular shaped magnetic particles with different aspect

ratios (c) Star shaped magnetic particles (d) Close-up view of cured crosslinked diacrylate based MR fluid in the star-shaped microparticle (e) Rectangular shaped magnetic microparticles (500 X 100 microns) (f) Close up view of (e).

Figure 5.11(a) illustrates a PDMS mold half-filled with MR fluid (5% v/v 1micron CIP in PEG-DA). The fluid is then cured using a UV light source to obtain anisotropic magnetic particles. Anisotropic particles such as rectangular and star shaped particles of different sizes synthesized using the batch mold technique are shown in figure 5.11(b)-(f). The shape and size of the synthesized particles is only limited by the resolution of the soft lithography technique (minimum feature size of 10 microns currently) and the size of the particles constituting the MR fluid (1-10 microns typically for carbonyl iron particles, 10-100 nanometers for co-precipitated and core-shell magnetic particles).

These magnetoresponsive microparticles hold tremendous potential for use as microrheology probes, ‘on-demand’ microfluidic valves and mixers etc. and a few of these applications are discussed in further detail in the following section.

5.2 Magnetic Microscale applications

5.2.1 Magnetic microfluidic separation chips

Microfluidic magnetic filters are attracting a lot of attention because of their ability to separate biological materials labeled with magnetic particles with a high degree of resolution. Further, these systems have the ability to be switched on and off at will and reduce the necessity of disassembly of filters to release the separated material (Deng *et al.*, 2002).

The field induced assembly of magnetic particles can also be used directly for separation of biomaterials such as DNA, cells, organelles etc. Doyle *et al.* (2002) have microfabricated DNA separation chips that use the magnetic field-induced assembly of superparamagnetic beads

(polystyrene latex beads with ferromagnetic inclusions) (figure 5.12). Using the microscale characterization of MR fluids described in detail in chapter 4, it is not possible to use different magnetic particle sizes, volume fractions, channel geometry and magnetic fields to control the porosity of the structures formed in the microchannels. Further, the same microfluidic device can be switched off and on and can be user-controlled to separate different sizes of biomaterials using different magnetic field dependent pore size.

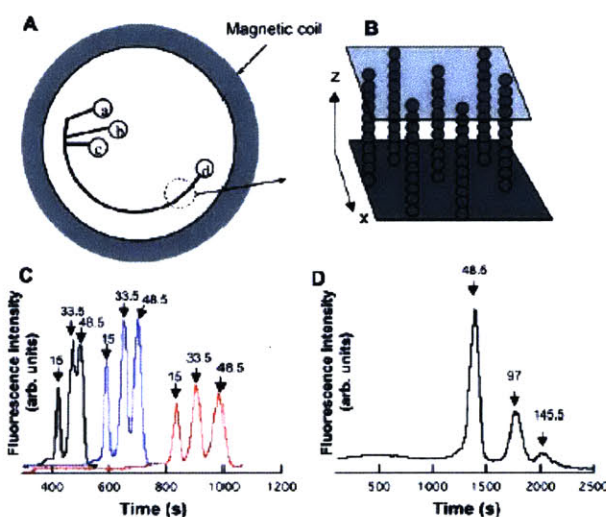


Figure 5.12 Field-induced assembly of superparamagnetic particles (discussed in detail in chapter 4) used in microfluidic chips for separation of DNA (Doyle *et al.*, 2002).

The aggregation dynamics of MR fluids characterized in chapter 4 can be used to optimize the DNA separation chip or design a microfluidic chromatography device for separation of bio molecules. Thus, a chip that has magnetic field strength varying along the length of the channel will have magnetic aggregates of varying porosity formed along the length of the channel which can then be used to separate DNA or biomolecules of different sizes at different points along the length of the channel.

5.2.2 Magnetic microrheology probes

Microrheology or measuring the response of fluid to thermal fluctuations or imposed strain on the microscale has been used to determine the linear viscoelastic response of complex fluids (Mason and Weitz, 1995). The mean square displacement of the probe particles dispersed within a fluid can be related to the storage and loss moduli depending on the imposed strain e.g. generalized Langevin equation incorporating a memory function to describe the average motion of probe particles undergoing thermal fluctuations.

Magnetic microparticles of anisotropic shapes described in section 5.1.2 can be used as probe particles that undergo a controlled strain imposed using two-directional magnetic fields. The microrheology technique is especially useful for in-vivo or in-situ rheological characterization of biomaterials such as actin gels, cellular network structures, tissues etc.

5.2.2 Magnetic microfluidic actuators and valves

Microvalves are basic components of microfluidic systems and as such have been the focus of numerous studies (Oh and Ahn, 2006). Traditionally, bulk and surface machining techniques have been used to fabricate mechanically active microvalves. Passive and active microvalves based on a number of different technologies such as pneumatic, piezoelectric, bimetallic, thermopneumatic, magnetic inductor, electrostatic, shape memory alloy, hydrogel-based and optical particle trapping based microvalves have been explored previously (Oh and Ahn, 2006; Terray *et al.*, 2002)

However, these techniques are limited to stiff materials ($E \sim 100$ GPa) which has led to widespread popularity of the replication molding technique or soft lithography (Xia and Whitesides, 1998; McDonald *et al.*, 2000) using elastomeric materials ($E \sim 750$ kPa). Soft lithography holds many advantages over traditional MEMS or photolithography techniques such as rapid prototyping, easy fabrication and replication, cost-effectiveness, biocompatibility while

providing a transparent optical window for analysis. Monolithic active elastomeric valves retain these advantages over traditional MEMS based microvalves and have been the focus of rapid development over the past few years. Stephen Quake's group have developed pneumatic based active elastomeric microvalves based on multilayer soft lithography that have allowed large scale integration of microfluidic components for the first time (Unger *et al.*, 2000; Thorsen *et al.*, 2001; Studer *et al.*, 2004). Figure 5.13 illustrates a push-down multilayer active elastomeric valve that can be actuated using an actuation pressure of 15-150 kPa (300 micron actuation and fluidic channel) depending on the membrane thickness (4-20 microns) (Studer *et al.*, 2004).

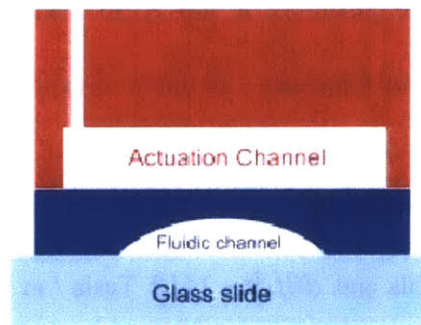


Figure 5.13 Schematic of a push-down valve that can be pneumatically actuated by applying pressures of nearly 15-150 kPa for 300 micron actuation and fluidic channels (Studer *et al.*, 2004). They also report the higher effectiveness (actuation pressure an order of magnitude lower) of a push-up valve geometry which has actuation and fluidic channels reversed.

The pneumatic valve have advantages of low cost and high effectiveness (on/ off flow ratio $\sim 10^4$) but suffer from the drawback of non-portability as they require a continuous pressure supply and an array of pressure regulators. Magnetic actuation allows this portability as miniature permanent magnets or coils can be used to obtain fairly high magnetic fields of 0-0.4 T over micrometer gaps.

A fairly simple modification to the push-down valve shown in figure 5.13 would allow this portability using magnetic actuation. The modification involves filling the actuation channel with MR fluid which is then actuated using miniature rare earth magnets. The magnetic actuation force comes from the gradient in the magnetic field known as the ponderomotive force as follows

$$F_B = \frac{\chi}{\mu_0} \int B \frac{dB}{dz} dV \quad (5.1)$$

where F_B is the magnetic actuation force.

The magnetic actuation force obtained using a 2mm rare earth magnet in the form of a wedge for a 300 X 50 micron actuation channel filled with a 36% v/v CIP based MR fluid with a magnetic susceptibility $\chi \sim 5$ to pinch off a 300 X 50 micron fluidic channel (glass slide thickness ~ 175 microns, membrane thickness ~ 20 microns) can be calculated as

$$\left[\frac{F_B}{WL} \right]_{\max} = \left(\frac{5}{4\pi(10^{-7})} \right) (0.468)(1412)(50)(10^{-6}) = 131.5kPa \quad (5.2)$$

where $B_{avg} = 0.468$ Tesla and $dB/dz \sim 1412$ Tesla / m is obtained as a estimate from FEMM 3.2 software. This is close to the 140 kPa actuation pressure reported by Studer *et al.* (2004) and hence magnetic actuation can potentially be used to modify the current active valves and obtain portable microfluidic devices. However, the experimental validation of this approach was fraught with a number of technical difficulties, as carbonyl iron particles are opaque to transmitted light and are difficult to flow at 36% v/v concentration. Further, silicone oil which is used as the carrier fluid for the MR fluid tends to swell thin actuation channels. All these difficulties can however be countered by using fluorescent particles in fluidic channels and micro-fabricating thicker actuation and fluidic channels using multilayer soft-lithography technique. Further, the use of a push-up valve geometry is reported to require an order of magnitude lower actuation pressures and hence, rare-earth magnets of smaller size can potentially be used. This remains to be investigated in the future.

MR fluids can be used directly as on-off valves if they are biocompatible with the working fluid. Figure 5.14 shows the valve action of the MR fluid (5% v/v 1 micron CIP in silicone oil) in a microchannel with hyperbolic contraction geometry. A constant pressure driven flow is used for this system so that as soon as a magnetic field is applied, columnar structures (as described in chapter 4) are formed which stop flow at the hyperbolic contraction. The system starts flowing again when the magnetic field is removed. The stiffness of this valve can be measured by increasing the pressure, in the presence of the magnetic field, until the column structures yield as shown in figure 5.14(c). Hence, for compatible working fluids, MR fluids can be used as controllable valves with variable magnetic field dependent stiffness.

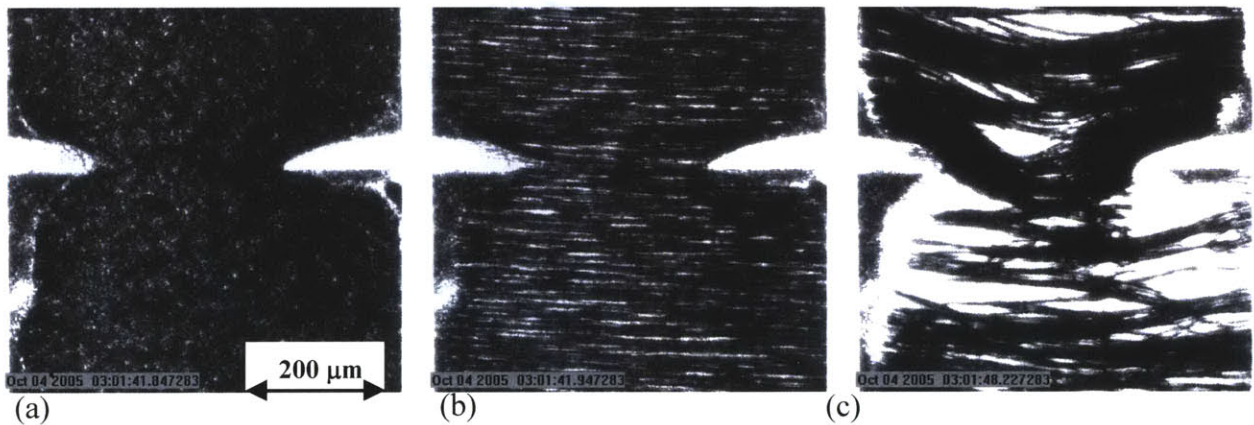


Figure 5.14 Valve action of MR fluid (5% v/v 1 micron CIP in silicone oil) in a constant pressure flow system. (a) MR fluid flowing in a hyperbolic contraction geometry ($B_{avg} = 0$ T) (b) Columnar aggregates stop flow at the contraction ($B_{avg} = 0.17$ T) (c) Increased pressure (5 to 25 psi) in the presence of field leads to breakdown of structure. Flow in the microchannel can simply be switched on by removing the magnetic field.

Another approach for developing magnetically actuated valve consists of doping elastomeric materials such as rubber, silicone elastomer with carbonyl iron particles (Jackson *et al.*, 2001). MR elastomers have been used previously for macroscale damping applications (Shiga

et al., 1992) and we explore the use of these controllable materials on the microscale. PDMS elastomeric microfluidic devices can themselves be doped with carbonyl iron particles during the curing process as shown in figure 5.15. The advantage of such a technique is that it allows the fabrication of magneto-responsive active elastomeric valves for portable microfluidic devices using a single step soft lithography process (unlike multilayer soft lithography for pneumatically actuated valves). Figure 5.15(b) shows a microfluidic device doped with carbonyl iron particles which can be actuated using magnetic fields.

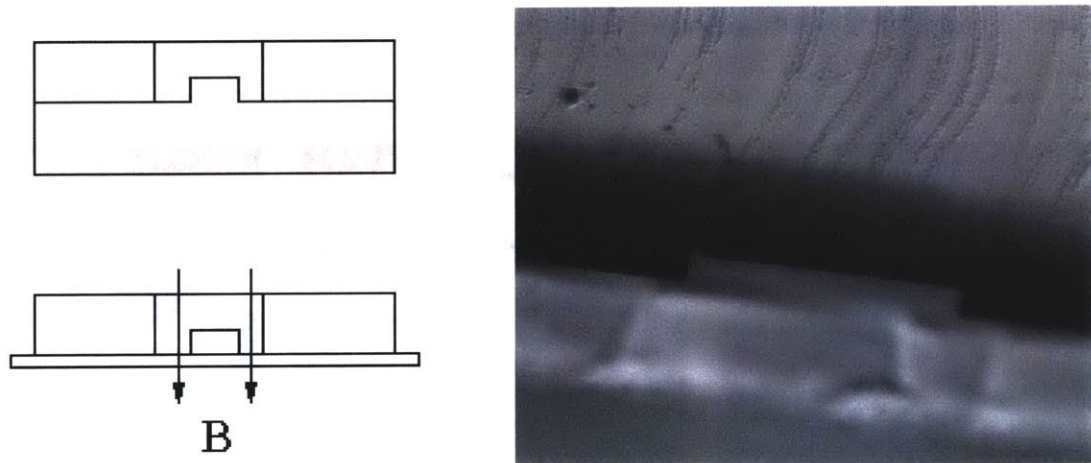


Figure 5.15 Carbonyl iron particle doped PDMS microfluidic device. This valve can be actuated using a magnetic field. (a) Schematic of doping during the curing process (b) Microfluidic channel doped with carbonyl iron particles

It is further advantageous to localize the doping of magnetic particles to a small area so that a number of valves can be molded separately and close to each other for large scale component integration. Also, a lightly doped PDMS channel as shown in figure 5.15(b) is not stiff enough to pinch off pressure driven flow completely. Hence, a cantilever type flap or heart valve structures can be used as shown in figure 5.16(a)-(b). Since the deflection of a flap valve is

a strong function of the thickness, valves of different stiffness can be easily incorporated into microfluidic devices.

$$\delta_{\max} = \frac{Pl^3}{3EI}; \quad I = \frac{bh^3}{12} \quad (5.3)$$

where P is the load on the valve, l is the length of the flap valve, b is the width of the valve or channel and h is the thickness of the valve.

PDMS doped with carbonyl iron particles (5% v/v 1 micron) and cured is shown in figure 5.16(a). Figure 5.16(b)-(c) show its response in the presence of magnetic field. It can be seen that the stiffness of cantilever flaps depends on the length of the valve as described by equation 4.3. Figure 5.16(d)-(e) show the SOLIDWORKS model of a microfluidic flap valve (500 X 100 X 25 microns) actuated with magnetic field (using a 2000 X 2000 X 50 micron neodymium-boron-iron permanent magnet). The valve shows a high effectiveness (high on/off flow ratio) and is able to sustain typical fluid pressures when actuated by magnetic fields obtained using miniature permanent magnets.

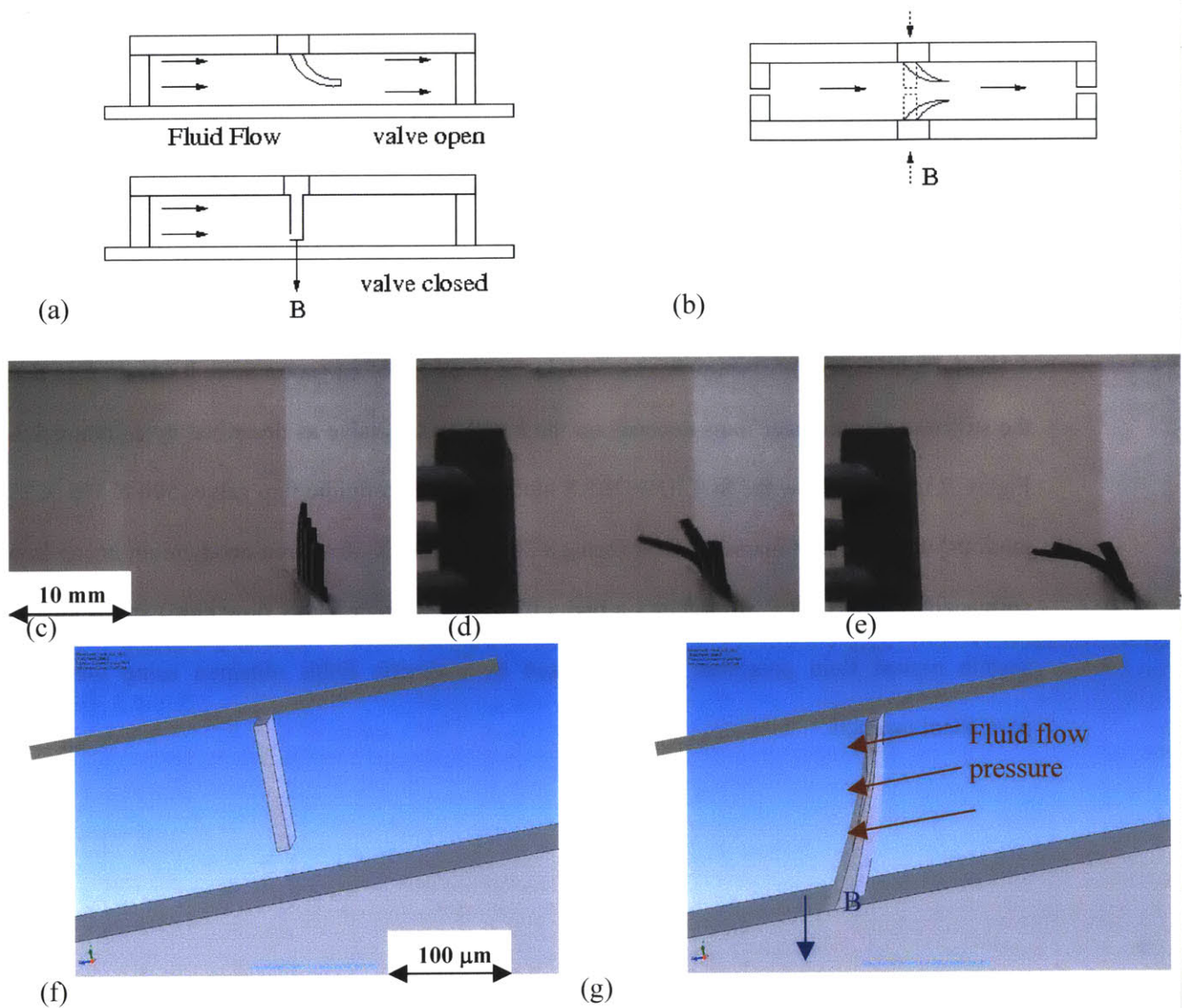


Figure 5.16 (a) Schematic of a cantilever type flap microfluidic valve fabricated by doping PDMS with carbonyl iron particles during the curing process. Magnetic field actuation leads to closing of the valve. (b) Heart-type valve structure (c) MR fluid doped PDMS (5% v/v 1 micron CIP) cured to obtain magneto-responsive elastomer (d)-(e) Magnetic field response of magnetic PDMS flaps. Stiffness is a function of the length of the valve. (f) Solidworks model of a microfluidic flap valve (500 X 100 X 25 microns) (g) Solidworks model of magnetic actuation of the valve using 2000 X 2000 X 50 micron neodymium-boron-iron permanent magnet to stop typical flows in a microfluidic channel.

The current challenge lies in fabrication of these small thickness flap valves as they tend to get separated from the rest of the microfluidic channel during the mold peel-off process as shown in figure 5.17.

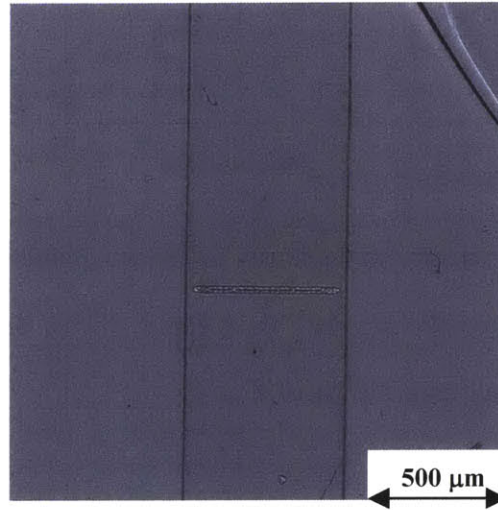


Figure 5.17 MR fluid doped PDMS microfluidic valve separated from the microfluidic channel during standard mold peel off step.

Hence, a controllable microfluidic valve with stiffness dependent on the thickness of the valve and magnetic field strength with its high effectiveness, portability, easy fabrication and manipulation holds tremendous potential for a wide variety of lab-on-chip applications.

Further, the magnetic doped PDMS material due to its natural-muscle like properties ($E \sim 750$ kPa & max strain 10^{-1} to 10^0 (Farshad and Benine, 2004; An and Montgomery, 2003)) also remains an exciting possibility for use as artificial muscle in robotic applications and haptic devices (figure 5.18).

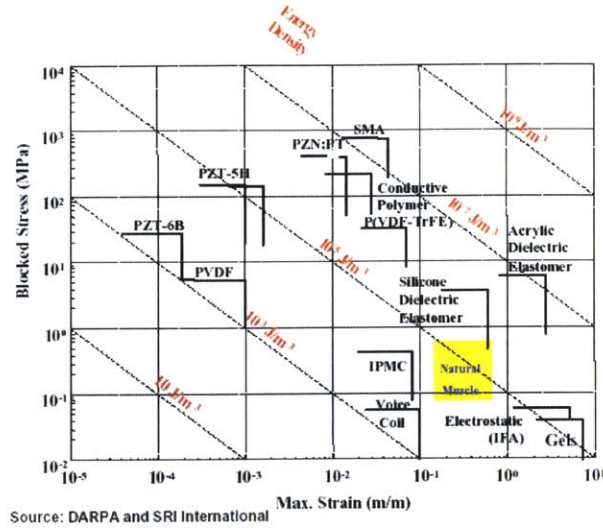


Figure 5.18 Comparison of actuator technologies for future robotic applications and haptic devices (Darpa and SRI International). MR fluid doped PDMS have natural muscle like properties ($E \sim 750 \text{ kPa}$ & max strain 10^{-1} to 10^0).

Magnetic microparticles synthesized from cured carbonyl iron particle doped diacrylate (section 5.1.2) can also be used as ‘on-demand’ valves in microfluidic channels. ‘On-demand’ refers to used-desired valve action at any given point along the microfluidic channel. These magnetic microparticles are inert to both organic and aqueous solvents so that they can be easily injected into any microfluidic channel with single or multiple streams and their magnetic field induced assembly exploited to provide a valve action at any desired location along the microchannel. This technique permits valves to be assembled “on-the-go” so that microfluidic channels with active microvalves do not need to predesigned using multilayer soft lithography techniques. Figure 5.19 shows the schematic of ‘brick-by-brick’ field-induced assembly of a valve at any user-specified location along the microchannel. Figure 5.19(b)-(c) shows the magnetic response of anisotropic particles in a microchannel.

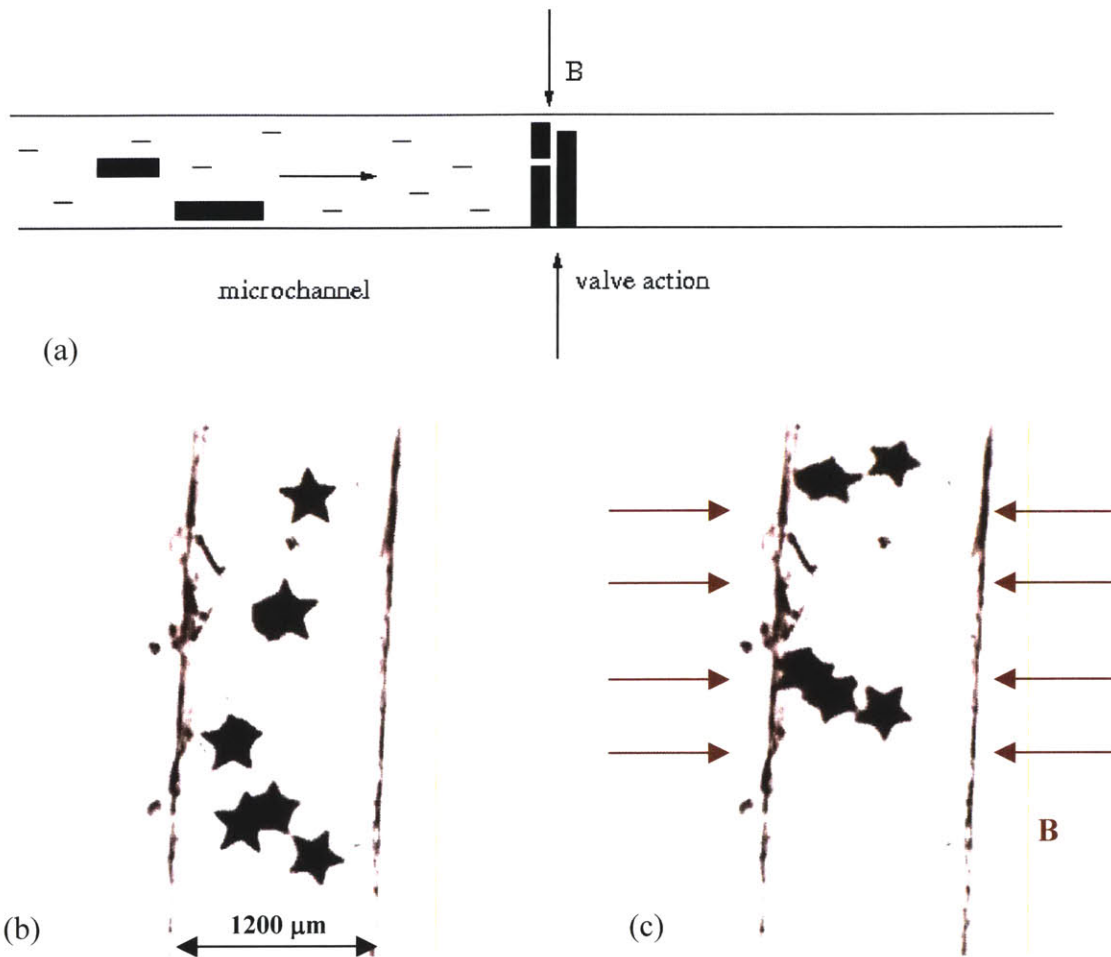


Figure 5.19 ‘On-demand’ valve using magnetic microparticles synthesized using batch mold technique (a) Schematic of field-induced assembly of microparticles providing valve-action at any desired location along the microchannel (b) Star-shaped magnetic microparticles in a microchannel geometry (c) Magnetic field induced assembly of microparticles.

This ‘on-demand’ valve technology provides many advantages such as ease of fabrication, manipulation and control besides a low cost and hence is an attractive alternative to pneumatic, piezoelectric, hydrogel etc. valve technology. The magnetic response is a function of the magnetic susceptibility (as magnetization is a function of volume of magnetic material in the

microparticle) and hence, microparticles with higher magnetic volume fraction will have higher effectiveness of valve action.

5.2.3 Magnetic microfluidic mixers

Microfluidic mixing is crucial to development of total analysis systems (μ -TAS) especially for reaction systems (Boccazzi *et al.*, 2006) and mixing of multiple streams in micro-devices. It is further desirable to have essential components such as mixers easy to fabricate and manipulate. Mixing is diffusion-limited in microchannel geometries due to low Reynolds number ($Re \ll 1$) and typical mixing lengths for laminar flow in microchannels are of the order of centimeters (since, $Pe \gg 1$). Hence, typical passive mixing methodologies consist of introducing chaotic mixing by using bas-relief structures fabricated using planar lithography technique (Stroock *et al.*, 2002), serpentine channels fabricated using micromachining technique or active mixing using magnetic microstirrers fabricated using surface micromachining technique.

Bulk and surface micromachining techniques have limited use due to difficult multistep photolithography and a technology involving rapid prototyping and ease of manipulation in soft lithographic devices is required. Passive mixing can be achieved using gaseous slugs to introduce chaotic transport in the fluid segments (Garstecki *et al.*, 2005; El-Ali *et al.*, 2005).

Magneto-responsive microparticles and structures provide a simple and elegant method to manipulate and use external magnetic fields for active microfluidic mixing. This technology doesn't require any pre-modifications and multistep fabrication in the design of the microfluidic device and can be used by simply streaking the streams or stream with these magnetic microparticles or chains whenever desired.

Biswal and Gast (2004) used permanently linked paramagnetic chains for active microfluidic mixing as shown in figure 5.20(a). Superparamagnetic particles (polystyrene beads with 40 wt% magnetite inclusions with amine functionalized groups at surface) linked with

glutaraldehyde or PEG (Furst *et al.*, 1998) are rotated in three-stream microfluidic channels using rotating magnetic field generated using two coils or a magnetic stir plate. The chains can rotate synchronously (defined phase lag between chain orientation and magnetic field direction) or asynchronously (the phase lag angle is periodic but not constant and the chain reverses direction periodically) depending on the strength of the magnetic torque as compared to the viscous torque.

$$\begin{aligned}\Gamma_m &= \frac{3m^2}{4\pi\mu_0} \frac{N^2}{2d^3} \sin(2\alpha) \\ \Gamma_v &= \kappa V \eta \omega\end{aligned}\tag{5.4}$$

where Γ_m is the magnetic torque using the dipolar approximation, Γ_v is the viscous torque given by stokes drag approximation, α is the phase lag, N is the number of beads in the chain and κ is the shape factor ($\kappa = 2N^2/\ln(N/2)$ for linear chains of N beads). Hence, the rotational dynamics of the chains is a function of the rotational Mason number and the geometrical shape of the chain.

$$\text{Mn}_{\text{rot}} = \frac{32\eta\omega}{\mu_0\chi^2 H^2}\tag{5.5}$$

Figure 5.20(b) shows the dependence of chain behavior in rotating magnetic fields as a function of Mason number and length of the chain

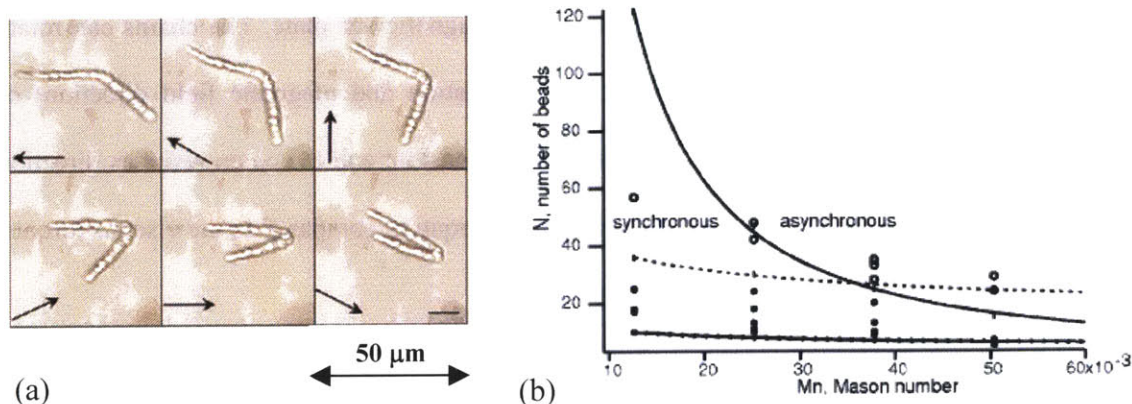


Figure 5.20 (a) Mixing in microfluidic channels using permanently linked magnetic chains (gluteraldehyde / PEG linked paramagnetic particles) and rotating in the presence of magnetic fields (1000 A/m) at 0.1 Hz. (b) Rotational dynamics of chains as a function of the rotational Mason number and number of beads in the chain

Biswal and Gast (2004) have been able to achieve effective mixing using 20-30 micron paramagnetic chains at maximum frequencies of 0.1-0.5 Hz. The frequency and size limitation is due to inefficient mixing for asynchronous rotations. Larger chains rotating at higher frequencies would have more efficient mixing if they were able to rotate synchronously.

Hence, carbonyl iron particle based microparticles and permanently linked chains with their higher magnetic susceptibility and saturation magnetization will prove as more efficient mixers. They have a lower rotational Mason numbers ($Mn \propto 1/\chi^2$) which allows us to overcome these size and frequency limitations. Figure 5.21(b)-(c) shows a needle shaped microstructure, 50 micron wide and 200 micron in length, (1 micron size carbonyl iron particles permanently linked using amidation chemistry as described in section 5.1.1) rotating at 5 Hz frequency at rotating magnetic fields of 1000 A/m. At comparable magnetic fields, at least an order of magnitude increase in size and frequency is obtained using carbonyl iron particle based magnetoresponsive chains.

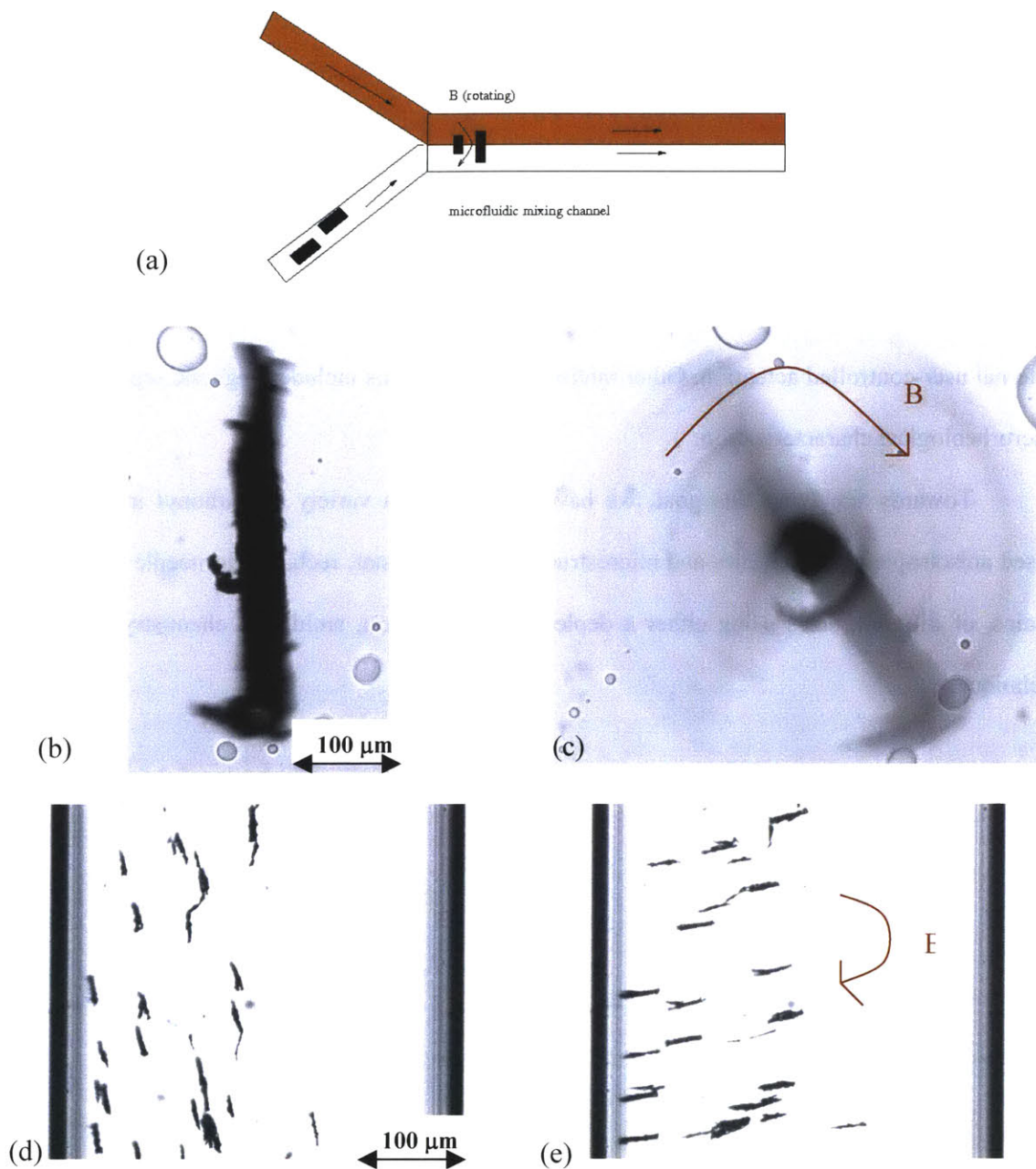


Figure 5.21 (a) Schematic of an ‘on-demand’ mixer using magnetoresponsive microstructures and particles (b) Needle shape synthesized from 1 micron carbonyl iron particles linked using amidation chemistry (500 X 50 microns) (c) Rotating synchronously at 5 Hz in presence of a rotating magnetic field 1000 A/m (d) Permanently linked carbonyl iron particle based chains (50 micron length) strewn in a microfluidic channel (500 X 50 microns) (e) Permanently

linked chains rotating in presence of rotating magnetic field.

5.3 Conclusions

Magnetically actuated components such as valves, mixers and pumps have tremendous potential in microfluidic applications due to their low cost, ease of fabrication, manipulation and external user-controlled actuation. Other microscale applications include magnetic separation and microrheological characterization.

Towards achieving this goal, we have synthesized a variety of carbonyl iron particle based anisotropic microparticles and microstructures, such as star, rectangular, needle shapes and chains, of different sizes using either a depletion flocculation, amidation chemistry or curing technique.

Chapter 6

Conclusions and Future Work

6.1 *Conclusions*

Adaptive materials based on field-responsive fluids have a myriad of applications ranging from automotive crash protection, tunable energy management in automobiles and protective armor to microfluidic devices, materials, chips etc. The success of these applications depends on the in-depth understanding of the fluid behavior and properties along with the application design and mechanical characterization.

In order to understand the field-dependent properties and rheological behavior of field-responsive fluids, a custom rheometer fixture has been designed with 1300 turns of wound magnetic coil. The fixture allows the measurement of field-dependent yield stress wherein the magnetic field strength can be varied upto 0.4 Tesla without water-cooling. Besides commercial fluids, laboratory synthesized MR fluids based on carbonyl iron particles dispersed in silicone oils have also been studied in detail under steady state flow, oscillatory shear and creep flow. Carbonyl iron particles of increasing size result in an increase in the magnetorheological effect (magnetic-field strength dependent yield stress) owing to a higher saturation magnetization. MR fluids stronger than commercial fluids have been synthesized by exploiting this size dependence.

Creep tests have provided us with useful information on the time response of the fluids, which varies from 1-20 ms depending on the magnetic field and the applied stress. Also, experimental data suggests a universal scaling with the scaled stress (σ/σ_y) . These large, reversible and fast changes in the rheological properties have been utilized to modulate the

energy-management capabilities of adaptive composites. MR fluids show highly nonlinear behavior in large amplitude oscillatory shear flow and the deviation of the Lissajous curves from elliptical shapes has been observed, analyzed and modeled.

MR fluid behavior shows striking similarities with the response of other “soft-glassy” materials and the behavior has been captured well by a “soft-glassy” rheology model. The scalings and nonlinearities observed in creep and large amplitude oscillatory shear flow are also well described by the visco-elasto-plastic model that is based on microscopic mechanisms of plastic deformation in yield stress fluids. We expect these scalings observed for MR fluids to be more general in nature and applicable to generalized yield stress fluids.

Field-responsive fluids can be used to modulate the stiffness and energy absorption capacity of cellular solids, fabrics, polymers etc. Shear-thickening fluids, which belong to the class of field-responsive fluids and respond when acted upon by a stress field, can also be impregnated into reticulated foams to provide a passive or even an active mechanism for adaptive energy absorption. Energy management is a vital concern for automobiles and a number of components are required to be occupant and pedestrian ‘safe’ according to new standards and legislations (FMVSS 201/202, EEC WG 17). These requirements usually conflict with passenger and design demands of thin, more compliant and comfortable materials. Also, energy absorption criteria vary depending on whether the occupant is an adult or a child. A ‘novel’ energy absorbing material which provides the automotive industry with a solution to this ‘conflict of stiffness’ problem has been conceptualized, designed and tested in this work. The material consists of a cellular solid or a fibrous matrix impregnated with a field-responsive fluid like a magnetorheological (MR) fluid. This fluid-solid composite has magnetic-field-dependent energy absorption and stiffness and can be user-controlled in tune with the application requirements.

Thus, a ‘novel’ class of conformable field-responsive fluid based composites has been developed so that they can be used for wide-ranging rapidly switching energy absorbing applications.

The study of aggregation dynamics and structure formation of MR fluids in microchannel geometries in the presence of bulk fluid flow has provided us with useful insights into development and further improvement of applications both on the microscale and macroscale. The fast dynamics and aggregation phenomena of MR fluids based on carbonyl iron particles have been captured using the high-speed video microscopy technique for the first time. This has helped us understand the pattern and structure formation at short time scales and how it evolves with time. A wide variety of geometries (shape and size of microchannels) such as the hyperbolic geometry, contraction and obstacle geometries have been used to elucidate the effect of geometry on this structure formation. The cluster distribution has also been captured using a variety of techniques such as the mean cluster size, vertical & horizontal connectivity and two-dimensional image FFT.

The understanding gained from the aggregation phenomena studied in earlier studies involving the quiescent case has been extended to understand the effect of flow on the dynamics. The cluster size distribution is found to be a function of the magnetic field strength, flow rate, volume fraction and the geometry. The longstanding question of the mechanism behind the formation of fibrous, interconnected network structures in MR fluids at higher volume fractions has been answered to a fair degree using this high-speed video-microscopy technique. The defect-driven coarsening that occurs at a faster time scale quickly results in a ‘percolated’ network structure at higher volume fractions. The viscous forces are unable to disrupt these interconnected, fibrous structures which could be primarily responsible to for the high yield stress observed in these fluids.

The presence of flow leads to the formation of a wide variety of structures depending on the interplay of magnetic and hydrodynamic interactions and this study has endeavored to capture the important scalings and mechanisms behind these structure formations. A number of uncorrelated processes with different time scales together govern the structure formation and dynamics of MR fluids in microchannels. The tip-to-tip aggregation process is the dominant

mechanism behind the chain formation at low volume fractions. At longer time scales or at higher volume fractions, the defect-driven coarsening and lateral interactions due to convection dominate the structure formation process. A scaling analysis of the cluster distribution at different time-scales has elucidated these mechanisms.

Even though good qualitative agreement has been obtained between the experimental and simulation results for flow of MR fluids in microchannels, quantitative comparison after refinements in both the experimental setup and the modeling of particle interactions used in the simulation study needs to be investigated in future.

Magnetically actuated components such as valves, mixers and pumps have tremendous potential in microfluidic applications due to their low cost, ease of fabrication, manipulation and external user-controlled actuation. Other microscale applications include magnetic separation and microrheological characterization.

Towards achieving this goal, we have synthesized a variety of carbonyl iron particle based anisotropic microparticles and microstructures, such as star, rectangular, needle shapes and chains, of different sizes using either a depletion flocculation, amidation chemistry or curing technique.

6.2 Future Work

MR fluids with a higher yield stress than currently available commercial MR fluids are desirable not only for the wide range of applications discussed in this thesis but also for many commercial applications such as dampers, brakes, automotive suspensions etc. Exploiting the use of higher magnetization at higher particle sizes, we were able to obtain higher yield-stress fluids. A number of other fluid modifications have the potential of increasing the yield stress and need to be investigated in the future. The use of bidisperse fluids can create a synergy effect at specific

volume fractions, when the cluster packing fraction density increases, leading to a higher yield stress as shown in figure 6.1.

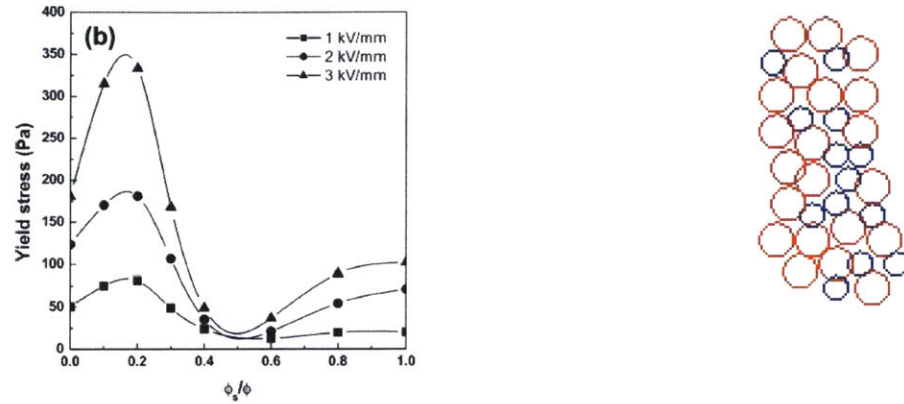


Figure 6.1 (a) Bidisperse ER fluid showing a synergy effect at when the two particles are in 1:4 ratio (Jun *et al.*, 2004). (b) Schematic of a cluster in a bidisperse magnetorheological fluid that have a potential to increase the yield stress for the same magnetic field strength when the cluster packing fraction is higher than that in monodisperse magnetorheological fluids.

The yield stress is limited by the critical plastic strain ($\gamma_c \sim 10^{-2}$) when the chains and column structures collapse. Wormlike flexible magnetic chains (synthesis described in chapter 5) doped in small amounts in a MR fluid have the potential of increasing this critical strain as they would form the backbone of these clusters around which other particles will aggregate and resist collapse at small strains.

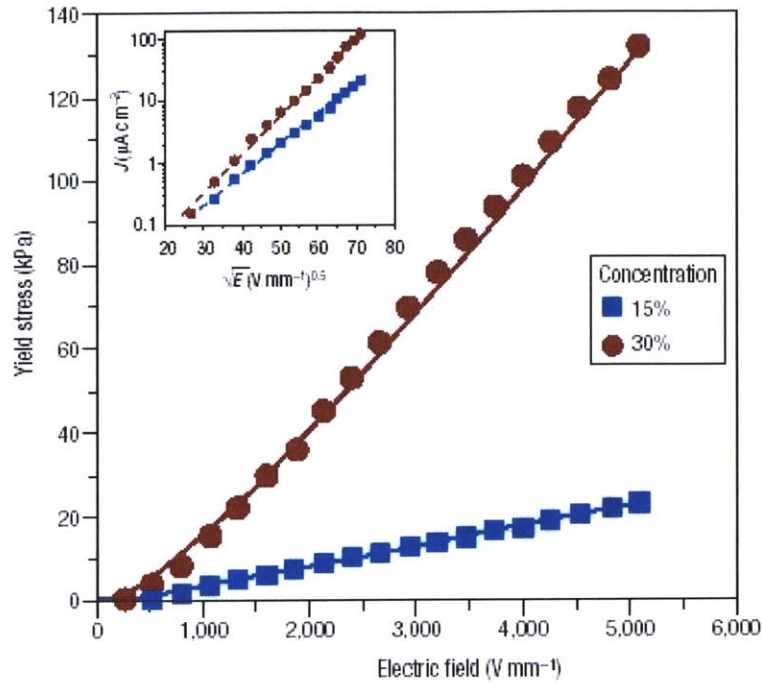


Figure 6.2 Giant electrorheological effect (GER) – nanocoated particles where the coating and the based particle have a huge difference in the conductivity have a yield stress comparable to MR fluids.

The advances that have been made in the synthesis of giant electrorheological fluids (GER) can potentially be applied to magnetorheological fluids and used to improve the yield stress.

Rheological characterization of the field-responsive fluids is essential to successful application design and development and towards this goal, building the version 2 of the custom rheometer fixture described in chapter 2 could be advantageous. Further, fourier-transform rheology could further elucidate the mechanisms behind the nonlinearities observed in large amplitude oscillatory shear flow and could be used as an analysis tool in the future.

Understanding the structure and dynamics on the micro scale during this thesis work has been hampered by the limitations of the measurement systems available for the field of

microfluidics. Since, microfluidics is an area of great interest and continually improving technology, future improvements in the optical and pressure-sensing equipment would help in further refining the knowledge of the dynamics of responsive fluids in microchannels. Capturing the pressure change when a field is applied to a field-responsive fluid flowing in a microchannel can then be related to the bulk yield-stress measurement.

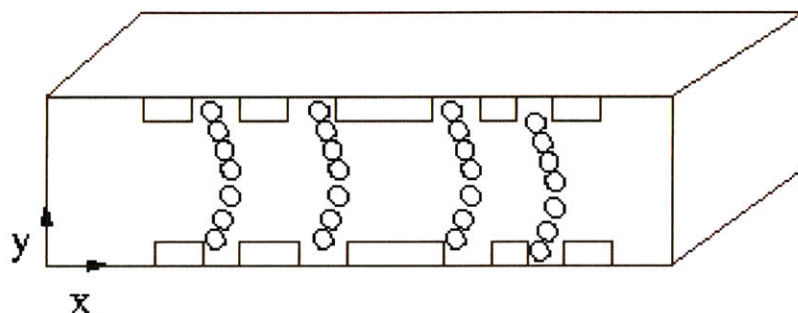


Figure 6.3 Chains slip in pressure driven flow. In order to correlate the yield stress found through bulk rheological characterization with the structures and clusters formed in the microscale, microchannels with roughened surfaces need to be used.

Further, roughened channels can help in reducing the slip of chains along the channel side-walls and hence a more accurate and direct comparison of the bulk yield stress with the pressure change would be possible.

A handful of adaptive composite applications such as energy management systems in automobiles, protective armor and microfluidic valves, mixers have been developed and characterized in this thesis work. However, there is a huge potential for use of tunable materials both on the micro and macro scale.

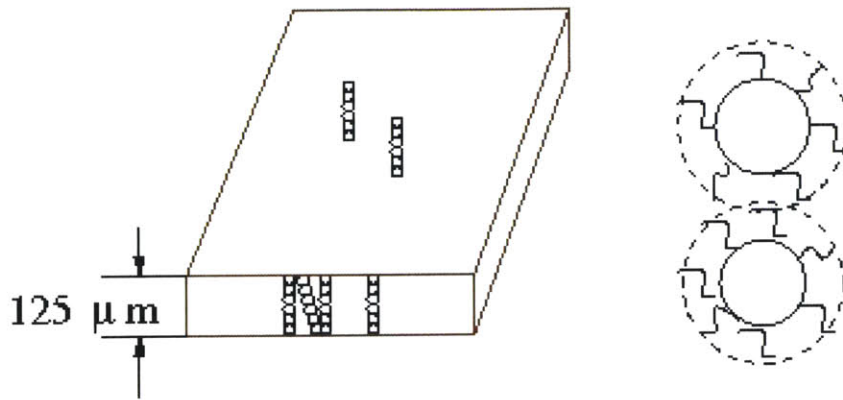


Figure 6.4 Magnetorheological elastomers are expected to have anisotropic thermal conductivity.

One such potential area is in thin films with anisotropic thermal conductivity, which could be useful in a number of defense and cooling applications. MR fluid thin films doped with carbonyl iron particles, aligned in the presence of strong magnetic fields, are expected to have a high thermal conductivity along the thickness as compared to the other orthogonal directions. The challenges in fabricating this elastomer lie in applying a strong enough magnetic field so that the Kapitza resistance (resistance at the boundary of particles to heat transfer) is small and does not decrease the thermal conductivity.

Adaptive ('Smart') materials have a myriad of applications and only a few of them namely in controllable energy absorption and as microfluidic elements have been explored by us. We can envision the extension of this concept to develop a variety of other composite materials that would adapt themselves to external conditions or that can be tuned by the user himself and hence will be useful in a number of commercial applications.

BIBLIOGRAPHY

- Amari, T., Watanabe, K., Macosko, C. W., and L. E. Scriven, (1987). "Creep Measurements on Magnetic Suspension." IEEE Transactions on Magnetics **23**(5): 3239-3241.
- An, Y. X. and M. T. Shaw (2003). "Actuating properties of soft gels with ordered iron particles: basis for a shear actuator." Smart Materials & Structures **12**(2): 157-163.
- Barnes, H. A. (1989). "Shear-Thickening (Dilatancy) in Suspensions of Nonaggregating Solid Particles Dispersed in Newtonian Liquids." Journal of Rheology **33**(2): 329-366.
- Barnes, H. A. (1999). "The yield stress - a review or 'pi alpha nu tau alpha rho epsilon iota' - everything flows?" Journal of Non-Newtonian Fluid Mechanics **81**(1-2): 133-178.
- Beebe, D. J., Moore, J. S., Yu, Q., Liu, R. H., Kraft, M. L., Jo, B. H. and C. Devadoss, (2000). "Microfluidic tectonics: A comprehensive construction platform for microfluidic systems." Proceedings of the National Academy of Sciences of the United States of America **97**(25): 13488-13493.
- Beebe, D. J., Moore, J. S., Bauer, J. M., Yu, Q., Liu, R. H., Devadoss, C. and B. H. Jo, (2000). "Functional hydrogel structures for autonomous flow control inside microfluidic channels." Nature **404**(6778): 588-.
- Bettin, G., Deshmukh, S. S. and G. H. McKinley (2006). "Active controlled energy absorber using responsive fluids. United States *Patent Application*. **11/270,971**.
- Bird, R. B., Stewart, W. E. and E. N. Lightfoot, (1987). Transport Phenomena, John Wiley and Sons.
- Bird, R. B., Armstrong, R. C. and O. Hassager, (1987). Dynamics of Polymeric Liquids, John Wiley and Sons.

- Biswal, S. L. and A. P. Gast (2003). "Mechanics of semiflexible chains formed by poly(ethylene glycol)-linked paramagnetic particles." Physical Review E **68**(2).
- Biswal, S. L. and A. P. Gast (2004). "Micromixing with linked chains of paramagnetic particles." Analytical Chemistry **76**(21): 6448-6455.
- Biswal, S. L. and A. P. Gast (2004). "Rotational dynamics of semiflexible paramagnetic particle chains." Physical Review E **69**(4).
- Boccazzi, P., Zhang, Z., Kurosawa, K., Szita, N., Bhattacharya, S., Jensen, K. F. and A. J. Sinskey, (2006). "Differential gene expression profiles and real-time measurements of growth parameters in *Saccharomyces cerevisiae* grown in microliter-scale bioreactors equipped with internal stirring." Biotechnology Progress **22**(3): 710-717.
- Bombard, A. J. F., Knobel, M., Alcantara, M. R., and I. Joeke, (2002). "Evaluation of magnetorheological suspensions based on carbonyl iron powders." Journal of Intelligent Material Systems and Structures **13**(7-8): 471-478.
- Bombard, A. J. F., Alcantara, M. R., Knobel, M. and P. L. O. Volpe, (2005). "Experimental study of MR suspensions of carbonyl iron powders with different particle sizes." International Journal of Modern Physics B **19**(7-9): 1332-1338.
- Bonnecaze, R. T. and J. F. Brady (1992). "Dynamic Simulation of an Electrorheological Fluid." Journal of Chemical Physics **96**(3): 2183-2202.
- Bonnecaze, R. T. and J. F. Brady (1992). "Yield Stresses in Electrorheological Fluids." Journal of Rheology **36**(1): 73-115.
- Bostrom, O., Fredriksson, R., Haland, Y., Jakobsson, L., Krafft, M., Lovsund, P., Muser, M. H. and M. Y. Svensson, (2000). "Comparison of car seats in low speed rear-end impacts using the BioRID dummy and the new neck injury criterion (NIC)." Accid Anal Prev **32**(2): 321-8.

- Brunet, E., Degre, G., Okkels, F. and P. Tabeling, (2005). "Aggregation of paramagnetic particles in the presence of a hydrodynamic shear." Journal of Colloid and Interface Science **282**(1): 58-68.
- Carlson, J. D. (1999). "Low-cost MR fluid sponge devices." Journal of Intelligent Material Systems and Structures **10**(8): 589-594.
- Carlson, J. D. and M. R. Jolly (2000). "MR fluid, foam and elastomer devices." Mechatronics **10**(4-5): 555-569.
- Carlson, J. D. (2001). What makes a good MR fluid. 8th International Conference on Electrorheological (ER) Fluids and Magnetorheological (MR) Suspensions., Nice, France.
- Cheeseman, B. A. and T. A. Bogetti (2003). "Ballistic impact into fabric and compliant composite laminates." Composite Structures **61**(1-2): 161-173.
- Chin, B. D., Park, J. H., Kwon, M. H. and O. O. Park, (2001). "Rheological properties and dispersion stability of magnetorheological (MR) suspensions." Rheologica Acta **40**(3): 211-219.
- Cho, M. S., Lim, S. T., Jang, I. B., Choi, H. J. and M. S. Jhon, (2004). "Encapsulation of spherical iron-particle with PMMA and its magnetorheological particles." IEEE Transactions on Magnetics **40**(4): 3036-3038.
- Citerne, G. P., Carreau, P. J., and M. Moan, (2001). "Rheological properties of peanut butter." Rheologica Acta **40**(1): 86-96.
- Claracq, J., Sarrazin, J. and J. P. Montfort, (2004). "Viscoelastic properties of magnetorheological fluids." Rheologica Acta **43**(1): 38-49.
- Climent, E., Maxey, M. R. and G. E. Karniadakis, 2004). "Dynamics of self-assembled chaining in magnetorheological fluids." Langmuir **20**(2): 507-513.
- Courtney, W. A. (1999). Improved elastomeric impact absorber with viscous damping.

- Courtney, W. A. and S. O. Oyadiji (2001). "Preliminary investigations into the mechanical properties of a novel shock absorbing elastomeric composite." Journal of Materials Processing Technology **119**(1-3): 379-386.
- Cutillas, S., Bossis, G. and A. Cebers, (1998). "Flow-induced transition from cylindrical to layered patterns in magnetorheological suspensions." Physical Review E **57**(1): 804-811.
- Davis, L. C. (1992). "Polarization Forces and Conductivity Effects in Electrorheological Fluids." Journal of Applied Physics **72**(4): 1334-1340.
- Davis, L. C. (1999). "Model of magnetorheological elastomers." Journal of Applied Physics **85**(6): 3348-3351.
- de Gans, B. J., Hoekstra, H. and J. Mellema, (1999). "Non-linear magnetorheological behaviour of an inverse ferrofluid." Faraday Discussions(112): 209-224.
- Dendukuri, D., Tsoi, K., Hatton, T. A. and P. S. Doyle, (2005). "Controlled synthesis of nonspherical microparticles using microfluidics." Langmuir **21**(6): 2113-2116.
- Dendukuri, D., Pregibon, D. C., Collins, J., Hatton, T. A. and P. S. Doyle, (2006). "Continuous-flow lithography for high-throughput microparticle synthesis." Nature Materials **5**(5): 365-369.
- Deng, T., Prentiss, M. and G. M. Whitesides, (2002). "Fabrication of magnetic microfiltration systems using soft lithography." Applied Physics Letters **80**(3): 461-463.
- Deshmukh, S. S. and G. H. McKinley (2003). Fluid-filled cellular solids for controlled energy absorption. United States *Patent Application* **2004/0173422**.
- Deshmukh, S. S. and G. H. McKinley (2007). "Adaptive energy-absorbing materials using field-responsive fluid-impregnated cellular solids." Smart Materials and Structures **16**(1): 106-113.
- Doyle, P. S., Bibette, J., Bancaud, A. and J. L. Viovy, (2002). "Self-assembled magnetic matrices for DNA separation chips." Science **295**(5563): 2237-2237.

- Dyke, S. J., Spencer, B. F., Sain, M. K. and Carlson, J. D. (1998). "An experimental study of MR dampers for seismic protection." Smart Materials & Structures **7**(5): 693-703.
- Falk, M. L. and J. S. Langer (1998). "Dynamics of viscoplastic deformation in amorphous solids." Physical Review E **57**(6): 7192-7205.
- Farshad, M. and A. Benine (2004). "Magnetoactive elastomer composites." Polymer Testing **23**(3): 347-353.
- Farshad, M. and M. Le Roux (2005). "Compression properties of magnetostrictive polymer composite gels." Polymer Testing **24**(2): 163-168.
- Fermigier, M. and A. P. Gast (1992). "Structure Evolution in a Paramagnetic Latex Suspension." Journal of Colloid and Interface Science **154**(2): 522-539.
- Fermigier, M. and A. P. Gast (1993). "Structure Evolution in a Paramagnetic Latex Suspension." Journal of Magnetism and Magnetic Materials **122**(1-3): 46-50.
- Fielding, S. M., Sollich, P. and M. E. Cates, (2000). "Aging and rheology in soft materials." Journal of Rheology **44**(2): 323-369.
- Furst, E. M., Suzuki, C., Fermigier, M. and A. P. Gast, (1998). "Permanently linked monodisperse paramagnetic chains." Langmuir **14**(26): 7334-7336.
- Furst, E. M. and A. P. Gast (1999). "Micromechanics of dipolar chains using optical tweezers." Physical Review Letters **82**(20): 4130-4133.
- Furst, E. M. and A. P. Gast (2000). "Dynamics and lateral interactions of dipolar chains." Physical Review E **62**(5): 6916-6925.
- Furst, E. M. and A. P. Gast (2000). "Micromechanics of magnetorheological suspensions." Physical Review E **61**(6): 6732-6739.
- Garstecki, P., Fischbach, M. A. and G. M. Whitesides, (2005). "Design for mixing using bubbles in branched microfluidic channels." Applied Physics Letters **86**(24).
- Genc, S. and P. P. Phule (2002). "Rheological properties of magnetorheological fluids." Smart Materials & Structures **11**(1): 140-146.

- Gibson, L. J. (1997). Cellular solids : structure and properties. Cambridge [England] ; New York, Cambridge University Press.
- Ginder, J. M. and L. C. Davis (1994). "Shear Stresses in Magnetorheological Fluids - Role of Magnetic Saturation." Applied Physics Letters **65**(26): 3410-3412.
- Ginder, J. M., Davis, L. C. and L. D. Elie, (1996). "Rheology of magnetorheological fluids: Models and measurements." International Journal of Modern Physics B **10**(23-24): 3293-3303.
- Ginder, J. M. (1996). Rheology controlled by magnetic fields. Encyclopedia of Applied Physics, VCH Publishers Inc. **16**: 487-.
- Goncharenko, A. (2004). "Optical properties of core-shell particle composites. I. Linear response." Chemical Physics Letters **386**(1-3): 25-31.
- Gooding, E. (1999). Adaptive, energy absorbing structure. US **5915819**.
- Goubault, C., Jop, P., Fermigier, M., Baudry, J., Bertrand, E. and J. Bibette, (2003). "Flexible magnetic filaments as micromechanical sensors." Physical Review Letters **91**(26).
- Haghighi, R. and P. S. Doyle (2004). "Structural analysis of a dipole system in two-dimensional channels." Physical Review E **70**(6).
- Haghighi, R. and P. S. Doyle (2005). "Structure and dynamics of repulsive magnetorheological colloids in two-dimensional channels." Physical Review E **72**(1).
- Halsey, T. C. and W. Toor (1990). "Structure of Electrorheological Fluids." Physical Review Letters **65**(22): 2820-2823.
- Halsey, T. C. (1992). "Electrorheological Fluids." Science **258**(5083): 761-766.
- Hatch, A., Kamholz, A. E., Holman, G., Yager, P. and K. F. Bohringer, (2001). "A ferrofluidic magnetic micropump." Journal of Microelectromechanical Systems **10**(2): 215-221.
- Hayes, W. C., Robinovitch, S. N. and T. A. McMahon, (1996). Bone fracture prevention method. United States **5545128 A**.

- Hebraud, P. and F. Lequeux (1998). "Mode-coupling theory for the pasty rheology of soft glassy materials." Physical Review Letters **81**(14): 2934-2937.
- Holnicki-Szulc, J., Pawlowski, P. and M. Wiklo, (2003). "High-performance impact absorbing materials - the concept, design tools and applications." Smart Materials & Structures **12**(3): 461-467.
- Ismagilov, R. F., Rosmarin, D., Kenis, P. J. A., Chiu, D. T., Zhang, W., Stone, H. A. and G. M. Whitesides, (2001). "Pressure-driven laminar flow in tangential microchannels: an elastomeric microfluidic switch." Analytical Chemistry **73**(19): 4682-4687.
- Jackson, W. C., Tran, H. D., O'Brien, M. J., Rabinovich, E. and G. P. Lopez, (2001). "Rapid prototyping of active microfluidic components based on magnetically modified elastomeric materials." Journal of Vacuum Science & Technology B **19**(2): 596-599.
- Jakobsson, L., Lundell, B., Norin, H. and I. Isaksson-Hellman, (2000). "WHIPS--Volvo's Whiplash Protection Study." Accid Anal Prev **32**(2): 307-19.
- Jenkins, P. and M. Snowden (1996). "Depletion flocculation in colloidal dispersions." Advances in Colloid and Interface Science **68**: 57-96.
- Jiang, P., Bertone, J. F. and V. L. Colvin, (2001). "A lost-wax approach to monodisperse colloids and their crystals." Science **291**(5503): 453-457.
- Jolly, M. R., Carlson, J. D. and B. C. Munoz, (1996). "A model of the behaviour of magnetorheological materials." Smart Materials & Structures **5**(5): 607-614.
- Jolly, M. R., Bender, J. W. and J. D. Carlson, (1999). "Properties and applications of commercial magnetorheological fluids." Journal of Intelligent Material Systems and Structures **10**(1): 5-13.
- Kanianthra, J. N. (1996). Side impact energy absorber, United States **5564535**.
- Kaschta, J. and F. R. Schwarzl (1994). "Calculation of Discrete Retardation Spectra from Creep Data .I. Method." Rheologica Acta **33**(6): 517-529.

- Kaschta, J. and F. R. Schwarzl (1994). "Calculation of Discrete Retardation Spectra from Creep Data .2. Analysis of Measured Creep Curves." Rheologica Acta **33**(6): 530-541.
- Khoo, M. and C. Liu (2001). "Micro magnetic silicone elastomer membrane actuator." Sensors and Actuators a-Physical **89**(3): 259-266.
- Kittipoomwong, D., Klingenberg, D. J. and J. C. Ulicny (2005). "Dynamic yield stress enhancement in bidisperse magnetorheological fluids." Journal of Rheology **49**(6): 1521-1538.
- Klingenberg, D. J., Vanswol, F. and C. F. Zukoski, (1989). "Dynamic Simulation of Electrorheological Suspensions." Journal of Chemical Physics **91**(12): 7888-7895.
- Klingenberg, D. J. and C. F. Zukoski (1990). "Studies on the Steady-Shear Behavior of Electrorheological Suspensions." Langmuir **6**(1): 15-24.
- Klingenberg, D. J., Vanswol, F. and C. F. Zukoski, (1991). "The Small Shear Rate Response of Electrorheological Suspensions .1. Simulation in the Point-Dipole Limit." Journal of Chemical Physics **94**(9): 6160-6169.
- Klingenberg, D. J., Vanswol, F. and C. F. Zukoski, (1991). "The Small Shear Rate Response of Electrorheological Suspensions .2. Extension Beyond the Point-Dipole Limit." Journal of Chemical Physics **94**(9): 6170-6178.
- Klingenberg, D. J., Zukoski, C. F. and J. C. Hill, (1993). "Kinetics of Structure Formation in Electrorheological Suspensions." Journal of Applied Physics **73**(9): 4644-4648.
- Klingenberg, D. J. (2001). "Magnetorheology: Applications and challenges." Aiche Journal **47**(2): 246-249.
- Kormann, C., Laun, H. M. and H. J. Richter (1996). "MR fluids with nano-sized magnetic particles." International Journal of Modern Physics B **10**(23-24): 3167-3172.
- Laeuger, J., Wollny, K., Stettin, H. and S. Huck (2005). "New device for the full rheological characterization of magneto-rheological fluids." International Journal of Modern Physics B **19**(7-9): 1353-1359.

- Larson, R. G. (1999). The Structure and Rheology of Complex Fluids, Oxford University Press.
- Lee, Y. S., Wetzel, E. D. and N. J. Wagner (2003). "The ballistic impact characteristics of Kevlar (R) woven fabrics impregnated with a colloidal shear thickening fluid." Journal of Materials Science **38**(13): 2825-2833.
- Lee, Y. S. and N. J. Wagner (2003). "Dynamic properties of shear thickening colloidal suspensions." Rheologica Acta **42**(3): 199-208.
- Lemaire, E. and G. Bossis (1991). "Yield Stress and Wall Effects in Magnetic Colloidal Suspensions." Journal of Physics D-Applied Physics **24**(8): 1473-1477.
- Lemaire, E., Meunier, A. and G. Bossis (1995). "Influence of the Particle-Size on the Rheology of Magnetorheological Fluids." Journal of Rheology **39**(5): 1011-1020.
- Li, W. H., Chen, G. and S. H. Yeo (1999). "Viscoelastic properties of MR fluids." Smart Materials & Structures **8**(4): 460-468.
- Li, W. H., Yao, G. Z., Chen, G., Yeo, S. H. and F. F. Yap (2000). "Testing and steady state modeling of a linear MR damper under sinusoidal loading." Smart Materials & Structures **9**(1): 95-102.
- Li, W. H., Du, H., Chen, G., Yeo, S. H. and N. Q. Guo (2002). "Nonlinear rheological behavior of magnetorheological fluids: step-strain experiments." Smart Materials & Structures **11**(2): 209-217.
- Li, W. H., Du, H., Chen, G. and S. H. Yeo (2002). "Experimental investigation of creep and recovery behaviors of magnetorheological fluids." Materials Science and Engineering a-Structural Materials Properties Microstructure and Processing **333**(1-2): 368-376.
- Li, W. H., Du, H. J., Chen, G., Yeo, S. H. and N. Q. Guo (2003). "Nonlinear viscoelastic properties of MR fluids under large-amplitude-oscillatory-shear." Rheologica Acta **42**(3): 280-286.
- Li, H., Peng, X. and W. Chen (2005). "Simulation of the chain-formation process in magnetic fields." Journal of Intelligent Material Systems and Structures **16**(7-8): 653-658.

- Liang, W., Tadros, T. F. and P. F. Luckham (1994). "Flocculation of Sterically Stabilized Polystyrene Latex-Particles by Adsorbing and Nonadsorbing Poly(Acrylic Acid)." Langmuir **10**(2): 441-446.
- Linder, A. (2000). "A new mathematical neck model for a low-velocity rear-end impact dummy: evaluation of components influencing head kinematics." Accid Anal Prev **32**(2): 261-9.
- Liu, R. H., Stremmer, M. A., Sharp, K. V., Olsen, M. G., Santiago, J. G., Adrian, R. J., Aref, H. and D. J. Beebe (2000). "Passive mixing in a three-dimensional serpentine microchannel." Journal of Microelectromechanical Systems **9**(2): 190-197.
- Lu, L. H., Ryu, K. S. and C. Liu (2002). "A magnetic microstirrer and array for microfluidic mixing." Journal of Microelectromechanical Systems **11**(5): 462-469.
- Ly, H. V., Reitich, E., Jolly, M. R., Banks, H. T. and K. Ito (1999). "Simulations of particle dynamics in magnetorheological fluids." Journal of Computational Physics **155**(1): 160-177.
- Madden, J. D. W., Vandesteeg, N. A., Anquetil, P. A., Madden, P. G. A., Takshi, A., Pytel, R. Z., Lafontaine, S. R., Wieringa, P. A. and I. W. Hunter, (2004). "Artificial muscle technology: Physical principles and naval prospects." Ieee Journal of Oceanic Engineering **29**(3): 706-728.
- Martin, J. E., Odinek, J. and T. C. Halsey, (1992). "Evolution of Structure in a Quiescent Electrorheological Fluid." Physical Review Letters **69**(10): 1524-1527.
- Martin, J. E. and J. Odinek (1995). "A Light-Scattering Study of the Nonlinear Dynamics of Electrorheological Fluids in Oscillatory Shear." Journal of Rheology **39**(5): 995-1009.
- Martin, J. E., Anderson, R. A. and C. P. Tigges, (1998). "Simulation of the athermal coarsening of composites structured by a biaxial field." Journal of Chemical Physics **108**(18): 7887-7900.

- Martin, J. E., Anderson, R. A. and C. P. Tigges, (1998). "Simulation of the athermal coarsening of composites structured by a uniaxial field." Journal of Chemical Physics **108**(9): 3765-3787.
- Martin, J. E., Odinek, J., Halsey, T. C. and R. Kamien, (1998). "Structure and dynamics of electrorheological fluids." Physical Review E **57**(1): 756-775.
- Martin, J. E., Hill, K. M. and C. P. Tigges, (1999). "Magnetic-field-induced optical transmittance in colloidal suspensions." Physical Review E **59**(5): 5676-5692.
- Martin, J. E., Anderson, R. A. and C. P. Tigges, (1999). "Thermal coarsening of uniaxial and biaxial field-structured composites." Journal of Chemical Physics **110**(10): 4854-4866.
- Mason, T. G. and D. A. Weitz (1995). "Optical Measurements of Frequency-Dependent Linear Viscoelastic Moduli of Complex Fluids." Physical Review Letters **74**(7): 1250-1253.
- McDonald, J. C. and G. M. Whitesides (2002). "Poly(dimethylsiloxane) as a material for fabricating microfluidic devices." Accounts of Chemical Research **35**(7): 491-499.
- McMurry, J. and R. C. Fay (2004). Chemistry, Prentice Hall.
- Meakin, P. (1992). "Aggregation Kinetics." Physica Scripta **46**(4): 295-331.
- Melle, S., Rubio, M. A. and G. G. Fuller, (2001). "Time scaling regimes in aggregation of magnetic dipolar particles: Scattering dichroism results." Physical Review Letters **87**11(11): art. no.-115501.
- Melle, S., Rubio, M. A. and G. G. Fuller, (2001). "Structure and dynamics of magnetorheological fluids in rotating magnetic fields (vol E 61, pg 4111, 2000)." Physical Review E **63**05(5).
- Minc, N., Futterer, C., Dorfman, K., Bancaud, A., Gosse, C., Goubault, C. and J. L. Viovy, (2004). "Quantitative microfluidic separation of DNA in self-assembled magnetic matrixes." Analytical Chemistry **76**(13): 3770-3776.
- Mohebi, M., Jamasbi, N. and J. Liu, (1996). "Simulation of the formation of nonequilibrium structures in magnetorheological fluids subject to an external magnetic field." Physical Review E **54**(5): 5407-5413.

- Niklasson, G. A., Torebring, A., Larsson, C., Granqvist, C. G. and T. Farestam, (1988). "Fractal Dimension of Gas-Evaporated Co Aggregates - Role of Magnetic Coupling." Physical Review Letters **60**(17): 1735-1738.
- Nisisako, T., Torii, T., Takahashi, T. and Y. Takizawa, (2006). "Synthesis of monodisperse bicolored janus particles with electrical anisotropy using a microfluidic co-flow system." Advanced Materials **18**(9): 1152-+.
- Oh, K. W. and C. H. Ahn (2006). "A review of microvalves." Journal of Micromechanics and Microengineering **16**(5): R13-R39.
- Pamme, N. (2006). "Magnetism and microfluidics." Lab on a Chip **6**(1): 24-38.
- Pan, X. D. and G. H. McKinley (1997). "Structural limitation to the material strength of electrorheological fluids." Applied Physics Letters **71**(3): 333-335.
- Pan, X. D. and G. H. McKinley (1997). "Characteristics of electrorheological responses in an emulsion system." Journal of Colloid and Interface Science **195**(1): 101-113.
- Pan, X. D. and G. H. McKinley (1998). "Simultaneous measurement of viscoelasticity and electrical conductivity of an electrorheological fluid." Langmuir **14**(5): 985-989.
- Parthasarathy, M. and D. J. Klingenberg (1996). "Electrorheology: Mechanisms and models." Materials Science & Engineering R-Reports **17**(2): 57-103.
- Parthasarathy, M. and D. J. Klingenberg (1999). "Large amplitude oscillatory shear of ER suspensions." Journal of Non-Newtonian Fluid Mechanics **81**(1-2): 83-104.
- Phule, P. P. (1999). Magnetorheological Fluid. United States **5985168A**.
- Promislow, J. H. E., Gast, A. P. and M. Fermigier, (1995). "Aggregation Kinetics of Paramagnetic Colloidal Particles." Journal of Chemical Physics **102**(13): 5492-5498.
- Quake, S. R. and A. Scherer (2000). "From micro- to nanofabrication with soft materials." Science **290**(5496): 1536-1540.
- Rankin, P. J., Horvath, A. T. and D. J. Klingenberg, (1999). "Magnetorheology in viscoplastic media." Rheologica Acta **38**(5): 471-477.

- Rida, A. and M. A. M. Gijs (2004). "Manipulation of self-assembled structures of magnetic beads for microfluidic mixing and assaying." Analytical Chemistry **76**(21): 6239-6246.
- Rolland, J. P., Maynor, B. W., Euliss, L. E., Exner, A. E., Denison, G. M. and J. M. DeSimone, (2005). "Direct fabrication and harvesting of monodisperse, shape-specific nanobiomaterials." Journal of the American Chemical Society **127**(28): 10096-10100.
- Sanchez, R. D., Rivas, J., Vaqueiro, P., Lopez-Quintela, M. A. and D. Caeiro, (2002). "Particle size effects on magnetic garnets prepared by a properties of yttrium iron sol-gel method." Journal of Magnetism and Magnetic Materials **247**(1): 92-98.
- Sandrin, G. and J. D. Carlson (2001). Controllable device having a matrix medium retaining structure. United States **6202806 B1**.
- See, H. and M. Doi (1991). "Aggregation Kinetics in Electrorheological Fluids." Journal of the Physical Society of Japan **60**(8): 2778-2782.
- See, H., Chen, R. and M. Keentok, (2004). "The creep behaviour of a field-responsive fluid." Colloid and Polymer Science **282**(5): 423-428.
- Sim, H. G., Ahn, K. H. and S. J. Lee, (2003). "Large amplitude oscillatory shear behavior of complex fluids investigated by a network model: a guideline for classification." Journal of Non-Newtonian Fluid Mechanics **112**(2-3): 237-250.
- Singh, H., Laibinis, P. E. and T. A. Hatton (2005). "Synthesis of flexible magnetic nanowires of permanently linked core-shell magnetic beads tethered to a glass surface patterned by microcontact printing." Nano Letters **5**(11): 2149-2154.
- Singh, H., Laibinis, P. E. and T. A. Hatton (2005). "Rigid, superparamagnetic chains of permanently linked beads coated with magnetic nanoparticles. Synthesis and rotational dynamics under applied magnetic fields." Langmuir **21**(24): 11500-11509.
- Sollich, P., Lequeux, F., Hebraud, P. and M. E. Cates, (1997). "Rheology of soft glassy materials." Physical Review Letters **78**(10): 2020-2023.

- Sollich, P. (1998). "Rheological constitutive equation for a model of soft glassy materials." Physical Review E **58**(1): 738-759.
- Spencer, B. F., Dyke, S. J., Sain, M. K. and Carlson, J. D. (1997). "Phenomenological model for magnetorheological dampers." Journal of Engineering Mechanics-Asce **123**(3): 230-238.
- Stroock, A. D., Dertinger, S. K. W., Ajdari, A., Mezic, I., Stone, H. A. and G. M. Whitesides, (2002). "Chaotic mixer for microchannels." Science **295**(5555): 647-651.
- Studer, V., Hang, G., Pandolfi, A., Ortiz, M., Anderson, W. F. and S. R. Quake, (2004). "Scaling properties of a low-actuation pressure microfluidic valve." Journal of Applied Physics **95**(1): 393-398.
- Svensson, M. Y., Lovsund, P., Haland, Y. and S. Larsson, (1996). "The influence of seat-back and head-restraint properties on the head-neck motion during rear-impact." Accid Anal Prev **28**(2): 221-7.
- Tang, X., Zhang, X., Tao, R. and Y. Rong, (2000). "Structure-enhanced yield stress of magnetorheological fluids." Journal of Applied Physics **87**(5): 2634-2638.
- Thorsen, T., Roberts, R. W., Arnold, F. H. and S. R. Quake, (2001). "Dynamic pattern formation in a vesicle-generating microfluidic device." Physical Review Letters **86**(18): 4163-4166.
- Thorsen, T., Maerkl, S. J. and S. R. Quake, (2002). "Microfluidic large-scale integration." Science **298**(5593): 580-584.
- Trlica, J., Saha, P., Quadrat, O. and J. Stejskal, (2000). "Electrorheology of polyaniline-coated silica particles in silicone oil." Journal of Physics D-Applied Physics **33**(15): 1773-1780.
- Unger, M. A., Chou, H. P., Thorsen, T., Scherer, A. and S. R. Quake, (2000). "Monolithic microfabricated valves and pumps by multilayer soft lithography." Science **288**(5463): 113-116.
- Volkova, O., Cutillas, S., Carletto, P., Bossis, G., Cebers, A. and A. Meunier, (1999). "Flow-induced structures in magnetorheological suspensions." Journal of Magnetism and Magnetic Materials **201**: 66-69.

- Wang, J. and G. Meng (2001). "Magnetorheological fluid devices: principles, characteristics and applications in mechanical engineering." Proceedings of the Institution of Mechanical Engineers Part L- Journal of Materials-Design and Applications **215**(L3): 165-174.
- Weiss, K. D., Carlson, J. D. and D. A. Nixon, (1994). "Viscoelastic Properties of Magnetorheological and Electrorheological Fluids." Journal of Intelligent Material Systems and Structures **5**(6): 772-775.
- Welcher, J. B. and T. J. Szabo (2001). "Relationships between seat properties and human subject kinematics in rear impact tests." Accid Anal Prev **33**(3): 289-304.
- Wen, W. J., Huang, X. X., Yang, S. H., Lu, K. Q. and P. Sheng, (2003). "The giant electrorheological effect in suspensions of nanoparticles." Nature Materials **2**(11): 727-730.
- Wen, W. J., Huang, X. X. and P. Sheng, (2004). "Particle size scaling of the giant electrorheological effect." Applied Physics Letters **85**(2): 299-301.
- Whitesides, G. M. (2006). "The origins and the future of microfluidics." Nature **442**(7101): 368-373.
- Wilhelm, M., Maring, D. and H. W. Spiess (1998). "Fourier-transform rheology." Rheologica Acta **37**(4): 399-405.
- Wollny, K., Lauger, J. and H. Siegfried (2002). "Magneto sweep – a new method for characterizing the viscoelastic properties of magneto-rheological fluids." Applied Rheology **12**(1): 25-31.
- Wu, C. W. and H. Conrad (1997). "Influence of a surface film on conducting particles on the electrorheological response with alternating current fields." Journal of Applied Physics **81**(12): 8057-8063.
- Yang, G., Spencer, B. F., Carlson, J. D. and M. K. Sain (2002). "Large-scale MR fluid dampers: modeling and dynamic performance considerations." Engineering Structures **24**(3): 309-323.

- Yoshimura, A. S., Prudhomme, R. K., Princen, H. M. and A. D. Kiss (1987). "A Comparison of Techniques for Measuring Yield Stresses." Journal of Rheology **31(8)**: 699-710.
- Yoshimura, A. and R. K. Prudhomme (1988). "Wall Slip Corrections for Couette and Parallel Disk Viscometers." Journal of Rheology **32(1)**: 53-67.
- Young, B. O. (1972). Liquid shock absorbing buffer, Energy absorption systems, Inc., United States **3672657**.

2001.12